4d and 5d compounds as the new frontier of the anisotropic spin physics

A DISSERTATION
SUBMITTED TO THE FACULTY OF THE GRADUATE SCHOOL
OF THE UNIVERSITY OF MINNESOTA
BY

Yuriy Sizyuk

IN PARTIAL FULFILLMENT OF THE REQUIREMENTS
FOR THE DEGREE OF
DOCTOR OF PHILOSOPHY

Natalia Perkins

July, 2017

Acknowledgements

There are many people that have helped me in my journey in graduate school. First and foremost I would like to thank my advisor, Natalia Perkins. She has taught me a lot and I can only hope to eventually repay her for everything she has done for me. I would also like to give special thanks to Peter Wölfle whose insight has been invaluable in this work.

I would also like to express my gratitude to all other collaborators: Ioannis Rousochatzakis, Gia-Wei Chern, Craig Price, David Hsieh, and Darius Torchinsky.

Useful discussions and moral support were also provided by my friends and fellow graduate students. Among them of particular note were: Alberto Hinojosa Alvarado, Andrew Loveridge, Samuel Ducatman, Nicholas Brewer, Yushan Wang, Nicholas Vanderslice, and James Kapaldo.

Dedication

To my parents for putting up with me all this time.

Abstract

I perform a series of studies of the magnetism of 4d and 5d transition metal compounds. In particular I concentrate on the realization of anisotropic magnetic Hamiltonians by use of the spin-orbit coupling to tie together the real space geometry and spin space magnetism.

In the first part, I derive the magnetic Hamiltonians of Sr_2IrO_4 and Na_2IrO_3 from microscopic parameters. The difficulty of these calculation arises from the fact that many microscopic parameters, such as Hund's coupling, spin-orbit coupling, and crystal field distortions are all of the same order and thus have to be treated on an equal footing. The competition and cooperation of these interactions leads to a rich magnetic Hamiltonians with many different anisotropic interactions. My calculations provide a clear dependence of these interactions on the microscopic parameters. This in turn can be used experimentally to single out and enhance given anisotropies by changing the microscopic parameters.

In the second part I propose experimental measurements for the anisotropic interactions. In particular I study how different anisotropic interactions contribute to the anisotropy in the Curie-Weiss temperatures of these compounds. I show that the difference of Curie-Weiss temperatures along particular axes gives a way to measure the strength of the anisotropic interactions in the compounds.

In the last part, I study how the multitude of the magnetic anisotropies determine the magnetic ground state in 4d and 5d compounds. We have developed a new method to calculate the fluctuational contribution to the free energy in anisotropic Hamiltonians at any temperature within the magnetically ordered phase. The calculation can be done for both classical (which includes only thermal fluctuations) and quantum (quantum and thermal fluctuations) systems. I also study the effects of external magnetic field applied to the nearest neighbor Kitaev-Heisenberg model, a model of particular interest for $\alpha-RuCl_3$.

Contents

List of Tables

List of Figures

Chapter 1

Introduction

1.1 Motivation for studying 4d and 5d transition metal compounds

The interest in the magnetism of 4d and 5d transition metal compounds started from two separate sources. The first source is the comparison to the high-T_C unconventional superconductors. The similarities between iridates and cuprates led to a still ongoing search for a new family of superconductors in the former. The second source of interest in 4d and 5d compounds is the possibility of realizing anisotropic magnetic Hamiltonians. Strong spin-orbit coupling (SOC) in the heavy elements plays an important role in allowing anisotropic magnetic interactions by entangling real space geometry with spin space magnetism. Anisotropic magnetic Hamiltonians such as the honeycomb Kitaev model [3] are of interest as possible realizations of topological quantum computers that are immune to the problem of decoherence of quantum states due to local noise. By storing the quantum information in inherently non-local topological states it becomes safe from noise that affects only a part of the system.

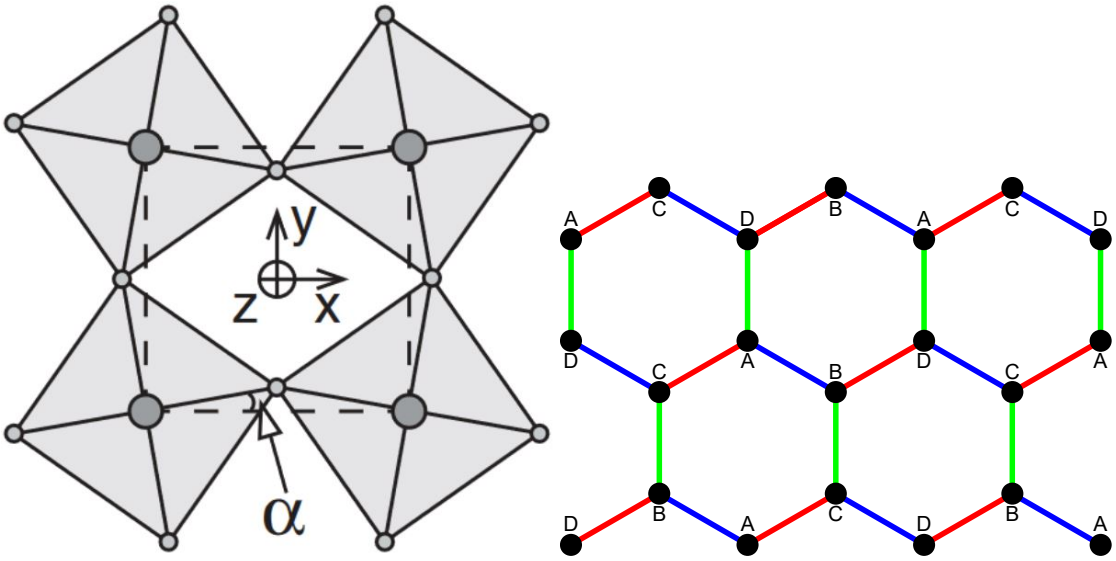

Figure 1.1: (a) Square lattice formed by Ir atoms (big circles) encapsulated by corner sharing oxygen (small circles) octahedra with staggered pattern of rotation of the octahedra. Figure taken from [1]. (b) The honeycomb lattice with 3 types of Kitaev bonds: red, blue, and green bonds have the Kitaev interaction of x, y, and z spin components, respectively. The site labels A-D are the labels of the 4 sublattices in the Klein transformation of the Kitaev-Heisenberg model.

1.2 Strong magnetic interactions as a possible source of superconductivity

The details of the pairing mechanism in cuprates and iron pnictides are still unknown, however it has been speculated that it is magnetic in origin. The idea was to search for compounds with similar, but stronger magnetic properties which would have a stronger pairing and as a result a higher T_C. This sparked a particular interest in Sr_2IrO_4 [4, 5], which has a very similar structure to cuprate parent compounds La_2IrO_4 and Ba_2IrO_4. Each of the magnetic sites of these compounds (Ir and Cu) are surrounded by an oxygen octahedron. The octahedra form a square lattice with a staggered rotation pattern (see Fig.1.1a). The square lattice layers of the magnetic sites are separated by layers of nonmagnetic Sr, La, or Ba atoms. This allows us to view the compounds as a set of isolated 2D magnetic layers with negligible interlayer coupling.

Sr_2IrO_4 has a particularly large "weak" ferromagnetic moment of $\sim 0.14\mu_B$ [5] per

site in the layer, which is about 2 orders of magnitude larger than the corresponding ferromagnetic moment in La_2IrO_4. This sparked an ongoing search for the superconductivity in doped Sr_2IrO_4. So far a pseudogap phase with Fermi arcs have been detected [6], however no smoking gun evidence of superconductivity.

1.3 Spin orbit coupling as a source of anisotropic spin Hamiltonians

The second source of interest in the 4d and 5d compounds stems from the possibility of realizing anisotropic spin models, such as the exactly solvable Kitaev honeycomb model [3]. In the Kitaev model the honeycomb lattice consists of 3 types of bonds (see Fig.1.1b). On each bond type only one component of the spins interacts. Namely, red bonds only interact via x components, blue via y components, and green via z components:

$$\mathcal{H} = \sum_{<ij>^{red}} S_i^x S_j^x + \sum_{<ij>^{blue}} S_i^y S_j^y + \sum_{<ij>^{green}} S_i^z S_j^z \tag{1.1}$$

This Hamiltonian is anisotropic and thus very different from the isotropic Heisenberg interactions that usually results from superexchange calculations in one-band Hubbard model. The standard superexchange calculation runs as follows: suppose there are two sites with one electron (or hole) on a single orbital on each site. If the orbitals of the two sites have a finite overlap integral, then an electron from one site has a finite probability to hop to its neighbor. This costs electrostatic energy since it brings the two electrons close to each other on a single site. However, in the context of second order perturbation theory we can use this as a virtual, temporary state to lower the energy of the ground state of the system:

$$\delta E = \frac{< 1,1|T_{j,i}|0,2 >< 0,2|T_{i,j}|1,1 >}{E_{\text{gs}} - E_{\text{vs}}} \tag{1.2}$$

where $T_{i,j}$ is the hopping operator from site i to j, E_{gs} is the ground state energy and E_{vs} is the energy of the virtual, excited state. The $|n_i, n_j >$ represent states with n_i electrons on site i and n_j electrons on site j. Note that this correction to the ground state energy is identically zero when the two electrons have the same spin due to the Pauli principle. Thus, the closer the spins are to antiferromagnetic (AFM) alignment,

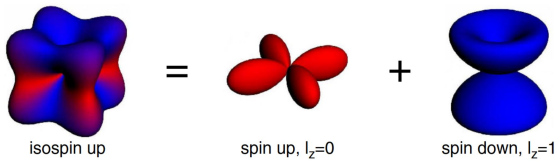

Figure 1.2: Orbital composition of the pseudospins. Figure taken from [1].

the lower the energy of the state is due to this correction. Rewriting this in terms of spin variables leads to an isotropic AFM ($J > 0$) Heisenberg interaction:

$$\mathcal{H} = J\vec{S}_i \cdot \vec{S}_j \tag{1.3}$$

Thus, in order to get an anisotropic Hamiltonian, like the Kitaev model of equation 1.1, something beyond this simple approach is needed. SOC binds together the spin space and the real space of orbitals into a total angular momentum, which will act as the magnetic degrees of freedom, pseudospins (schematically presented in Fig. 1.2). The orbital character of these pseudospins means that different pseudospin states will have different overlap integrals, namely they have a real space shape. As a result we can use this shape and real space geometry in order to construct anisotropic types of interaction. Note that SOC is only possible with multiple orbitals per site. This allows ferromagnetic (FM) interactions since the two spins on the same site can be on different orbitals, avoiding the Pauli principle.

1.4 Mott insulating state assisted by spin-orbit coupling

Since the superexchange calculations are perturbative by nature, they are only valid when when the hopping is small. In other words, the compound in question has to be insulating. Iridates have an odd number of valence electrons per site, which necessarily leads to a metallic state from a naive band theory picture. Coulomb repulsion can localize the odd electrons on their sites giving rise to a Mott insulator [7]. However, the Coulomb repulsion in iridates, $U \approx 1.8$ eV, is too small to provide a gap for the broad 5d bands of such a heavy atom as Ir. Since experimentally it has been shown that the compounds are indeed insulators [4, 8], there has to be something else to explain the insulating behavior. The answer was found by B. J. Kim et al [2]: other interactions

in the system split off parts of the 5d bands leaving only a small portion that is thin enough to open a gap with the modest Coulomb interaction. First, the cubic crystal field of the oxygen octahedron surrounding each Ir ion splits the 5d orbitals into the e_g and t_{2g} (see Fig. 1.3). The splitting is $10Dq \approx 3.5$ eV, which is relatively large. Since there are 5 electrons in the Ir^{4+}, they all occupy the three low-energy t_{2g} orbitals. 5d orbitals have an angular momentum of $l = 2$. However, if we project out the high-energy e_g orbitals the three remaining t_{2g} orbitals effectively behave like $l_{eff} = 1$, up to an overall sign of the angular momentum matrices.

The SOC (with $\lambda \approx 0.4$ eV) couples the spin $s = 1/2$ with $l = 1$ orbital momentum. As a result of this we get a lower laying manifold of eigenstates of total angular momentum $\mathbf{J} = 3/2$ and higher doublet of $\mathbf{J} = 1/2$. Four out of five electrons in Ir^{4+} completely fill the $\mathbf{J} = 3/2$ quadruplet. The fifth electron half-fills the $\mathbf{J} = 1/2$ states. Thus the strong crystal field raises in energy completely empty portions of the 5d orbitals. Simultaneously, SOC lowers completely full portions. This leaves only the $\mathbf{J} = 1/2$ bands close to the Fermi energy. The $\mathbf{J} = 1/2$ bands are considerably narrower (bandwidth of about 0.5 eV) and thus the small Coulomb interaction is now sufficient to open up a gap, leading to a spin-orbit assisted Mott insulator state. The $\mathbf{J} = 1/2$ states act as the pseudospins in the magnetic superexchange.

1.5 Research summary

In this dissertation I explore the many consequences that large SOC has on the magnetism of the 4d and 5d compounds. I start by calculating the effective magnetic Hamiltonians using superexchange in Sr_2IrO_4 and Na_2IrO_3 [9, 10]. I include the tetragonal and trigonal distortions of the cubic crystal field present in these two compounds, respectively. In Na_2IrO_3 due to the the extended nature of the 5d orbitals as well as the honeycomb geometry with Na atoms at the center the further neighbor interactions are also found to be important and anisotropic in nature. My calculations lead to the J-D model for Sr_2IrO_4 and J_1-K_1-Γ_1-J_2-K_2-J_3 model for Na_2IrO_3. Corrections to the J-D model accounting for staggered tetragonal distortions suggested by optical experiments are made to account for the spin canting angle disparity.

I then calculate the effects of the various anisotropic interactions on the anisotropy of

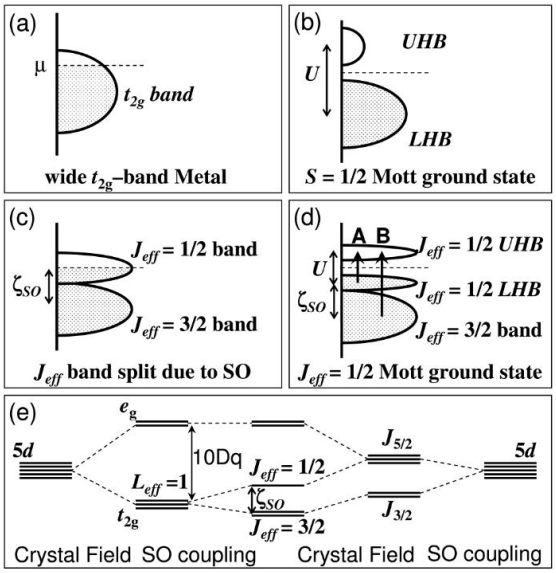

Figure 1.3: Spin-orbit assisted Mott insulating state in Sr_2IrO_4. Figure taken from [2].

the Curie-Weiss temperatures and the gyromagnetic tensor for the most general models proposed for Sr_2IrO_4, Na_2IrO_3, α-$RuCl_3$, (α, β, γ)-Li_2IrO_3 [9, 10, 11, 12]. We propose that experimental measurements of the anisotropy in the Curie-Weiss temperatures can be used to estimate the anisotropic Γ_1 superexchange constant as well as bond dependent anisotropy due to further crystal distortions, such as the monoclinic distortion in Na_2IrO_3. We also show that the staggered crystal field pattern suspected in Sr_2IrO_4 can be observed in the anisotropy of the Curie-Weiss temperatures.

The J_1-K_1 model has been of a particular interest as this is the minimal model that can explain a zigzag pattern state experimentally found in α-$RuCl_3$ [13, 14, 15]. We explore the effects that a uniform external magnetic field has on this model using Monte-Carlo simulations [16]. We find a competition of the anisotropic thermal fluctuations with the magnetic field, which leads to many new phases, including partially- and fully-incommensurate spiral states.

Anisotropic magnetic models can often lead to accidental degeneracies, lifted via the order-by-disorder mechanism [17, 18]. We developed a new method for calculating the free energy corrections due to the thermal and quantum fluctuations in generic bilinear anisotropic Hamiltonians [19, 20]. We use this method to show how the direction of the

zigzag order parameter is chosen in Na_2IrO_3 and α-$RuCl_3$ [21].

1.6 Outline of the dissertation

The dissertation is structured as follows:

- In Chapter 2 I present a derivation of the minimal magnetic model of Sr_2IrO_4 from microscopic parameters. Keeping SOC, crystal field distortions, and Hund's coupling all on equal footing I have arrived at a highly anisotropic J_1-D_1 model. The competition between the isotropic Heisenberg interaction J_1 and the anisotropic Dzyaloshinsky-Moriya interaction D_1 lead to a canted AFM structure as the magnetic ground state [1, 9]. The canted component from all sites adds up to give the experimentally observed small ferromagnetic moment in the compound.

- In Chapter 3 I have performed a similar calculation for Na_2IrO_3. This lead to the J_1-K_1-Γ_1-J_2-K_2-J_3 [10], a model with many competing anisotropic interactions. I show that this model gives the experimentally observed zigzag phase as the ground state. Interestingly, unlike most 3d compounds, where the magnetic ground state usually stems from one or two dominant interactions while the rest only account for small corrections, in Na_2IrO_3 there are many interactions of the same order. Their competition and cooperation is what drives the zigzag phase with the particular direction of the magnetic moments, a topic that I discuss in more detail in the final chapter of the dissertation.

- Next Chapter 4 focuses on the J_1-K_1 model, relevant to $RuCl_3$. I explore how this model behaves when uniform external magnetic field is applied using classical Monte-Carlo simulation. We find a competition between thermal fluctuations of the Kitaev interaction and the magnetic field that leads to a plethora of new interesting phases. A linear superposition of 3 zigzag states with peculiar canting pattern exists at low magnetic fields. At intermediate field strengths we found a partially incommensurate spiral phase, in which 2 spin components are incommensurate, while the third is commensurate. At higher fields a fully commensurate spiral phase sets in. At fields just below saturation a more standard 120° order

sets in [22, 16]. We presented a phase diagram of the model as a function of field strength and temperature.

- Chapter 5 focuses on the effects the anisotropic interactions have on the Curie-Weiss (CW) temperatures. We show that the measurement of the anisotropic Curie-Weiss temperatures presents a way to estimate the different anisotropies found in the compounds. In tri-coordinated Kitaev compounds the antisymmetric off-diagonal interaction Γ_1 as well as the bond dependence of the anisotropic interactions due to structural distortions can be measured from the CW. In Sr_2IrO_4 we also found that, unlike most case, the anisotropic gyromagnetic factor also enters the CW temperature expressions.

- Chapters 6 and 7 present a method for calculating the fluctuational contribution to the free energy of classical and quantum anisotropic spin systems, respectively, using Hubbard-Stratonovich transformation. The method gives the means to predict direction of the order parameter chosen via order-by-disorder in systems with degenerate ground states [19, 20]. We use this method to show that the Kitaev interactions in minimal models of Na_2IrO_3 and $RuCl_3$ prefer magnetic moments along cubic axes. While this fits the experimental observations in $RuCl_3$, the direction magnetic moments in Na_2IrO_3 is settled by another mechanism, which I discuss in the following chapter.

- In the final Chapter 8 I show how the competition and cooperation of the various interactions in Na_2IrO_3 and $RuCl_3$ selects the direction of the zigzag order parameter [21]. Particularly, I pointed out the importance of symmetric off-diagonal interaction Γ_1 in the selection of the 45° direction between cubic axes experimentally observed in Na_2IrO_3. I find that the mean field contribution of the relatively small Γ_1 coupling prefers to put the magnetic moments in the 45° direction. This puts it at a competition with the fluctuational contribution from the considerably larger Kitaev interactions, K_1 and K_2. However, due to the difference in order of the contribution (MF vs fluctuations) the smaller Γ_1 interaction wins over K_1 and K_2 interactions.

Chapter 2

Interplay of many-body and single-particle interactions in iridates and rhodates.

2.1 Introduction

5*d* transition metal oxides, in which orbital degeneracy is accompanied by strong relativistic SOC, recently received considerable attention, both in experiment and in theory. In these systems the SOC might be comparable to, or even stronger than the Coulomb and Hund's couplings, and the CF interactions arising from surrounding oxygen atoms in a nearly octahedral environment. As a result of this unusual hierarchy of on-site interactions, novel quantum and classical states with non-trivial topology and interesting magnetic properties might be stabilized. Fascinating examples of such properties include the Mott insulator ground state of Sr_2IrO_4 [5, 2, 23, 24, 25, 26, 27, 28, 29, 30, 1, 31, 32, 33, 34], the potential spin-liquid ground state of $Na_4Ir_3O_8$ [35, 36], the anomalous Hall effect in the metallic frustrated pyrochlore $Pr_2Ir_2O_7$ [37, 38, 39, 40, 41, 42], non-trivial long-range order, and moment fluctuations in its sister compound $Eu_2Ir_2O_7$ [43, 44], unusual magnetic orderings in the honeycomb compounds Na_2IrO_3 and Li_2IrO_3 [45, 46, 8, 47, 48, 49, 50, 51], and others.

The main focus of this chapter is on developing a theoretical framework which will

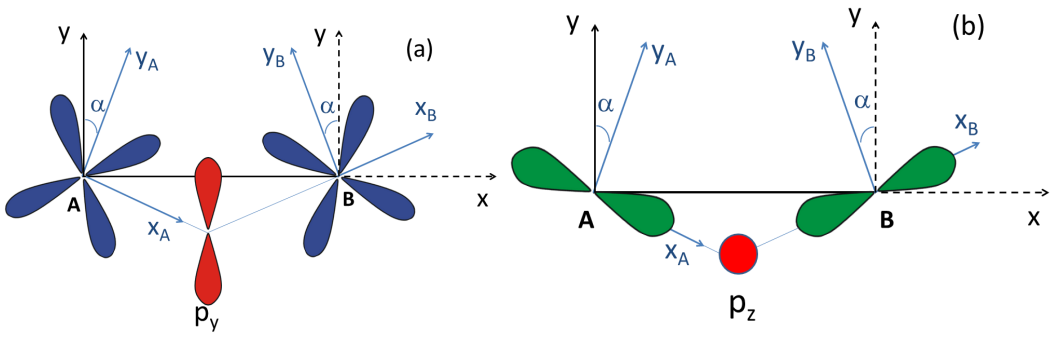

Figure 2.1: Ir-O-Ir bond in the presence of octahedra rotations in one IrO_2 layer. x and y are the global axes adopted for the intermediate oxygen atoms. $x_{A(B)}$ and $y_{A(B)}$ are local axes on sublattices A and B. (a): local $\tilde{Z}$ orbital on Ir ion overlaps with p_y oxygen orbital in the global reference frame. (b): local $\tilde{Y}$ orbital on Ir ion overlaps with p_z oxygen orbital in the global reference frame.

allow us to understand the microscopic nature of magnetism in the iridium compounds described above. In these systems, the magnetic degrees of freedom are determined by Ir^{4+} ions in $5d^5$ electronic configurations.

The super-exchange Hamiltonians for layered iridium oxides were firstly derived in the seminal paper by Jackeli and Khalliulin [1]. They found that the super-exchange Hamiltonian describing the coupling between $\mathbf{J} = 1/2$ Kramers doublet states on the square lattice, like in Sr_2IrO_4, is predominantly of isotropic Heisenberg super-exchange character, while anisotropic terms become relevant only in the presence of lattice distortions. On the honeycomb lattice, like in Na_2IrO_3, the interaction between $\mathbf{J} = 1/2$ Kramers doublet states is highly anisotropic even in the absence of lattice distortions. The anisotropic part of the super-exchange coupling has the very peculiar form of the Kitaev interaction. This originates from the competition between SOC and correlation effects, and is non-zero only in the presence of Hund's coupling.

In the present study, we go beyond this work and derive effective super-exchange spin Hamiltonians rigorously starting from the exact eigenstates of the single ion microscopic Hamiltonian. Here, we will be primarily interested in the magnetic properties of the insulating iridium oxides with tetragonal symmetry, in which the Ir ions occupy a square lattice, as in the case of Sr_2IrO_4. While this particular compound is very interesting and

has recently attracted much attention [5, 2, 23, 24, 25, 26, 27, 28, 30, 1, 31, 32, 33, 34], the approach proposed here can not only be easily used to understand the magnetic properties of other iridates belonging to the Ruddlesden-Popper series $Sr_{n+1}Ir_nO_{3n+1}$, but can also be applied to systems with different lattice geometries.

The magnetic properties of Sr_2IrO_4 are very unusual. Below 240 K, Sr_2IrO_4 is a canted antiferromagnet with a small in-plane ferromagnetic moment ($\sim 0.1\mu_B$) [5], which, however, is one to two orders of magnitude larger than that of the analogous canted antiferromagnet La_2CuO_4. Another important experimental finding is that this canting disappears with pressure [28]. These two observations indicate a very strong coupling between magnetic properties and the crystal lattice, which in the presence of SOC can be understood through the coupling of orbital magnetization to the lattice. Consequently, as the orbital magnetic moment contributes to the total magnetic moment of Ir ions, there is a strong dependence of the magnetic degrees on lattice degrees of freedom.

Two types of lattice distortions are present in Sr_2IrO_4 even at ambient pressure: tetragonal distortion and staggered rotation of IrO_6 octahedra (see Fig.2.1). The staggered nature of the IrO_6 octahedra rotation leads to a doubling of the unit cell and the formation of a two-sublattice structure. The tetragonal distortion moves the electronic ground state away from the strong SO limit $\mathbf{J} = 1/2$ state by mixing $\mathbf{J} = 1/2$ and $\mathbf{J} = 3/2$ states. Thus in order to understand the magnetism of this system, one needs first to understand the nature of the magnetic degrees of freedom. In our approach we identify the magnetic degrees of freedom by dealing with the exact eigenstates of the full single ion microscopic Hamiltonian which includes both SOC and CF interactions.

In this work, we will obtain dependencies of the magnetic interactions on microscopic parameters characterizing the system. In addition, we will study how the properties of Sr_2IrO_4 depend on external pressure [28] and chemical substitution [29, 52, 53]. In particular, we will discuss the case when iridium is substituted with rhodium [52, 53]. Rh substitution, unlike other chemical substitutions, does not change the band filling. However, it varies the SOC, and the Coulomb and Hund's coupling strengths, because on one side the $4d$ orbitals of Rh ions are less extended, tending to enhance the electronic repulsion and thereby increasing correlation effects, and on the other side, as Rh is a lighter ion, the SOC is smaller. Thus, when the content of Rh increases, the overall

balance of on-site interactions changes, and as a result one might expect the appearance of new magnetic phases and doping-driven phase transitions. Although this direction has been recently explored experimentally in a few cases [52, 53], it still remains to be investigated theoretically.

The chapter is organized as follows. In Sec. 2.2, we introduce the single ion microscopic model appropriate for the description of the physical properties of the iridates and rhodates, in which five electrons or, equivalently, one hole occupy the three-fold degenerate t_{2g} orbitals and experience strong SOC and crystal field (CF) interactions. We first obtain one-particle eigenstates taking into account only SOC and CF interactions, and then compute two-particle excited eigenstates fully considering correlation effects. In Sec. 2.3 we derive an effective super-exchange Hamiltonian by integrating out the intermediate oxygen ions and performing a second order perturbation expansion in the hopping parameters around the atomic limit. In Sec. 2.4, we present our results on the magnetic interactions and show how these interactions depend on various microscopic parameters of the model. We also discuss the application of the results obtained to real compounds. Finally, in Sec. 2.5 a summary of the work is presented.

2.2 Single ion Hamiltonian

2.2.1 One-particle eigenstates

In Sr_2IrO_4, the Ir^{+4} ions are sitting inside an oxygen cage forming an octahedron. The octahedral crystal field splits the five $5d$ orbitals of Ir into a doublet of e_g orbitals at higher energy and into the low-lying three-fold degenerate t_{2g} multiplet. In iridates, the energy difference between the e_g and t_{2g} levels is large. Because of this, the five electrons occupy the low lying t_{2g} orbitals and the on-site interactions, such as the SOC, Coulomb and Hund's interactions, and the crystal field interactions, lowering the symmetry further, can be considered within the t_{2g} manifold only. In this limit, the SOC has to be projected to the t_{2g} manifold, resulting in an effective orbital angular momentum $l_{eff} = 1$.

It is more convenient to describe the low-spin state of the d^5-configuration of Ir^{+4} ions by using the hole description. In the local axes bound to the oxygen octahedron the t_{2g} orbitals of Ir ions are $|X\rangle = |yz\rangle$, $|Y\rangle = |zx\rangle$, and $|Z\rangle = |xy\rangle$. Examples of the

lobe structure of the d-wave orbital $|xy\rangle$ of Ir are shown in Fig.2.1 (blue lobes). In the absence of interactions, these one-hole states are completely degenerate. The SOC and CF interactions, described by the single-ion Hamiltonian

$$H_{\lambda,\Delta} = \lambda \overrightarrow{S} \cdot \overrightarrow{L} + \Delta L_z^2, \tag{2.1}$$

give rise to a splitting of the levels according to the symmetry of the underlying lattice. In the tetragonal system, the orbital angular momentum basis is defined by $|L_z = 0\rangle = |Z\rangle$, $|L_z = \pm 1\rangle = -\frac{1}{\sqrt{2}}(\pm|X\rangle + \imath|Y\rangle)$, where the quantization axis is taken along the tetragonal z axis. In the absence of tetragonal distortion, the energy eigenstates are the angular momentum eigenstates $|J, J_z\rangle$. The full single-particle Hilbert space is, thus, given by a six-component vector $\hat{J} = \{|\frac{1}{2}, \frac{1}{2}\rangle, |\frac{1}{2}, -\frac{1}{2}\rangle, |\frac{3}{2}, \frac{3}{2}\rangle, |\frac{3}{2}, \frac{1}{2}\rangle, |\frac{3}{2}, -\frac{1}{2}\rangle, |\frac{3}{2}, \frac{-3}{2}\rangle\}$. The vector $\hat{J}$ can be expressed in terms of the basis set of t_{2g}-orbitals as

$$\hat{J} = \begin{pmatrix} 0 & -\frac{1}{\sqrt{3}} & 0 & -\frac{\imath}{\sqrt{3}} & -\frac{1}{\sqrt{3}} & 0 \\ -\frac{1}{\sqrt{3}} & 0 & \frac{\imath}{\sqrt{3}} & 0 & 0 & \frac{1}{\sqrt{3}} \\ -\frac{1}{\sqrt{2}} & 0 & -\frac{\imath}{\sqrt{2}} & 0 & 0 & 0 \\ 0 & -\frac{1}{\sqrt{6}} & 0 & -\frac{\imath}{\sqrt{6}} & \sqrt{\frac{2}{3}} & 0 \\ \frac{1}{\sqrt{6}} & 0 & -\frac{\imath}{\sqrt{6}} & 0 & 0 & \sqrt{\frac{2}{3}} \\ 0 & \frac{1}{\sqrt{2}} & 0 & -\frac{\imath}{\sqrt{2}} & 0 & 0 \end{pmatrix} \hat{A}_1 \ , \tag{2.2}$$

where $\hat{A}_1 = \{|X_\uparrow\rangle, |X_\downarrow\rangle, |Y_\uparrow\rangle, |Y_\downarrow\rangle, |Z_\uparrow\rangle, |Z_\downarrow\rangle\}$ is a six-component vector, and $\uparrow, \downarrow$ indicate spin states. The ground state is a Kramers doublet $|J = \frac{1}{2}, J_z\rangle$ at energy $E_0 = -\lambda$ and the excited state form a quartet $|J = \frac{3}{2}, J_z\rangle$ at energy $E_1 = \frac{1}{2}\lambda$. However, in Sr_2IrO_4, the tetragonal distortion is present and is not small. It arises because the oxygen octahedra are elongated along the z axis. In the hole representation, $\Delta = \Delta_{tet} > 0$ and the t_{2g} orbitals are split into a singlet state $|Z\rangle$ with energy $-\Delta$ and a doublet state ($|X\rangle \& |Y\rangle$) with energy $\Delta/2$. In the presence of both the tetragonal distortion and the SOC, the eigenfunctions of the Hamiltonian (2.1) are given by components of a vector $\hat{\Psi} = \{|\Psi_1\rangle, |\Psi_2\rangle, |\Psi_3\rangle, |\Psi_4\rangle, |\Psi_5\rangle, |\Psi_6\rangle\}$, which in terms of t_{2g}-orbitals are given by

$$\hat{\Psi} = \hat{M}_\theta^{tet} \hat{A}_1 \ , \tag{2.3}$$

where

$$\hat{M}_{\theta}^{tet} = \begin{pmatrix} 0 & \frac{1}{\sqrt{2}}\, c_\theta & 0 & \frac{\imath}{\sqrt{2}}\, c_\theta & s_\theta & 0 \\ -\frac{1}{\sqrt{2}}\, c_\theta & 0 & \frac{\imath}{\sqrt{2}}\, c_\theta & 0 & 0 & s_\theta \\ -\frac{1}{\sqrt{2}} & 0 & -\frac{\imath}{\sqrt{2}} & 0 & 0 & 0 \\ 0 & -\frac{1}{\sqrt{2}}\, s_\theta & 0 & -\frac{\imath}{\sqrt{2}}\, s_\theta & c_\theta & 0 \\ \frac{1}{\sqrt{2}}\, s_\theta & 0 & -\frac{\imath}{\sqrt{2}}\, s_\theta & 0 & 0 & c_\theta \\ 0 & -\frac{1}{\sqrt{2}} & 0 & \frac{\imath}{\sqrt{2}} & 0 & 0 \end{pmatrix},$$

where, for shortness, we denote $c_\theta = \cos\theta$ and $s_\theta = \sin\theta$. The angle variable θ is determined by $\tan(2\theta) = 2\sqrt{2}\frac{\lambda}{\lambda - 2\Delta}$ and takes care of the competition between the tetragonal distortion and the SOC [1].

The eigenstates of the Hamiltonian (2.1) are given by the following three doublets: the ground state doublet ($|\Psi_1\rangle \& |\Psi_2\rangle$) with energy $E^{(1,2)} = \frac{1}{2}(\Delta - \frac{\lambda}{2}) - \frac{1}{2}\sqrt{2\lambda^2 + (\Delta - \frac{\lambda}{2})^2} = -\frac{\lambda}{\sqrt{2}}\cot\theta$, the intermediate doublet ($|\Psi_4\rangle \& |\Psi_5\rangle$) with energy $E^{(4,5)} = \frac{1}{2}(\Delta - \frac{\lambda}{2}) + \frac{1}{2}\sqrt{2\lambda^2 + (\Delta - \frac{\lambda}{2})^2} = \frac{\lambda}{\sqrt{2}}\tan\theta$ and the upper doublet ($|\Psi_3\rangle \& |\Psi_6\rangle$) with energy $E^{(3,6)} = \Delta + \frac{\lambda}{2}$. Note that the ground state doublet $|\Psi_1\rangle \& |\Psi_2\rangle$ is different from the $|J = \frac{1}{2}, J_z\rangle$ doublet as well as the $L_z = 0$ doublet!

In Sr_2IrO_4, there is also a staggered rotation of neighboring oxygen octahedra by an angle $\pm\alpha$ about the z-axis (see Fig.2.1 (a) and (b)) leading to the formation of a two-sublattice structure. We denote these two sublattices as A and B. Because the crystal-field interaction on Ir $5d$ orbitals is diagonal only in the local cubic axes bound to the oxygen octahedron, in the presence of the octahedra rotations, atomic states on sublattices A and B have to be defined in the local basis. Then, the states on sublattices A and B are given by

$$\hat{\Psi}_A = \hat{M}_{\theta}^{tet} \begin{pmatrix} |\tilde{X}_\uparrow e^{-\frac{\imath\alpha}{2}}\rangle \\ |\tilde{X}_\downarrow e^{\frac{\imath\alpha}{2}}\rangle \\ |\tilde{Y}_\uparrow e^{-\frac{\imath\alpha}{2}}\rangle \\ |\tilde{Y}_\downarrow e^{\frac{\imath\alpha}{2}}\rangle \\ |\tilde{Z}_\uparrow e^{-\frac{\imath\alpha}{2}}\rangle \\ |\tilde{Z}_\downarrow e^{\frac{\imath\alpha}{2}}\rangle \end{pmatrix} \tag{2.4}$$

and

$$\hat{\Psi}_B = \hat{M}_\theta^{tet} \begin{pmatrix} |\tilde{X}_\uparrow e^{\frac{\imath\alpha}{2}}\rangle \\ |\tilde{X}_\downarrow e^{-\frac{\imath\alpha}{2}}\rangle \\ |\tilde{Y}_\uparrow e^{\frac{\imath\alpha}{2}}\rangle \\ |\tilde{Y}_\downarrow e^{-\frac{\imath\alpha}{2}}\rangle \\ |\tilde{Z}_\uparrow e^{\frac{\imath\alpha}{2}}\rangle \\ |\tilde{Z}_\downarrow e^{-\frac{\imath\alpha}{2}}\rangle \end{pmatrix}, \tag{2.5}$$

where the phase factors $e^{\pm\frac{\imath\alpha}{2}}$ appear after the projection of the spin states onto the local reference frame. Initially the spin states are defined in the global reference frame.

2.2.2 Two-hole states in the presence of interactions, SOC and tetragonal distortion.

The many-body part of the single ion Hamiltonian is given by the three-band Hubbard Hamiltonian of the form:

$$\begin{aligned} H_{int} &= U_1 \sum_{i,\alpha} n_{i\alpha\uparrow} n_{i\alpha\downarrow} + \frac{1}{2}(U_2 - J_H) \sum_{i,\sigma,\alpha\neq\alpha'} n_{i\alpha\sigma} n_{i\alpha'\sigma} \\ &+ U_2 \sum_{i,\alpha\neq\alpha'} n_{i\alpha\uparrow} n_{i\alpha'\downarrow} + J_H \sum_{i,\alpha\neq\alpha'} d^\dagger_{i\alpha\uparrow} d^\dagger_{i\alpha\downarrow} d_{i\alpha'\downarrow} d_{i\alpha'\uparrow} \\ &- J_H \sum_{i,\alpha\neq\alpha'} d^\dagger_{i\alpha\uparrow} d_{i\alpha\downarrow} d^\dagger_{i\alpha'\downarrow} d_{i\alpha'\uparrow} \,, \end{aligned} \tag{2.6}$$

where U_1 and U_2 are the Coulomb repulsion among electrons in the same and in different t_{2g} orbitals, respectively, and J_H is the Hund's coupling constant. Due to the cubic symmetry, the relation $U_1 = U_2 + 2J_H$ holds. The annihilation and creation electron operators, $d_{i\alpha\sigma}$ and $d^\dagger_{i\alpha\sigma}$ refer to Ir orbitals at site i, of type α (X, Y or Z) and with spin $\sigma = \uparrow, \downarrow$, $n_{i\alpha\sigma} = d^\dagger_{i\alpha\sigma} d_{i\alpha\sigma}$. In order to obtain H_{int} in the hole picture, we substitute $d^\dagger_{\alpha\sigma} \rightarrow a_{\alpha\sigma}$ and $n_{\alpha\sigma} \rightarrow 1 - h_{\alpha\sigma}$, where $h_{\alpha\sigma} = a^\dagger_{\alpha\sigma} a_{\alpha\sigma}$, and $a^\dagger_{\alpha\sigma}$ and $a_{\alpha\sigma}$ are the hole creation and annihilation operators.

We first compute energy eigenvalues of H_{int}. We consider ground states with one hole on the Ir ion and excited states, in which the Ir ion can have two holes or no holes.

The corresponding energies are

$$\begin{aligned} E_{1h} &= 10U_2 \\ E_{0h} &= 15U_2 \\ E_{2h}^{(1)} &= 6U_2 - J_H \\ E_{2h}^{(0)} &= 6U_2 + J_H \\ E_{2h}^{(00)} &= 6U_2 + 4J_H \end{aligned} \tag{2.7}$$

There are $6 \times 5/2 = 15$ partly degenerate two-hole states: six spin singlets and three triplets. Let the vector $|\mathcal{I}\rangle = |\mathcal{I}; n\rangle$ denote the two-hole eigenstates. It is convenient to represent them using the cubic orbital basis:

$$\hat{\mathcal{I}} = \hat{\mathcal{M}}_2 \hat{A}_2, \tag{2.8}$$

where

$$\begin{aligned} \hat{A}_2 = \quad \{ \quad & X_\uparrow X_\downarrow, X_\uparrow Y_\uparrow, X_\uparrow Y_\downarrow, X_\uparrow Z_\uparrow, X_\uparrow Z_\downarrow, X_\downarrow Y_\uparrow, X_\downarrow Y_\downarrow, \\ & X_\downarrow Z_\uparrow, X_\downarrow Z_\downarrow, Y_\uparrow Y_\downarrow, Y_\uparrow Z_\uparrow, Y_\uparrow Z_\downarrow, Y_\downarrow Z_\uparrow, Y_\downarrow Z_\downarrow, Z_\uparrow Z_\downarrow \} \end{aligned}$$

is the two-hole orbital basis, and the transformation matrix $\hat{\mathcal{M}}_2$ can be easily obtained. Explicitly, vector $\hat{\mathcal{I}}$ consists of the following elements:
(i) symmetric state with singlet pairs on the same orbital $S = 0, \alpha = \alpha'$

$$|\mathcal{I}; 1\rangle = \frac{1}{\sqrt{3}} \left(a_{X\downarrow}^\dagger a_{X\uparrow}^\dagger + a_{Y\downarrow}^\dagger a_{Y\uparrow}^\dagger + a_{Z\downarrow}^\dagger a_{Z\uparrow}^\dagger \right)$$

with energy equal to $E_1 = E_{2h}^{(00)} = 6U_2 + 4J_H = E_d$.
(ii) two degenerate antisymmetric states with singlet pairs on the same orbital $S = 0, \alpha = \alpha'$

$$\begin{aligned} |\mathcal{I}; 2\rangle &= \frac{1}{\sqrt{2}} \left(a_{X\downarrow}^\dagger a_{X\uparrow}^\dagger - a_{Y\downarrow}^\dagger a_{Y\uparrow}^\dagger \right) \\ |\mathcal{I}; 3\rangle &= \frac{1}{\sqrt{6}} \left(a_{X\downarrow}^\dagger a_{X\uparrow}^\dagger + a_{Y\downarrow}^\dagger a_{Y\uparrow}^\dagger - 2a_{Z\downarrow}^\dagger a_{Z\uparrow}^\dagger \right) \end{aligned}$$

with energies equal to $E_{2,3} = E_{2h}^{(0)} = 6U_2 + J_H = E_s$.
(iii) three states with singlet pairs on different orbitals $S = 0, \alpha \neq \alpha'$:

$$
\begin{aligned}
|\mathcal{I};4\rangle &= \frac{1}{\sqrt{2}}\left(a^\dagger_{X\downarrow}a^\dagger_{Y\uparrow} - a^\dagger_{X\uparrow}a^\dagger_{Y\downarrow}\right)\\
|\mathcal{I};5\rangle &= \frac{1}{\sqrt{2}}\left(a^\dagger_{Y\downarrow}a^\dagger_{Z\uparrow} - a^\dagger_{Z\uparrow}a^\dagger_{Y\downarrow}\right)\\
|\mathcal{I};6\rangle &= \frac{1}{\sqrt{2}}\left(a^\dagger_{Z\downarrow}a^\dagger_{X\uparrow} - a^\dagger_{X\uparrow}a^\dagger_{Z\downarrow}\right)
\end{aligned}
$$

with $E_{4,5,6} = E^{(0)}_{2h} = 6U_2 + J_H = E_s$.
(iv) Nine states with triplet pairs on different orbitals $S = 1, \alpha \neq \alpha'$:

$$
\begin{aligned}
|\mathcal{I};7\rangle &= \frac{1}{\sqrt{2}}\left(a^\dagger_{X\downarrow}a^\dagger_{Y\uparrow} + a^\dagger_{X\uparrow}a^\dagger_{Y\downarrow}\right)\\
|\mathcal{I};8\rangle &= a^\dagger_{X\uparrow}a^\dagger_{Y\uparrow}\\
|\mathcal{I};9\rangle &= a^\dagger_{X\downarrow}a^\dagger_{Y\downarrow}\\
|\mathcal{I};10\rangle &= \frac{1}{\sqrt{2}}\left(a^\dagger_{Y\downarrow}a^\dagger_{Z\uparrow} + a^\dagger_{Y\uparrow}a^\dagger_{Z\downarrow}\right)\\
|\mathcal{I};11\rangle &= a^\dagger_{Y\uparrow}a^\dagger_{Z\uparrow}\\
|\mathcal{I};12\rangle &= a^\dagger_{Y\downarrow}a^\dagger_{Z\downarrow}\\
|\mathcal{I};13\rangle &= \frac{1}{\sqrt{2}}\left(a^\dagger_{Z\downarrow}a^\dagger_{X\uparrow} + a^\dagger_{Z\uparrow}a^\dagger_{X\downarrow}\right)\\
|\mathcal{I};14\rangle &= a^\dagger_{Z\uparrow}a^\dagger_{X\uparrow}\\
|\mathcal{I};15\rangle &= a^\dagger_{Z\downarrow}a^\dagger_{X\downarrow}
\end{aligned}
$$

with energies $E_{7,..,15} = E^{(1)}_4 = 6U_2 - J_H = E_t$. This gives three different excitation energies:

$$
\begin{aligned}
\Delta E_1 &= E_d + E_{0h} - 2E_{1h} = U_2 + 4J_H\\
\Delta E_2 &= E_s + E_{0h} - 2E_{1h} = U_2 + J_H\\
\Delta E_3 &= E_t + E_{0h} - 2E_{1h} = U_2 - J_H
\end{aligned}
\tag{2.9}
$$

In the presence of the SOC and lattice distortions, the two-hole states $|\mathcal{I};n\rangle$ are mixed, and the true two-hole eigenstates are obtained by diagonalization of the full on-site Hamiltonian

$$
H_{int+\lambda,\Delta} = H_{int} + H_{\lambda,\Delta}\ . \tag{2.10}
$$

To this end, it is convenient first to represent the $|\mathcal{I};n\rangle$ states in terms of the eigenstates of $H_{\lambda,\Delta}$. The two-hole eigenstates of the SOC part of the Hamiltonian are simply given by product states $|\mathcal{J},\mu\rangle \equiv |J_1,J_{1z};J_2,J_{2z}\rangle$:

$$\begin{aligned}
|\mathcal{J},1\rangle &\equiv |\tfrac{1}{2},\tfrac{1}{2};\tfrac{3}{2},\tfrac{3}{2}\rangle \\
|\mathcal{J},2\rangle &\equiv |\tfrac{1}{2},-\tfrac{1}{2};\tfrac{3}{2},\tfrac{3}{2}\rangle \\
|\mathcal{J},3\rangle &\equiv |\tfrac{1}{2},\tfrac{1}{2};\tfrac{3}{2},\tfrac{1}{2}\rangle \\
|\mathcal{J},4\rangle &\equiv |\tfrac{1}{2},-\tfrac{1}{2};\tfrac{3}{2},\tfrac{1}{2}\rangle \\
|\mathcal{J},5\rangle &\equiv |\tfrac{1}{2},\tfrac{1}{2};\tfrac{3}{2},-\tfrac{1}{2}\rangle \\
|\mathcal{J},6\rangle &\equiv |\tfrac{1}{2},-\tfrac{1}{2};\tfrac{3}{2},-\tfrac{1}{2}\rangle \\
|\mathcal{J},7\rangle &\equiv |\tfrac{1}{2},\tfrac{1}{2};\tfrac{3}{2},-\tfrac{3}{2}\rangle \\
|\mathcal{J},8\rangle &\equiv |\tfrac{1}{2},-\tfrac{1}{2};\tfrac{3}{2},-\tfrac{3}{2}\rangle \\
|\mathcal{J},9\rangle &\equiv |\tfrac{1}{2},\tfrac{1}{2};\tfrac{1}{2},-\tfrac{1}{2}\rangle \\
|\mathcal{J},10\rangle &\equiv |\tfrac{3}{2},\tfrac{1}{2};\tfrac{3}{2},\tfrac{3}{2}\rangle \\
|\mathcal{J},11\rangle &\equiv |\tfrac{3}{2},-\tfrac{1}{2};\tfrac{3}{2},\tfrac{3}{2}\rangle \\
|\mathcal{J},12\rangle &\equiv |\tfrac{3}{2},-\tfrac{3}{2};\tfrac{3}{2},\tfrac{3}{2}\rangle \\
|\mathcal{J},13\rangle &\equiv |\tfrac{3}{2},-\tfrac{1}{2};\tfrac{3}{2},\tfrac{1}{2}\rangle \\
|\mathcal{J},14\rangle &\equiv |\tfrac{3}{2},-\tfrac{3}{2};\tfrac{3}{2},\tfrac{1}{2}\rangle \\
|\mathcal{J},15\rangle &\equiv |\tfrac{3}{2},-\tfrac{3}{2};\tfrac{3}{2},-\tfrac{1}{2}\rangle
\end{aligned} \tag{2.11}$$

In short, these states can be written as

$$|\mathcal{J},\mu\rangle = \sum_{\gamma_1,\gamma_2=1}^{6} m^{\mu}_{\gamma_1,\gamma_2} b^{\dagger}_{\gamma_1} b^{\dagger}_{\gamma_2} |vac\rangle, \tag{2.12}$$

where $\mu = 1,...,15$ refers to the component of the vector $\hat{\mathcal{J}}$, $b^{\dagger}_{\gamma}$ is an operator creating a hole of the type $\gamma = 1,...6$, which refers to the component of the single-hole vector $\hat{J}$. The tensor $\hat{m}$ has the following non-zero elements

$$\begin{aligned}
m^{1}_{1,3} &= m^{2}_{2,3} = m^{3}_{1,4} = m^{4}_{2,4} = m^{5}_{1,5} = \\
m^{6}_{2,5} &= m^{7}_{1,6} = m^{8}_{2,6} = m^{9}_{1,2} = m^{10}_{4,3} = \\
m^{11}_{5,3} &= m^{12}_{6,3} = m^{13}_{5,4} = m^{14}_{6,4} = m^{15}_{6,5} = 1 \ .
\end{aligned}$$

If, in addition to the SOC, the lattice distortion is present, the two-hole states $|\tilde{\mathcal{J}},\mu\rangle$ are given by the products of two $|\Psi_n\rangle$ states. The explicit form of the vector $|\tilde{\mathcal{J}},\mu\rangle$ can be easily obtained from Eq.(2.11) by the following substitution:

$$\begin{aligned}
|\tfrac{1}{2},\tfrac{1}{2}\rangle &\rightarrow |\Psi_1\rangle,\\
|\tfrac{1}{2},-\tfrac{1}{2}\rangle &\rightarrow |\Psi_2\rangle,\\
|\tfrac{3}{2},\tfrac{3}{2}\rangle &\rightarrow |\Psi_3\rangle,\\
|\tfrac{3}{2},\tfrac{1}{2}\rangle &\rightarrow |\Psi_4\rangle,\\
|\tfrac{3}{2},-\tfrac{1}{2}\rangle &\rightarrow |\Psi_5\rangle,\\
|\tfrac{3}{2},-\tfrac{3}{2}\rangle &\rightarrow |\Psi_6\rangle.
\end{aligned} \tag{2.13}$$

The complete Hamiltonian matrix has the same block diagonal structure in the space of states $|\mathcal{J},\mu\rangle$ and $\left|\tilde{\mathcal{J}},\mu\right\rangle$. Therefore, below we will omit the tilde sign and use notations $|\mathcal{J},\mu\rangle$ in a general sense.

In the $|\mathcal{J},\mu\rangle$ basis, the Hamiltonian matrix is given by

$$\begin{aligned}
&\langle\mathcal{J},\mu'|H_{int+\lambda,\Delta}|\mathcal{J},\mu\rangle = \epsilon_\mu\delta_{\mu'\mu} + \\
&\sum_{n=1}^{15} E_n\langle\mathcal{J},\mu'|\mathcal{I},n\rangle\langle\mathcal{I},n|\mathcal{J},\mu\rangle
\end{aligned} \tag{2.14}$$

where ϵ_μ is the energy of the $|\mathcal{J},\mu\rangle$ state, and the $\langle\mathcal{J},\mu|\mathcal{I},n\rangle$ denote components of the overlap matrix. The diagonalization of (2.14) gives energy eigenstates of the full Hamiltonian

$$|D,\xi\rangle = \sum_{\mu=1}^{15} c_{\xi\mu}|\mathcal{J},\mu\rangle \ , \tag{2.15}$$

where $\xi = 1,...15$ and $c_{\xi\mu}$ denote the eigenvectors. We denote the energy eigenvalues as E_ξ. As a final remark, we also note that in the limit $J_H = 0$ and $\Delta = 0$, the Hamiltonian matrix (2.14) is diagonal with $E_1 = ... = E_8 = -\lambda/2 - U_2$, $E_9 = -2\lambda - U_2$, and $E_{10} = ... = E_{15} = -\lambda - U_2$.

2.3 Derivation of the super-exchange Hamiltonian

In systems with tetragonal symmetry, the Ir-O-Ir bonds are close to 180°. In these systems, in general, the contribution to the super-exchange coupling from direct Ir-Ir

hopping may be neglected because the Ir ions are quite far from each other. The dominant contribution to the super-exchange is from the hopping via intermediate oxygen ions, so-called oxygen-assisted hopping. Because intermediate states with two holes on the oxygen ion have high-energy and, thus, can be neglected, we may integrate out the oxygen degrees of freedom to obtain an effective oxygen-assisted hopping between Ir $5d$-states. Then applying a second order perturbation theory expansion in the effective hopping parameters, we obtain a super-exchange Hamiltonian in the following form:

$$H_{ex,n,n'} = \sum_{\xi} \frac{1}{\epsilon_\xi} P H_{t,n,n'} Q_{\xi,n'} H_{t,n',n} P \ , \tag{2.16}$$

where

$$P = \sum_{\sigma_n = \pm 1} |1/2, \sigma_n/2; n\rangle\langle n; 1/2, \sigma_n/2| \tag{2.17}$$

is the projection operator onto the ground states with one hole at site n. The projection operators onto two-hole intermediate states $|D, \xi; n'\rangle$ with excitation energy ϵ_ξ at site n' are then given by

$$Q_{\xi,n'} = |D, \xi; n'\rangle\langle n'; D, \xi| = D^\dagger_{\xi,n'} D_{\xi,n'} \ . \tag{2.18}$$

The excitation energies of the intermediate states are $\epsilon_\xi = E_{0h} + E_\xi - 2E_{1h}$.

The connection between the Kramers doublet ground states at site n ($\gamma = 1, 2$) and the full manifold of states at site n' ($\gamma' = 1, 2, ..., 6$) is given by the projected hopping term:

$$P H_{t,n,n'} = \sum_{\gamma=1}^{2} \sum_{\gamma'=1}^{6} T^{\gamma,\gamma'}_{n,n'} b^\dagger_{n,\gamma} b_{n',\gamma'} \ , \tag{2.19}$$

where the elements of the matrix $T^{\gamma,\gamma'}_{n,n'}$ describe an overlap between $|J, J_z\rangle$ or $|\Psi_\gamma\rangle$ states in the absence or in the presence of the tetragonal distortion, respectively.

To obtain the matrix elements of $T^{\gamma,\gamma'}_{n,n'}$ we first consider the hopping operator on the square lattice in the simplest case with no tetragonal distortion, $\Delta = 0$, and no rotations of the IrO_6 octahedra. Without loss of generality we consider x-bonds, and then using symmetry arguments we obtain transfer matrix elements along y-bonds. Along an x-bond the hopping occurs either through p_y- or p_z-orbitals of oxygen. The

p_y- orbital overlaps with $|Z\rangle = |xy\rangle$ and p_z- orbital overlaps with $|Y\rangle = |zx\rangle$ orbitals of iridium. Correspondingly, we denote the hopping amplitudes as $t_{Z,y}$ and $t_{Y,z}$. However, on the undistorted lattice $t_{Z,y} = t_{Y,z}$ and to simplify notations we denote the hopping amplitude as t. Integrating over the oxygen ions, the effective hopping between Ir ions can be approximated as $t_{eff} = t^2/\Delta_{pd}$, where Δ_{pd} is the charge-transfer gap. In our calculations we consider $t_{eff} = 0.13$ eV. The effective hopping Hamiltonian between Ir ions along the x-bond is then given by

$$H_t^x = t_{eff} \sum_n \left(a^\dagger_{Z\sigma,n} a_{Z\sigma,n+x} + a^\dagger_{Y\sigma,n} a_{Y\sigma,n+x} + h.c. \right) \tag{2.20}$$

Expressing operators $a^\dagger_{Z\sigma,n}$, etc., in terms of $b^\dagger_{\gamma,n}$ operators, we get

$$H_t^x = \sum_n \sum_{\gamma,\gamma'} T^{\gamma,\gamma'}_{n,n+x} (b^\dagger_{n,\gamma} b_{n+x,\gamma'} + h.c.) \tag{2.21}$$

where the elements of the effective transfer matrix, $T^{\gamma,\gamma'}_{n,n+x}$, between γ and γ' orbitals can be written as

$$T^{\gamma,\gamma'}_{n,n+x} = t_{eff} \left(\tau_Z^{\gamma,\gamma'} + \tau_Y^{\gamma,\gamma'} \right). \tag{2.22}$$

Here we use the following notation:

$$\begin{aligned} \tau_Z^{\gamma,\gamma'} &= {}_{\gamma'}\langle J, J_z | \hat{T} | p^y_\sigma \rangle \langle p^y_\sigma | \hat{T} | J, J_z \rangle_\gamma, \\ \tau_Y^{\gamma,\gamma'} &= {}_{\gamma'}\langle J, J_z | \hat{T} | p^z_\sigma \rangle \langle p^z_\sigma | \hat{T} | J, J_z \rangle_\gamma \ , \end{aligned} \tag{2.23}$$

where $\hat{T}$ are hopping operators connecting neighboring Ir and O orbitals. In matrix form τ_Z, τ_Y are given by

$$\hat{\tau}_Z = \frac{1}{3} \begin{pmatrix} 1 & 0 & 0 & -\sqrt{2} & 0 & 0 \\ 0 & 1 & 0 & 0 & \sqrt{2} & 0 \\ 0 & 0 & 0 & 0 & 0 & 0 \\ -\sqrt{2} & 0 & 0 & 2 & 0 & 0 \\ 0 & \sqrt{2} & 0 & 0 & 2 & 0 \\ 0 & 0 & 0 & 0 & 0 & 0 \end{pmatrix} \tag{2.24}$$

and

$$\hat{\tau}_Y = \frac{1}{6}\begin{pmatrix} 2 & 0 & 0 & \sqrt{2} & 0 & -\sqrt{6} \\ 0 & 2 & \sqrt{6} & 0 & -\sqrt{2} & 0 \\ 0 & \sqrt{6} & 3 & 0 & -\sqrt{3} & 0 \\ \sqrt{2} & 0 & 0 & 1 & 0 & -\sqrt{3} \\ 0 & -\sqrt{2} & -\sqrt{3} & 0 & 1 & 0 \\ -\sqrt{6} & 0 & 0 & -\sqrt{3} & 0 & 3 \end{pmatrix} \tag{2.25}$$

In the presence of tetragonal distortion and octahedra rotations, as in the case of Sr_2IrO_4, the transfer matrix elements are more conveniently described using the global coordinate system. The hopping between γ and γ' states is then given by

$$\bar{T}^{\gamma,\gamma'}_{n,n+x} = t_{eff}\left(\bar{\tau}^{\gamma,\gamma'}_Z + \bar{\tau}^{\gamma,\gamma'}_Y\right), \tag{2.26}$$

where modified transfer matrices are defined as

$$\begin{aligned} \bar{\tau}^{\gamma,\gamma'}_Z &= {}_{\gamma'}\langle\Psi_B|\hat{T}|p^y_\sigma\rangle\langle p^y_\sigma|\hat{T}|\Psi_A\rangle_\gamma, \\ \bar{\tau}^{\gamma,\gamma'}_Y &= {}_{\gamma'}\langle\Psi_B|\hat{T}|p^z_\sigma\rangle\langle p^z_\sigma|\hat{T}|\Psi_A\rangle_\gamma. \end{aligned} \tag{2.27}$$

Explicitly, $\hat{\bar{\tau}}_Z$ and $\hat{\bar{\tau}}_Y$ are given by

$$\hat{\bar{\tau}}_Z = c^2_\alpha\begin{pmatrix} s^2_\theta & 0 & 0 & s_\theta c_\theta & 0 & 0 \\ 0 & s^2_\theta & 0 & 0 & s_\theta c_\theta & 0 \\ 0 & 0 & 0 & 0 & 0 & 0 \\ s_\theta c_\theta & 0 & 0 & c^2_\theta & 0 & 0 \\ 0 & s_\theta c_\theta & 0 & 0 & c^2_\theta & 0 \\ 0 & 0 & 0 & 0 & 0 & 0 \end{pmatrix} \tag{2.28}$$

and

$$\hat{\bar{\tau}}_Y = \frac{1}{2}\begin{pmatrix} c_\theta^2 e^{2\imath\alpha} & 0 & 0 & -s_\theta c_\theta & 0 & c_\theta e^{2\imath\alpha} \\ 0 & c_\theta^2 e^{-2\imath\alpha} & -c_\theta e^{-2\imath\alpha} & 0 & -s_\theta c_\theta & 0 \\ 0 & -c_\theta e^{-2\imath\alpha} & e^{2\imath\alpha} & 0 & s_\theta & 0 \\ -s_\theta c_\theta & 0 & 0 & s_\theta^2 e^{2\imath\alpha} & 0 & -s_\theta \\ 0 & -s_\theta c_\theta & s_\theta & 0 & s_\theta^2 e^{-2\imath\alpha} & 0 \\ c_\theta e^{-2\imath\alpha} & 0 & 0 & -s_\theta & 0 & e^{-2\imath\alpha} \end{pmatrix} \tag{2.29}$$

Next, we apply $PH_{t,n,n'}$ to the $D^\dagger_{\xi,n'}$ state and obtain

$$\begin{aligned} & PH_{t,n,n'}D^\dagger_{\xi,n'} = \\ & \sum_{\gamma=1}^{2}\sum_{\gamma'=1}^{6} T^{\gamma,\gamma'}_{n,n'} b^\dagger_{n,\gamma} b_{n',\gamma'} \sum_{\nu=1}^{15}\sum_{\gamma_1,\gamma_2=1}^{6} c_{\xi,\nu} m^\nu_{\gamma_1\gamma_2} b^\dagger_{n',\gamma_1} b^\dagger_{n',\gamma_2} \\ & = \sum_{\gamma,\gamma'=1}^{2}\sum_{\gamma_1=1}^{6}\sum_{\nu=1}^{15} T^{\gamma,\gamma_1}_{n,n'} c_{\xi,\nu}(m^\nu_{\gamma_1\gamma'} - m^\nu_{\gamma'\gamma_1}) b^\dagger_{n,\gamma} b^\dagger_{n',\gamma'} \ . \end{aligned} \tag{2.30}$$

Here the terms with $b^\dagger_{n',\gamma_1} b^\dagger_{n',\gamma_2}$ for $\gamma_1, \gamma_2 > 2$ are projected out by the operator $P_{n'}$. Finally, using the following relation,

$$PH_t Q_{\xi,n'} H_t P = [PH_t D^\dagger_{\xi,n'}][PH_t D^\dagger_{\xi,n'}]^\dagger, \tag{2.31}$$

where

$$PH_{t,n,n'}D^\dagger_{\xi,n'} = \sum_{\sigma,\sigma'=\pm 1} A^\xi_{\sigma,\sigma'} b^\dagger_{n,\sigma} b^\dagger_{n',\sigma'} \tag{2.32}$$

with

$$A^\xi_{n,n';\sigma,\sigma'} = \sum_{\gamma_1=1}^{6}\sum_{\nu=1}^{15} T^{\sigma,\gamma_1}_{n,n'} c_{\xi,\nu}(m^\nu_{\gamma_1\sigma'} - m^\nu_{\sigma'\gamma_1}) \ , \tag{2.33}$$

we write the exchange Hamiltonian as

$$\begin{aligned} H_{ex,n,n'} \ = \ & \sum_{\sigma,\sigma'=1}^{2}\sum_{\sigma_1,\sigma_1'=1}^{2}\sum_{\xi=1}^{15} \\ & \frac{1}{\epsilon_\xi}\{A^\xi_{n,n';\sigma,\sigma'} b^\dagger_{n,\sigma} b^\dagger_{n',\sigma'} A^\xi_{n',n;\sigma_1',\sigma_1} b_{n',\sigma_1'} b_{n,\sigma_1}\} \ . \end{aligned} \tag{2.34}$$

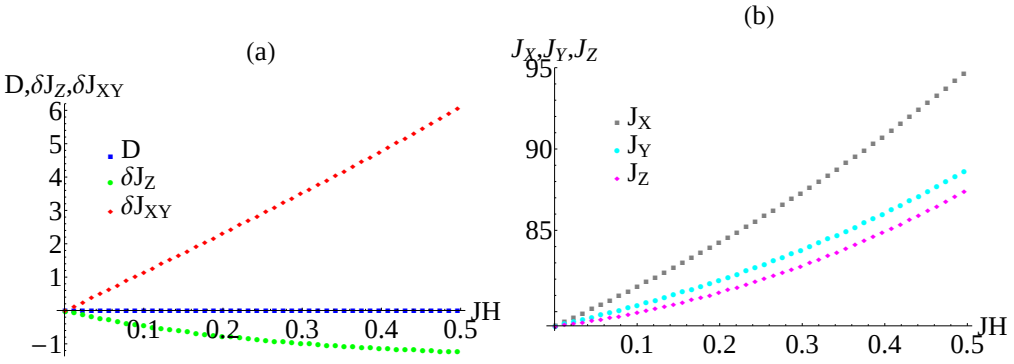

Figure 2.2: (a) The anisotropic exchange couplings $\delta J_{xy}, \delta J_z$ and the DM constant D in meV (shown by red diamonds, green circles and blue squares lines, respectively) as functions of Hund's coupling, J_H. (b) The exchange couplings J_x, J_y, J_z in meV (shown by gray squares, cyan circles and magenta diamonds lines, respectively) as functions of Hund's coupling, J_H. The microscopic parameters of the model are considered to be $\alpha = 0$ rad, $\Delta = 0.15$ eV, $U_2 = 1.8$ eV, $\lambda = 0.4$ eV, $t_{eff} = 0.13$ eV.

We note that $A^{\xi}_{n',n;\sigma',\sigma} = \left(A^{\xi}_{n,n';\sigma,\sigma'}\right)^*$. In the following, in order to shorten notations, we omit the site indices denoting $A^{\xi}_{n,n';\sigma,\sigma'} \equiv A^{\xi}_{\sigma,\sigma'}$ and $A^{\xi}_{n',n;\sigma',\sigma} \equiv \left(A^{\xi}_{\sigma,\sigma'}\right)^*$. We also observe that $\sum_{\xi} \frac{1}{\epsilon_\xi} A^{\xi}_{\sigma,\sigma} A^{\xi}_{\sigma_1,-\sigma_1} = 0$, since $A^{\xi}_{\sigma,\sigma}$ and $A^{\xi}_{\sigma_1,-\sigma_1}$ connect different groups of states $|D,\xi\rangle$ and are therefore "orthogonal". Defining operators $B_{n\sigma\sigma'} = b^{\dagger}_{n,\sigma} b_{n,\sigma'}$, we may write the superexchange Hamiltonian (2.34) in the form

$$
\begin{aligned}
H_{ex,n,n'} = \sum_{\xi=1}^{15} \frac{1}{\epsilon_\xi} \{ & \\
& A^{\xi}_{\uparrow\uparrow} \left(A^{\xi}_{\uparrow\uparrow}\right)^* \left(B_{n\uparrow\uparrow} B_{n'\uparrow\uparrow} + B_{n\downarrow\downarrow} B_{n'\downarrow\downarrow}\right) + \\
& A^{\xi}_{\uparrow\downarrow} \left(A^{\xi}_{\uparrow\downarrow}\right)^* \left(B_{n\uparrow\uparrow} B_{n'\downarrow\downarrow} + B_{n\downarrow\downarrow} B_{n'\uparrow\uparrow}\right) + \\
& A^{\xi}_{\uparrow\downarrow} \left(A^{\xi}_{\downarrow\uparrow}\right)^* \left(B_{n\uparrow\downarrow} B_{n'\downarrow\uparrow} + B_{n\downarrow\uparrow} B_{n'\uparrow\downarrow}\right) + \\
& A^{\xi}_{\uparrow\uparrow} \left(A^{\xi}_{\downarrow\downarrow}\right)^* \left(B_{n\uparrow\downarrow} B_{n'\uparrow\downarrow} + B_{n\downarrow\uparrow} B_{n'\downarrow\uparrow}\right) \}
\end{aligned}
\tag{2.35}
$$

Next, we introduce pseudospin operators $S^{\alpha}_n = \frac{1}{2} \sum_{\sigma,\sigma'=\pm1} \tau^{\alpha}_{\sigma,\sigma'} b^{\dagger}_{\sigma,n} b_{\sigma',n}$ with the Pauli matrices $\tau^{\alpha}_{\sigma,\sigma'}, \alpha = x, y, z$ and $\rho_n = \sum_{\sigma=\pm1} b^{\dagger}_{\sigma,n} b_{\sigma,n}$ and express operators $B_{n\sigma\sigma'}$

in terms of pseudospin operators as

$$\begin{aligned} B_{n\uparrow\uparrow} &= S_n^z + \rho_n \\ B_{n\downarrow\downarrow} &= -S_n^z + \rho_n \\ B_{n\uparrow\downarrow} &= S_n^+ \\ B_{n\downarrow\uparrow} &= S_n^-. \end{aligned} \tag{2.36}$$

This allows us to write the super-exchange Hamiltonian (2.35) on the bond n, n' in terms of the magnetic degrees of freedom of Ir^{4+} as

$$\begin{aligned} H_{ex,n,n'} = \quad & J_z S_n^z S_{n'}^z + J_x S_n^x S_{n'}^x + J_y S_n^y S_{n'}^y \\ & -D(S_n^x S_{n'}^y - S_n^y S_{n'}^x) + W\rho_n\rho_{n'} \ , \end{aligned} \tag{2.37}$$

where the coupling constants are given by the following expressions:

$$\begin{aligned} J_z = -2\sum_\xi \frac{1}{\epsilon_\xi} \quad & \Big(A^\xi_{\uparrow\uparrow}\left(A^\xi_{\uparrow\uparrow}\right)^* + A^\xi_{\downarrow\downarrow}\left(A^\xi_{\downarrow\downarrow}\right)^* \\ & -A^\xi_{\uparrow\downarrow}\left(A^\xi_{\uparrow\downarrow}\right)^* - A^\xi_{\downarrow\uparrow}\left(A^\xi_{\downarrow\uparrow}\right)^*\Big), \end{aligned} \tag{2.38}$$

$$\begin{aligned} J_x = -2\sum_\xi \frac{1}{\epsilon_\xi} \quad & \Big(A^\xi_{\uparrow\uparrow}\left(A^\xi_{\downarrow\downarrow}\right)^* + A^\xi_{\downarrow\downarrow}\left(A^\xi_{\uparrow\uparrow}\right)^* \\ & +A^\xi_{\uparrow\downarrow}\left(A^\xi_{\downarrow\uparrow}\right)^* + A^\xi_{\downarrow\uparrow}\left(A^\xi_{\uparrow\downarrow}\right)^*\Big), \end{aligned} \tag{2.39}$$

$$\begin{aligned} J_y = 2\sum_\xi \frac{1}{\epsilon_\xi} \quad & \Big(A^\xi_{\uparrow\uparrow}\left(A^\xi_{\downarrow\downarrow}\right)^* + A^\xi_{\downarrow\downarrow}\left(A^\xi_{\uparrow\uparrow}\right)^* \\ & -A^\xi_{\uparrow\downarrow}\left(A^\xi_{\downarrow\uparrow}\right)^* - A^\xi_{\downarrow\uparrow}\left(A^\xi_{\uparrow\downarrow}\right)^*\Big), \end{aligned} \tag{2.40}$$

$$D = 2\imath\sum_\xi \frac{1}{\epsilon_\xi}\Big(A^\xi_{\uparrow\downarrow}\left(A^\xi_{\downarrow\uparrow}\right)^* - A^\xi_{\downarrow\uparrow}\left(A^\xi_{\uparrow\downarrow}\right)^*\Big), \tag{2.41}$$

$$\begin{aligned} W = -2\sum_\xi \frac{1}{\epsilon_\xi} \quad & \Big(A^\xi_{\uparrow\uparrow}\left(A^\xi_{\uparrow\uparrow}\right)^* + A^\xi_{\downarrow\downarrow}\left(A^\xi_{\downarrow\downarrow}\right)^* + \\ & A^\xi_{\uparrow\downarrow}\left(A^\xi_{\uparrow\downarrow}\right)^* + A^\xi_{\downarrow\uparrow}\left(A^\xi_{\downarrow\uparrow}\right)^*\Big) \end{aligned} \tag{2.42}$$

The last interaction term W gives a constant energy shift and we will omit it. It is also convenient to rewrite the remaining terms introducing the following notations: $\delta J_z = J_z - J_y$, $\delta J_{xy} = J_x - J_y$ on x-bond and $\delta J_z = J_z - J_x$, $\delta J_{xy} = J_y - J_x$ on y-bond. Then, $H_{ex,n,n'}$ can be written as

$$H_{ex,n,n'} = J\mathbf{S}_n\mathbf{S}_{n'} - D(S_n^x S_{n'}^y - S_n^y S_{n'}^x) \\ +\delta J_z S_n^z S_{n'}^z + \delta J_{xy}\left(\mathbf{S}_n \cdot \mathbf{r}_{n,n'}\right)\left(\mathbf{S}_{n'} \cdot \mathbf{r}_{n,n'}\right) \ , \tag{2.43}$$

where $\mathbf{r}_{n,n'}$ is the unit vector along the n, n' bond. In this form the nature of interactions between pseudospin moments S is more clear. The first term describes the Heisenberg isotropic interaction with a coupling constant $J = J_y$ on the x-bond. We note that for any possible set of microscopic parameters, the isotropic exchange is the dominant exchange and has AFM nature. The second term is a Dzyaloshinsky-Moriya (DM) interaction with a coupling constant D, which leads to a spin canting in the xy-plane proportional to the ratio D/J. The third term describes an additional Ising-like interaction of z-components of spins. $\delta J_z > 0$ favors AFM ordering of spins along the z axis and works as an easy axis anisotropy. $\delta J_z < 0$ supports FM ordering of spins along the z axis and works as an easy plane anisotropy. The last term is a pseudo-dipolar interaction. Finally, the total superexchange Hamiltonian is given by

$$H = \sum_{\langle n,n' \rangle} H_{ex,n,n'}, \tag{2.44}$$

where summation is over all bonds of the lattice.

2.4 Results and discussions

2.4.1 Application to Sr_2IrO_4

Below we present our results on how the exchange coupling constants J_x, J_y, J_z and anisotropic couplings $\delta J_{xy}, \delta J_z$ and D depend on the microscopic parameters of the system. We first note that the main role of the Coulomb repulsion is to determine the overall energy scale for the couplings. In all computations we take $U_2 = 1.8$ eV, which lays inside the range of values, 1.5 eV-2.5 eV, characteristic for iridates [32, 34]. We will mostly set the SOC constant to be equal to $\lambda = 0.4$ eV - the value associated with

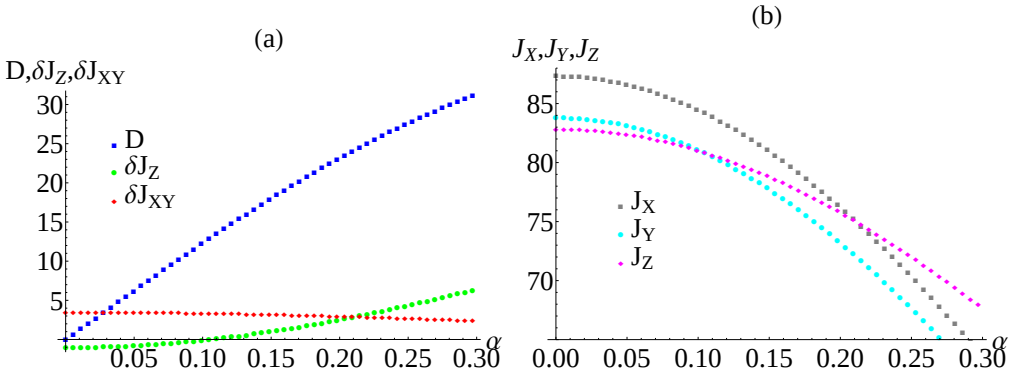

Figure 2.3: (a) The anisotropic exchange couplings $\delta J_{xy}, \delta J_z$ and DM constant D in meV (shown by red diamonds, green circles and blue squares lines, respectively) and (b) the exchange couplings J_x, J_y, J_z in meV (shown by gray squares, cyan circles and magenta diamonds lines, respectively) as functions of the rotation angle α. The other microscopic parameters considered to be $\Delta = 0.15$ eV, $U_2 = 1.8$ eV, $J_H = 0.3$ eV, $\lambda = 0.4$ eV and $t_{eff} = 0.13$ eV.

Ir ions in the literature, however, we will also consider the smaller value $\lambda = 0.22$ eV, which was suggested in the experimental work by Haskel *et al* [28].

Sr_2IrO_4 is also characterized by various structural distortions, the most important of which are the tetragonal distortion and rotations of the oxygen octahedra. Both of them are present even at ambient pressure. In calculations we either consider the tetragonal distortion and the angle of rotation to be equal to $\Delta = 0.15$ eV and $\alpha = 0.2$ rad, respectively, or we study how the exchange parameters depend on these quantities.

Finally, we consider the hopping parameter between Ir ions to be equal to $t_{eff} = 0.13$ eV, which is slightly lower than the values 0.2-0.3 eV suggested by ab-initio calculations. These values of hoppings give too large values of exchange couplings if all other parameters are set as we described above. We believe, however, that hopping parameters obtained within density functional theory are often reduced when correlations are taken into account.

The effect of Hund's coupling. In Fig.2.2 (a) we plot the anisotropic couplings $\delta J_{xy}, \delta J_z$ and the DM interaction constant D as functions of Hund's coupling, J_H, in the absence of octahedral rotations, $\alpha = 0$. In this case, the components of the vectors

$A^{\xi}_{\sigma,\sigma'}$ (2.33) satisfy the following conditions:

$$\begin{aligned} \sum_{\xi} \frac{1}{\epsilon_{\xi}} (A^{\xi}_{\uparrow\uparrow})^2 &= \sum_{\xi} \frac{1}{\epsilon_{\xi}} (A^{\xi}_{\downarrow\downarrow})^2 \ , \\ \sum_{\xi} \frac{1}{\epsilon_{\xi}} (A^{\xi}_{\uparrow\downarrow})^2 &= \sum_{\xi} \frac{1}{\epsilon_{\xi}} (A^{\xi}_{\downarrow\uparrow})^2 \ . \end{aligned} \tag{2.45}$$

This symmetry reflects the fact that in the absence of the octahedra rotations there is no spin dependent hopping and, consequently, no DM interaction. The anisotropic terms δJ_z and δJ_{xy} are also zero at $\alpha = 0$ and $J_H = 0$ eV, but they acquire finite values at $J_H \neq 0$. We note that the Ising-like interaction, $\delta J_z < 0$, makes the xy-plane the pseudospin's easy plane.

In Fig. 2.2 (b) we plot the exchange couplings J_x, J_y, J_z as functions of the Hund's coupling. On the x-bond, the isotropic exchange $J = J_y$. It is antiferromagnetic for all considered values of J_H and its strength varies in the range $J \in (78 - 95)$ meV for $J_H \in (0 - 0.5)$ eV. This compares well not only with an estimate $J = 51$ meV obtained by ab initio many-body quantum-chemical calculations [54], but also with experimental findings in $SrIr_2O_4$, for which resonant inelastic x-ray scattering [25] and resonant magnetic x-ray diffuse scattering measurements [27] indicate the isotropic exchange to be $J \simeq 60$ meV and $J \simeq 100$ meV, respectively.

The effect of staggered rotations of IrO_6 octahedra. The dependencies of the anisotropic couplings $\delta J_{xy}, \delta J_z$ and D and the exchange constants J_x, J_y, J_z on the strength of the staggered rotations of the IrO_6 octahedra, α, are presented in Fig.2.3 (a) and (b). We first note that the isotropic exchange coupling $J = J_y \in (64 - 87)$ meV remains in good agreement with experimental estimates in the whole range of values of α considered. However, most importantly, the DM interaction becomes the dominant anisotropy even at small α. At $\alpha \simeq 0.2$ rad (11.5°), the DM interaction is already about 23 meV, which roughly corresponds to third of the isotropic interaction (see Fig.2.3 (b)). Such a large ratio between the DM interaction and the isotropic Heisenberg exchange is very unusual and has never been observed in 3d transition metal oxides.

The other anisotropic interactions, both the pseudo-dipolar in-plane interaction, δJ_{xy}, and the Ising-like term, δJ_z, remain relatively small at finite values of α. We note that δJ_z changes sign above some angle of octahedra rotation, $\alpha_c \simeq 0.1$ rad, but, as it remains a subdominant interaction, the magnetic moments remain lying in the

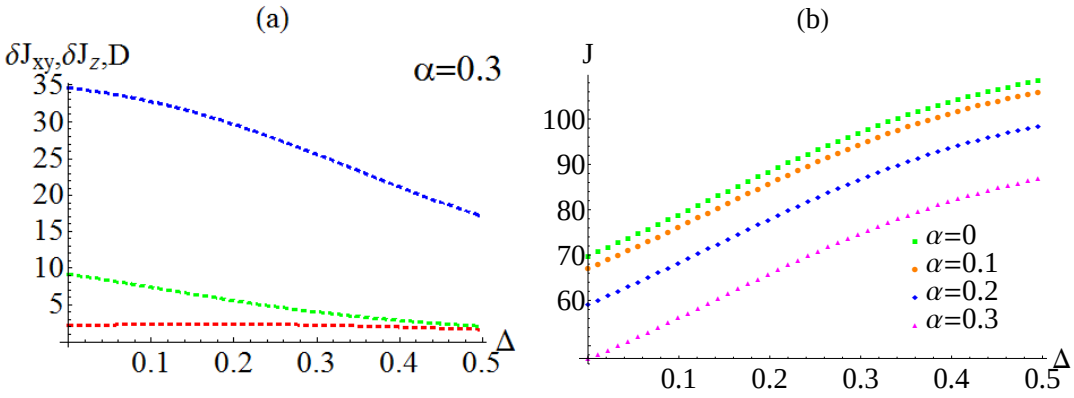

Figure 2.4: (a) The anisotropic exchange couplings $\delta J_{xy}, \delta J_z$ and DM constant D in meV (shown by red diamonds, green circles and blue squares lines, respectively) as functions of the tetragonal CF splitting computed for $\alpha = 0.2$ rad (b) The dependencies of the isotropic exchange J on the strength of the tetragonal CF splitting Δ. Green squares, orange circles, blue diamonds, magenta triangles lines correspond to $\alpha = 0; 0.1; 0.2; 0.3$ rad, respectively. The other parameters are $\lambda = 0.4$ eV, $U_2 = 1.8$ eV, $J_H = 0.3$ eV and $t_{eff} = 0.13$ eV.

xy-plane.

The effect of tetragonal distortion. Significant changes in the super-exchange parameters are caused by the tetragonal distortion. At ambient pressure the tetragonal distortion is about $\Delta \simeq 0.1$ eV, however, larger values can be easily reached under pressure [28]. In Fig.2.4 (a) we plot the dependencies of the anisotropic exchange couplings $\delta J_{xy}, \delta J_z$ and the DM coupling, D, on the strength of the tetragonal distortion, Δ. An increased tetragonal distortion leads to a substantial decrease of both D and δJ_z, but the overall hierarchy of anisotropic interactions remains the same. We see that if α was not changing under pressure, the magnetic anisotropy would remain an easy plane anisotropy for all values of the tetragonal distortion.

In Fig. 2.4 (b) we present the results on how the isotropic exchange depends on Δ at different values of α. We see that the isotropic part of the exchange coupling increases with increasing strength of the tetragonal distortion. We also see that its dependence on Δ has a quantitatively similar character for all α, with the largest values of J reached at $\alpha = 0$. Importantly, for all values of α and Δ, the isotropic exchange remains the dominant interaction with respect to the anisotropic terms.

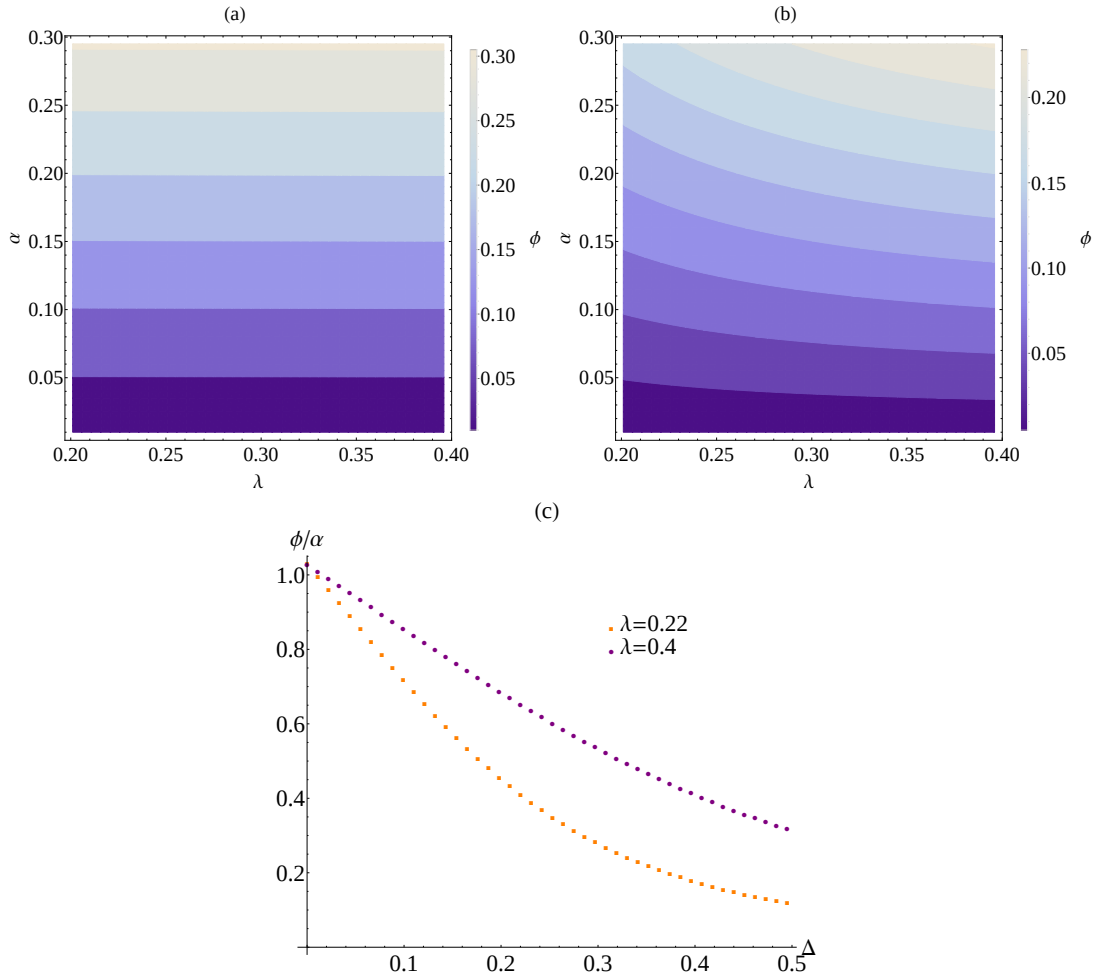

Figure 2.5: The mean field magnetic phase diagram in the parameter space of rotation angle α and the SOC coupling λ computed (a) in the absence of the tetragonal distortion, $\Delta = 0$ eV and (b) in the presence of the tetragonal distortion, $\Delta = 0.15$ eV. In both parameter sets, the obtained magnetic structure is coplanar antiferromagnet with varying spin canting angle $\phi = [\pi - (\phi_A - \phi_B)]/2$, where ϕ_A and ϕ_B are the polar angles of spins on sublattices A and B. The color on the plots indicates the scale for which the angle ϕ changes with dark blue being the smallest and gray being the highest value of the angle ϕ. The canted spin order is stabilized by a staggered rotations of oxygen tetrahedra in the presence of the SOC. (c) The dependence of the spin canting angle $\phi = 1/2 \tan^{-1}(D/J)$ (in units of α) on the strength of the tetragonal CF splitting Δ computed for $\lambda = 0.22$ eV (orange squares line) and $\lambda = 0.4$ eV (purple circles line). The other microscopic parameters are chosen to be $U_2 = 1.8$ eV, $J_H = 0.3$ eV, and $t_{eff} = 0.13$ eV, $\alpha = 0.2$ rad.

Magnetic phase diagram. Finally, we compute a magnetic phase diagram of the model 2.43. The model allows for two distinct magnetic phases: a coplanar (or collinear) two-sublattice antiferromagnet with spins lying in the xy-plane, and a collinear phase with spins pointing along the c-axis. The coplanar phase is characterized by a spin canting angle ϕ, which is simply given by $\phi = 1/2 \tan^{-1}(D/J)$. The dependence of the spin canting angle ϕ (in units of α) on Δ computed for $\alpha = 0.2$ rad, corresponding to the angle of octahedral rotations at ambient pressure, and $J_H = 0.3$ is presented in Fig. 2.5 (c). We can see that in the cubic case, $\Delta = 0$, the ratio ϕ/α is equal to unity and, therefore, spins are canted exactly like the IrO_6 octahedra. At finite Δ, the ratio ϕ/α is smaller than one, suggesting that in the presence of the tetragonal distortion the spin structure has an additional rigidity with respect to canting.

A magnetic structure can be determined by minimizing the classical energy taking into account *all* exchange couplings present in the model. Assuming that in the presence of a staggered rotation of oxygen octahedra, the magnetic structure is defined by two magnetic sublattices, A and B, and that the orientation of the magnetic moments can be described with the help of four angles, $\theta_A, \theta_B, \phi_A, \phi_B$, we can write the classical energy as

$$\begin{aligned} &E_{cl}(\theta_A, \theta_B, \phi_A, \phi_B) = J_z \cos\theta_A \cos\theta_B + \\ &\frac{(J_x + J_y)}{2} \sin\theta_A \sin\theta_B (\cos\phi_A \cos\phi_B + \sin\phi_A \sin\phi_B) \\ &-D \sin\theta_A \sin\theta_B (\cos\phi_A \sin\phi_B - \sin\phi_A \cos\phi_B) \ . \end{aligned} \tag{2.46}$$

One can easily check that the contribution of the pseudo-dipolar interaction to the classical energy cancels out. Thus, for any set of microscopic parameters, the classical ground state is determined by the competition between the DM interaction and the Ising-like anisotropy in the presence of a dominating AFM isotropic exchange.

In Fig.2.5 (a) and (b) we present a mean field magnetic phase diagram, where for each set of parameters the magnetic structure is determined by minimizing E_{cl} with respect to $\theta_A, \theta_B, \phi_A, \phi_B$. We considered two cases: Fig.2.5 (a) displays a phase diagram computed in the absence of tetragonal distortion ($\Delta = 0$ eV) and Fig.2.5 (a) displays a phase diagram computed in the presence of the tetragonal distortion ($\Delta = 0.15$ eV). In both cases we considered the Hund's coupling to be equal to $J_H = 0.3$ eV. Both phase diagrams contain only the coplanar antiferromagnet with varying canting angle

$\phi = [\pi - (\phi_A - \phi_B)]/2$, where ϕ_A and ϕ_B are polar angles of spins on sublattices A and B. The color on the plots indicates the magnitude scale of the angle ϕ: dark blue colors correspond to the smallest and light gray colors correspond to the highest values of the angle ϕ. As we discussed above, in the absence of the tetragonal distortion, the canting of magnetic moments rigidly follows the octahedral rotation and the canting angle ϕ is exactly equal to the rotation angle α for all values of the SOC strength (see Fig.2.5(a)). However, once the tetragonal distortion is present, the canting angle ϕ becomes smaller than α. Moreover, the ratio ϕ/α decreases with decrease of the SOC constant (see Fig.2.5(b)).

We have to note that our findings are not in full agreement with the phase diagram presented by Jackeli and Khalliulin in Ref. [1], which shows that at large values of tetragonal distortion the spin-flop transition from the in-plane canted spin state happens to a collinear antiferromagnetic order along the z-axis. Instead, we found that at the considered set of parameters the tetragonal distortion may lead to a disappearance of the ferromagnetic moment and a stabilization of the antiferromagnetic order in the easy xy plane.

Our findings are, however, in qualitative agreement with both pressure experiments in $SrIr_2O_4$ [28] and the x-ray resonant magnetic scattering study comparing the magnetic and electronic structures of $SrIr_2O_4$ and $BaIr_2O_4$. [29] The first study shows that when the tetragonal distortion due to pressure becomes relatively strong, about 17 GPa, the ferromagnetic order disappears. This magnetic transition was not attributed to the gradual disappearance of the IrO_6 rotations under pressure, because it would have likely resulted in some kind of structural transition which was not observed. They also found that the application of pressure up to at least 40 GPa does neither destroy the insulating behavior nor, probably, the antiferromagnetic order. However, the direction of the antiferromagnetic order parameter was not determined. The second study shows the general robustness of the basal-plane antiferromagnetic order in single-layer iridates. They found that in both $SrIr_2O_4$ and $BaIr_2O_4$, the antiferromagnetic component is oriented along the [110] direction despite the fact that moving from $SrIr_2O_4$ to $BaIr_2O_4$ the tetragonal distortion is nearly doubled.

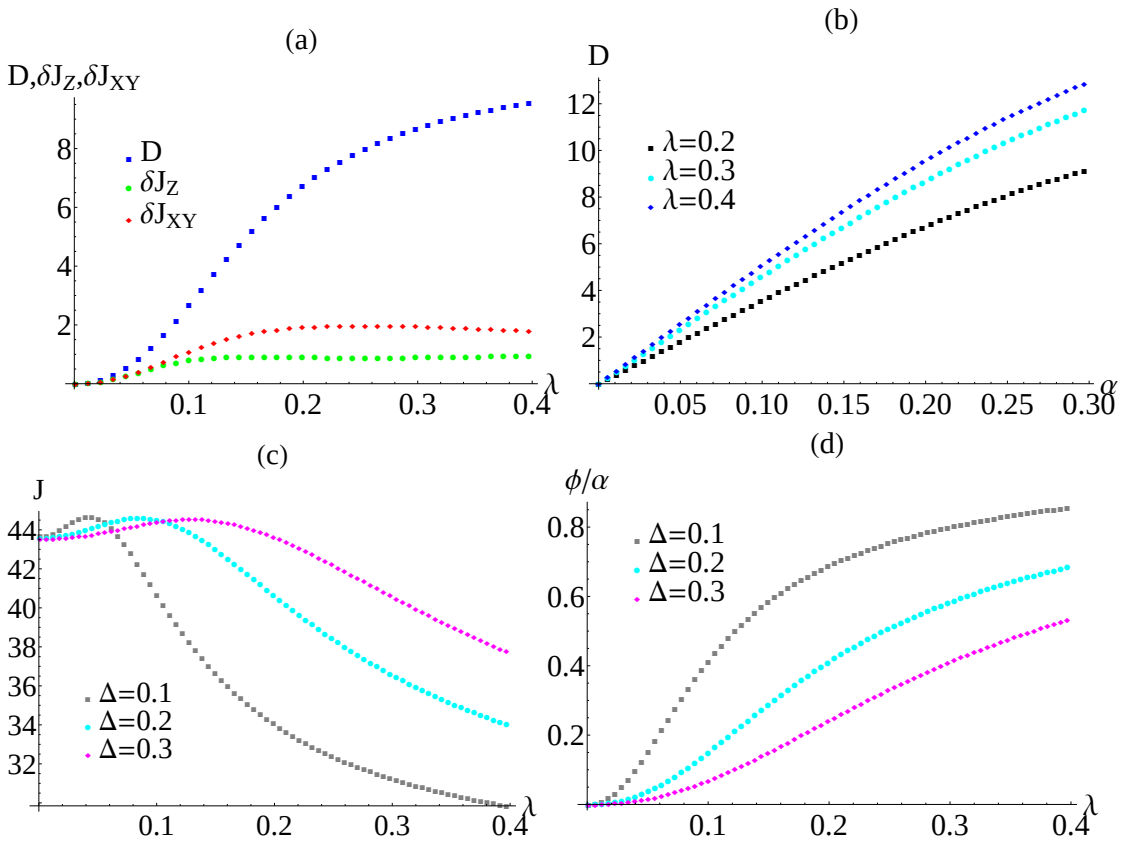

Figure 2.6: (a) The anisotropic exchange couplings $\delta J_{xy}, \delta J_z$ and the DM constant D (in meV) as functions of SOC constant λ shown by red diamonds, green circles and blue squares lines, respectively. (b) The DM constant D (in meV) as function of rotation angle α. Black squares, cyan circles, blue diamonds lines correspond to $\lambda = 0.2; 0.3; 0.4$ eV, respectively. (a) and (b) The tetragonal field is considered to be equal to $\Delta = 0.2$ eV. (c) The isotropic exchange J (in meV) and (d) the spin canting angle ϕ (in units of α) as functions of SOC constant λ. Gray squares, cyan circles, magenta diamonds lines correspond to $\Delta = 0.1; 0.2; 0.3$ eV, respectively. (a),(c) and (d) The rotation angle is considered to be equal to $\alpha = 0.2$ rad. The remaining parameters are $J_H = 0.5$ eV, $U_2 = 2.5$ eV, and $t_{eff} = 0.1$ eV.

2.4.2 Application to $Sr_2Ir_{1-x}Rh_xO_4$.

In this section we take a look at the properties of the $Sr_2Ir_{1-x}Rh_xO_4$ family of compounds, which results from substituting Sr_2IrO_4 by Rh ions [52]. Doping iridates with Rh ions does not change the band filling since Rh and Ir are in the same family of elements. However, the 4d orbitals of Rh are smaller than the 5d orbitals of Ir, which leads to a higher Coulomb repulsion, Hund's coupling and tetragonal CF splitting. Smaller atoms (such as Rh) also have reduced relativistic effects, including SO coupling. The effective hopping is reduced both due to a smaller overlap of the less extended 4d orbitals as well as due to the increased Coulomb repulsion. All of this increases the importance of correlation effects and CF splitting as compared to that of SOC.

We also note that Sr_2RhO_4, the limiting case of Rh doping, shares with Sr_2IrO_4 the structural feature of staggered octahedra rotations about the axis perpendicular to the Rh/Ir planes. The angles of rotation are similar to each other: $\sim 9.4^\circ$ for Sr_2RhO_4 and $\sim 12^\circ$ for Sr_2IrO_4 [52]. This structure is preserved at intermediate levels of doping. As a result in the doped compounds the same interaction components are present as in pure Sr_2IrO_4 (Coulomb, Hund, SOC, CF, oxygen-assisted hopping, lattice distortions). Thus we expect the magnetic Hamiltonian to have the same structure of interactions. What changes is the overall energy balance of on-site interactions, which in the Rh-doped iridates eventually leads to the appearance of different magnetic phases compared to those in pure iridium compounds.

Let us note that a reduced hopping simply leads to a decrease of the energy scale of all interactions (both the isotropic term and the anisotropies). The effects of reduced SOC are more intricate since SOC is the only interaction that mixes the orbital and the spin degrees of freedom of the holes. Thus we also expect the energy scale of the anisotropies to be reduced as compared to the isotropic term. This, however, does not diminish the importance of the anisotropic terms as their essential role is to break the SU(2) symmetry of the isotropic interaction.

In Fig. 2.6 (a) and (c) we plot the dependencies of the anisotropic and isotropic interactions, respectively, on the strength of λ. We adjust all other parameters in accordance with the rhodium doping picture discussed above: $\Delta = 0.2$ eV, $\alpha = 0.2$ rad, $J_H = 0.5$ eV, $U_2 = 2.5$ eV, and $t_{eff} = 0.1$ eV. A similar set of parameters might be realized at low Rh doping. As expected the overall energy scale of the magnetic

interactions is decreased due to Coulomb repulsion and smaller hopping. In Fig. 2.6 (a) we also see that once the SOC becomes too small relative to other interactions to effectively mix the orbital and spin degrees of freedom the anisotropic interactions quickly drop and reach zero in the limit of no SOC.

The behavior of the isotropic interaction is more interesting as it is weakly nonmonotonic as a function of SO-coupling. This can be explained when we look at different values of Δ. Gray, cyan, and magenta lines in Fig. 2.6 (c) show the isotropic interaction corresponding to $\Delta = 0.1, 0.2, 0.3$ eV, respectively. Since cubic orbitals have different hopping amplitudes due to the staggered rotations of the octahedra and the orbital symmetries, the orbital composition of the ground state also determines the isotropic part of the exchange Hamiltonian. As the orbital composition is very sensitive to the interplay between the SOC and the CF, the small changes in their relative contribution lead to a non-monotonic behavior of J.

Fig. 2.6 (b) shows the dependence of the DM anisotropy on the staggered rotation angle α computed for $\lambda = 0.2; 0.3; 0.4$ eV (respectively, black, cyan and blue lines). As is the case for the pure Sr_2IrO_4 compound the DM interaction depends heavily on the angle but as we discussed above the overall range of DM interactions is smaller.

Finally, in Fig. 2.6 (d) we present the spin canting angle ϕ (in units of α) as a function of the SOC constant λ for various values of the tetragonal distortion Δ. As expected, the canting angle is zero in the limit of zero SOC and is increasing with increasing λ, demonstrating the key role of SOC in the entanglement of the spin and lattice degrees of freedom. As we discussed above, the spin canting angle is suppressed by the tetragonal distortion.

Our findings are in a qualitative agreement with experimental findings for the $Sr_2Ir_{1-x}Rh_xO_4$ family of compounds showing that Rh doping rapidly suppresses the magnetic transition temperature T_C from 240 K at $x = 0$ to almost zero at $x = 0.16$ [52]. The disappearance of long range magnetic order at small doping in real compounds is a rather complicated phenomenon, related to both the reduction of magnetic interactions but also to the more metallic behavior of doped compounds. This aspect, however, can not be considered in our approach based on the assumption of a Mott insulator. We can only speculate that in Rh-doped iridates the splitting between the $\mathbf{J} = 1/2$ and the $\mathbf{J} = 3/2$ states is substantially smaller than in pure iridium systems

and, consequently, these two manifolds are strongly mixed by both Hund's coupling and tetragonal CF. The latter leads to a wider bandwidth and more metallic behavior. Interestingly, at high Rh doping, the system again becomes insulating, however for rather different reasons. There is an energy level mismatch for the Rh and Ir sites that makes the hopping of the carriers between Rh and Ir ions more difficult. The randomness of the Rh/Ir occupations gives rise to Anderson localization and an insulating state [52]. The magnetically ordered phase reappeared at $x > 0.4$, but because of frustration it has rather low ordering temperature T_C of the order half a Kelvin. This magnetic phase needs to be studied in details both experimentally and theoretically.

2.5 Summary

In this chapter we provided a theoretical framework for the derivation of the effective super-exchange Hamiltonian governing magnetic properties of transition metal oxides with partially filled 4d and 5d shells. We particularly focused on iridates and rhodates – materials which exhibit a rich variety of behavior owing to the interplay of correlation effects, strong SOC and lattice distortions. Our approach allows one to relate the non-trivial magnetic behavior observed in these materials to their microscopic parameters. We show that the pseudospin super-exchange interactions governing the magnetic properties of this class of insulating materials have anisotropic components of unusual types, leading not only to a dimensional reduction in pseudospin space (i.e. easy plane or easy axis anisotropy), but also to the chiral DM interaction and to additional frustration by bond-dependent interactions.

How to derive exchange couplings from a given Hubbard-type Hamiltonian in the Mott-insulating regime is generally well understood. What gives rise to a certain complexity in our case is the combination of interactions and single particle energy shifts operating in different Hilbert subspaces. We restrict our consideration to the case of a ground state configuration of a single hole per transition metal ion in a pseudospin doublet state in one of the d-orbital multiplets. The exchange process then involves intermediate states with either zero holes or two holes. The latter states are governed by the Coulomb interaction components, especially the Hund's coupling. These ionic eigenstates need to be constructed and must be projected on to the single particle states

describing the hopping processes. The resulting exchange couplings are then given by summation over all relevant intermediate eigenstates of the corresponding hopping element squared over the excitation energy of the intermediate state.

The proposed theoretical approach can be applied to compute exchange couplings in iridium and rhodium oxides with different lattice geometries. Many of these systems have been suggested as candidates for either interesting magnetic orders or spin-liquid behavior in the Mott insulator regime. Although the approach is quite general and can be applied to a variety of compounds, in this chapter we focused on the single-layer Sr_2IrO_4 and $Sr_2Ir_{1-x}Rh_xO_4$ compounds, which have received much attention recently. For these systems we first derive the isotropic and anisotropic interactions analytically and then study their dependencies on microscopic parameters such as Hund's and SOC coupling, and the strength of the lattice distortions.

Our results are the following. First, the overall strengths of the exchange couplings calculated by us appear to be in good agreement with experimental data, where available. While the Ising-like and pseudospin anisotropic interactions are typically not larger than ten percent of the isotropic exchange, the DM coupling is unusually large. It may be as large as 50% of the isotropic exchange coupling for realistic values of the octahedra rotation angle. This emphasizes the importance of the SOC.

We computed the magnetic phase diagram of the model in the approximation of treating the pseudospins as classical objects.. We show that for the parameter set most closely corresponding to the actual microscopic parameters of Sr_2IrO_4, the magnetic ground state of this compound is a coplanar canted antiferromagnet. This finding is in agreement with the experimental observation of the weak ferromagnetic moment accompanying the ground-state antiferromagnetic order in Sr_2IrO_4. We computed the spin canting angle and show that its magnitude scales with the angle of the staggered rotations of the IrO_6 octahedra, as observed experimentally.

Finally, we studied how the properties of the pure iridium systems are changed with Rh doping. We show that Rh doping significantly modifies the hierarchy of many-body and single-particle interactions: the weaker SOC combined with a stronger Coulomb interaction on Rh sites lead to overall smaller magnetic interactions and a weaker coupling between magnetic and structural degrees of freedom.

Chapter 3

Importance of anisotropic exchange interactions in honeycomb iridates. Minimal model for zigzag antiferromagnetic order in Na_2IrO_3.

3.1 Introduction

In the previous chapter, we applied the Mott insulator scenario, extending the original study by Jackeli and Khaliullin [1], and developed a theoretical framework for the derivation of effective super-exchange Hamiltonians that govern the magnetic properties of systems with strong SO coupling. We showed that the super-exchange Hamiltonian describing interactions between the pseudospins might have unusual anisotropic components. Moreover, these anisotropic interactions might be the dominating interactions between magnetic moments. The form of these anisotropic interactions may also be quite unusual. In particular, they do not need to be confined to the traditional anisotropic

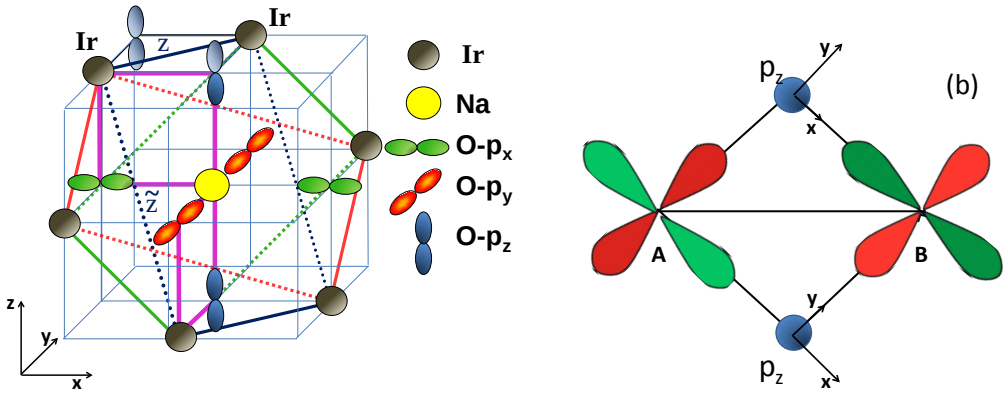

Figure 3.1: (a) Schematic representation of A_2IrO_3 structure. $x-$, $y-$ and $z-$ n.n. Ir-Ir bonds are shown by red, green and blue solid lines. $\tilde{x}-$, $\tilde{y}-$ and $\tilde{z}-$ second n. n. Ir-Ir bonds are shown by red, green and blue dotted lines. Thick magenta lines represents Ir-O-Na-O-Ir second n. n. super-exchange paths. (b) Undistorted 90° Ir-O-Ir bond. Local axes for Ir^{4+} ions on A and B sublattices are the same as the global axes. Two possible super-exchange paths via upper or lower oxygen are shown.

interaction types acting equally on all sites of the lattice (i.e. easy-plane or easy-axis anisotropy). Instead, the anisotropic interactions might involve coupling between different components of spins sitting on different lattice sites. The Dzyaloshinskii-Moriya (DM) interaction [55, 56] and the Kitaev interaction on the honeycomb lattice [3, 46] are salient examples of such interactions. We focused on iridates and rhodates with tetragonal symmetry, e.g. we studied in detail the magnetic interactions in Sr_2IrO_4 [5, 2, 23, 24, 57, 58].

In this chapter, we study the magnetic properties of A_2IrO_3 [8, 47, 48, 49, 59] (A=Na,Li) in which the Ir^{4+} ions occupy the sites of a honeycomb lattice. The nearest-neighbor (n. n.) super-exchange in honeycomb iridates in the absence of lattice distortions, the so-called Kitaev-Heisenberg (KH) model, was first proposed in Refs. [1, 46]. They showed that in these systems the coupling between n. n. Ir magnetic moments occurs through both direct exchange between Ir^{4+} ions and through a super-exchange coupling mediated by an intermediate oxygen along the 90° Ir-O-Ir bond. The latter process gives rise to a nonzero anisotropic interaction between pseudospins, which has the form of the aforementioned Kitaev interactions, but only for a finite value of the Hund's coupling. The KH model correctly captures the nature of the anisotropic part

of the magnetic interactions in Na_2IrO_3 honeycomb compounds and also predicts some non-trivial properties of these compounds at finite temperatures [50, 51]. Nevertheless, the model does miss some essential features: it does not account for both the zigzag magnetic order and for the spectrum of magnetic excitations in Na_2IrO_3 measured in neutron scattering experiments [48, 49, 59]. Partly, this is because the original KH model neither includes further neighbor interactions, which have been shown to play a significant role in stabilizing the zigzag antiferromagnetic ordering in Na_2IrO_3 [12, 59], nor lattice distortions, which might also be essential for these compounds.

Here we revisit the KH model [1, 46] and derive its extension up to second neighbor's interactions, starting from the exact eigenstates of the single-ion microscopic Hamiltonian which equally includes both the SO coupling and the trigonal distortion. In this context, our work differs from the recent study by Bhattacharjee, Lee and Kim [60], in which the effective spin Hamiltonian was derived by setting the energy scale associated with trigonal distortion to infinity first, followed by that of the SO energy scale. We show that the effective spin Hamiltonian on the honeycomb lattice, whose bonding geometry is shown in Fig. 3.1 (a), contains several anisotropic spin interactions among which the strongest is the Kitaev interaction between nearest neighbors.

We also compute the super-exchange interaction between the second neighbors forming two triangular sublattices, and find that it is of a form similar to the n. n. interaction, i.e. the dominant part can be written as a sum of isotropic Heisenberg and anisotropic Kitaev terms. These interactions are only slightly smaller than the n. n. Kitaev interactions. Other anisotropic interactions, which couple different components of spins on a given bond, are significantly smaller and most of them are non-zero only in the presence of trigonal lattice distortions. In this respect they are different from the Kitaev-like interactions which are present even in the ideal structure.

The magnetic phase diagram which emerges from our study is presented in Fig. 3.5. This is the key result of this chapter. We argue that the zigzag magnetic order, experimentally observed in Na_2IrO_3, is stabilized by the interplay of four major interactions: isotropic *antiferromagnetic* and anisotropic *ferromagnetic* Kitaev interactions for n. n. bonds, isotropic *ferromagnetic* and anisotropic *antiferromagnetic* Kitaev interactions for the next-nearest neighbors. Unlike in other theoretical studies of magnetic properties of Na_2IrO_3 [12, 14, 61, 62], in our model the zigzag phase is stabilized for both the correct

signs of n. n. interactions, and even without invoking third neighbor interactions.

The rest of the chapter is organized as follows. In Sec. 3.2, we introduce the single ion microscopic model appropriate for the description of the physical properties of iridates on the honeycomb lattice. We first obtain one-particle eigenstates taking into account only SO coupling and trigonal CF interaction. We then compute two-particle excited eigenstates fully considering correlation effects. Then, in Sec. 3.3, we briefly review the derivation of an effective super-exchange Hamiltonian for these systems. All technical details of the derivation can be found in the previous chapter. In Sec. 3.4, we obtain hopping matrices for neighboring iridium ions. Our calculation is based on a tight-binding fitting of ab-initio electronic structure in the presence of trigonal distortion performed by Foyevtsova *et al* [63]. In Sec. 3.5, we present our results on the magnetic interactions. We show that these interactions can be most generally represented by a 3×3 bond-dependent exchange coupling matrix. We show that, while the Kitaev-type of anisotropy is determined by the inequality of its diagonal elements due to the Hund's coupling, the off-diagonal matrix elements are anisotropies mostly caused by the trigonal crystal field. In Sec. 3.6, taking into account only the dominant interactions, we perform classical Monte Carlo simulations and obtain the low-temperature phase diagram of the minimal super-exchange model for honeycomb iridates. We conclude in Sec. 3.7 with a summary and discussion of our results.

3.2 Single-ion Hamiltonian

3.2.1 One-particle eigenstates

In all iridates considered here, the Ir^{4+} ions sit inside an oxygen cage forming an octahedron. This octahedral CF splits the five $5d$ orbitals of Ir^{4+} into doubly degenerate e_g orbitals at higher energy and into the three-fold degenerate t_{2g} multiplet. In iridates, the energy difference between e_g and t_{2g} levels is large and is typically of the order 2-3 eV. Because of this, the five electrons occupy only the low lying t_{2g} orbitals. As a consequence, the on-site interactions, such as the SO, Coulomb and Hund's interactions, as well as additional symmetry-lowering CF interactions, e.g. the trigonal CF, can be considered within the t_{2g} manifold only. In this limit of large octahedral CF, the SO coupling has to be projected onto the t_{2g} manifold, assuming an effective orbital angular

momentum $L = 1$. In terms of local axes, which are bound to the oxygen octahedron, the t_{2g} orbitals of Ir ions are $|X\rangle \equiv |yz\rangle$, $|Y\rangle \equiv |zx\rangle$, and $|Z\rangle \equiv |xy\rangle$. The SO and trigonal CF interactions give rise to a splitting of the levels according to the symmetry of the underlying lattice. In the case of the honeycomb iridates, A_2IrO_3, the trigonal CF arises from a compression of the oxygen cages along the [111] directions (local C_3 axis). At ambient pressure, the splitting of the t_{2g} levels due to the trigonal CF is about 110 meV [64] which is smaller, but of the same order of magnitude as the SO coupling, which is about 400 meV. Therefore, here we treat the SO coupling and the trigonal CF interactions on the same footing. Also, it is believed that much larger values of the trigonal distortion can be reached by applying uniaxial pressure.

Since the Hamiltonian is time-reversal invariant, the ground-state of the single-ion single-hole ($5d^5$ configuration of Ir^{4+} ion) is a Kramer's doublet, which we represent as a pseudospin-1/2. However, the choice of the two orthonormal states within the doublet that would represent the pseudospin-up and pseudospin-down states deserves some well-inspired consideration, as this choice determines the coordinate system of the final super-exchange Hamiltonian. Since the most prominent anisotropy, the Kitaev interaction, has the simplest form in the coordinate system bound to the cubic axes of the oxygen octahedron environment, we choose the two orthogonal states that correspond to this particular Cartesian reference frame. In the absence of the trigonal distortion, the ground state doublet is simply a $J_{\text{eff}} = 1/2$ doublet and the good choice of the states within it are the $J^z_{\text{eff}} = \pm 1/2$ states. In the presence of the trigonal distortion, the choice of the representation is not as straightforward since the ground state doublet contains a mixture of both $J_{\text{eff}} = 1/2$ and $J_{\text{eff}} = 3/2$ states. To resolve this, we first find a random set of orthonormal states within the doublet and then make linear combinations of them in such a way that pseudospin-1/2 "up-state" has no $|J_{\text{eff}} = 1/2, J^z_{\text{eff}} = -1/2\rangle$ component, whereas pseudospin-1/2 "down-state" has no $|J_{\text{eff}} = 1/2, J^z_{\text{eff}} = 1/2\rangle$ component. Namely, we allow the trigonal CF to admix the $J_{\text{eff}} = 3/2$ states to the $J_{\text{eff}} = 1/2$ states, but we do not allow the latter to mix among themselves.

In the most simple form, the single-ion Hamiltonian can be written when the axis of the quantization of angular momentum is along the [111] direction:

$$H_{\lambda,\Delta} = \lambda \mathbf{S} \cdot \mathbf{L} + \Delta L^2_{[111]}, \tag{3.1}$$

where $L_{[111]}$ denotes the component of the angular momentum along the [111] axis. Here the first term describes the SO coupling and the second term describes the trigonal CF. However, this form is not useful if we want to obtain our final result in the Cartesian reference frame bounded to the cubic crystallographic axes. If now we rewrite the CF term in terms of it's eigenstates, then the Hamiltonian (3.1) becomes:

$$H_{\lambda,\Delta} = \lambda \mathbf{S}\cdot\mathbf{L} + \frac{\Delta}{3}\left(-2|a_{1g}\rangle\langle a_{1g}| + |e_g^+\rangle\langle e_g^+| + |e_g^-\rangle\langle e_g^-|\right), \tag{3.2}$$

where the crystal field eigenstates include the low-energy singlet $|a_{1g}\rangle$ and the higher energy doublet $|e_g^{\pm}\rangle$. The singlet state can be written as

$$|a_{1g}\rangle = \hat{\nu}_x|X\rangle + \hat{\nu}_y|Y\rangle + \hat{\nu}_z|Z\rangle, \tag{3.3}$$

where $\hat{\boldsymbol{\nu}} = (\hat{\nu}_x, \hat{\nu}_y, \hat{\nu}_z)$ is the unit vector parallel to the [111] trigonal axis ($\hat{\nu}_j = 1/\sqrt{3}$). The doublet state can be conveniently written using the following chiral basis:

$$\begin{aligned} |e_g^+\rangle &= \hat{\nu}_x e^{-i\omega}|X\rangle + \hat{\nu}_y e^{+i\omega}|Y\rangle + \hat{\nu}_z|Z\rangle, \\ |e_g^-\rangle &= \hat{\nu}_x e^{+i\omega}|X\rangle + \hat{\nu}_y e^{-i\omega}|Y\rangle + \hat{\nu}_z|Z\rangle, \end{aligned} \tag{3.4}$$

where $\omega \equiv 2\pi/3$. Now, that the CF part of the Hamiltonian is written in an L-independent way, we are free to choose the angular momentum quantization axis along the cubic z direction for our basis.

The basis we use is $\hat{J} = \{|\frac{1}{2},\frac{1}{2}\rangle, |\frac{1}{2},-\frac{1}{2}\rangle, |\frac{3}{2},\frac{3}{2}\rangle, |\frac{3}{2},\frac{1}{2}\rangle, |\frac{3}{2},-\frac{1}{2}\rangle, |\frac{3}{2},-\frac{3}{2}\rangle\}$. The details of this basis and its relation to the basis of the cubic orbitals are given in the previous chapter. The Hamiltonian matrix in this basis is given by

$$\hat{H} = \begin{pmatrix} -\lambda & 0 & -\frac{(1-\imath)\Delta}{3\sqrt{6}} & 0 & \frac{(1+\imath)\Delta}{3\sqrt{2}} & \frac{\imath\Delta}{3}\sqrt{\frac{2}{3}} \\ 0 & -\lambda & \frac{\imath\Delta}{3}\sqrt{\frac{2}{3}} & \frac{(1-\imath)\Delta}{3\sqrt{2}} & 0 & -\frac{(1+\imath)\Delta}{3\sqrt{6}} \\ -\frac{(1+\imath)\Delta}{3\sqrt{6}} & -\frac{\imath\Delta}{3}\sqrt{\frac{2}{3}} & \frac{\lambda}{2} & \frac{(1+\imath)\Delta}{3\sqrt{3}} & \frac{\imath\Delta}{3\sqrt{3}} & 0 \\ 0 & \frac{(1+\imath)\Delta}{3\sqrt{2}} & \frac{(1-\imath)\Delta}{3\sqrt{3}} & \frac{\lambda}{2} & 0 & \frac{\imath\Delta}{3\sqrt{3}} \\ \frac{(1-\imath)\Delta}{3\sqrt{2}} & 0 & -\frac{\imath\Delta}{3\sqrt{3}} & 0 & \frac{\lambda}{2} & -\frac{(1+\imath)\Delta}{3\sqrt{3}} \\ -\frac{\imath\Delta}{3}\sqrt{\frac{2}{3}} & -\frac{(1-\imath)\Delta}{3\sqrt{6}} & 0 & -\frac{\imath\Delta}{3\sqrt{3}} & -\frac{(1-\imath)\Delta}{3\sqrt{3}} & \frac{\lambda}{2} \end{pmatrix}. \tag{3.5}$$

Diagonalization of $\hat{H}$ leads to three doublets at energies

$$E^{(1,2)} = -\frac{\Delta}{6} - \frac{\lambda}{4} - \frac{1}{2}\sqrt{2\lambda^2 + (\Delta - \frac{\lambda}{2})^2},$$

corresponding to eigenstates $|\Phi_1\rangle$ and $|\Phi_2\rangle$,

$$E^{(3,4)} = -\frac{\Delta}{6} - \frac{\lambda}{4} + \frac{1}{2}\sqrt{2\lambda^2 + (\Delta - \frac{\lambda}{2})^2},$$

corresponding to eigenstates $|\Phi_3\rangle$ and $|\Phi_4\rangle$, and

$$E^{(5,6)} = \frac{\Delta}{3} + \frac{\lambda}{2},$$

corresponding to eigenstates $|\Phi_5\rangle$ and $|\Phi_6\rangle$. Within the ground state doublet ($|\Phi_1\rangle$ and $|\Phi_2\rangle$) we choose the orthonormal states such that the $J^z_{\text{eff}} = \pm 1/2$ states do not mix with each other as mentioned above.

3.2.2 Two-hole states

In Chapter 2 we explained how to obtain two-hole eigenstates. We refer the reader there for details, as we only briefly outline the main steps and set notations here.

The full two-hole Hamiltonian is the sum of two contributions: a single-particle term, $H_{\lambda,\Delta}$, which includes the SO coupling and trigonal CF, and the many-body part, H_{int}, given by the Coulomb interaction, U_2, and the Hunds coupling, J_H. There are $6 \times 5/2 = 15$ partly degenerate two-hole eigenstates obtained by diagonalization of the full on-site Hamiltonian

$$H_{\text{int}+\lambda,\Delta} \equiv H_{\text{int}} + H_{\lambda,\Delta} \ . \tag{3.6}$$

We denote energy eigenstates of the full Hamiltonian (3.6) as

$$|D, \xi\rangle = \sum_{\mu=1}^{15} c_{\xi\mu} |\oplus\oplus, \mu\rangle \ , \tag{3.7}$$

where the two-hole basis states $|\oplus\oplus, \mu\rangle$ are simply given by direct products of eigenstates

$|\Phi_1\rangle, ...|\Phi_6\rangle$ diagonalizing one-particle Hamiltonian (3.5):

$$\begin{aligned}
|\oplus\oplus, 1\rangle &\equiv |\Phi_1\Phi_2\rangle \\
|\oplus\oplus, 2\rangle &\equiv |\Phi_1\Phi_3\rangle \\
|\oplus\oplus, 3\rangle &\equiv |\Phi_1\Phi_4\rangle \\
|\oplus\oplus, 4\rangle &\equiv |\Phi_1\Phi_5\rangle \\
|\oplus\oplus, 5\rangle &\equiv |\Phi_1\Phi_6\rangle \\
|\oplus\oplus, 6\rangle &\equiv |\Phi_2\Phi_3\rangle \\
|\oplus\oplus, 7\rangle &\equiv |\Phi_2\Phi_4\rangle \\
|\oplus\oplus, 8\rangle &\equiv |\Phi_2\Phi_5\rangle \\
|\oplus\oplus, 9\rangle &\equiv |\Phi_2\Phi_6\rangle \\
|\oplus\oplus, 10\rangle &\equiv |\Phi_3\Phi_4\rangle \\
|\oplus\oplus, 11\rangle &\equiv |\Phi_3\Phi_5\rangle \\
|\oplus\oplus, 12\rangle &\equiv |\Phi_3\Phi_6\rangle \\
|\oplus\oplus, 13\rangle &\equiv |\Phi_4\Phi_5\rangle \\
|\oplus\oplus, 14\rangle &\equiv |\Phi_4\Phi_6\rangle \\
|\oplus\oplus, 15\rangle &\equiv |\Phi_5\Phi_6\rangle
\end{aligned} \tag{3.8}$$

We denote by $c_{\xi\mu}$ and E_ξ, correspondingly, the eigenvectors and eigenvalues and $\xi = 1, ...15$.

3.3 Derivation of the super-exchange Hamiltonian

The super-exchange process which couples the magnetic moments of Ir^{4+} ions originating from the Kramers' doublet ground states involves intermediate states with either zero holes or two holes. As discussed in Sec.3.2.2, the latter states are governed by the Coulomb and the Hund's interaction, as well as by the SO coupling and the trigonal CF. The connection between the Kramers' doublet ground states Φ_1 and Φ_2 at site n ($\gamma = 1, 2$) and the full manifold of Φ-states at site n' ($\gamma' = 1, 2, ..., 6$) is given by the

projected hopping term:

$$PH_{t,n,n'} = \sum_{\gamma=1}^{2} \sum_{\gamma'=1}^{6} T_{n,n'}^{\gamma,\gamma'} b_{n,\gamma}^{\dagger} b_{n',\gamma'} \ , \tag{3.9}$$

where the elements of the matrix $T_{n,n'}^{\gamma,\gamma'}$ will be derived in the next section. For the moment, let us derive the super-exchange Hamiltonian treating $T_{n,n'}^{\gamma,\gamma'}$ as generic hopping matrix between either n. n. or next n. n. Ir^{4+} ions.

The super-exchange Hamiltonian, obtained by the second order perturbation theory, can be written as

$$H_{\mathrm{ex},n,n'} = \sum_{\xi} \frac{1}{\epsilon_\xi} P H_{t,n,n'} Q_{\xi,n'} H_{t,n',n} P \ , \tag{3.10}$$

where

$$P = \prod_{n} \sum_{\sigma_n = \pm 1} |1/2, \sigma_n/2; n\rangle\langle n; 1/2, \sigma_n/2| \tag{3.11}$$

is the projection operator onto the ground states with one hole at site n. The projection operators onto two-hole intermediate states $|D, \xi; n'\rangle$ with excitation energy ϵ_ξ at site n' are given by

$$Q_{\xi,n'} = |D, \xi; n'\rangle\langle n'; D, \xi| = D_{\xi,n'}^{\dagger} D_{\xi,n'} \ . \tag{3.12}$$

The excitation energies of the intermediate states are $\epsilon_\xi = E_{0h} + E_\xi - 2E_{1h}$. Rewriting operator $D_{\xi,n}$ as $D_{\xi,n} = \sum_{\nu=1}^{15} \sum_{\gamma_1,\gamma_2=1}^{6} c_{\xi,\nu} m_{\gamma_1\gamma_2}^{\nu} b_{\gamma_1,n}^{\dagger} b_{\gamma_2,n}^{\dagger}$, where by $b_{\gamma,n}^{\dagger}$ we denote an operator creating a hole of the type $\gamma = 1, ...6$, which refers to the component of the single-hole vector $\hat{\Phi}$ at the site n and the tensor $\hat{m}$ has only two non-zero elements for each state ν:

$$\begin{aligned} m_{1,2}^{1} &= m_{1,3}^{2} = m_{1,4}^{3} = m_{1,5}^{4} = m_{1,6}^{5} = \\ m_{2,3}^{6} &= m_{2,4}^{7} = m_{2,5}^{8} = m_{2,6}^{9} = m_{3,4}^{10} = \\ m_{3,5}^{11} &= m_{3,6}^{12} = m_{4,5}^{13} = m_{4,6}^{14} = m_{5,6}^{15} = 1 \end{aligned}$$

and

$$\begin{aligned} m_{2,1}^{1} &= m_{3,1}^{2} = m_{4,1}^{3} = m_{5,1}^{4} = m_{6,1}^{5} = \\ m_{3,2}^{6} &= m_{4,2}^{7} = m_{5,2}^{8} = m_{6,2}^{9} = m_{4,3}^{10} = \\ m_{5,3}^{11} &= m_{6,3}^{12} = m_{5,4}^{13} = m_{6,4}^{14} = m_{6,5}^{15} = -1 \ . \end{aligned}$$

It is convenient to rewrite the Hamiltonian (3.10) in the second-quantized form:

$$H_{\mathrm{ex},n,n'} = \sum_{\sigma,\sigma'=1}^{2} \sum_{\sigma_1,\sigma_1'=1}^{2} \sum_{\xi=1}^{15} \frac{1}{\epsilon_\xi} \{ A^{\xi}_{n,n';\sigma,\sigma'} b^{\dagger}_{n,\sigma} b^{\dagger}_{n',\sigma'} A^{\xi}_{n',n;\sigma_1',\sigma_1} b_{n',\sigma_1'} b_{n,\sigma_1} \} \ , \quad (3.13)$$

where we have defined coefficients $A^{\xi}_{n,n';\sigma,\sigma'}$ as

$$A^{\xi}_{n,n';\sigma,\sigma'} = \sum_{\gamma_1=1}^{6} \sum_{\nu=1}^{15} T^{\sigma,\gamma_1}_{n,n'} c_{\xi,\nu} (m^{\nu}_{\gamma_1\sigma'} - m^{\nu}_{\sigma'\gamma_1}) \ . \quad (3.14)$$

Next, we define the magnetic degrees of freedom with the help of the pseudospin operators $S^{\alpha}_{n} = \frac{1}{2} \sum_{\sigma,\sigma'=\pm1} \tau^{\alpha}_{\sigma,\sigma'} b^{\dagger}_{\sigma,n} b_{\sigma',n}$ and the density operator $\rho_n = \sum_{\sigma=\pm1} b^{\dagger}_{\sigma,n} b_{\sigma,n}$. With $\alpha = x, y, z$, we denote the spin component index and $\tau^{\alpha}_{\sigma,\sigma'}$ are the Pauli matrices. Then, the super-exchange Hamiltonian (3.13) on the bond n, n' can be written in terms of the magnetic degrees of freedom of Ir^{4+} as

$$H_{\mathrm{ex},n,n'} = \sum_{\alpha\beta} \Xi^{\alpha\beta}_{n,n'} S^{\alpha}_{n} S^{\beta}_{n'} + W \rho_n \rho_{n'}, \quad (3.15)$$

α, β label Cartesian components of pseudospins. The first term represents the most general bilinear form of the super-exchange Hamiltonian. The second term gives a constant energy shift and we shall hereafter omit it. We also note that because of time reversal symmetry, there are no terms of the kind $S^{\alpha}_{n} \rho_{n'}$. The exchange coupling matrix $\Xi^{\alpha\beta}$ on the bond n, n' has the form

$$\Xi_{n,n'} = \begin{pmatrix} J^{x} & J^{xy} & J^{xz} \\ J^{yx} & J^{y} & J^{yz} \\ J^{zx} & J^{zy} & J^{z} \end{pmatrix} \quad (3.16)$$

The hermiticity property of the Hamiltonian implies $\Xi^{\dagger}_{n',n} = \Xi_{n,n'}$. In the following, we shall call $\Xi^{\alpha\beta}_{1}$ and $\Xi^{\alpha\beta}_{2}$ the exchange coupling matrix for nearest and second nearest neighbors, respectively. Because of the lack of the tight-binding parameters for third nearest neighbors, we will not derive the $\Xi^{\alpha\beta}_{3}$ matrix and treat the third neighbor coupling as isotropic.

3.4 The hopping matrix

3.4.1 The nearest neighbors hopping matrix

In A_2BO_3 compounds, the honeycomb lattice of Ir^{4+} ions is embedded in the cubic lattice and corresponds to one of the (111) planes. Three kinds of honeycomb lattice bonds, denoted as x, y and z and drawn by red, green and blue solid lines in Fig. 3.1 (a), correspond to the cubic face diagonals along vectors (0,1,1), (1,0,1) and (1,1,0), respectively.

We first consider the hopping matrix between neighboring Ir^{4+} ions. The strongest n. n. hopping is via an intermediate oxygen ion. For each pair of n. n. Ir^{4+} ions, there are two Ir-O-Ir paths and the total hopping amplitude arises as a sum of these two hoppings. The direct hopping between nearest Ir ions is also not negligible due to the extended nature of $5d$ orbitals. Thus, the total hopping Hamiltonian comes from two contributions: $H_t = H_{\mathrm{O-assist}} + H_{\mathrm{dir}}$.

We focus our discussion on the hopping along a single z-bond because the system is translationally invariant and contributions from x and y bonds can be obtained by rotational symmetry. Along the $z-$bond, the 90° hopping occurs via p_z-orbitals of oxygen ions, which, following Ref. [1], we call the upper and the lower one (see Fig. 3.1 (b)). The upper p_z-orbital overlaps with the X orbital of the Ir^{4+} ion on the A sublattice and with the Y orbital on the B sublattice. Vice versa, the lower p_z-orbital overlaps with the Y orbital of the Ir^{4+} ion on the A sublattice and with the X orbital of the Ir^{4+} ion on the B sublattice. The overlaps of X and p_z and Y and p_z are equal. Thus, we have $t_{X,z} = t_{Y,z} = t_{pd\pi}$. We next integrate out the upper oxygen ion and compute the effective hopping between Ir^{4+} ions through the upper Ir-O-Ir bond. The amplitude of the effective Ir-Ir hopping is then equal to $t_{1o} = t_{pd\pi}^2/\Delta_p$ and Δ_p stands for the charge transfer gap. The hopping via the lower oxygen is just the complex conjugate of the hopping via the upper oxygen. The direct hopping along a z-bond has the biggest matrix element for diagonal hopping between nearest Z orbitals. We denote the amplitude of this hopping as t_d. In our calculations for n. n. hoppings, we will use the value of the oxygen assisted hopping equal to $t_{1o} = 230$ meV and the direct hopping equal to $t_d = 67$ meV. These values were obtained by Foyevtsova *et al* [63]. by tight-binding fitting of ab-initio electronic structure calculations in the presence of

trigonal distortion.

For the ultimate derivation of the super-exchange Hamiltonian we do not need the whole 6×6 hopping matrix but only its first two lines connecting ground state doublet Φ_1 and Φ_2 to all six states belonging to $\hat{\Phi}$. Combining contributions from the two paths (via the upper and via the lower oxygens), and adding direct hopping, we obtain the effective hopping Hamiltonian between n. n. Ir^{4+} ions along the z-bond

$$H_t^z = \sum_n \sum_{\gamma,\gamma'} T_{1,n,n+z}^{\gamma,\gamma'} (b_{n,\gamma}^\dagger b_{n+z,\gamma'} + h.c.), \tag{3.17}$$

where $b_{\gamma,n}^\dagger$ is an operator creating a hole on site n of the type $\gamma = 1, ...6$, which refers to the components of the vector $\hat{\Phi}$. The hopping matrix is given by

$$T_{1,n,n+z} = \begin{pmatrix} \langle\Phi_1|\hat{T}_1|\Phi_1\rangle & \langle\Phi_1|\hat{T}_1|\Phi_2\rangle & \langle\Phi_1|\hat{T}_1|\Phi_3\rangle & \langle\Phi_1|\hat{T}_1|\Phi_4\rangle & \langle\Phi_1|\hat{T}_1|\Phi_5\rangle & \langle\Phi_1|\hat{T}_1|\Phi_6\rangle \\ \langle\Phi_2|\hat{T}_1|\Phi_1\rangle & \langle\Phi_2|\hat{T}_1|\Phi_2\rangle & \langle\Phi_2|\hat{T}_1|\Phi_3\rangle & \langle\Phi_2|\hat{T}_1|\Phi_4\rangle & \langle\Phi_2|\hat{T}_1|\Phi_5\rangle & \langle\Phi_2|\hat{T}_1|\Phi_6\rangle \end{pmatrix} \tag{3.18}$$

Let us analyze the structure of the hopping matrix (3.18) in the absence of trigonal distortion, $\Delta = 0$. In this case, the single-hole vector $\hat{\Phi}$ is nothing else but the vector $\hat{J} = \{|\frac{1}{2}, \frac{1}{2}\rangle, |\frac{1}{2}, -\frac{1}{2}\rangle, |\frac{3}{2}, \frac{3}{2}\rangle, |\frac{3}{2}, \frac{1}{2}\rangle, |\frac{3}{2}, -\frac{1}{2}\rangle, |\frac{3}{2}, -\frac{3}{2}\rangle\}$ diagonalizing the SO interaction. In this limit, the two transfer amplitudes via upper and lower oxygen interfere in a destructive manner and, because of this, the only non-zero elements of the effective transfer matrix are

$$T_{n,n+z}^{1,6} = T_{n,n+z}^{2,3} = -\frac{2\imath}{\sqrt{6}} t_{1o}^2$$

and their complex conjugates, where $\gamma = 1, 2$ correspond to $|1/2, \pm 1/2\rangle$ and $\gamma = 3, 6$ correspond to $|3/2, \pm 3/2\rangle$ states. As was shown in Refs. [65, 1] this massive cancellation of hopping terms in the absence of trigonal distortion leads to a vanishing isotropic part of the super-exchange mediated by oxygen ions. The non-zero n. n. isotropic term is, therefore, entirely determined by the direct hopping t_d between d-orbitals of the Ir ions.

3.4.2 The second neighbor hopping matrix

Next, we derive the hopping matrix for second neighbors. Six bonds between second neighbors Ir^{4+} ions on the honeycomb lattice correspond to (2,1,-1), (1,2,1), (-1,1,2), (-2,-1,1), (-1-2,-1), (1,-1,-2) bonds, which we call $\tilde{x}$, $\tilde{y}$, $\tilde{z}$, and $\tilde{x}$, $\tilde{y}$, $\tilde{z}$ bonds, respectively. Then, the second neighbor $\tilde{x}-$bond connects two Ir ions which are also connected by

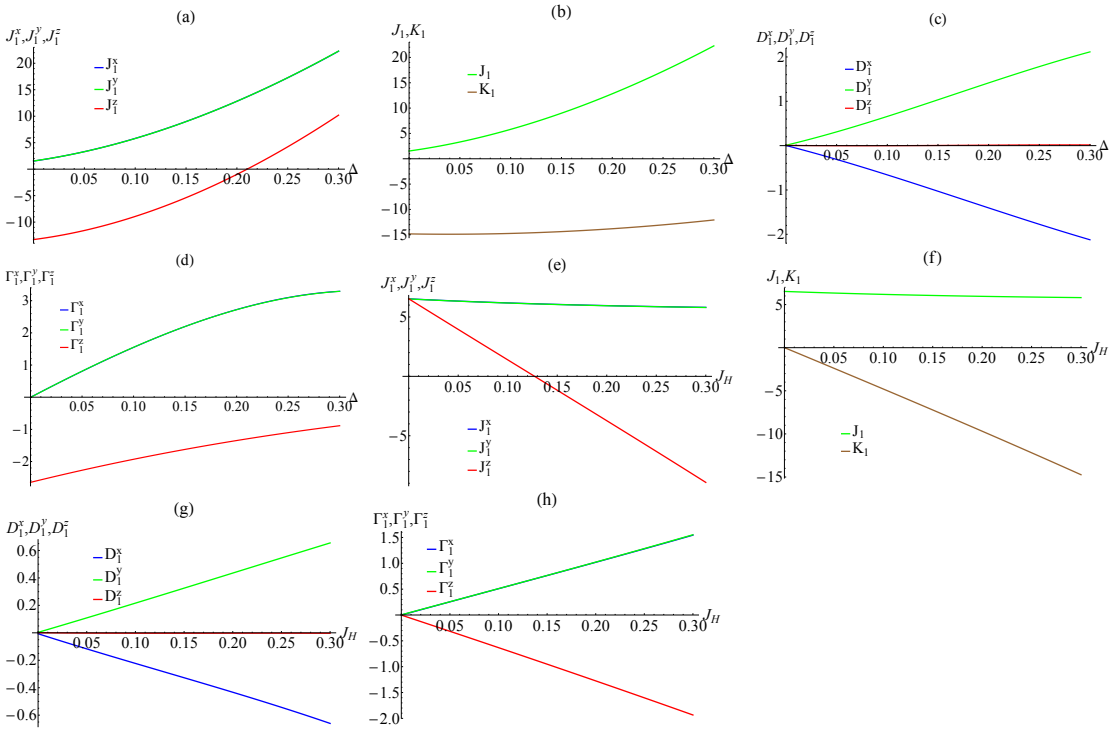

Figure 3.2: The matrix elements of the tensor $\Xi_1^{\alpha\beta}$ on the z-bond as functions of trigonal crystal field, Δ, and Hund's coupling, J_H. The diagonal n. n. exchange couplings J_1^x, J_1^y, J_1^z in meV (shown by blue, green and red lines, respectively) plotted as functions of (a) Δ (in eV) and (e) J_H (in eV). The n. n. Kitaev interaction K_1 and the n. n. isotropic exchange J_1 (shown by brown and green lines, respectively) plotted as functions of (b) Δ (in eV) and (f) J_H (in eV). The DM-type antisymmetric off-diagonal interactions D_1^x, D_1^y, D_1^z in meV (shown by blue, green and red lines, respectively) plotted as functions of (c) Δ (in eV) and (g) J_H (in eV). The symmetric off-diagonal interactions Γ_1^x, Γ_1^y, Γ_1^z in meV (shown by blue, green and red lines, respectively) plotted as functions of (d) Δ (in eV) and (h) J_H (in eV). For (a)-(d) and (e)-(h) plots we put $J_H = 0.3$ eV and $\Delta = 0.1$ eV, respectively. Other microscopic parameters of the model are considered to be $U_2 = 1.8$ eV, $\lambda = 0.4$ eV, $t_{1o} = 230$ meV, $t_d = 67$ meV and $t_{2o} = 95$ meV.

two n. n. Ir-Ir bonds of $y-$ and $z-$ type, and $\tilde{y}-$ and $\tilde{z}-$bonds connect Ir^{4+} ions which are connected by $x-$ and $z-$, and $x-$ and $y-$bonds, respectively. In Fig. 3.1 (a), we also use the same color coding for the second neighbor bonds as for n. n. bonds: $\tilde{x}-$, $\tilde{y}-$, $\tilde{z}-$ bonds are shown by red, green and blue dotted lines.

Similarly to the hopping between nearest neighbors, there are also two kinds of hoppings connecting second neighbors (see Fig. 3.1 (a)): the hopping along the path Ir-O-Na-O-Ir, and the direct one. The indirect hopping t_{2o} is large both because it comes from four Ir-O-Na-O-Ir paths but also because it takes advantage of the extended nature of the $s-$orbital of the Na ion. In the ideal structure, it is equal to $t_{2o} = 82.1$ meV, and in the presence of the trigonal distortion it is even larger, $t_{2o} = 94.7$ meV [63]. The direct hopping between second neighbors is significantly smaller than the one between nearest neighbors and also significantly smaller than the hopping along the Ir-O-Na-O-Ir path. In our derivation of the second neighbor super-exchange Hamiltonian, we will neglect all second neighbor hoppings except t_{2o}.

Explicitly, the hopping matrix element between second neighbor Ir ions along the $\tilde{z}$-bond comes from the following processes:

$$\begin{aligned}
&\text{Path1}: \text{Ir}\,(Y) \to \text{O}\,(p_z) \to \text{Na}\,(s) \to \text{O}\,(p_z) \to \text{Ir}\,(X)\\
&\text{Path2}: \text{Ir}\,(Y) \to \text{O}\,(p_z) \to \text{Na}\,(s) \to \text{O}\,(p_y) \to \text{Ir}\,(X)\\
&\text{Path3}: \text{Ir}\,(Y) \to \text{O}\,(p_x) \to \text{Na}\,(s) \to \text{O}\,(p_z) \to \text{Ir}\,(X)\\
&\text{Path4}: \text{Ir}\,(Y) \to \text{O}\,(p_x) \to \text{Na}\,(s) \to \text{O}\,(p_y) \to \text{Ir}\,(X)
\end{aligned}$$

Summing over all these four paths, shown by thick magenta lines in Fig. 3.1 (a), we obtain the effective hopping Hamiltonian between second neighbor Ir^{4+} ions along the $\tilde{z}$-bond

$$H_t^{\tilde{z}} = \sum_n \sum_{\gamma,\gamma'} T_{2,n,n+\tilde{z}}^{\gamma,\gamma'} (b_{n,\gamma}^\dagger b_{n+\tilde{z},\gamma'} + h.c.), \tag{3.19}$$

where, formally, the hopping matrix $T_{2,n,n+\tilde{z}}$ has the same structure as $T_{1,n,n+z}$ given by Eq. (3.18).

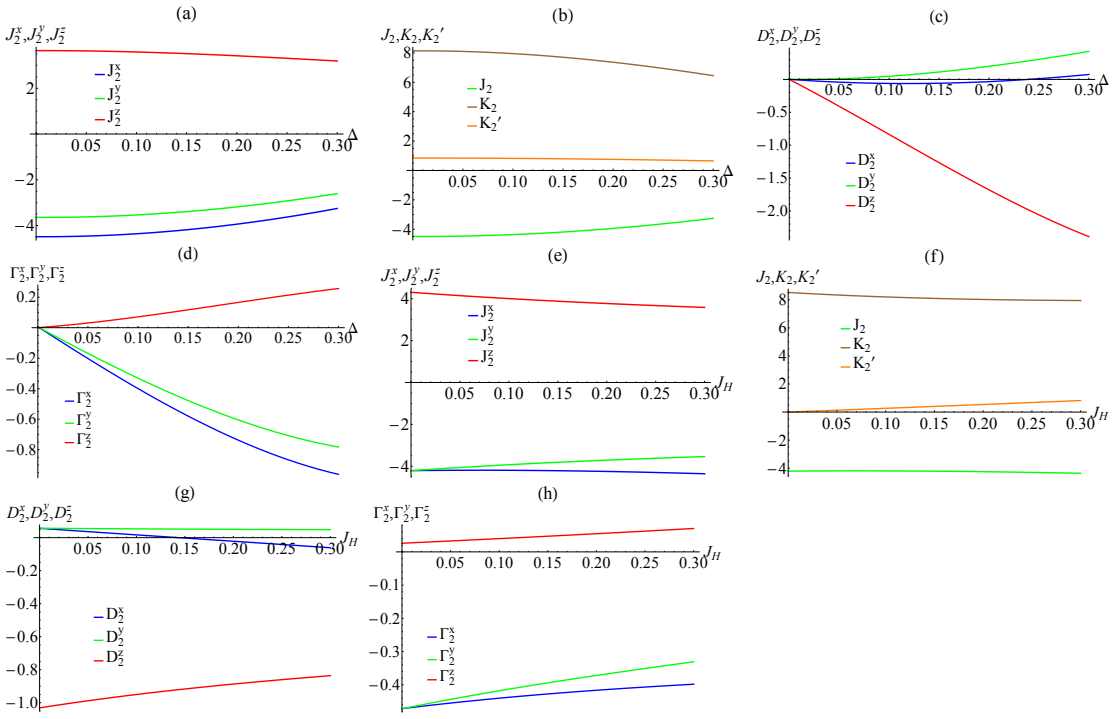

Figure 3.3: The matrix elements of the tensor $\Xi_2^{\alpha\beta}$ on the z-bond as functions of trigonal crystal field, Δ, and Hund's coupling, J_H. The diagonal n. n. exchange couplings J_2^x, J_2^y, J_2^z in meV (shown by blue, green and red lines, respectively) plotted as functions of (a) Δ (in eV) and (e) J_H (in eV). The second neighbor Kitaev interactions K_2 and K_2', as well as the second neighbor isotropic exchange J_2 in meV (shown by brown, orange and green lines, respectively) plotted as functions of (b) Δ (in eV) and (f) J_H (in eV). The DM-type antisymmetric off-diagonal interactions D_2^x, D_2^y, D_2^z in meV (shown by blue, green and red lines, respectively) plotted as functions of (c) Δ (in eV) and (g) J_H (in eV). The symmetric off-diagonal interactions Γ_2^x, Γ_2^y, Γ_2^z in meV (shown by blue, green and red lines, respectively) plotted as functions of (d) Δ (in eV) and (h)J_H (in eV). For (a)-(d) and (e)-(h) plots we put $J_H = 0.3$ eV and $\Delta = 0.1$ eV, respectively. Other microscopic parameters of the model are considered to be $U_2 = 1.8$ eV, $\lambda = 0.4$ eV, $t_{1o} = 230$ meV, $t_d = 67$ meV and $t_{2o} = 95$ meV.

3.5 The exchange coupling tensors $\Xi_1^{\alpha\beta}$ and $\Xi_2^{\alpha\beta}$

We show in Fig. 3.2 and Fig. 3.3 how the matrix elements of the exchange coupling tensor $\Xi^{\alpha\beta}$, defined in Eq.(3.16), computed for both nearest and second neighbor Ir^{4+} ions depend on the microscopic parameters (trigonal distortion, Hund's coupling, Coulomb interaction and SO coupling). We note right away that the main role of the Coulomb repulsion is to determine the overall energy scale for the couplings. Thus, in all computations we take, for definitiveness, $U_2 = 1.8$ eV, which is lying inside the range of values, 1.5 eV-2.5 eV, characteristic to iridates. We also set the SO coupling constant to $\lambda = 0.4$ eV since it is the value associated with Ir^{4+} ions in the literature [62]. As we already mentioned before, we compute all exchange interactions for either z-nearest or for $\tilde{z}$ next n. n. bonds. Interactions for other bonds can be obtained using symmetry arguments or, even simpler, one needs to permute indices of bonds and couplings. This is illustrated in Fig. 3.4.

3.5.1 Effect of trigonal distortion.

Here we study the dependencies of the exchange couplings on the trigonal distortion, Δ. At ambient pressure, the trigonal crystal field splitting in both Na_2IrO_3 and Li_2IrO_3 is about 110 meV [64]. However, it is also believed that a much stronger trigonal distortion can be reached under pressure. In this subsection, the exchange parameters were computed for a fixed Hund's coupling, $J_H = 0.3$ eV.

In Fig. 3.2 (a)-(d), we plot the Δ-dependencies of the matrix elements of the tensor $\Xi_1^{\alpha\beta}$ on the z-bond. The diagonal matrix elements J_1^x, J_1^y, J_1^z are shown in Fig. 3.2 (a). We see that while the J_1^x and J_1^y couplings are positive and degenerate for all values of the trigonal splitting, $J_1^x = J_1^y = J_1$, the J_1^z coupling is first negative but then changes sign at $\Delta \simeq 0.21$ eV. The anisotropic n. n. Kitaev interaction, K_1, may be defined as the difference between diagonal elements. On the z-bond, it is simply given by $K_1 \equiv J_1^z - J_1$. We plot J_1 and K_1 in Fig. 3.2 (b). Notice that while the n. n. isotropic exchange is *antiferromagnetic* and is rapidly growing with Δ, the Kitaev interaction is *ferromagnetic* and is almost independent of the magnitude of the trigonal field.

The behavior of the off-diagonal terms J_1^{xy}, J_1^{yx}, J_1^{xz}, J_1^{zx}, J_1^{yz}, J_1^{zy} is shown in Fig.

3.2 (c) and (d). All the matrix elements are real valued. In these plots, instead of showing the off-diagonal elements explicitly, we plot their DM-like antisymmetric (c) and symmetric combinations (d). We define them as follows:

$$\begin{aligned} D_1^x &= \frac{1}{2}(J_1^{yz} - J_1^{zy}) \\ D_1^y &= \frac{1}{2}(J_1^{zx} - J_1^{xz}) \\ D_1^z &= \frac{1}{2}(J_1^{xy} - J_1^{yx}) \\ \Gamma_1^x &= \frac{1}{2}(J_1^{yz} + J_1^{zy}) \\ \Gamma_1^y &= \frac{1}{2}(J_1^{zx} + J_1^{xz}) \\ \Gamma_1^z &= \frac{1}{2}(J_1^{xy} + J_1^{yx}) \end{aligned} \tag{3.20}$$

In the absence of the trigonal distortion, $\Delta = 0$, the inversion symmetry prohibits the existence of DM-type antisymmetric interactions, and thus $D_1^x = D_1^y = D_1^z = 0$. The symmetric combinations are allowed but at $\Delta = 0$ only $\Gamma_1^z \neq 0$. The symmetric interactions $\Gamma_1^x = \Gamma_1^y$ become non-zero at finite Δ. The DM terms $D_1^x = D_1^y$ also become non-zero at $\Delta \neq 0$, and then linearly grow with Δ.

In Fig. 3.3 (a)-(d), we plot the Δ-dependencies of the second neighbor interactions. The diagonal elements of the tensor $\Xi_2^{\alpha\beta}$ on the $\tilde{z}$-bond are presented in Fig. 3.3 (a). We see that at small Δ, J_2^x, J_2^y, J_2^z are only slightly weaker than the n. n. diagonal interactions (see Fig. 3.2 (a)). There is also no degeneracy between them: all of the second neighbor diagonal elements are different from each other except $J_2^z = -J_2^y$. If we define the isotropic exchange as $J_2^y = J_2$, and anisotropic second neighbor Kitaev interactions as $K_2 \equiv J_2^z - J_2^y = -2J_2$ and $K_2' \equiv J_2^y - J_2^x$, then the interaction on the $\tilde{z}$-bond can be written as $J_2\mathbf{SS} + K_2 S^z S^z - K_2' S^x S^x$. We plot J_2, K_2 and K_2' as a function of Δ in Fig. 3.3 (b). Note that for all values of the trigonal distortion, $J_2 < 0$, $K_2 > 0$ and $K_2' > 0$, and also $K_2 \gg K_2'$. It is also important to remember that J_2, K_2 and K_2' all come from the same process and are governed by the same hopping parameter t_{2o}. This is in the contrast to the n. n. couplings, J_1 and K_1, for which the super-exchange processes in the absence of the trigonal distortion are completely distinct – J_1 is determined by the direct hopping, with amplitude t_d, and K_1 is determined with amplitude t_{1o}, mediated by the hopping through the intermediate oxygen.

The second neighbor off-diagonal couplings are plotted in Fig. 3.3 (c) and (d). Again, we combine them into antisymmetric and symmetric combinations, using definitions similar to Eq.(3.20). Contrary to the n. n. case, at $\Delta = 0$ we see that all interactions $D_2^x = D_2^y = D_2^z = \Gamma_2^x = \Gamma_2^y = \Gamma_2^z = 0$. At finite value of the trigonal distortion, all of them acquire non-zero values but remain subdominant interactions even at relatively large Δ.

3.5.2 Effect of Hund's coupling.

Before concluding this section, here we look in detail on the dependence of the exchange couplings on the Hund's interaction, J_H. Here we fix the trigonal distortion equal to $\Delta = 0.1$ eV.

In Fig. 3.2 (e) and Fig. 3.3 (e), we plot J_1^x, J_1^y, J_1^z and J_2^x, J_2^y, J_2^z diagonal elements of $\Xi_1^{\alpha\beta}$ and $\Xi_2^{\alpha\beta}$, respectively. We see (Fig. 3.2 (e)) that at $J_H = 0$, the n. n. diagonal couplings are all equal, $J_1^x = J_1^y = J_1^z$. Consequently, in the absence of the Hund's interaction, the n. n. Kitaev interaction $K_1 = 0$ (Fig. 3.2 (f)). All n. n. off-diagonal couplings are also zero at $J_H = 0$ (see Fig. 3.2 (g) and (h)). On the contrary, at $J_H = 0$ the next n. n. diagonal couplings are only partially degenerate: $J_2^x = J_2^y = -J_2^z$. As a result, the dominant Kitaev interaction is between the second neighbors $K_2 \neq 0$ (Fig. 3.3 (f)). The smaller Kitaev interaction is still zero, $K_2' = 0$. The second neighbor off-diagonal couplings are all non-zero but very small (see Fig. 3.3 (g) and (h)). Thus, at $J_H = 0$ the leading anisotropic term is the Kitaev interaction between second neighbors, K_2.

With increasing J_H, the n. n. Kitaev interaction K_1 rapidly grows while the second n. n. K_2 very slightly decreases. As a result, K_1 becomes the dominant interaction at values of Hund's coupling larger than 0.15 eV. The other exchange couplings also change with J_H, but they remain subdominant interactions. Overall, we note that the n. n. interactions are more sensitive to the strength of the Hund's coupling than the second neighbors.

Let us summarize the results obtained in this section. From Fig. 3.2 and Fig. 3.3 we see that for reasonable values of microscopic parameters, the dominant interactions are J_1, K_1, J_2 and K_2 couplings. Moreover, at $\Delta = 0.11$ eV and $J_H = 0.3$ eV, the values of the trigonal distortion and the Hund's coupling characteristic for Na_2IrO_3 compound,

the Kitaev interactions K_1 and K_2 are the largest interactions dominating not only all other anisotropic interactions but even the n. n. and second n. n. isotropic interactions.

3.6 Magnetic phase diagram

3.6.1 Effective super-exchange model for Na_2IrO_3.

We now discuss how the above results apply to the case of Na_2IrO_3. As we already discussed above, we take the values of the microscopic parameters most closely related to Na_2IrO_3: $\lambda = 0.4$ eV, $\Delta = 0.1$ eV, $J_H = 0.3$ eV, $U_2 = 1.8$ eV, and hopping matrix elements equal to $t_{1o} = 0.23$ eV, $t_d = 0.067$ eV and $t_{2o} = 0.095$ eV [63]. We obtain the following values of the exchange couplings: $J_1 = 5.8$ meV, $K_1 = -14.8$ meV, $J_2 = -4.4$ meV, $K_2 = 7.9$ meV. The calculated n. n. exchange constants are in fair agreement with the results of ab-initio quantum chemistry calculations by Katukuri *et al* [61]: $J_1 \simeq 3$ meV and $K_1 \simeq -17$ meV.

Our results for the n. n. couplings confirm the previous conclusion [8, 47, 48, 49, 59] that the super-exchange model with only n. n. couplings is insufficient to explain the experimentally observed zigzag magnetic order even in the presence of the trigonal distortion. Recall that in the original Kitaev-Heisenberg model [1, 46], the isotropic and Kitaev exchange couplings were parametrized by a single parameter α as $J_1 = 1 - \alpha$ and $K_1 = 2\alpha$. Taking J_1 and K_1 obtained for the trigonal distortion $\Delta \simeq 0.1$ eV, we get $\alpha \simeq 0.57$, which corresponds to the stripy antiferromagnetic order instead of the zigzag-type order. Neglecting the trigonal distortion and taking $J_1 = 1.4$ meV and $K_1 = -15.2$ meV obtained at $\Delta = 0$ eV, we get $\alpha \simeq 0.83$ corresponding to the spin liquid, which was desired but not observed in Na_2IrO_3 [8, 47, 48, 49, 59].

This shows that, in addition to the *antiferromagnetic* Heisenberg and *ferromagnetic* Kitaev n.n. interactions, the minimal model has to include further neighbor interactions. As we saw in Sec.3.5, the dominant microscopic Ir-Ir couplings also include next n. n. *ferromagnetic* Heisenberg and *antiferromagnetic* Kitaev interactions, which also must be considered.

Thus, let us study the following super-exchange Hamiltonian:

$$\mathcal{H} = J_1 \sum_{\langle n,n' \rangle_\gamma} \mathbf{S}_n \mathbf{S}_{n'} + K_1 \sum_{\langle n,n' \rangle_\gamma} S_n^\gamma S_{n'}^\gamma$$

$$+J_2 \sum_{\langle\langle n,n'\rangle\rangle_{\tilde{\gamma}}} \mathbf{S}_n \mathbf{S}_{n'} + K_2 \sum_{\langle\langle n,n'\rangle\rangle_{\tilde{\gamma}}} S_n^{\gamma} S_{n'}^{\tilde{\gamma}} \tag{3.21}$$

$$+J_3 \sum_{\langle\langle\langle n,n'\rangle\rangle\rangle} \mathbf{S}_n \mathbf{S}_{n'},$$

where $J_1 > 0$, $K_1 < 0$, $J_2 < 0$, $K_2 = -2J_2 > 0$, and $J_3 > 0$. Note that in our formulation of the minimal model (3.21), we also include the third neighbor antiferromagnetic coupling, which was suggested to be crucial for stabilizing the zigzag magnetic order in the previous works [12, 59].

It is very important that the presence of the second n. n. Kitaev interaction does not change the space group symmetries of the effective model: the model (3.21) has the same symmetries as the original Kitaev-Heisenberg model. The schematic representation of the n.n. and second n. n. interactions is shown in Fig. 3.4. As in Fig. 3.1 (a), the solid lines correspond to n. n. bonds and dotted lines correspond to the second n. n. Kitaev interaction. We also note that the same form of the second neighbor interactions was previously obtained [66, 67] in the limit $U \to \infty$ of the Kane-Mele-Hubbard model [68, 69]. It was shown that the second n. n. Kitaev interaction might be an important interaction necessary to stabilize the incommensurate spiral order with ordering peaks located inside the first Brillouin zone in Li_2IrO_3 [70].

3.6.2 The magnetic phase diagram

We computed the phase diagram of the effective model (3.21) with classical Monte Carlo simulations based on the standard Metropolis algorithm. To explore the physics of the model (3.21), we fix n. n. interactions to $J_1 = 3$ meV and $K_1 = -17$ meV values, which were obtained by quantum chemistry calculations by Katukuri *et al* [61] and are within the range of parameters obtained by us. We compute the phase diagram not only for ferromagnetic, $J_2 < 0$, but also for antiferromagnetic, $J_2 > 0$, second neighbor interaction. This allows us to compare our findings with other phase diagrams that were previously obtained in the literature [12, 61]. The simulations were performed at low temperature $T = 0.1J_1$, at which for the full range of the considered parameters the model is in the magnetically ordered state.

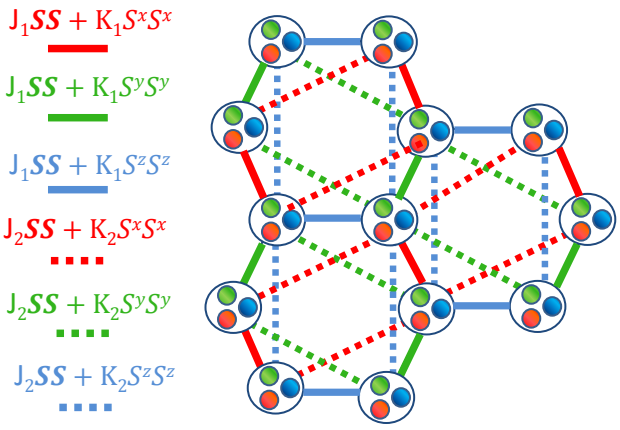

Figure 3.4: Schematic representation of the effective super-exchange model for Na_2IrO_3. Color coding is the same as in Fig. 3.1 (a). X, Y and Z t_{2g} electronic orbitals, participating in the super-exchange, are shown by red, green and blue small circles.

The phase diagram of the model (3.21) in the limit of zero second neighbor Kitaev interaction, $K_2 = 0$, is presented in Fig. 3.5 (a). A more realistic phase diagram computed with $K_2 = -2J_2$ is presented in Fig. 3.5 (b). Even at first glance, we see that the second n. n. Kitaev interaction suppresses the ferromagnetic and spiral phases and stabilizes the antiferromagnetic zigzag and stripy phases.

In order to get a better sense of the basic structure of the different states composing the phase diagrams, we also performed a numerical Fourier transform of a snapshot of the ground state spin configuration at a given point of the phase diagram. From that Fourier transform, we computed the corresponding spin structure factor, which allows us to determine the dominant wavevectors of that configuration. We plot the spin structure factors in Fig. 3.5 (c).

Phase diagram of the $J_1 - J_2 - J_3 - K_1 - 0$ model (Fig.3.5 (a)).

The $K_2 = 0$ phase diagram is very rich, but overall it is qualitatively similar to both the classical phase diagram of the $J_1 - J_2 - J_3 - K_1$ [12, 61] and of the pure Heisenberg $J_1 - J_2 - J_3$ model on the honeycomb lattice [59]. It displays the ferromagnetic (blue

region), the stripy (rose region) and the zigzag antiferromagnetic states (green region), the 3**Q**−incommensurate spiral state (white region), the 120° order (cyan region) and a very particular multi-**Q** incommensurate state (dark cyan region), which we call an "intermediate" phase, as it always separates the 120° order from either the stripy or the zigzag phases. The Néel antiferromagnetic order is also one of the possible ground states of the model. However, the n. n. Kitaev term, K_1, and the second neighbor Heisenberg term, J_2, destabilize it in favor of the stripy and zigzag phases. The Néel order is realized only at values of $J_3/J_1 > 1$, which are not shown in the Fig. 3.5 (a).

The simplest state we find on the phase diagram is the ferromagnetic state which is characterized by a single $\mathbf{Q} = (0, 0)$ wavevector. This state is the ground state in the region of large ferromagnetic J_2 and small J_3 couplings. As J_2 is decreased and J_3 is increased, the ferromagnetic state becomes unstable with respect to a spiral state, which is built out of three incommensurate wavevectors related by C_3 rotation. Because the ordering $\mathbf{Q}$ vectors are not connected by reciprocal lattice vectors, the spiral phase represents an example of a 3**Q**−incommensurate order. Note that the magnitude of the ordering wavevector $|\mathbf{Q}|$ varies throughout the phase.

The stripy and zigzag antiferromagnetic orders are found for both ferromagnetic and antiferromagnetic J_2 interaction of intermediate strength. However, while the stripy order is found at small values of the third n. n. interaction, J_3, the experimentally observed zigzag order is found only at values $J_3 \geq 0.35J_1$ which seem too large given that tight-binding hopping amplitudes are clearly dominated by the n. n. and the second neighbor terms [63]. Both the stripy and the zigzag phases are single-**Q** orders, characterized by one of the symmetry related wavevectors: $\mathbf{Q}_1 = (0, \frac{2\pi}{3})$, $\mathbf{Q}_2 = (\frac{\pi}{3}, \frac{\pi}{\sqrt{3}})$ and $\mathbf{Q}_3 = (-\frac{\pi}{3}, \frac{\pi}{\sqrt{3}})$.

The stripy and the zigzag phases are separated by a 120° state characterized by one of the $\mathbf{Q}_1 = (\frac{4\pi}{3\sqrt{3}}, 0)$, $\mathbf{Q}_2 = (\frac{2\pi}{3\sqrt{3}}, \frac{2\pi}{3})$ and $\mathbf{Q}_3 = (-\frac{2\pi}{3\sqrt{3}}, \frac{2\pi}{3})$ wavevectors. Because these vectors are connected by the reciprocal lattice vectors, this is a coplanar single-**Q** spiral which describes the 120° spin ordering within each of the two sublattices forming the honeycomb lattice. As x, y and z components of spins are all equally modulated in this 120° state, the spins in this state are lying in one of the (111) planes.

The transition from the stripy and the zigzag states into the 120° state is not direct; it happens through the intermediate phase. This transition can be understood by looking

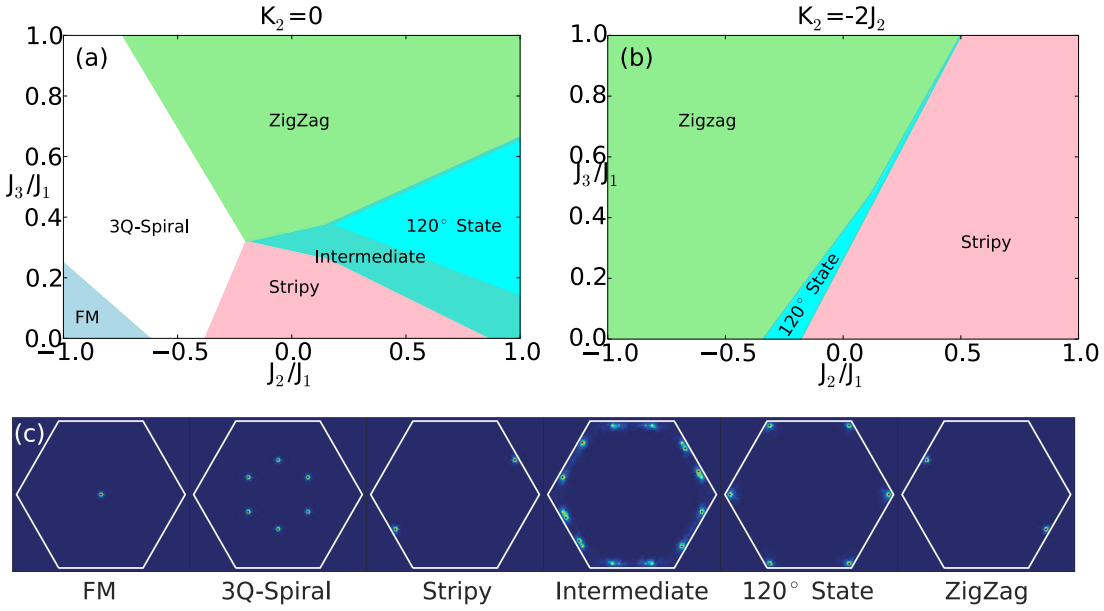

Figure 3.5: Phase diagrams of the effective model (3.21) obtained with the classical Monte Carlo simulations at low temperature $T = 0.1J_1$ for (a) second neighbor Kitaev interaction equal to $K_2 = 0$, (b) second neighbor Kitaev interaction $K_2 = -2J_2$. The simulation is done for $J_1 = 3$ meV and $K_1 = -17$ meV. The blue, rose, green, white, cyan and emerald regions show the ferromagnetic (FM), the stripy, the zigzag, the incommensurate $3\mathbf{Q}-$spiral, the 120° structure and the intermediate state, respectively. (c) The structure factors obtained as a Fourier transform of a snapshot of a given configuration for each of these magnetic phases. Sharp peaks appear at the corresponding ordering wavevector.

at the evolution of the spin structure factors. We find that before the onset of the 120° state the transition from a single-**Q** stripy (or a single-**Q** zigzag) state to a state defined by a superposition of the three different stripy (zigzag) phases occurs. The structure factor for this state is characterized by the presence of six peaks situated in the middle of the edges of the first BZ hexagon. These peaks split into two incommensurate peaks with **Q** vectors sliding along the edges (see Fig. 3.5 (c) for the structure factor corresponding to the Intermediate phase) until they reach wavevectors at the hexagon's corners characterizing the 120° structure. Here, we note that this 120° state separating the stripy and the zigzag phases was also obtained by Rau *et al* [71] as a classical ground state of the n. n. super-exchange in the presence of the symmetric off-diagonal exchange.

Here a comment is in order. In each of the stripy and the zigzag phases obtained in the Kitaev-Heisenberg models without further neighbor interactions [46, 14, 50, 51], the spins were aligned along one of the cubic directions. The spin direction was locked to the spatial orientation of a stripy or a zigzag pattern defined by the wavevector **Q**. Both the locking of the spin direction and the way the translational symmetry is broken, i.e. the choice of **Q**, are defined on the classical level.

In the absence of J_2 and J_3 interactions, the stripy phase is stabilized only for the ferromagnetic n. n. Kitaev interaction, $K_1 < 0$, and the zigzag phase is stabilized only for the antiferromagnetic n. n. Kitaev interaction, $K_1 > 0$. Consider the stripy order with ferromagnetic z-bonds. In this state, the spins and, therefore, the order parameter are pointing along z cubic axis. This state has the lowest classical energy, because such a direction of the order parameter maximizes the energy gain due to the ferromagnetic Kitaev interaction on ferromagnetic z-bonds. The same reasoning explains why the spins in x and y stripes are pointing along the x and y axes respectively.

Next, consider the zigzag order characterized by ferromagnetic $x-$ and $y-$bonds. In this state, the spins also point along the z cubic axis because it maximizes the energy gain due to the antiferromagnetic Kitaev interaction on the antiferromagnetic $z-$ bonds.

In the presence of further neighbor couplings the situation is different. As we can see in Fig. 3.5 (a), both the stripy and the zigzag order can be stabilized for the ferromagnetic n. n. Kitaev interaction. While the situation for the stripy phase is the same as before, where the spins point along the cubic direction corresponding to the label

of the ferromagnetic bond to gain energy from the ferromagnetic Kitaev interaction, the direction of the zigzag order parameter is not defined on the classical level. Instead, there are two ferromagnetic bonds in the zigzag phase, e.g. x and y. Thus, all zigzag states characterized by an order parameter pointing along any direction in the xy-plane are classically degenerate. The direction of the order parameter is then selected by order from disorder mechanism, in which spin fluctuations (quantum or thermal) remove the accidental degeneracy and select the true ordered state. We have checked with Monte Carlo simulations that thermal fluctuations again choose the states in which spins point along either x or y cubic directions. The full finite-temperature phase diagram for the model (3.21) will be published elsewhere.

Phase diagram of the $J_1 - J_2 - J_3 - K_1 - K_2$ model (Fig. 3.5 (b)).

In Fig. 3.5 (b), we present the magnetic phase diagram of the model (3.21) when the second neighbor Kitaev interaction is equal to $K_2 = -2J_2$, as predicted by our theory when the second neighbors are coupled only through the Ir-O-Na-O-Ir superexchange path. We see that the phase diagram greatly simplifies. The second neighbor Kitaev term suppresses the spiral and the ferromagnetic phases in favor of the stripy and zigzag order which now dominate for antiferromagnetic and ferromagnetic J_2, respectively. These two phases are still separated by the 120° order and Intermediate phase, but both the 120° phase and, especially, the Intermediate phase shrink significantly. However, the most important effect of the second neighbor Kitaev term is that for sufficient ferromagnetic $J_2 < 0$, it stabilizes the zigzag even for $J_3 = 0$.

It is worth noting that addition of non-zero K_2 interaction also does not determine the direction of zigzag order parameter on the classical level. For the zigzag order with antiferromagnetic z-bonds discussed above, all states with spins lying in the xy-plane remain classically degenerate. This can be understood as follows. In the zigzag order with antiferromagnetic z-bonds, the second n. n. $\tilde{z}$-bonds are ferromagnetic while the $\tilde{x}$- and $\tilde{y}$-bonds are antiferromagnetic. Thus, the antiferromagnetic K_2 coupling on these bonds will keep the spins in the xy-plane. However, since there is an equal number of $\tilde{x}$- and $\tilde{y}$-bonds, the K_2 interaction does not lift the classical degeneracy. A particular spin direction, x or y, is again chosen by fluctuations.

3.7 Conclusions

Spin interactions beyond nearest neighbors in honeycomb iridates may change the phase diagram in essential ways. Our aim in the present chapter has been to derive the spin exchange interactions from a plausible microscopic model and to determine the corresponding phase diagram. In the first part we have calculated the effective super-exchange Hamiltonian in second order perturbation theory in the hopping amplitudes, treating the many-body and the single-electron aspects on an equal footing. We demonstrated that in the presence of strong SO coupling, this effective Hamiltonian forms a tensor with non-equivalent diagonal and non-zero off-diagonal elements. We performed a detailed analysis of the magnetic interactions as a function of the Hund's coupling representing the electronic correlations and the trigonal CF splitting which governs the single-electron physics. We showed that the main role of the Hund's coupling is that it is responsible for the appearance of the Kitaev anisotropic interactions via the non-equivalence of the diagonal elements. The trigonal CF also affects the diagonal interactions, however, it's dominating role is in controlling the strength of the off-diagonal interactions. While these interactions might be significantly increased by external pressure, at ambient pressure the trigonal CF distortion is small and, consequently, the off-diagonal interactions are subdominant. Thus, we neglected off-diagonal terms in the derivation of the super-exchange model (3.21), which we believe is the minimal model to describe the Na_2IrO_3 compound. This model includes five Ir-Ir couplings: n. n. *antiferromagnetic* Heisenberg and *ferromagnetic* Kitaev interactions, next n. n. *ferromagnetic* Heisenberg and *antiferromagnetic* Kitaev interactions, and third n. n. *antiferromagnetic* Heisenberg interaction.

The study of the classical phase diagram for this minimal model constitutes the second part of the chapter. We computed the low temperature phase diagram of the effective model (3.21) with classical Monte Carlo simulations. Due to the presence of the anisotropic Kitaev interactions and the frustration introduced by the competition of the spin couplings between n. n. and second neighbors, the resulting phase diagram is very rich. It contains both various commensurate states and incommensurate single-$\mathbf{Q}$ and multi-$\mathbf{Q}$ phases, whose regions of stability are controlled by the ratios between competing exchange constants. We showed that the second neighbor Kitaev term plays

an important role in the stabilization of the commensurate antiferromagnetic zigzag phase which has been experimentally observed in Na_2IrO_3. In our simulations, we found this phase to be the ground state for parameters of the model of both the correct signs and magnitudes.

Chapter 4

Kitaev-Heisenberg model in a magnetic field: order-by-disorder and commensurate-incommensurate transitions

4.1 Introduction

In this chapter, we discuss field-induced phenomena in the honeycomb KH model based on a complete temperature-field phase diagram obtained from our extensive classical Monte Carlo simulations. We focus on the fate of the zigzag phase, which is relevant for Na_2IrO_3 and α-$RuCl_3$, when the magnetic field is applied perpendicular to the honeycomb plane, i.e. along the [111] direction, and the discrete rotational symmetry of the lattice is preserved. Our main findings are summarized in the field-temperature H-T phase diagram of the KH model presented in Fig. 4.1. In addition to the low-temperature commensurate phases discussed in Ref. [22], we have uncovered intriguing

discontinuous commensurate-incommensurate transitions and novel triple-**Q** incommensurate zigzag states at high magnetic field. We show that while our findings are reminiscent of the Z_2 vortex crystal one encounters in looking at the triangular KH model [72, 73], which arises from the commensurate 120° state through a kind of a nucleation transition, in our case the origin of the incommensurate zigzag state is different and is driven by entropic selection.

The chapter is organized as follows. In section 4.2, we briefly review the basics of the KH model and discuss the states constituting the zero-field ground state phase diagram of the model. In section 4.3, we present the main results of this chapter. We show that at low fields and low temperatures the commensurate triple-**Q** zigzag state is stabilized by the magnetic field. On the other hand, thermal fluctuations at finite temperatures select the collinear single-**Q** zigzag order. The transition between these two phases is, therefore, determined by the competition between the entropic and Zeeman energy gain. At intermediate field strength, our Monte Carlo simulations uncover other phase transitions, first into the partially incommensurate and then into the fully incommensurate zigzag phases. Importantly, all these low- and intermediate-field transitions are hidden in the magnetization curves. Also, our analysis suggests that the observed commensurate-incommensurate transitions are driven by entropic selection. At high magnetic fields, our Monte Carlo simulations and the classical instability analysis at the saturation field show that a $\sqrt{3} \times \sqrt{3}$ order is stabilized below the saturation field. In section 4.4, we discuss the nature of the field induced phase transitions based on the annealing and heating simulations and present the temperature dependence of the zigzag order parameters. We conclude in section 4.5. After the summary I provide some technical details of the calculations in Sec 4.6

4.2 Model

We consider the KH model subject to a magnetic field

$$\mathcal{H} = J \sum_{\langle ij \rangle} \mathbf{S}_i \cdot \mathbf{S}_j + 2K \sum_{\langle ij \rangle_\gamma} S_i^\gamma S_j^\gamma - \mathbf{H} \cdot \sum_i \mathbf{S}_i. \tag{4.1}$$

Here $\gamma = x$, y, and z denote the three distinct NN bonds of a honeycomb lattice. The spin quantization axes are taken along the cubic axes of the IrO_6 octahedra. The first J

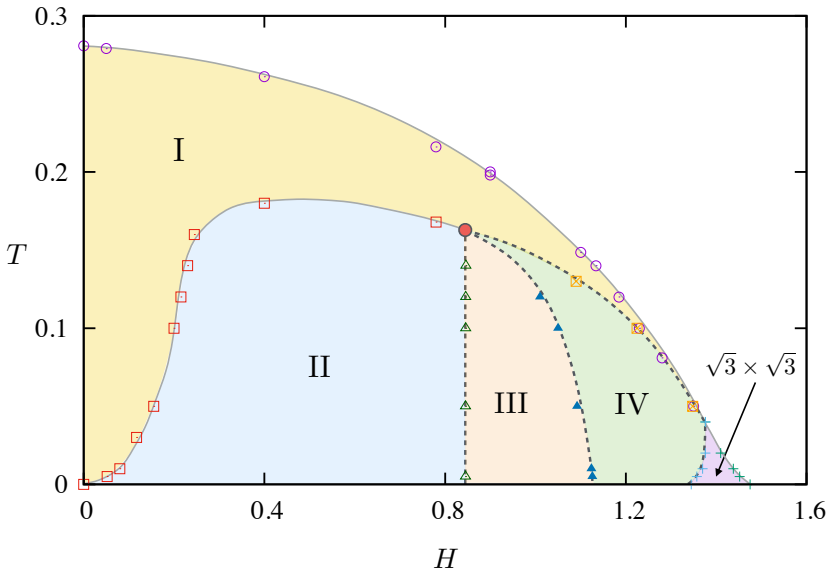

Figure 4.1: The field-temperature (H-T) phase diagram of the KH model with parameter $\varphi = 0.7\pi$. Dashed and solid lines denote first and second-order phase transitions, respectively. There are five ordered phases at low temperatures. Other than the $\sqrt{3} \times \sqrt{3}$ order at high field, the phase diagram is dominated by four distinct zigzag phases: single-**Q** canted zigzag (I), triple-**Q** commensurate zigzag (II), triple-**Q** partial incommensurate zigzag (III), and fully incommensurate 3**Q** zigzag (IV). The corresponding structure factors and spin snapshots are shown in Fig. 4.2. T and H are measured in units of overall exchange energy scale A.

term is the isotropic Heisenberg exchange, while the second Kitaev term describes the bond-dependent Ising coupling between spin components.

Already at zero field, the KH model exhibits several interesting phases depending on the relative strength of the two competing terms. A convenient parametrization is to write $J = A\cos\varphi$ and $K = A\sin\varphi$, where $A > 0$ is the overall energy scale of exchange interaction. In addition to the conventional ferromagnetic and Néel orders, the classical phase diagram includes two collinear antiferromagnetic (AF) states with spontaneously broken C_3 symmetry, called the zigzag and stripy AF orders. Remarkably, all magnetic phases survive quantum fluctuations and remain stable in the limit of $S = 1/2$, except for two small regions of φ close to $\pi/2$ and $3\pi/2$ where quantum spin liquids emerge as the ground states.

4.3 Classical H-T phase diagram

The zigzag phase, which is our primary interest in this work, occupies almost a quarter of the phase space ($0.501\,\pi \lesssim \varphi \lesssim 0.9\,\pi$) of the KH model at $T = H = 0$ [14]. Here we focus on the KH model with parameter $\varphi = 0.7\pi$ and employ Monte Carlo simulations to study the H-T phase diagram. Our extensive simulations result in an unexpectedly rich phase diagram shown in Fig. 4.1, which is dominated by four distinct zigzag phases labeled by I, II, III, and IV. In addition, a non-collinear $\sqrt{3} \times \sqrt{3}$ order is stable in a magnetic field just below the saturation and low temperature regime. The representative snapshots and the corresponding spin structure factors of these five ordered phases are shown in Fig. 4.2. In the following, we discuss the properties of these phases and their numerical characterizations.

4.3.1 Low field strength: triple-Q zigzag order

We begin with the single-$\mathbf{Q}$ zigzag order (phase I), which is the low-T phase of the KH model at $H = 0$. This ordered state is characterized by collinear spins forming ferromagnetic zigzag chains, which are anti-collinearly staggered along the direction perpendicular to the chains; see Fig. 4.2(a). Importantly, the direction of collinear spins is locked to orientation of the zigzags. There are three degenerate zigzag states that are related to each other by symmetry; they correspond to the three staggering wavevectors: $\mathbf{Q}_{1,2} = (\pm\pi, -\pi/\sqrt{3})$, and $\mathbf{Q}_3 = (0, 2\pi/\sqrt{3})$, which are the middle M points of the Brillouin zone (BZ) edges. The collinear zigzag phase can be characterized by an Ising order parameter ϕ_m, which is the odd-parity one-dimensional irreducible representation of the little group corresponding to wavevector $\mathbf{Q}_m$. A general multiple-$\mathbf{Q}$ zigzag state is then described by a pseudo-vector of three Ising parameters: $\boldsymbol{\phi} = (\phi_1, \phi_2, \phi_3)$. In terms of the triplet order parameter, the spins in a general zigzag state are expressed as $S_i^\gamma = \pm\phi_m\, S \exp(i\mathbf{Q}_m \cdot \mathbf{r}_i)$; where $\pm$ is used for the two sublattices of honeycomb, and the spin component $\gamma = x, y, z$ corresponds to $m = 1, 2, 3$, respectively.

In the framework of the Ginzburg-Landau theory, the transition into the zigzag phase is described by a free-energy expansion in terms of the pseudo-vector order parameter $\boldsymbol{\phi}$.

Up to quartic order, it reads:

$$\mathcal{F} = r|\boldsymbol{\phi}|^2 + u|\boldsymbol{\phi}|^4 + g\,\phi_1\phi_2\phi_3 + v\sum_{m\neq n}\phi_m^2\phi_n^2. \tag{4.2}$$

While this free energy respects the C_3 symmetry of the KH model, the first two terms actually preserve a $O(3)$ rotational symmetry of the pseudo-vector $\boldsymbol{\phi}$, indicating an emergent continuous degeneracy of the zigzag states. Indeed, explicit calculation shows that all multiple-$\mathbf{Q}$ zigzag states satisfying $|\boldsymbol{\phi}|$ = constant are degenerate at the mean-field level [46, 21].

This accidental degeneracy is lifted by the cubic g and quartic v terms of Eq. (4.2). In the absence of magnetic field, the cubic term is not allowed by time-reversal symmetry. On the other hand, thermal and quantum fluctuations select the collinear single-$\mathbf{Q}$ zigzag order [50, 74]. This order-by-disorder phenomenon indicates a repulsive interaction, $v \sim v_0 + v_1 T$, with $v_{0,1} > 0$; the two terms correspond to quantum and thermal contributions, respectively. On the other hand, a finite g is allowed when time-reversal symmetry is explicitly broken by a magnetic field. This cubic interaction term favors a zigzag order with coexisting ϕ_m, irrespective of the sign of g.

Physically, the accidental continuous degeneracy of the zigzag states results from the frustrated exchange interactions of the KH model. It also indicates that the phase might be very sensitive to magnetic field. Here we employ large-scale Monte Carlo simulations to investigate the thermodynamic phases induced by the external field along the [111] direction. Our Monte Carlo simulations indeed find a triple-$\mathbf{Q}$ zigzag order (phase II) that is favored by the cubic term in a large portion of the phase diagram; see Fig. 4.1. The spin configuration of the triple-$\mathbf{Q}$ zigzag corresponding to a pseudo-vector $\boldsymbol{\phi} \propto (1,1,1)$ is shown in Fig. 4.2(b). The three spin components participate in ordering along different zigzag directions characterized by the three wavevectors $\mathbf{Q}_m$, giving rise to a non-coplanar magnetic structure. Our variational calculations based on a quadrupled unit cell, which encompasses general zigzag patterns, also verifies that the triple-$\mathbf{Q}$ zigzag state is energetically favored by any finite H.

The transition between phases I and II results from the competition between the v and g terms in $\mathcal{F}$, i.e., between the entropic selection and Zeeman energy gain. As the system crosses this phase boundary from the low field side, the broken C_3 symmetry of phase I is restored. Interestingly, this phase transition has almost no noticeable

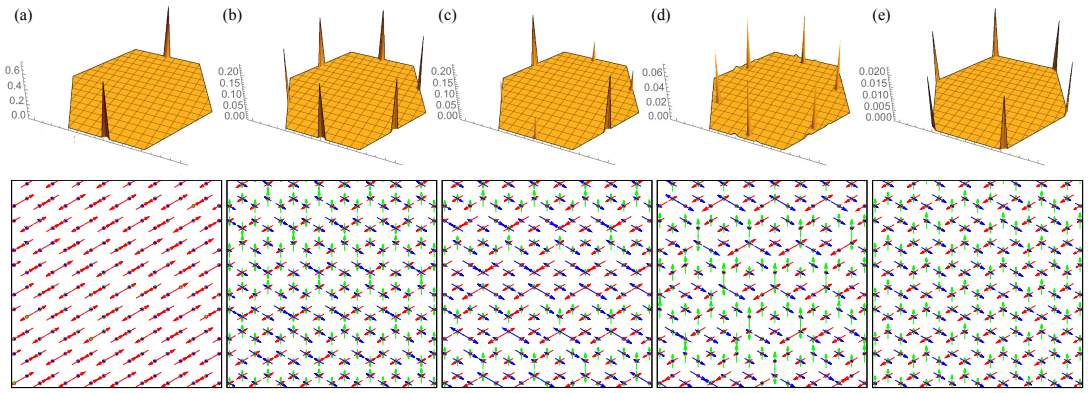

Figure 4.2: Magnetic phases in the honeycomb KH model. Top row shows the spin structure factors obtained from simulations at $T = 0.005$; Corresponding snapshots of the spin configurations are shown in the bottom row. The three spin components are shown here with red, green, and blue colors. The five phases shown here are (a) single-$\mathbf{Q}$ collinear zigzag order ($H = 0.016$), (b) commensurate triple-$\mathbf{Q}$ non-coplanar zigzag ($H = 0.48$), (c) coexistence of commensurate and incommensurate triple-$\mathbf{Q}$ zigzag phase ($H = 1.02$), (d) incommensurate triple-$\mathbf{Q}$ zigzag phase ($H = 1.34$), and (e) $\sqrt{3} \times \sqrt{3}$ order ($H = 1.4$). T and H are measured in units of A.

effects on the magnetization curve, as shown in Fig. 4.3(a). It is clearly seen that the magnetization increases smoothly with H in the small to intermediate field regime. On the other hand, the field dependence of the zigzag order amplitude $|\boldsymbol{\phi}|$, shown in Fig. 4.3(b), exhibits a small kink and a conspicuous drop at intermediate fields, respectively, indicating hidden phase transitions in the seemingly linear magnetization curves.

To distinguish the various zigzag orders and particularly to quantify the broken C_3 symmetry, we introduce a doublet order parameter $\boldsymbol{\zeta}$ with components:

$$\zeta_1 = (\phi_1^2 + \phi_2^2 - 2\phi_3^2)/\sqrt{6}, \quad \zeta_2 = (\phi_1^2 - \phi_2^2)/\sqrt{2}, \tag{4.3}$$

which characterizes the disparity of the three zigzag patterns. Physically, a nonzero $\boldsymbol{\zeta}$ corresponds to a spontaneously broken C_3 symmetry. As discussed above, thermal fluctuations at zero field select one of the three collinear zigzag orders, giving rise to a large $|\boldsymbol{\zeta}|$, while the doublet parameter vanishes in the symmetric triple-$\mathbf{Q}$ zigzag phase at low temperatures. Indeed, as shown in Fig. 4.3(c), the amplitude of the doublet order parameter decreases with increasing field strength, signaling a transition into a more

symmetric zigzag phase.

4.3.2 Intermediate field strength: novel commensurate-incommensurate transitions

At intermediate field strength, our Monte Carlo simulations uncover another phase transition hidden in the seemingly smooth magnetization curve. As shown in Fig. 4.3(b) and (c), both order parameters $\boldsymbol{\phi}$ and $\boldsymbol{\zeta}$ exhibit a pronounced discontinuity at $H \sim 0.8$ for temperatures $T \lesssim 0.02$. In particular, the sudden increase of $|\boldsymbol{\zeta}|$ indicates that the C_3 symmetry is again broken when crossing this first-order transition from the low-field side. Detailed examinations show that this new zigzag order (phase III in Fig. 4.1) is a novel partially incommensurate (IC) phase. Its spin structure factor, shown in Fig. 4.2(c), exhibits four peaks at IC wavevectors close to the M points, along with two larger peaks remaining at the midpoints of the BZ edges.

A particular IC zigzag order can be understood as the corresponding order parameter acquiring a long-wavelength modulation, i.e. $\phi_m(\mathbf{r}) \sim \cos(\mathbf{k}_m \cdot \mathbf{r} + \theta_0)$, where θ_0 is a constant phase, $\mathbf{k}_m = \varepsilon\, \mathbf{Q}_m$ is parallel to the corresponding zigzag wavevector and $\varepsilon \ll 1$. The corresponding spin component thus has a spatial dependence: $S_i^\gamma \sim e^{i\mathbf{Q}_m \cdot \mathbf{r}_i} \cos(\mathbf{k}_m \cdot \mathbf{r}_i + \theta_0)$. In momentum space, since $\mathbf{Q}_m \equiv -\mathbf{Q}_m$ up to a reciprocal lattice vector, the single peak at the original commensurate M point splits into two IC peaks at $(1 \pm \epsilon)\mathbf{Q}_m$.

In phase III, two of the zigzag order parameters, say ϕ_1 and ϕ_2, undergo this modulation instability while the third one ϕ_3 remains commensurate. This asymmetry is responsible for the broken C_3 symmetry. In real space, this phase exhibits a stripy superstructure on top of the underlying zigzag pattern. As the field is further increased, the remaining commensurate zigzag parameter also undergoes a C-IC transition, giving rise to a fully IC state corresponding to phase IV in Fig. 4.1. As shown in Fig. 4.2(d), the structure factor of this fully IC zigzag exhibits six peaks at momenta that are close to the M points, but inside the BZ. This second C-IC transition is also marked by the decrease of the ζ parameter, hence partially restoring the C_3 symmetry of the system; see Fig. 4.3(c).

The observed C-IC transitions might be partially driven by entropic selection. Since

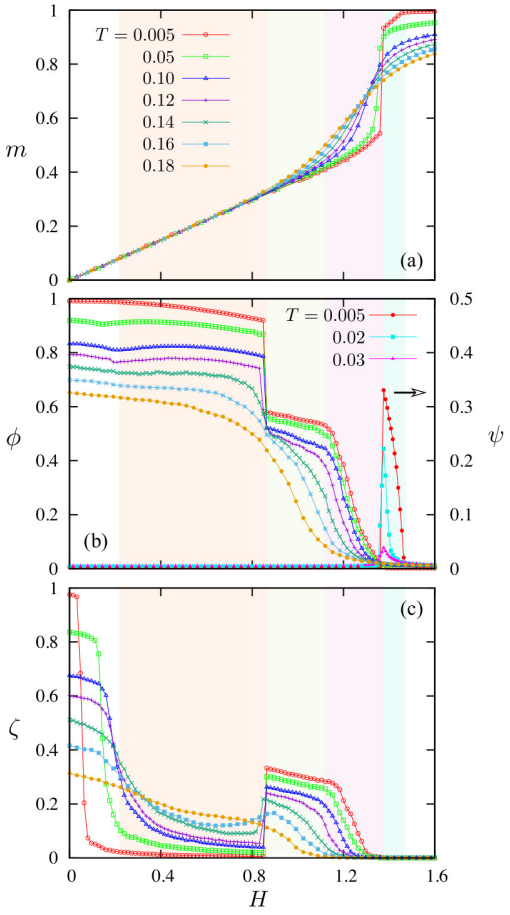

Figure 4.3: Monte Carlo simulations of KH model subject to a magnetic field along the [111] symmetric direction. (a) Magnetization projected onto the field direction as a function of H for varying temperatures. (b) Amplitude of zigzag order parameter $\phi = |\boldsymbol{\phi}|$ (left axis) and the $\sqrt{3}\times\sqrt{3}$ order parameter ψ (right axis) versus field strength. (c) Field dependence of the order parameter $\zeta = |\boldsymbol{\zeta}|$ characterizing the disparity of the three zigzags. Both temperature T and field strength H are in units of the exchange energy scale A. The simulations are performed on the KH model with parameter $\varphi = 0.7\pi$, where single-$\mathbf{Q}$ collinear zigzag order is the ground state. The number of spins is $N_s = 2\times 60^2$.

thermal fluctuations tend to favor collinear spin configurations, one of the reasons behind the stabilization of the IC order can be due to the increase of spin collinearity. The technical details section 4.6.2 at the end of the chapter characterizes various zigzag phases using the nematic order parameter. Indeed, we find that the IC zigzag state has a larger value of the nematic order than in the triple-$\mathbf{Q}$ zigzag phase. Phenomenologically, these two C-IC transitions result from the softening of the gradient terms of the zigzag order parameters. We can again understand the nature of these two transitions from the Ginzburg-Landau formalism. For convenience, we introduce a triplet of order parameters $\boldsymbol{\xi} = (\xi_1, \xi_2, \xi_3)$ which measure the incommensurability of the corresponding zigzag ordering. More specifically, we define $\xi_m = \hat{\mathbf{Q}}_m \cdot \nabla \phi_m$. Note that modulations of ϕ_m that are perpendicular to $\mathbf{Q}_m$ are not considered here, since they are not observed in our simulations. Up to the sixth-order, the free-energy of the gradient terms reads

$$\mathcal{F}_{\text{grad}} = a|\boldsymbol{\xi}|^2 + b|\boldsymbol{\xi}|^4 + c|\boldsymbol{\xi}|^6 + d\sum_{m\neq n} \xi_m^2 \xi_n^2 + e\,\xi_1^2\,\xi_2^2\,\xi_3^2. \tag{4.4}$$

Interestingly, the conventional scenario in which the IC phase is caused by the softening of the stiffness constant $a \to 0$ would lead to a continuous phase transition in the Landau theory. Moreover, the quartic interaction term will immediately select a zigzag state with either a single IC zigzag ($d > 0$) or a fully IC zigzag ($d < 0$). These results are inconsistent with our numerical simulations. Instead, the observed discontinuous C-IC transitions can be attributed to a negative quartic term $b < 0$ while a remains positive throughout the transitions, a scenario similar to the first-order transition close to a tricritical point [75]. Here a sixth-order term with $c > 0$ is required for stability of the system.

The first three terms preserve a pseudo-$O(3)$ rotational symmetry of the modulation parameters $\boldsymbol{\xi}$. Similar to the free-energy in Eq. (4.2), this symmetry indicates a continuous degeneracy of IC zigzag orders. The exact IC order is determined by the interactions among the ξ_m parameters, which are represented by the last two terms in $\mathcal{F}_{\text{grad}}$. A dominant $e > 0$, corresponding to a strong repulsion between the modulation parameters, favors the partially IC phase III in which one of the three ξ_m is zero. On the other hand, a large attractive interaction among the modulations ξ_m, represented by a $d < 0$ term, would drive the system into a fully IC state with restored C_3 symmetry.

4.3.3 High field strength: $\sqrt{3} \times \sqrt{3}$ magnetic ordering

At large magnetic field, the IC zigzag phase is connected to a $\sqrt{3} \times \sqrt{3}$ order through a first-order transition, which manifests itself in the huge jump in magnetization at $H \sim 1.35$ at low temperatures (see Fig. 4.3(a)). This phase is characterized by a Bragg peak at the K point of the BZ, which also serves as the relevant order parameter. A clear jump of the $\sqrt{3} \times \sqrt{3}$ order parameter ψ can be seen in Fig. 4.3(b).

To verify our numerical results for high values of magnetic field, here we perform an explicit stability analysis of the fully polarized state. Specifically, we search for the most unstable normal mode of the KH Hamiltonian in a magnetic field. In a large field limit, all spins are polarized: $\mathbf{S}_i = S\,\hat{\mathbf{n}}$, where $\hat{\mathbf{n}} = \hat{\mathbf{e}}_{[111]}$ is a unit vector pointing along the [111] direction. For convenience, we will set $S = 1$ in the following discussion. We next introduce two unit vectors $\hat{\mathbf{e}}_a = (\hat{\mathbf{e}}_x + \hat{\mathbf{e}}_y - 2\hat{\mathbf{e}}_z)/\sqrt{6}$ and $\hat{\mathbf{e}}_b = (\hat{\mathbf{e}}_y - \hat{\mathbf{e}}_x)/\sqrt{2}$, where $\hat{\mathbf{e}}_{x,y,z}$ are unit vectors pointing along the three cubic axes. The three vectors $\hat{\mathbf{e}}_a$, $\hat{\mathbf{e}}_b$ and $\hat{\mathbf{n}}$ form an orthonormal basis.

As field is decreased, spins start to deviate from the $\hat{\mathbf{n}}$ direction. We next introduce a two-component vector $\boldsymbol{\sigma}_i = (\sigma_i^a, \sigma_i^b)$ and write the spin field as

$$\mathbf{S}_i = \sqrt{1 - |\boldsymbol{\sigma}_i|^2}\,\hat{\mathbf{n}} + \sigma_i^a\,\hat{\mathbf{e}}_a + \sigma_i^b\,\hat{\mathbf{e}}_b. \tag{4.5}$$

It is then easy to see that the individual spin component can be expressed as

$$S_i^\gamma = \frac{1}{\sqrt{3}}\sqrt{1 - |\boldsymbol{\sigma}_i|^2} + \sqrt{\frac{2}{3}}\,\boldsymbol{\sigma}_i \cdot \boldsymbol{t}^\gamma, \tag{4.6}$$

where $\boldsymbol{t}^x = (\frac{1}{2}, \frac{-\sqrt{3}}{2})$, $\boldsymbol{t}^y = (\frac{1}{2}, \frac{\sqrt{3}}{2})$, and $\boldsymbol{t}^z = (-1, 0)$ are the lattice vectors (see Fig. 4.4). Using this expression, we expand the spin interaction term $S_i^\gamma S_j^\gamma$ to second order in σ:

$$\begin{aligned} S_i^\gamma\, S_j^\gamma = \frac{1}{3}\left(1 - \frac{|\boldsymbol{\sigma}_i|^2}{2} - \frac{|\boldsymbol{\sigma}_j|^2}{2}\right) \\ + \frac{\sqrt{2}}{3}\boldsymbol{t}^\gamma \cdot (\boldsymbol{\sigma}_i + \boldsymbol{\sigma}_j) + \frac{2}{3}(\boldsymbol{\sigma}_i \cdot \boldsymbol{t}^\gamma)(\boldsymbol{\sigma}_j \cdot \boldsymbol{t}^\gamma), \end{aligned} \tag{4.7}$$

In particular, the isotropic Heisenberg exchange interaction $\mathbf{S}_i \cdot \mathbf{S}_j = \sum_\gamma S_i^\gamma S_j^\gamma$ becomes

$$\mathbf{S}_i \cdot \mathbf{S}_j = \left(1 - \frac{|\boldsymbol{\sigma}_i|^2}{2} - \frac{|\boldsymbol{\sigma}_j|^2}{2}\right) + \boldsymbol{\sigma}_i \cdot \boldsymbol{\sigma}_j. \tag{4.8}$$

Substituting these expressions into the KH Hamiltonian, we obtain

$$\mathcal{H} = E_0 + \frac{1}{2}(H - 3J - 2K)\sum_i |\boldsymbol{\sigma}_i|^2 \qquad (4.9)$$
$$+J\sum_{\langle ij\rangle} \boldsymbol{\sigma}_i \cdot \boldsymbol{\sigma}_j + \frac{4K}{3}\sum_{\langle ij\rangle_\gamma} (\boldsymbol{\sigma}_i \cdot \boldsymbol{t}^\gamma)(\boldsymbol{\sigma}_j \cdot \boldsymbol{t}^\gamma).$$

where $E_0 = (3J + 2K)N - 2HN$, and N is the number of unit cells of the honeycomb lattice. The terms linear in σ in Eq. (4.7) cancel each other in the lattice sum. We note that the Hamiltonian Eq. (4.9) can serve as a starting point for the quantum mechanical treatment of the magnon condensation. The spin "deviations" $\sigma_i^{a,b}$ are now quantum operators satisfying the commutation relations $[\sigma_i^a, \sigma_j^a] = [\sigma_i^b, \sigma_j^b] = 0$, and $[\sigma_i^a, \sigma_j^b] = iS\delta_{ij}$. In fact, the Holstein-Primarkoff boson operators are expressed as $a_i = (\sigma_i^a + i\sigma_i^b)/\sqrt{2S}$. The magnon bandstructure is then obtained by diagonalizing the resultant magnon Hamiltonian using the Bogoliubov transformation. Magnetic instability occurs when one of the magnon bands touches zero as the field strength is decreased.

Here we treat the spin deviations $\boldsymbol{\sigma}_i$ as classical variables and simply analyze the eigenmodes of the corresponding classical Hamiltonian. In particular, this classical instability analysis provides a direct comparison with the classical Monte Carlo simulations presented in the main text. To this end, we introduce Fourier transformation $\boldsymbol{\sigma}_i = \frac{1}{\sqrt{N}}\sum_{\mathbf{k}} \boldsymbol{\sigma}_s(\mathbf{k}) e^{i\mathbf{k}\cdot\mathbf{r}_i}$ to diagonalize the quadratic Hamiltonian Eq. (4.9). Here each site $i = (\mathbf{r}, s)$ is labeled by the Bravais lattice point $\mathbf{r}$ and the sublattice index $s = 1, 2$, $\mathbf{r}_i = \mathbf{r} + \mathbf{d}_s$ is the actual physical position of site-i, $\mathbf{r} = n_1\boldsymbol{t}^x + n_2\boldsymbol{t}^y$ are Bravais lattice points, and $\mathbf{d}_1 = (0, 0)$ and $\mathbf{d}_2 = \mathbf{d}_z = (0, \frac{1}{\sqrt{3}})$ are basis vectors for the two sublattices. The lattice geometry is shown in Fig. 4.4.

Substituting the Fourier expansion into Eq. (4.9), the spin Hamiltonian becomes

$$\mathcal{H} = E_0 + \sum_{\mathbf{k}} \mathbb{U}_{\mathbf{k}}^* \cdot \mathbb{H}_{\mathbf{k}} \cdot \mathbb{U}_{\mathbf{k}} \qquad (4.10)$$

where the 4-component vector $\mathbb{U}_{\mathbf{k}} = [\sigma_{1\mathbf{k}}^a, \sigma_{1\mathbf{k}}^b, \sigma_{2\mathbf{k}}^a, \sigma_{2\mathbf{k}}^b]$. The interaction matrix $\mathbb{H}_{\mathbf{k}}$ has the following form:

$$\mathbb{H}_{\mathbf{k}} = \begin{bmatrix} \varepsilon_H & 0 & f_{\mathbf{k}} + g_{\mathbf{k}}^{aa} & g_{\mathbf{k}}^{ab} \\ 0 & \varepsilon_H & g_{\mathbf{k}}^{ab} & f_{\mathbf{k}} + g_{\mathbf{k}}^{bb} \\ f_{-\mathbf{k}} + g_{-\mathbf{k}}^{aa} & g_{-\mathbf{k}}^{ab} & \varepsilon_H & 0 \\ g_{-\mathbf{k}}^{ab} & f_{-\mathbf{k}} + g_{-\mathbf{k}}^{bb} & 0 & \varepsilon_H \end{bmatrix}. \qquad (4.11)$$

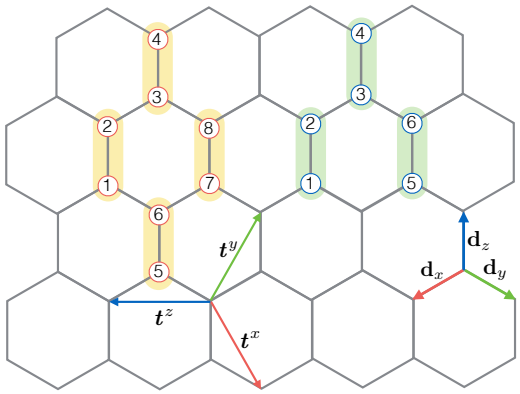

Figure 4.4: The honeycomb lattice with three types of nearest neighbor bonds. Here $\boldsymbol{t}^x = (\frac{1}{2}, \frac{-\sqrt{3}}{2})$, $\boldsymbol{t}^y = (\frac{1}{2}, \frac{\sqrt{3}}{2})$ are two primitive translations. Extended magnetic unit cells used in our variational calculation of the KH model. The quadrupled unit cell (yellow shaded sites) corresponding to the general ordering composed of three wavevectors $\mathbf{Q}_1 = (-\pi, -\pi/\sqrt{3})$, $\mathbf{Q}_2 = (0, 2\pi/\sqrt{3})$, and $\mathbf{Q}_3 = (+\pi, -\pi/\sqrt{3})$. The tripled unit cell (green shaded sites), on the other hand, describes the $\sqrt{3}\times\sqrt{3}$ type ordering with a wavevector $\mathbf{K} = (4\pi/3, 0)$.

The matrix elements are

$$\varepsilon_H = \frac{1}{2}(H - 3J - 2K), \tag{4.12}$$

$$f_{\mathbf{k}} = = \frac{J}{2}\left(e^{i\mathbf{k}\cdot\mathbf{d}_x} + e^{i\mathbf{k}\cdot\mathbf{d}_y} + e^{i\mathbf{k}\cdot\mathbf{d}_z}\right), \tag{4.13}$$

$$g^{aa}_{\mathbf{k}} = \frac{K}{6}\left(e^{i\mathbf{k}\cdot\mathbf{d}_x} + e^{i\mathbf{k}\cdot\mathbf{d}_y} + 4e^{i\mathbf{k}\cdot\mathbf{d}_z}\right), \tag{4.14}$$

$$g^{bb}_{\mathbf{k}} = \frac{K}{2}\left(e^{i\mathbf{k}\cdot\mathbf{d}_x} + e^{i\mathbf{k}\cdot\mathbf{d}_y}\right), \tag{4.15}$$

$$g^{ab}_{\mathbf{k}} = -\frac{K}{2\sqrt{3}}\left(e^{i\mathbf{k}\cdot\mathbf{d}_x} - e^{i\mathbf{k}\cdot\mathbf{d}_y}\right). \tag{4.16}$$

Here the three vectors $\mathbf{d}_{x,y} = (\pm\frac{1}{2}, \frac{-1}{2\sqrt{3}})$, and $\mathbf{d}_z = (0, \frac{1}{\sqrt{3}})$ connect nearest-neighbors in honeycomb lattice. As the field strength H is reduced, the magnetic instability starts at the $\mathbf{k}^*$ points at which $\lambda_{\min}(\mathbf{k}^*)$ touches zero; here $\lambda_{\min}(\mathbf{k})$ is the smallest eigenvalue of the matrix $\mathbb{H}(\mathbf{k})$. Figure. 4.5 shows the contour plot of $\lambda_{\min}(\mathbf{k})$ in k-space. As can be seen, the function $\lambda_{\min}(\mathbf{k})$ has minima at the K points, indicating that the instability will take place at the corner of the Brillouin zone. The resultant $\sqrt{3}\times\sqrt{3}$ magnetic ordering is consistent with our Monte Carlo simulation results at high field.

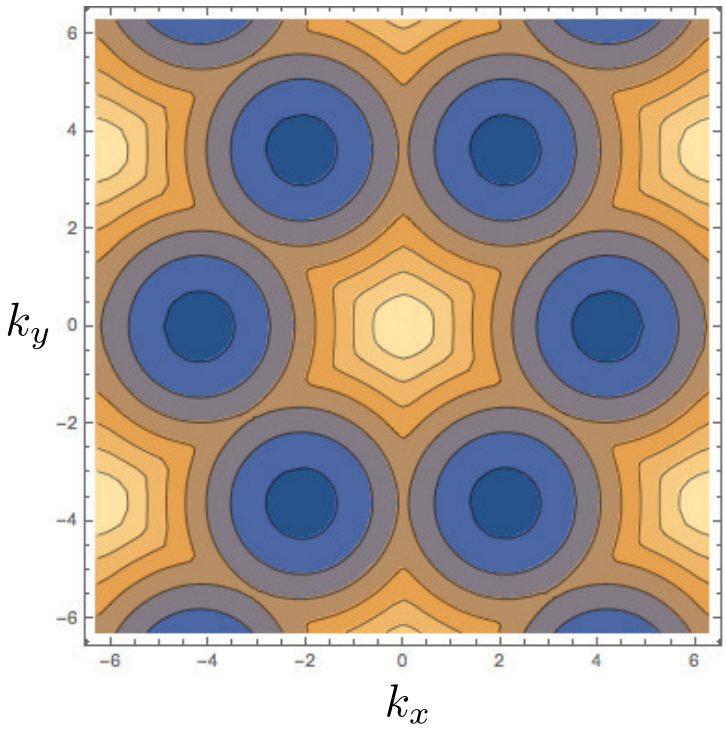

Figure 4.5: Contour plot of the minimum eigenvalue of $\mathbb{H}(\mathbf{k})$, showing minimum at the K points $\mathbf{Q}_K = (\frac{4\pi}{3}, 0)$.

4.4 Temperature dependence and hysteresis

Here we present the temperature dependence of the zigzag order parameter ϕ and ζ computed from annealing and heating simulations. At small field, as shown in Fig. 4.6(a) for $H = 0.2$, the zigzag order parameter ϕ increases monotonically as temperature is lowered. On the other hand, the amplitude of the doublet order parameter $\boldsymbol{\zeta}$, which characterizes the disparity of the three zigzag Ising parameters ϕ_m, shows a non-monotonic temperature dependence; see Fig. 4.6(b). As discussed in section 4.3.1, the doublet order parameter vanishes identically in a perfect triple-$\mathbf{Q}$ zigzag state, while $\zeta = |\boldsymbol{\zeta}|$ reaches its maximum value in a single-$\mathbf{Q}$ zigzag. The re-entrant behavior shown in Fig. 4.6(b) thus corresponds to an intermediate single-$\mathbf{Q}$ zigzag phase that is stabilized by thermal fluctuations at finite temperatures. The absence of hysteresis from the annealing and heating simulations points to a continuous transition between the single and triple $\mathbf{Q}$ zigzag phases.

At high field $H = 0.92$, annealing simulation from a disordered state shows a monotonic growth for both order parameters ϕ and ζ with decreasing temperature; see Fig. 4.6(c) and (d). From the H-T phase diagram shown in Fig. 1, there are two low-T zigzag phases at this field value: the single-$\mathbf{Q}$ commensurate phase I and the partially incommensurate phase III at lowest temperatures. Since the C_3 symmetry is broken in both phases, the ζ order parameter describing the disparity of the three zigzag chains is nonzero throughout the low-T ordered regime. Interestingly, our simulations also find that the incommensurate zigzag phase III coexists with the commensurate triple-$\mathbf{Q}$ zigzag II state over a wide range of temperatures, as demonstrated by the pronounced hysteresis loop from the annealing and heating simulations shown in Fig. 4.6(c) and (d). In the heating simulations, the spins are initialized to the commensurate triple-$\mathbf{Q}$ zigzag state obtained from the variational minimization discussed above. At zero temperature, this triple-$\mathbf{Q}$ phase with three coexisting zigzag Ising order parameters $\phi_1 = \phi_2 = \phi_3$ is characterized by a vanishing ζ. As T increases, we find that the triple-$\mathbf{Q}$ state is a very robust local minimum and remains stable until $T \sim 0.1$, above which the system decays spontaneously into the partially incommensurate zigzag phase III as indicated by a sudden increase of the ζ order parameter.

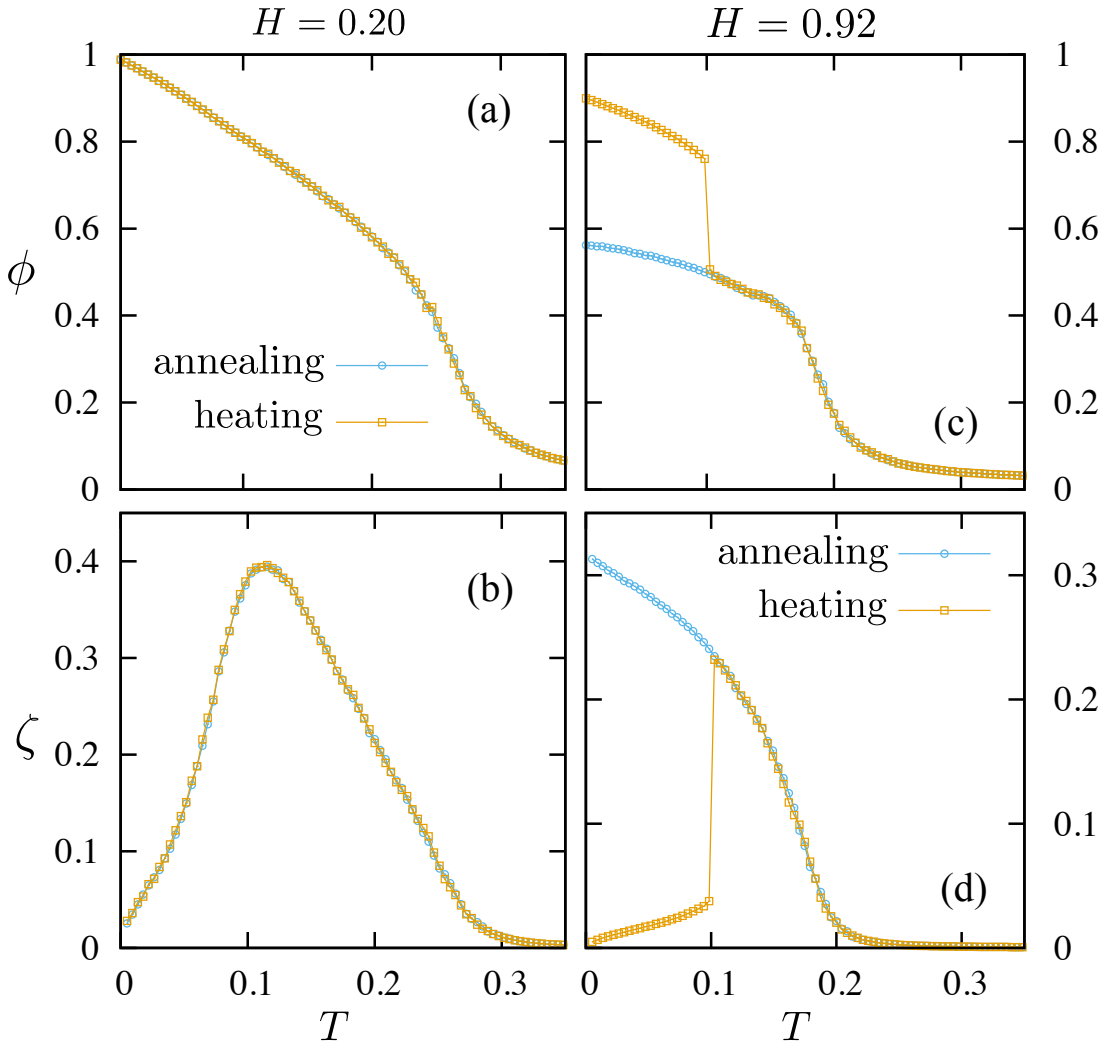

Figure 4.6: Temperature dependence of order parameters $\phi = |\boldsymbol{\phi}|$ and $\zeta = |\boldsymbol{\zeta}|$ from annealing and heating simulations. Panels (a) and (b) are obtained with $H = 0.2$, while (c) and (d) are obtained with $H = 0.96$.

4.5 Summary

To summarize, we have investigated the finite temperature phase diagram of the KH model subject to a magnetic field. Our extensive Monte Carlo simulations have uncovered several novel zigzag orders and phase transitions. Of particular interest is the existence of two intriguing IC zigzag orderings at intermediate to large field regime. Interestingly, these unusual zigzag states are completely hidden in the magnetization measurement, which shows a smooth growth of magnetic moment with increasing field. These intriguing IC zigzags might be identified in high-field μSR experiments which provide a powerful means of measuring the internal magnetic field distribution caused by the presence of the peculiar field texture. The C-IC transition could be observed experimentally using inelastic neutron scattering techniques.

One last and yet very important question to address is the relevance of the obtained results to the real materials. Although zigzag phases have been detected in Na_2IrO_3 and α-$RuCl_3$, the spin Hamiltonian of both compounds remains uncertain, and it probably involves both other anisotropic interactions and further neighbor isotropic couplings [71, 11, 76, 21, 77, 78, 79]. In particular, the NN off-diagonal exchange Γ may play an important role in both Na_2IrO_3 and α-$RuCl_3$, e.g. in fixing the global directions of the spins in the zigzag state at zero field [21]. Although the effects of a magnetic field in these more realistic models have yet to be investigated in detail, given the frustrated nature of spin interactions in such spin-orbit Mott insulators, we expect similar field-induced phases to occur in real materials, which is left for future studies.

4.6 Technical details

4.6.1 Variational ground states

In this technical section, we present a variational calculation for the classical ground states of the KH Hamiltonian. We consider magnetic structures with both a quadrupled unit cell and a tripled unit cell as our ansatz; see Fig. 4.4. In the former case, the 8-site spin structure includes the simple ferromagnetic and Néel orders with $\mathbf{Q}_0 = 0$, as well as the general zigzag and stripe orders characterized by wavevectors $\mathbf{Q}_1 = (-\pi, -\pi/\sqrt{3})$, $\mathbf{Q}_2 = (0, 2\pi/\sqrt{3})$, and $\mathbf{Q}_3 = (+\pi, -\pi/\sqrt{3})$. As discussed in the previous

section, magnetic instability from the saturated state starts at the $\mathbf{K} = (4\pi/3, 0)$ points of the BZ. The corresponding eigen-mode belongs to the class of magnetic states with a tripled unit cell containing 6 inequivalent spins. In both cases, each spin in the extended unit cell is parametrized by two angles: $\mathbf{S}_i = S(\sin\beta_i\cos\alpha_i, \sin\beta_i\sin\alpha_i, \cos\beta_i)$. The total variational energy $E_{\rm var}(\{\alpha_i, \beta_i\})$, which is a function of these angle variables, is then minimized to obtain the variational ground states.

Next we discuss the characterization of the minimum-energy solution in the quadrupled unit cell. We first define vector order parameters that correspond to wavevector $\mathbf{Q}_0$ and the three $\mathbf{Q}_m$ $(m = 1, 2, 3)$ at the M-points of the BZ. By labeling the 8 inequivalent sites according to Fig. 4.4, these vector order parameters are basically linear transformations of the eight spins $\{\mathbf{S}_i\}$:

$$\begin{aligned}
\mathbf{M} &= \tfrac{1}{8}(\mathbf{S}_1 + \mathbf{S}_2 + \mathbf{S}_3 + \mathbf{S}_4 + \mathbf{S}_5 + \mathbf{S}_6 + \mathbf{S}_7 + \mathbf{S}_8),\\
\mathbf{L} &= \tfrac{1}{8}(\mathbf{S}_1 - \mathbf{S}_2 + \mathbf{S}_3 - \mathbf{S}_4 + \mathbf{S}_5 - \mathbf{S}_6 + \mathbf{S}_7 - \mathbf{S}_8),\\
\mathbf{N}_1 &= \tfrac{1}{8}(\mathbf{S}_1 - \mathbf{S}_2 - \mathbf{S}_3 + \mathbf{S}_4 + \mathbf{S}_5 - \mathbf{S}_6 - \mathbf{S}_7 + \mathbf{S}_8),\\
\mathbf{N}_2 &= \tfrac{1}{8}(\mathbf{S}_1 + \mathbf{S}_2 - \mathbf{S}_3 - \mathbf{S}_4 - \mathbf{S}_5 - \mathbf{S}_6 + \mathbf{S}_7 + \mathbf{S}_8),\\
\mathbf{N}_3 &= \tfrac{1}{8}(\mathbf{S}_1 - \mathbf{S}_2 + \mathbf{S}_3 - \mathbf{S}_4 - \mathbf{S}_5 + \mathbf{S}_6 - \mathbf{S}_7 + \mathbf{S}_8),\\
\mathbf{R}_1 &= \tfrac{1}{8}(\mathbf{S}_1 + \mathbf{S}_2 - \mathbf{S}_3 - \mathbf{S}_4 + \mathbf{S}_5 + \mathbf{S}_6 - \mathbf{S}_7 - \mathbf{S}_8),\\
\mathbf{R}_2 &= \tfrac{1}{8}(\mathbf{S}_1 - \mathbf{S}_2 - \mathbf{S}_3 + \mathbf{S}_4 - \mathbf{S}_5 + \mathbf{S}_6 + \mathbf{S}_7 - \mathbf{S}_8),\\
\mathbf{R}_3 &= \tfrac{1}{8}(\mathbf{S}_1 + \mathbf{S}_2 + \mathbf{S}_3 + \mathbf{S}_4 - \mathbf{S}_5 - \mathbf{S}_6 - \mathbf{S}_7 - \mathbf{S}_8).
\end{aligned} \tag{4.17}$$

Here the $\mathbf{Q}_0 = 0$ part includes $\mathbf{M}$, which is the simple ferromagnetic order, and $\mathbf{L}$ which describes the staggering of sublattice magnetization. The vectors $\mathbf{N}_m$ characterize the odd-parity zigzag order with wavevectors $\mathbf{Q}_m$. And finally, the even-parity combinations corresponding to the stripe order are given by the three vector parameters $\mathbf{R}_m$. For spin Hamiltonians that preserve the SU(2) or O(3) spin rotational symmetry, or if the spin rotations are decoupled from the real-space symmetry operations, these vectors are the appropriate order parameters for the characterization of the magnetically ordered states.

However, the presence of the anisotropic Kitaev term in the KH Hamiltonian explicitly breaks the spin rotational symmetry, and only generalized symmetry operations

that involve discrete rotations in both spatial and spin spaces are preserved. For example, permutations of the three vector parameters $\mathbf{N}_m$ (by the C_3 rotations) must be accompanied by the corresponding rotation in spin space. Consequently, instead of the vector parameters listed above, the proper order parameters are given by the irreducible representations of the group of combined symmetry operations. For instance, as discussed in the main text, a multiple-$\mathbf{Q}$ zigzag order is characterized by a triplet of Ising parameters $\boldsymbol{\phi} = (\phi_1, \phi_2, \phi_3)$. Similarly, a multiple-$\mathbf{Q}$ stripe order is described by a triplet $\boldsymbol{\eta} = (\eta_1, \eta_2, \eta_3)$. In terms of these Ising order parameters, the corresponding vector parameters are $\mathbf{N}_m = \phi_m \hat{\mathbf{e}}_\gamma$ and $\mathbf{R}_m = \eta_m \hat{\mathbf{e}}_\gamma$. Here $m = 1, 2, 3$ corresponds to $\gamma = x$, y, z. Our direct numerical minimization finds that combined C_3 symmetry is preserved in the variational ground states in the parameter regime of our interest. As a result, for example, the symmetric zigzag order with $\phi_1 = \phi_2 = \phi_3$ is specified by only one scalar parameter.

In the limit of $H \to 0$, the only nonzero order parameters are the three vectors $\mathbf{N}_m$ while all other vectors vanish. The magnetic field not only induces a finite magnetization $\mathbf{M}$, but also generates other small secondary order parameters due to the hard constraint of fixed spin length $|\mathbf{S}_i| = S$. Through our direct numerical minimization, we find that the variational ground state of the KH model can be described by six scalar parameters m, ℓ, ϕ, $\bar{\phi}$, η, and $\bar{\eta}$:

$$\begin{aligned}
\mathbf{M} &= m\,(\hat{\mathbf{e}}_x + \hat{\mathbf{e}}_y + \hat{\mathbf{e}}_z)/\sqrt{3}, \\
\mathbf{L} &= \ell\,(\hat{\mathbf{e}}_x + \hat{\mathbf{e}}_y + \hat{\mathbf{e}}_z)/\sqrt{3}, \\
\mathbf{N}_1 &= \phi\,\hat{\mathbf{e}}_x/\sqrt{3} + \bar{\phi}\,(\hat{\mathbf{e}}_y + \hat{\mathbf{e}}_z)/\sqrt{6}, \\
\mathbf{N}_2 &= \phi\,\hat{\mathbf{e}}_y/\sqrt{3} + \bar{\phi}\,(\hat{\mathbf{e}}_z + \hat{\mathbf{e}}_x)/\sqrt{6}, \\
\mathbf{N}_3 &= \phi\,\hat{\mathbf{e}}_z/\sqrt{3} + \bar{\phi}\,(\hat{\mathbf{e}}_x + \hat{\mathbf{e}}_y)/\sqrt{6}, \\
\mathbf{R}_1 &= \eta\,(\hat{\mathbf{e}}_y + \hat{\mathbf{e}}_z)/\sqrt{6} + \bar{\eta}\,\hat{\mathbf{e}}_x/\sqrt{3}, \\
\mathbf{R}_2 &= \eta\,(\hat{\mathbf{e}}_z + \hat{\mathbf{e}}_x)/\sqrt{6} + \bar{\eta}\,\hat{\mathbf{e}}_y/\sqrt{3}, \\
\mathbf{R}_3 &= \eta\,(\hat{\mathbf{e}}_x + \hat{\mathbf{e}}_y)/\sqrt{6} + \bar{\eta}\,\hat{\mathbf{e}}_z/\sqrt{3},
\end{aligned} \tag{4.18}$$

With these variational parametrization, the energy density of the 8-site spin structure

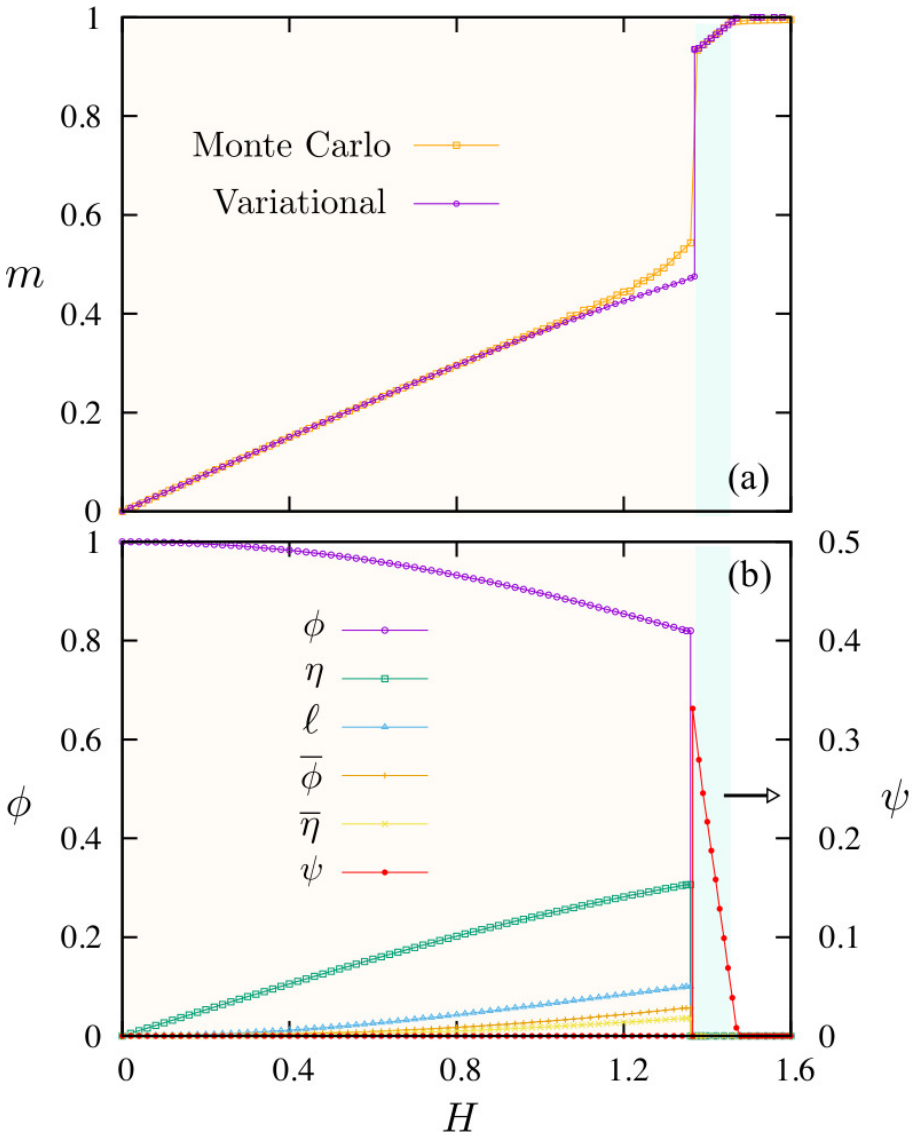

Figure 4.7: Variational ground-state calculation of KH model at $\varphi = 0.7\pi$ in the magnetic field along the [111] direction : (a) Magnetization given by the ferromagnetic order parameter m as a function of field strength. Also shown for comparison is the magnetization curve obtained from Monte Carlo simulations at a temperature $T = 0.005$. (b) The amplitude of the various order parameters defined in Eqs. (4.18) and (4.21) versus H. T and H are measured in units of A.

is

$$\begin{aligned}\varepsilon &= -Hm - \frac{1}{2}(3J+2K)(\ell^2 - m^2) \\ &\quad + \frac{J}{2}\left(\phi^2 + \bar{\phi}^2 - \eta^2 - \bar{\eta}^2\right) \\ &\quad - K\left(\phi^2 - \bar{\phi}^2 + \eta^2 - \bar{\eta}^2\right).\end{aligned} \tag{4.19}$$

The two exchange terms of the KH Hamiltonian are parametrized as $J = A\cos\varphi$, and $K = A\sin\varphi$. For a strong ferromagnetic Kitaev interaction ($K > 0$), as in the case of KH parameter $\varphi = 0.7\pi$, the two dominant orderings are zigzag order characterized by ϕ and the stripe order characterized by η. The zigzag pattern is further favored by a ferromagnetic Heisenberg term with $J < 0$, again as in the case of $\varphi = 0.7\pi$. Indeed, as shown in Fig. 4.7, a significant stripe order η appears at high field in addition to the dominant zigzag order ϕ. Finally, we note that the Néel order ℓ and $\bar{\phi}$, $\bar{\eta}$ are secondary parameters with small amplitude.

We next turn to the characterization of the magnetic structure with tripled unit cell. Other than the usual ferromagnetic $\mathbf{M}$ and Néel order $\mathbf{L}$, we are most interested in the order parameter corresponding to the $\sqrt{3}\times\sqrt{3}$ type pattern. This long-range order is characterized by a wavevector $\mathbf{K} = (4\pi/3, 0)$. For convenience, we define $\omega = \exp(i\,\mathbf{K}\cdot\mathbf{t}^x) = \exp(i\,2\pi/3)$. Using the labeling of the six inequivalent spins in Fig. 4.4, the appropriate vector order parameters are then given by

$$\begin{aligned}\mathbf{V}_1 &= \tfrac{1}{3}\left(\mathbf{S}_1 + \omega\,\mathbf{S}_3 + \omega^2\,\mathbf{S}_5\right), \\ \mathbf{V}_2 &= \tfrac{1}{3}\left(\mathbf{S}_2 + \omega\,\mathbf{S}_4 + \omega^2\,\mathbf{S}_6\right).\end{aligned} \tag{4.20}$$

Here the subscript 1, 2 refers to the two sublattices of the honeycomb lattice. Consistent with the linear stability analysis discussed in the previous section, we find that the $\sqrt{3}\times\sqrt{3}$ structure indeed has a lower energy compared with the general 8-site ansatz in the high field regime. Moreover, our direct minimization shows that the $\sqrt{3}\times\sqrt{3}$ order can be characterized by a complex order parameter ψ as follows:

$$\begin{aligned}\mathbf{V}_1 &= +\psi\left(\hat{\mathbf{e}}_x + \omega\,\hat{\mathbf{e}}_y + \omega^2\,\hat{\mathbf{e}}_z\right), \\ \mathbf{V}_2 &= -\psi\left(\omega^2\hat{\mathbf{e}}_x + \omega\,\hat{\mathbf{e}}_y + \hat{\mathbf{e}}_z\right),\end{aligned} \tag{4.21}$$

where the phase of ψ is field dependent. Fig. 4.7 summarizes our numerical calculation of the variational ground states. Other than the fully polarized state at high field,

there are two nontrivial ordered states separated by a first-order phase transition at $H_c \sim 1.37$. The low-field phase is the symmetric triple-$\mathbf{Q}$ order with a dominant zigzag order parameter ϕ. While the only nonzero order at $H \to 0$ is given by $\phi = 1$, all other order parameters are induced by the magnetic field and grow gradually with increasing H. Interestingly, a small Néel order is generated by the field. Moreover, the stripe order characterized by η becomes quite significant in the intermediate field regime. For field strength above H_c, all order parameters related to three $\mathbf{Q}_\gamma$ wavevectors suddenly drop to zero. The high-field ground state corresponds to a finite ψ, indicating the $\sqrt{3} \times \sqrt{3}$ type long-range order.

We note that the variational ground states are consistent with the Monte Carlo simulations for regimes where the ground state is the commensurate triple-$\mathbf{Q}$ zigzag (small H), and the $\sqrt{3}\times\sqrt{3}$ order (large H). The two methods give very consistent values for the H_c of the first-order transition and the saturation field; see the comparison in Fig. 4.7(a). However, since the variational calculation is restricted to commensurate unit cells, it cannot address the commensurate-incommensurate transitions and the novel incommensurate zigzag orders observed in Monte Carlo simulations. The variational approach, nonetheless, provides a guideline of the underlying energetics and serves as a useful double check for the large-scale simulations.

The triple-$\mathbf{Q}$ zigzag order has an interesting canting pattern. At $H = 0$, the eight inequivalent spins point in the eight symmetry-related $\langle 111 \rangle$ directions. As H is increased, the two spins pointing along [111] and $[\bar{1}\bar{1}\bar{1}]$, are completely unaffected by the field. The other six spins cant towards the direction of the field, with the canting angle increasing as a function of the field magnitude. At intermediate field, this canted triple-$\mathbf{Q}$ zigzag gives way to the incommensurate zigzag orders, phases III and IV discussed in the main text. As discussed above, the variational calculation based on 8-sublattice unit cell cannot describe the corresponding C-IC transitions. Finally, at high enough magnetic field it is no longer energetically favorable to keep one spin in the direction opposite of the field and the results of the calculation revert back to single-$\mathbf{Q}$ commensurate zigzag phase with canted spins from our variational calculation. However, it should be noted that this high-field two-sublattice zigzag is only a metastable state. As shown in Fig. 4.7, the six-sublattice $\sqrt{3} \times \sqrt{3}$ order is the ground state in the field regime immediately below the saturation field.

4.6.2 Nematic order

In this section, we characterize the various zigzag phases using the nematic order parameter. The nematic phase of liquid crystals is marked by a preferred direction of the molecules. While ordered magnetic phases such as ferromagnetic or Néel order give rise to a nonzero nematic order parameter, an intriguing possibility is a phase which breaks the rotational symmetry while preserving the time-reversal symmetry. Such a spin nematic phase has been discussed in several quantum and frustrated magnetic systems. Here we are interested in the so-called uniaxial order parameter as a measure of the collinearity of spins. Specifically, we first compute the second-rank tensor order parameter:

$$Q_{\alpha\beta} = \frac{3}{2}\langle S^{\alpha}\, S^{\beta}\rangle - \frac{1}{2}\delta_{\alpha\beta}, \tag{4.22}$$

where S^{α} is the α component of spin. The uniaxial order parameter λ_Q is then given by the largest eigenvalue of a 3×3 matrix whose elements correspond to the above second-rank tensor. A full collinear spin configuration, e.g., a ferromagnetic or Néel order, is characterized by a maximum $\lambda_Q = 1$, while a completely disordered state has a vanishing uniaxial order parameter.

Fig. 4.8 shows the field dependence of the uniaxial order parameter λ_Q obtained from our Monte Carlo simulations for three different temperatures. As discussed in the main text, the low-temperature phase at small field is the collinear single-$\mathbf{Q}$ zigzag state. A rather large $\lambda_Q \approx 1$ in this regime is consistent with this conclusion. As H is increased, the transition into the triple-$\mathbf{Q}$ zigzag phase is marked by a pronounced drop of the uniaxial order parameter as demonstrated in Fig. 4.8. In fact, the second-rank tensor $Q_{\alpha\beta}$ vanishes identically in a perfect triple-$\mathbf{Q}$ zigzag state. As the field strength is further increased, the tilting of spins toward the [111] direction gradually increases the uniaxial parameter. Interestingly, λ_Q exhibits small jumps at the two C-IC transitions, i.e. from zigzag phase II to III and from III to IV. Since thermal fluctuations tend to favor collinear spin configurations, the observed jumps of λ_Q imply that the C-IC transitions might be partially driven by entropic selection. Finally, the transition from the zigzag phase IV to the $\sqrt{3}\times\sqrt{3}$ order at $H_c \sim 1.37$ is accompanied by a pronounced increase of the uniaxial order parameter.

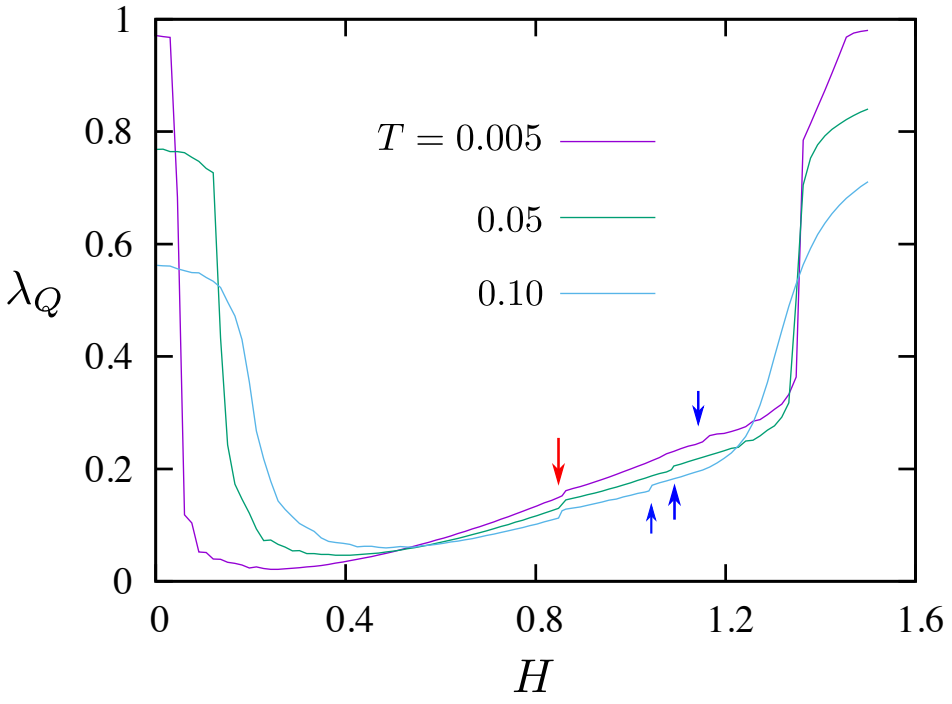

Figure 4.8: Field dependence of the uniaxial nematic order parameter λ_Q at various temperatures. The arrows indicate the small jumps of λ_Q at the commensurate-incommensurate phase transitions. T and H are measured in units of A.

Chapter 5

Calculation of gyromagnetic tensor and Curie-Weiss temperatures in anisotropic spin systems

5.1 Introduction

In this chapter I discuss how the anisotropic nature of the interactions is explicitly revealed in the anisotropy of the magnetic susceptibility, gyromagnetic factors and Curie-Weiss (CW) temperatures. Indeed, this has been observed in all 4d and 5d SOC assisted Mott insulators which we consider here. For instance, in α-$RuCl_3$ the ab-component of the susceptibility in the honeycomb plane is almost an order of magnitude larger than the component perpendicular to the plane [15]. In most of the compounds with bond-dependent interactions, all three components of susceptibility also show strong deviation from the CW behavior as a function of temperature [80]. This is in stark contrast with Heisenberg exchange systems where the low-temperature susceptibility reflects the g-factor anisotropy observed at high temperatures, even in the presence of spatially anisotropic exchange interactions.

The observed anisotropy of the magnetic susceptibilities and CW temperatures raises

an important question of how to extract the CW temperatures and the elements of anisotropic susceptibility tensor in real systems. This question is far from being trivial as it requires a more accurate analysis of the experimental data as now all these quantities should be described in a tensorial form. Though, it is not new and has been discussed in the literature, we believe it is worth providing a systematic description for a proper procedure.

In this context, we first focus on deriving a general procedure for calculating CW temperatures for generic bilinear anisotropic magnetic Hamiltonians with anisotropic gyromagnetic tensor. We then apply this method to find the effect these anisotropies have on the CW temperatures of $\alpha-RuCl_3$, Na_2IrO_3, $(\alpha,\beta,\gamma)-Li_2IrO_3$, and Sr_2IrO_4. We find that in all but the last material the anisotropy of the CW temperatures are caused by the symmetric off-diagonal interaction Γ as well as bond dependence of Kitaev and Γ interactions caused by structural distortions. While the role of Γ interaction in the generation of the CW anisotropy has been discussed before [71], not much is known about the effect of the bond dependent anisotropies. We note that experimental measurements of CW temperatures along all three principal axes allow to estimate the anisotropies independently. In Sr_2IrO_4 we also find that the two sublattices have different anisotropic gyromagnetic tensors due to staggered tetragonal distortions. The components of the gyromagnetic tensors enter the CW temperature expressions and as a result contribute to the anisotropy of the CW latter.

The chapter is organized as follows: In section 5.2 we give a general procedure for deriving the magnetic susceptibility of materials with anisotropic Hamiltonians. We also calculate the anisotropic gyromagnetic tensor for ions in octahedral local environment with tetragonal or trigonal distortions. In section 5.3 we focus on tri-coordinated with subsection 5.3.1 dedicated to layered 2D honeycomb materials and calculation of the CW temperatures for the most general models proposed for the compounds. We discuss the specific applicability of the model to $\alpha-RuCl_3$ and Na_2IrO_3. In subsection 5.3.2 we consider the nearest neighbor (n.n.) models on 3D honeycomb materials, $(\beta,\gamma)-Li_2IrO_3$. In section 5.4 we study the Sr_2IrO_4 CW temperatures. We give our conclusions and final remarks in section 5.5.

5.2 Magnetic susceptibility in anisotropic magnetic Hamiltonian

5.2.1 General formalism

A general anisotropic magnetic Hamiltonian in the applied magnetic field term has the following form:

$$\mathcal{H} = \sum_{\langle i,j\rangle,\alpha,\beta} \mathcal{S}_i^\alpha \mathcal{J}_{ij}^{\alpha\beta} \mathcal{S}_j^\beta - \sum_{\alpha,\beta,i} \mathcal{S}_i^\alpha g_i^{\alpha\beta} B^\beta, \tag{5.1}$$

where $\mathcal{J}_{ij}^{\alpha\beta}$ is the interaction matrix, $g_i^{\alpha\beta}$ is the gyromagnetic tensor. In the mean field (MF) approach, this lattice Hamiltonian is replaced by the energy of a non-interacting system of pseudospins:

$$\mathcal{H}_{MF} = -\sum_{i,\alpha} \mathcal{S}_i^\alpha h_i^\alpha = -N_{uc} \sum_{\mu,\alpha} \mathcal{S}_\mu^\alpha h_\mu^\alpha, \tag{5.2}$$

where in the last equality μ is the sublattice index, and N_{uc} is the number of unit cells in the sample. The local field is defined as

$$h_\mu^\alpha = -\sum_\beta \left(\sum_j J_{\mu j}^{\alpha\beta} \langle \mathcal{S}_j^\beta \rangle - g_\mu^{\alpha\beta} B^\beta \right). \tag{5.3}$$

Its magnitude and direction, h_0 and $\vec{e}_\mu$, are respectively given by

$$h_\mu = \sqrt{\sum_\alpha \left(h_\mu^\alpha\right)^2}, \quad e_\mu^\alpha = \frac{h_\mu^\alpha}{h_\mu} = \frac{h_\mu^\alpha}{\sqrt{\sum_\alpha \left(h_\mu^\alpha\right)^2}}. \tag{5.4}$$

In the MF approximation, we can easily write down the partition function for a single pseudospin as

$$Z = \mathrm{Tr} e^{\beta \sum_\alpha \mathcal{S}_\mu^\alpha h_\mu^\alpha} = \mathrm{Tr} e^{\beta \vec{\mathcal{S}}_\mu^{e_\mu} \vec{h}_\mu}, \tag{5.5}$$

where $\vec{\mathcal{S}}_\mu^{e_\mu}$ is a spin operator, representing the spin on sublattice μ, measured along the direction of $\vec{h_\mu}$. Naturally, there are two more spin operators orthogonal to $\mathcal{S}_\mu^{e_\mu}$ that we can define, however their expectation values are zero since they are directed perpendicular to the magnetic field. Thus we can find the expectation value of $\mathcal{S}_\mu^{e_\mu}$:

$$\langle \mathcal{S}_\mu^\alpha \rangle \quad = e_\mu^\alpha \langle \mathcal{S}_\mu^{e_\mu} \rangle = e_\mu^\alpha \frac{\mathrm{Tr} \mathcal{S}_\mu^{e_\mu} e^{\beta \mathcal{S}_\mu^{e_\mu} h_\mu}}{\mathrm{Tr} e^{\beta \mathcal{S}_\mu^{e_\mu} h_\mu}} = \tfrac{1}{2} e_\mu^\alpha \tanh(\tfrac{\beta h_\mu}{2}) \approx \tfrac{\beta}{4} h_\mu^\alpha = \textstyle\sum_\beta \chi_0^{\alpha\beta} h_\mu^\beta \tag{5.6}$$

where we use $\beta \ll 1$ to approximate the hyperbolic tangent and $\chi_0^{\alpha\beta} = \frac{\beta}{4}\delta^{\alpha\beta}$. The result was derived for $\mathcal{S} = 1/2$, but can be generalized to any $\mathcal{S}$ leading to $\chi_0^{\alpha\beta} = \frac{\beta}{3}\mathcal{S}(\mathcal{S}+1)\delta^{\alpha\beta}$ as the bare spin susceptibility. Explicitly, we have

$$\langle \mathcal{S}_\mu^\alpha \rangle \;\; = \sum_\beta \chi_0^{\alpha\beta} h_\mu^\beta = -\sum_\beta \chi_0^{\alpha\beta} \sum_\gamma \left(\sum_j J_{\mu j}^{\beta\gamma} \langle \mathcal{S}_j^\gamma \rangle - g_\mu^{\beta\gamma} B^\gamma \right). \tag{5.7}$$

Collecting terms with spin expectation values on the left side, this equation can be rewritten in matrix form as

$$\hat{\Lambda} \langle \vec{\mathcal{S}} \rangle = \hat{\mathcal{G}} \vec{B}, \tag{5.8}$$

where the $\hat{\Lambda}$ and $\hat{\mathcal{G}}$ are block-diagonal matrices (each block corresponding to a sublattice μ) with elements equal to:

$$\Lambda^{\alpha\gamma} = \delta^{\alpha\gamma} + \sum_{\beta,j} \chi_0^{\alpha\beta} J_{\mu j}^{\beta\gamma} = \delta^{\alpha\gamma} + \frac{\beta}{3}\mathcal{S}(\mathcal{S}+1) \sum_j J_{\mu j}^{\alpha\gamma}, \tag{5.9}$$

and

$$\mathcal{G}^{\alpha\gamma} = \sum_\beta \chi_0^{\alpha\beta} g_\mu^{\beta\gamma} = \frac{\beta}{3}\mathcal{S}(\mathcal{S}+1) g_\mu^{\alpha\gamma}. \tag{5.10}$$

By inverting the $\hat{\Lambda}$ matrix, we get an expression for the full pseudospin susceptibility with respect to applied field:

$$\langle \vec{\mathcal{S}} \rangle = \hat{\Lambda}^{-1} \hat{\mathcal{G}} \vec{B} = \hat{\chi}_s \vec{B}, \tag{5.11}$$

where $\hat{\chi}_s = \hat{\Lambda}^{-1}\hat{\mathcal{G}}$. However, in experiments a magnetic susceptibility is measured instead. To find it, the spin susceptibility should be multiplied by the gyromagnetic factor:

$$\vec{m} = \hat{g} \langle \vec{\mathcal{S}} \rangle = \hat{g} \hat{\Lambda}^{-1} \hat{\mathcal{G}} \vec{B} = \hat{\chi} \vec{B}, \tag{5.12}$$

where

$$\hat{\chi} = \hat{g} \hat{\Lambda}^{-1} \hat{\mathcal{G}} \tag{5.13}$$

is the matrix that gives the magnetic response of individual sites in the unit cell.

Note that $\hat{g}$, $\hat{\Lambda}$, $\hat{\mathcal{G}}$, and $\hat{\chi}$ are $3N$ by $3N$ matrices, where N is the total number of sites μ in one unit cell. Inverting such large matrices analytically is computationally prohibitive. At high temperatures $\hat{\Lambda}^{-1}$ can be approximated in Eq. (5.9):

$$(\hat{\Lambda}^{-1})^{\alpha\gamma} \approx \delta^{\alpha\gamma} - \frac{\beta}{3}\mathcal{S}(\mathcal{S}+1) \sum_j J_{\mu j}^{\alpha\gamma}, \tag{5.14}$$

This greatly simplifies the calculation for systems with large unit cells and thus large matrices. The calculation of $\hat{\chi}$ according to Eq. (5.13) from here is a simple multiplication of matrices. We now calculate the susceptibility of the material as a whole by summing up the responses of the individual sites in the unit cell:

$$\hat{\chi}_m^{\alpha\beta} = \frac{1}{N}\sum_{\mu=1}^{N}\sum_{\nu=1}^{N}\hat{\chi}_{\mu,\nu}^{\alpha\beta} \tag{5.15}$$

where μ and ν label sites in the unit cell.The 3 by 3 matrix $\hat{\chi}_m$ is now the magnetic response of the whole material per unit atom (which gives that extra factor of $1/N$). Diagonalization and high temperature expansion of this matrix is the next step of the calculation. Comparison to the CW law in the form $\hat{\chi}_m = \frac{C}{T-\hat{\Theta}}$, where C is a Curie constant, and Θ is a Curie-Weiss constant, yields the expressions for the anisotropic Curie temperatures.

5.2.2 Ground state Kramers doublet in the tetragonally or trigonally distorted systems.

It is more convenient to describe the low-spin state of the d^5-configuration of Ir^{4+}, Rh^{4+} or Ru^{3+} ions by using the hole description. Then the ground state electronic structure of these ions is described by a Kramers doublet which is a combination of spin and orbital wave functions. If the local symmetry is cubic, i.e. in the absence of the trigonal or tetragonal distortions, the ground state doublet is simply a $\vec{\mathbf{J}} = \vec{l}_{eff} + \vec{s} = 1/2$ and the good choice of the states within it are the $\mathbf{J}^z = \pm 1/2$ states. Henceforth, we represent $\mathbf{J}$ by $\mathcal{S}$ and denote $\vec{l}_{eff} \equiv \vec{L}$. As the orbital composition of the $\mathbf{J}^z = \pm 1/2$ states has been discussed in chapters 2 and 3 I refer the reader there.

Note also that the eigenstates of the spin operators S_z and $S_{\mathbf{e}_3}$ are related to each other by

$$S_{\mathbf{e}_3} = \hat{\mathbf{e}}_3 \cdot \sigma = \begin{pmatrix} \frac{1}{2\sqrt{3}} & \frac{1-i}{2\sqrt{3}} \\ \frac{1+i}{2\sqrt{3}} & -\frac{1}{2\sqrt{3}} \end{pmatrix} \tag{5.16}$$

Diagonalization of this matrix gives the eigenstates of $S_{\mathbf{e}_3}$ in the basis of eigenstates of S_z.

In the presence of either tetragonal or trigonal distortion, the Kramers doublet states

can be now written in a common form as [1]

$$|\Psi_1\rangle = c_\theta|+1,\downarrow\rangle - s_\theta|0,\uparrow\rangle$$
$$|\Psi_2\rangle = -c_\theta|+1,\downarrow\rangle + s_\theta|0,\uparrow\rangle, \tag{5.17}$$

where $c_\theta \equiv \cos\theta$ and $s_\theta \equiv \sin\theta$. For the case of tetragonal distortions the states on the right are in the form $|L_z, S_z\rangle$ and for the case of trigonal distortions they are $|L_{\mathbf{e}_3}, S_{\mathbf{e}_3}\rangle$. Also, the angle

$$\theta = \frac{1}{2}\arctan\frac{2\sqrt{2}\lambda}{\lambda - 2\Delta}$$

gives the relative strength of the spin orbit coupling λ and tetragonal/trigonal splitting Δ. The choice of the overall phase of the Ψ_1 and Ψ_2 states corresponds to the choice of the $\hat{\mathbf{e}}_1$ and $\hat{\mathbf{e}}_2$ axes. In the case of no distortions the coefficients reduce to the Clebsch-Gordan coefficients. Here we note that the monoclinic distortion cannot lift the degeneracy of the ground state doublet. However, it can complicate the structure and analysis of the ground state wave-functions, so here we will not consider the monoclinic distortion for the purpose of calculating the gyromagnetic tensor.

Using Eq. (5.17), we can compute the matrix elements of $J_{\mathbf{e}_n}$ operators in the basis of the Ψ_1 and Ψ_2 states:

$$\begin{aligned}
&\langle\Psi_1|J_{\vec{e}_1}|\Psi_1\rangle = 0,\\
&\langle\Psi_1|J_{\mathbf{e}_1}|\Psi_2\rangle = \sqrt{2}\,c_\theta s_\theta - s_\theta^2/2,\\
&\langle\Psi_2|J_{\mathbf{e}_1}|\Psi_1\rangle = \sqrt{2}\,c_\theta s_\theta - s_\theta^2/2,\\
&\langle\Psi_2|J_{\mathbf{e}_1}|\Psi_2\rangle = 0,\\
&\langle\Psi_1|J_{\mathbf{e}_2}|\Psi_1\rangle = 0,\\
&\langle\Psi_1|J_{\mathbf{e}_2}|\Psi_2\rangle = -i\left(\sqrt{2}\,c_\theta s_\theta - s_\theta^2/2\right),\\
&\langle\Psi_2|J_{\mathbf{e}_2}|\Psi_1\rangle = i\left(\sqrt{2}\,c_\theta s_\theta - s_\theta^2/2\right),\\
&\langle\Psi_2|J_{\mathbf{e}_2}|\Psi_2\rangle = 0,\\
&\langle\Psi_1|J_{\mathbf{e}_3}|\Psi_1\rangle = 1/2,\\
&\langle\Psi_1|J_{\mathbf{e}_3}|\Psi_2\rangle = 0,\\
&\langle\Psi_2|J_{\mathbf{e}_3}|\Psi_1\rangle = 0,\\
&\langle\Psi_2|J_{\vec{e}_3}|\Psi_2\rangle = -1/2.
\end{aligned} \tag{5.18}$$

While the matrix elements of $J_{\mathbf{e}_3}$ are good quantum numbers even in the presence of trigonal distortions, the eigenvalues of $J_{\mathbf{e}_1}$ and $J_{\mathbf{e}_2}$ are no longer good quantum numbers

when the octahedra are distorted along the [111] axis. Note that the matrix elements of $J_{\mathbf{e}_1}$ are purely real and those of $J_{\mathbf{e}_2}$ are purely imaginary with the correct signs, so we made the correct choice of the phase/axes combination. When there is no distortion (Δ is set to zero) we recover the expected $\pm 1/2$ and $\pm i/2$ for $J_{\mathbf{e}_1}$ and $J_{\mathbf{e}_2}$ respectively.

5.2.3 The gyromagnetic tensor for pseudospins-1/2 in the tetragonally or trigonally distorted systems.

We derive the gyromagnetic tensor by equating the phenomenological Hamiltonian describing the coupling of magnetic field to the pseudospin-1/2 states, described by the Ψ_1 and Ψ_2 states, with the spin Hamiltonian describing the coupling of magnetic field to the spin and orbital angular momenta with the gyromagnetic factor of 2 and 1, respectively:

$$\mu_B \mathbf{B} \cdot (-\mathbf{L} + 2\mathbf{S}) = \sum_{\alpha\beta=x,y,z} B^{\alpha} g^{\alpha\beta} \mu_B \frac{1}{2} \sigma^{\beta} \tag{5.19}$$

where $\boldsymbol{\sigma}$ denoting the Pauli matrices representing the ground state Kramers doublet. The orbital contribution on the left hand side has an extra negative sign originating from the $l_{\text{eff}} = 1$ representation of the t_{2g} orbitals. The gyromagnetic tensor $g^{\alpha\beta}$ can now be found by calculating the matrix elements of both sides in the basis of Ψ_1 and Ψ_2 states defined in Eq.(5.17). We find that the gyromagnetic tensor is given by

$$\hat{g} = \begin{pmatrix} -2(\sqrt{2}\, c_\theta + s_\theta) s_\theta & 0 & 0 \\ 0 & -2(\sqrt{2}\, c_\theta + s_\theta) s_\theta & 0 \\ 0 & 0 & -1 - 3\, c_{2\theta} \end{pmatrix}, \tag{5.20}$$

where the principal axes for the tetragonal systems are the cubic directions $\hat{\mathbf{x}}$, $\hat{\mathbf{y}}$, and $\hat{\mathbf{z}}$ and for the trigonal systems are the $\hat{\mathbf{e}}_1$, $\hat{\mathbf{e}}_2$, and $\hat{\mathbf{e}}_3$. As expected, when distortion is set to zero, the gyromagnetic tensor is isotropic and its diagonal matrix elements are equal to -2.

For the case of the trigonal distortion, it is useful to rewrite the gyromagnetic factor

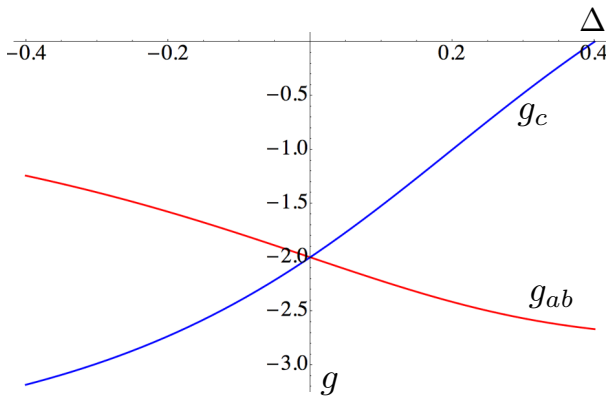

Figure 5.1: Dependence of the gyromagnetic factor on tetragonal (trigonal) distortion computed for $\lambda = 0.4$ meV.

in the cubic basis as well. For this purpose we use the rotation matrix:

$$R = \begin{pmatrix} \frac{1}{\sqrt{6}} & -\frac{1}{\sqrt{2}} & \frac{1}{\sqrt{3}} \\ \frac{1}{\sqrt{6}} & \frac{1}{\sqrt{2}} & \frac{1}{\sqrt{3}} \\ -\frac{2}{\sqrt{6}} & 0 & \frac{1}{\sqrt{3}} \end{pmatrix} \tag{5.21}$$

Then the gyromagnetic tensor in the cubic basis has the following form:

$$\hat{g}_{\text{cub}} = \hat{R}\hat{g}\hat{R}^T = \frac{1}{3}\begin{pmatrix} g_c + 2g_{ab} & g_c - g_{ab} & g_c - g_{ab} \\ g_c - g_{ab} & g_c + 2g_{ab} & g_c - g_{ab} \\ g_c - g_{ab} & g_c - g_{ab} & g_c + 2g_{ab} \end{pmatrix}, \tag{5.22}$$

where we denote $g_{ab} = -2(\sqrt{2}\, c_\theta + s_\theta)s_\theta$ and $g_c = -(1 + 3\, c_{2\theta})$.

We plot the dependence of the gyromagnetic factor on the distortion strength in Fig. 5.1. When there are no distortions the gyromagnetic factor is uniform and is equal to -2. As the distortion strength is increased the gyromagnetic factor along the distortion symmetry axis separates from the other two components.

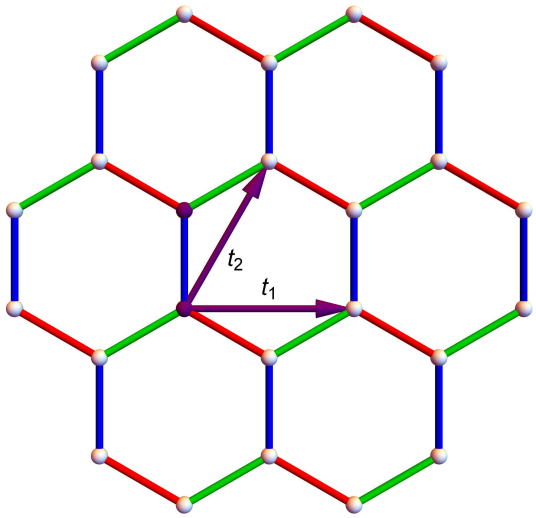

Figure 5.2: The 2D honeycomb lattice. The red, green and blue bonds label the n.n. Kitaev x, y, and z bonds, respectively.

5.3 Application I: Susceptibility and Curie temperature of the tri-coordinated Kitaev materials.

5.3.1 Layered honeycomb A_2IrO_3 materials.

Here we consider a general model relevant to layered honeycomb materials and in further subsections we will apply it to specific materials. The 2D honeycomb lattice can be seen in Fig. 5.2. We include Heisenberg isotropic interactions up to third neighbors, Kitaev interactions up to the second neighbor and Γ interaction on n.n. The Kitaev nearest neighbor bonds are colored red, green, and blue for x, y, and z Kitaev labels, respectively. The next nearest neighbor (n.n.n.) Kitaev label is the label missing from the two n.n. bonds connecting the sites. Namely, two next nearest neighbors connected by an x and a y nearest neighbor bonds are connected by a $\tilde{z}$ next nearest neighbor bond. Note that several of the materials of interest have a monoclinic distortion, reducing the crystal's symmetry from C_3 to C_2. In order to include the effects of the monoclinic distortion, we allow the interactions on the n.n. bonds parallel to the C_2 symmetry axis be different from those on the other two kinds of the n.n. bonds, and, similarly, the interactions on the n.n.n. bonds perpendicular to the C_2 symmetry axis be different from the other two

kinds of the n.n.n. bonds. For concreteness, we assume that the n.n. bond along the C_2 symmetry axis is the z bond, and we denote the interactions along this bond as $\bar{K}_1$ and $\bar{\Gamma}_1$. Consequently we denote the interactions on the n.n.n. z bond as $\bar{K}_2$. Note, that for our purposes here any bond anisotropy in the Heisenberg interactions is not relevant, because the Heisenberg interactions always enter the calculations as a sum over all bonds, and thus a system with bond-anisotropic Heisenberg interactions will yield the same result as the system with isotropic Heisenberg interactions equal to bond average of the anisotropic case. Thus we are considering the J_1^α-K_1-$\bar{K}_1$-Γ_1-$\bar{\Gamma}_1$-J_2^α-K_2-$\bar{K}_2$-J_3^α model:

$$\begin{aligned}
\mathcal{H} = \quad & \sum_{\langle i,j\rangle_\alpha} J_1^\alpha \boldsymbol{\mathcal{S}}_i \boldsymbol{\mathcal{S}}_j + \sum_{\langle\langle i,j\rangle\rangle_\alpha} J_2^\alpha \boldsymbol{\mathcal{S}}_i \boldsymbol{\mathcal{S}}_j + \sum_{\langle\langle\langle i,j\rangle\rangle\rangle_\alpha} J_3^\alpha \boldsymbol{\mathcal{S}}_i \boldsymbol{\mathcal{S}}_j \\
+ \quad & \sum_{\langle i,j\rangle_{\gamma=x,y}} K_1 \mathcal{S}_i^\gamma \mathcal{S}_j^\gamma + \Gamma_1(\mathcal{S}_i^\alpha \mathcal{S}_j^\beta + \mathcal{S}_i^\beta \mathcal{S}_j^\alpha) \\
+ \quad & \sum_{\langle i,j\rangle_z} \bar{K}_1 \mathcal{S}_i^z \mathcal{S}_j^z + \bar{\Gamma}_1(\mathcal{S}_i^x \mathcal{S}_j^y + \mathcal{S}_i^y \mathcal{S}_j^x) \\
+ \quad & \sum_{\langle\langle i,j\rangle\rangle_{\tilde{\gamma}}} K_2 \mathcal{S}_i^{\tilde{\gamma}} \mathcal{S}_j^{\tilde{\gamma}} + \sum_{\langle\langle i,j\rangle\rangle_{\tilde{z}}} \bar{K}_2 \mathcal{S}_i^{\tilde{z}} \mathcal{S}_j^{\tilde{z}}.
\end{aligned} \tag{5.23}$$

where the $\alpha = 1, 2, 3$ labels any generic bond anisotropy of the Heisenberg interaction For the monoclinic distortions it distinguishes one bond type ($\alpha = 3$) and the other two bond types ($\alpha = 1, 2$). As was noted above for the purposes of the CW calculations the Heisenberg interaction always enters the calculation as bond average. Thus in the following the Heisenberg interactions on different bonds will be united into:

$$J_1^{\text{av}} = \tfrac{1}{3}\textstyle\sum_\alpha J_1^\alpha \tag{5.24}$$

$$J_2^{\text{av}} = \tfrac{1}{3}\textstyle\sum_\alpha J_2^\alpha \tag{5.25}$$

$$J_3^{\text{av}} = \tfrac{1}{3}\textstyle\sum_\alpha J_3^\alpha \tag{5.26}$$

In this case, the Λ matrix of Eq. (5.9) in the Cartesian coordinates reads

$$\Lambda = \begin{pmatrix} \Lambda_1 & \Lambda_2' & \Lambda_1' \\ \Lambda_2' & \Lambda_1 & \Lambda_1' \\ \Lambda_1' & \Lambda_1' & \Lambda_2 \end{pmatrix} \tag{5.27}$$

where

$$\Lambda_1 = 1 + \tfrac{\beta}{3}\mathcal{S}(\mathcal{S}+1)(3J_1^{\rm av} + 6J_2^{\rm av} + 3J_3^{\rm av} + K_1 + 2K_2)$$
$$\Lambda_2 = 1 + \tfrac{\beta}{3}\mathcal{S}(\mathcal{S}+1)(3J_1^{\rm av} + 6J_2^{\rm av} + 3J_3^{\rm av} + \bar{K}_1 + 2\bar{K}_2)$$
$$\Lambda_1' = \tfrac{\beta}{3}\mathcal{S}(\mathcal{S}+1)\Gamma_1$$
$$\Lambda_2' = \tfrac{\beta}{3}\mathcal{S}(\mathcal{S}+1)\bar{\Gamma}_1$$

The $\hat{\mathcal{G}}$ matrix of Eq. (5.10) is simplest in the $\hat{\mathbf{e}}_1$, $\hat{\mathbf{e}}_2$, $\hat{\mathbf{e}}_3$ basis, in which the gyromagnetic tensor has the diagonal form of Eq. (5.20). We thus rotate the $\hat{\Lambda}$ matrix into this basis as well. The resulting $\tilde{\Lambda}$ matrix is not diagonal as the $\hat{\mathbf{e}}_1$ and $\hat{\mathbf{e}}_3$ components remain mixed:

$$\tilde{\Lambda} = \begin{pmatrix} \tilde{\Lambda}_{1,1} & 0 & \tilde{\Lambda}_{1,3} \\ 0 & \tilde{\Lambda}_{2,2} & 0 \\ \tilde{\Lambda}_{3,1} & 0 & \tilde{\Lambda}_{3,3} \end{pmatrix} \tag{5.28}$$

where

$$\begin{aligned}
\tilde{\Lambda}_{1,1} &= 1 + \frac{\beta}{3}\mathcal{S}(\mathcal{S}+1)\Big(3J_1^{\rm av} + 6J_2^{\rm av} + 3J_3^{\rm av} + \\
&\quad \frac{1}{3}(K_1 + 2(\bar{K}_1 + K_2 + 2\bar{K}_2 - 2\Gamma_1) + \bar{\Gamma}_1)\Big), \\
\tilde{\Lambda}_{2,2} &= 1 + \frac{\beta}{3}\mathcal{S}(\mathcal{S}+1)\Big(3J_1^{\rm av} + 6J_2^{\rm av} + 3J_3^{\rm av} + K_1 + 2K_2 - \bar{\Gamma}_1\Big), \\
\tilde{\Lambda}_{3,3} &= 1 + \frac{\beta}{3}\mathcal{S}(\mathcal{S}+1)\Big(3J_1^{\rm av} + 6J_2^{\rm av} + 3J_3^{\rm av} + \\
&\quad \frac{1}{3}(2K_1 + \bar{K}_1 + 2(2K_2 + \bar{K}_2 + 2\Gamma_1 + \bar{\Gamma}_1))\Big), \\
\tilde{\Lambda}_{1,3} = \tilde{\Lambda}_{3,1} &= \frac{\sqrt{2}\beta}{3}\mathcal{S}(\mathcal{S}+1)\Big(K_1 - \bar{K}_1 + 2K_2 - 2\bar{K}_2 - \Gamma_1 + \bar{\Gamma}_1\Big)
\end{aligned} \tag{5.29}$$

Consequently, the tensor of magnetic susceptibility, χ_m, is also not diagonal in the $\hat{\mathbf{e}}_1$, $\hat{\mathbf{e}}_2$, $\hat{\mathbf{e}}_3$ basis.

Diagonalization of χ_m gives the susceptibility along the three principle axes, from which we also calculate the CW temperatures. To simplify the calculations we use the high temperature approximation and expand all the expressions in β up to the second order. At this order, the $\hat{\mathbf{e}}_1$, $\hat{\mathbf{e}}_2$ and $\hat{\mathbf{e}}_3$ are the principal axes, and the three CW

temperatures are:

$$\Theta_{\hat{\mathbf{e}}_1} = -\frac{1}{3}\mathcal{S}(\mathcal{S}+1)\Big(3J_1^{\rm av}+6J_2^{\rm av}+3J_3^{\rm av}+\frac{1}{3}(K_1+2\bar{K}_1+2K_2+4\bar{K}_2-4\Gamma_1+\bar{\Gamma}_1)\Big)$$
$$\Theta_{\hat{\mathbf{e}}_2} = -\frac{1}{3}\mathcal{S}(\mathcal{S}+1)\big(3J_1^{\rm av}+6J_2^{\rm av}+3J_3^{\rm av}+K_1+2K_2-\bar{\Gamma}_1\Big)$$
$$\Theta_{\hat{\mathbf{e}}_3} = -\frac{1}{3}\mathcal{S}(\mathcal{S}+1)\Big(3J_1^{\rm av}+6J_2^{\rm av}+3J_3^{\rm av}+\frac{1}{3}(2K_1+\bar{K}_1+4K_2+2\bar{K}_2+4\Gamma_1+2\bar{\Gamma}_1)\Big)$$

The differences between these temperatures are:

$$\Theta_{\hat{\mathbf{e}}_1}-\Theta_{\hat{\mathbf{e}}_2} = -\frac{1}{9}\mathcal{S}(\mathcal{S}+1)\Big(2(\bar{K}_1-K_1)+4(\bar{K}_2-K_2)-4(\bar{\Gamma}_1-\Gamma_1)\Big) \tag{5.30}$$
$$\Theta_{\hat{\mathbf{e}}_2}-\Theta_{\hat{\mathbf{e}}_3} = -\frac{1}{9}\mathcal{S}(\mathcal{S}+1)\big((K_1-\bar{K}_1)+2(K_2-\bar{K}_2)-5\bar{\Gamma}_1-4\Gamma_1\Big) \tag{5.31}$$
$$= -\frac{1}{9}\mathcal{S}(\mathcal{S}+1)\big((K_1-\bar{K}_1)+2(K_2-\bar{K}_2)+5(\Gamma_1-\bar{\Gamma}_1)-9\Gamma_1\Big)$$
$$\Theta_{\hat{\mathbf{e}}_3}-\Theta_{\hat{\mathbf{e}}_1} = -\frac{1}{9}\mathcal{S}(\mathcal{S}+1)\Big((K_1-\bar{K}_1)+2(K_2-\bar{K}_2)+8\Gamma_1+\bar{\Gamma}_1\Big) \tag{5.32}$$
$$= -\frac{1}{9}\mathcal{S}(\mathcal{S}+1)\Big((K_1-\bar{K}_1)+2(K_2-\bar{K}_2)+(\bar{\Gamma}_1-\Gamma_1)+9\Gamma_1\Big)$$

From these expressions we see that in these models the anisotropy of CW temperature comes from two sources. First is the Γ_1 interaction that separates the $\Theta_{\hat{\mathbf{e}}_3}$ from $\Theta_{\hat{\mathbf{e}}_1}$ and $\Theta_{\hat{\mathbf{e}}_2}$. The second source is the monoclinic distortion which further separates $\Theta_{\hat{\mathbf{e}}_3}$, as well as splits $\Theta_{\hat{\mathbf{e}}_1}$ and $\Theta_{\hat{\mathbf{e}}_2}$.

The J_1^α-K_1-$\bar{K}_1$-Γ_1-$\bar{\Gamma}_1$-J_2^α-K_2-$\bar{K}_2$-J_3^α model is much more general and complex than necessary to describe any given layered honeycomb compound. However, by setting some of the interactions to zero we can easily specialize this model to different materials, which is what we do in the following subsections.

α-$\mathbf{RuCl_3}$

We now consider the physics of $\alpha-\mathrm{RuCl_3}$. The microscopic calculations for $\alpha-\mathrm{RuCl_3}$ showed that the super-exchange for this compound is dominated by the n.n. interactions and emphasized the importance of the off-diagonal n.n. Γ_1 interactions [11, 81, 82]. In the parameter range relevant to $\alpha-\mathrm{RuCl_3}$, all these studies agree that the n.n. Kitaev interaction, K_1, is ferromagnetic, and the off-diagonal exchange Γ_1 is antiferromagnetic, both of which are significantly larger than the Heisenberg interaction $J_1^{\rm av}$. We first

consider the case of C_3. Neglecting the monoclinic distortions for the moment allows us to give an estimate of Γ_1 from the anisotropy of the CW temperatures. To specialize the general equations of the previous section to this model with C_3 symmetry we set $J_1^{\rm av} = J_2^{\rm av} = K_2 = \bar{K}_2 = 0$, $K_1 = \bar{K}_1$, and $\Gamma_1 = \bar{\Gamma}_1$. Using the experimental values $\Theta_{ab} = 37$ K and $\Theta_c = -150$ K from Sears et al [15], we can calculate $\Gamma_1 \approx 21.5$ meV which is larger than the values *ab initio* calculations give ($\Gamma_1 \approx 8.0$ meV) [11]. This suggests that monoclinic distortions, do indeed play a significant role in this compound, accounting for at least some portion of the anisotropy of the CW temperatures.

Assuming the C2/m structure we now allow $K_1 \neq \bar{K}_1$ and $\Gamma_1 \neq \bar{\Gamma}_1$. As we are unaware of any experimental work that measures anisotropy between $\Theta_{\hat{\mathbf{e}}_1}$ and $\Theta_{\hat{\mathbf{e}}_2}$ for the compound, we are unable to separate out the monoclinic and Γ_1 contributions to the anisotropy. Instead we calculate the CW temperatures for the *ab initio* values of $K_1 = -7.5$ meV, $\bar{K}_1 = -5.0$ meV, $\Gamma_1 = 5.9$ meV, $\bar{\Gamma}_1 = 8.0$ meV, $J_3^{\rm av} = 2.8$ meV for comparison with future experiments: $\Theta_{\hat{\mathbf{e}}_1} = 7.6$ K, $\Theta_{\hat{\mathbf{e}}_2} = 20.6$ K, and $\Theta_{\hat{\mathbf{e}}_3} = -43.3$ K.

Na_2IrO_3

Here we consider the most general model J_1-K_1-Γ_1-J_2-K_2-J_3 model relevant for Na_2IrO_3 [10]: For realistic sets of the parameters describing Na_2IrO_3, one gets the following signs of the interactions: $J_1 > 0$, $K_1 < 0$, $\Gamma_1 > 0$, $J_2 < 0$, $K_2 > 0$, and $J_3 > 0$, and confirms that n.n. Kitaev interaction is the dominant one [10, 61, 11].

Substituting the values of interactions from Winter [11], we get $\Theta_{\hat{\mathbf{e}}_1} = 0.68$ K, $\Theta_{\hat{\mathbf{e}}_2} = -9.57$ K, $\Theta_{\hat{\mathbf{e}}_3} = -16.34$ K.

5.3.2 3D honeycomb materials

Here we study the susceptibility and CW temperature for β-Li_2IrO_3 and γ-Li_2IrO_3 compounds. Their bipartite orthorhombic tri-coordinated 3D lattice structures are shown in Fig. 5.3. The magnetic unit cell has four sites in $\beta-Li_2IrO_3$ (see Fig. 5.3(a)) and eight in γ-Li_2IrO_3 (see Fig. 5.3(b)). From the ab-initio calculations, the super-exchange interactions between magnetic moments on the Ir ions are expected to be dominated by n.n. interactions. Again, as in the case of α-$RuCl_3$, the off-diagonal exchange Γ_1 is expected to be important. We will focus on J_1-K_1-Γ_1-like models. Both compounds have several structurally different types of bonds. To keep with the spirit of generality

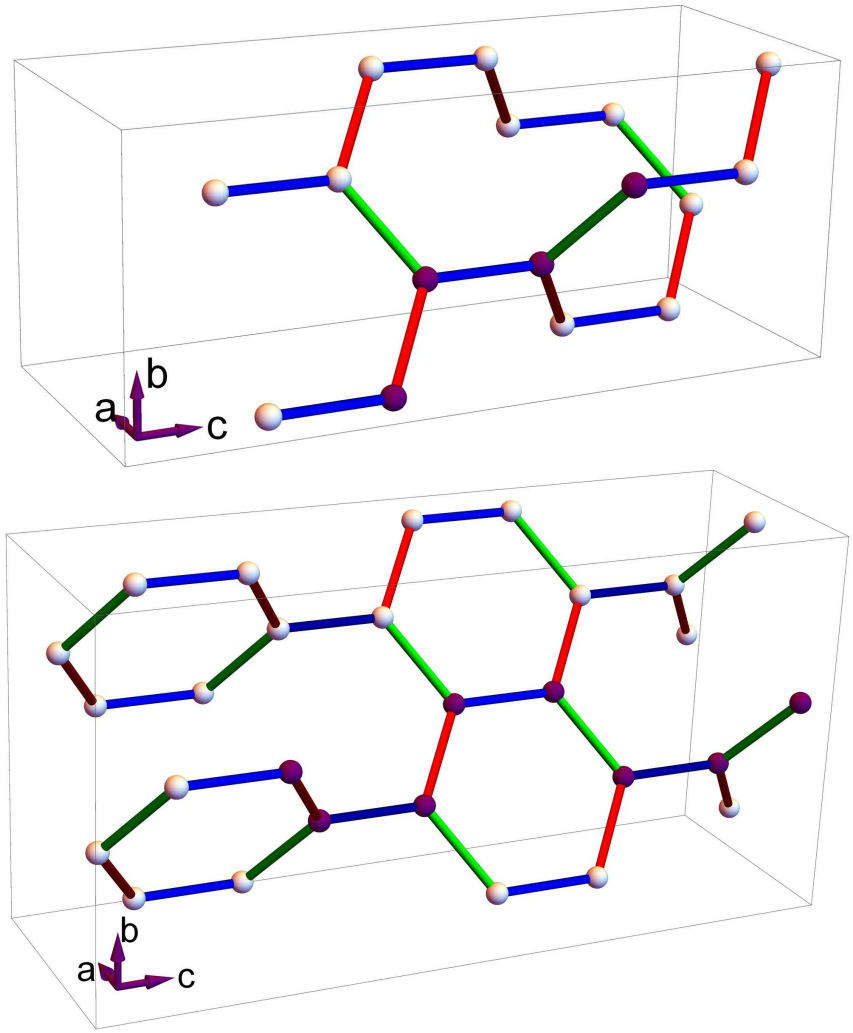

Figure 5.3: The structure of (a) β-Li_2IrO_3 and (b) γ-Li_2IrO_3. The bonds are color coded according to their Kitaev label: red, green and blue correspond to x, y and z bonds, respectively.

we will have different coupling constants for these bonds. Note that just as in the 2D materials the Heisenberg interaction enters the calculation only as a bond average, J_1^{av}.

The spin superexchange Hamiltonian for each lattice is expected to preserve the lattice symmetry, which, due to SOC, simultaneously acts on the spin and lattice basis vectors. The C_2 rotation symmetry present on both lattice structures interchanges x and y bonds, and thus the interactions on these bonds should be the same (up to the sign). The sign of Γ_1 interaction is bond dependent due to the crystal symmetry as was shown by Lee and Kim [83]. This bond dependence of sign plays an important role causing the Γ_1 contribution from x and y bonds to cancel out and completely disappear from the results of the calculation.

Since the exact local structure of the oxygen octahedra is not yet fully experimentally specified we use a uniform gyromagnetic factor g for both compounds. As a result we get a uniform Curie constant of $C = \frac{1}{3}g^2\mathcal{S}(\mathcal{S}+1)$.

Hyperhoneycomb β-Li_2IrO_3

In β-Li_2IrO_3 shown in Fig. 5.3(a) the Kitaev z-bonds (blue) are structurally different from x and y. Thus, we give the z-bonds different exchange parameters, namely $\bar{K}_1$ and $\bar{\Gamma}_1$, whereas x- and y- bonds will have K_1 and Γ_1.

Within this model the principal axes of the magnetic susceptibility tensor $\hat{\chi}_m$ in the $(\hat{\mathbf{x}}, \hat{\mathbf{y}}, \hat{\mathbf{z}})$ basis are $\hat{1} = (0,0,1)$, $\hat{2} = \frac{1}{\sqrt{2}}(1,1,0)$, and $\hat{3} = \frac{1}{\sqrt{2}}(-1,1,0)$. The CW temperatures along these axes are then:

$$\Theta_{\hat{1}} = -\tfrac{1}{3}S(S+1)(3J_1^{\text{av}} + \bar{K}_1) \tag{5.33}$$

$$\Theta_{\hat{2}} = -\tfrac{1}{3}S(S+1)(3J_1^{\text{av}} + K_1 + \bar{\Gamma}_1) \tag{5.34}$$

$$\Theta_{\hat{3}} = -\tfrac{1}{3}S(S+1)(3J_1^{\text{av}} + K_1 - \bar{\Gamma}_1) \tag{5.35}$$

And all the combinations of their differences are:

$$\Theta_{\hat{1}} - \Theta_{\hat{2}} = -\tfrac{1}{3}S(S+1)(\bar{K}_1 - K_1 - \bar{\Gamma}_1) \tag{5.36}$$

$$\Theta_{\hat{1}} - \Theta_{\hat{3}} = -\tfrac{1}{3}S(S+1)(\bar{K}_1 - K_1 + \bar{\Gamma}_1) \tag{5.37}$$

$$\Theta_{\hat{2}} - \Theta_{\hat{3}} = -\tfrac{2}{3}S(S+1)\bar{\Gamma}_1 \tag{5.38}$$

Note that the Γ_1 interaction on x and y bonds cancels out of the CW temperatures, leaving only $\bar{\Gamma}_1$ on the z bonds. This happens due to the bond dependence of the sign

on the x and y bonds. When the contribution of all bonds is summed up the equal number of bonds with positive and negative Γ_1 cancel each other out. Like in the 2D compounds $\bar{\Gamma}_1$ on the z bonds can be calculated from $\Theta_{\hat{2}} - \Theta_{\hat{3}}$.

γ-Li_2IrO_3

Here we again employ the J_1-K_1-Γ_1 model, however here there are 3 kinds of structurally different bonds. All x and y bonds have the same couplings (up to the sign of Γ_1), namely J_1, K_1, and Γ_1. The z bonds that are a part of a complete hexagon have couplings K_1^{in} and Γ_1^{in}. The z bonds that are not part of a complete hexagon and instead connect hexagons in different planes have couplings K_1^{out} and Γ_1^{out}. As before Heisenberg interactions enter the calculation only as a bond average, and thus there is no need to introduce different variable for J_1 or each bond. Just like in β-Li_2IrO_3 we use uniform gyromagnetic factor g, which gives the Curie constant of $C = \frac{1}{3}g^2\mathcal{S}(\mathcal{S}+1)$ across the board. The principal axes of this compound are the same as in β-Li_2IrO_3 as well: $\hat{1} = (0,0,1)$, $\hat{2} = \frac{1}{\sqrt{2}}(1,1,0)$, and $\hat{3} = \frac{1}{\sqrt{2}}(-1,1,0)$. The CW temperatures are then:

$$\Theta_{\hat{1}} = -\tfrac{1}{6}S(S+1)(6J_1^{\text{av}} + K_1^{\text{out}} + K_1^{\text{in}}) \tag{5.39}$$

$$\Theta_{\hat{2}} = -\tfrac{1}{6}S(S+1)(6J_1^{\text{av}} + 2K_1 + \Gamma_1^{\text{out}} + \Gamma_1^{\text{in}}) \tag{5.40}$$

$$\Theta_{\hat{3}} = -\tfrac{1}{6}S(S+1)(6J_1^{\text{av}} + 2K_1 - \Gamma_1^{\text{out}} - \Gamma_1^{\text{in}}) \tag{5.41}$$

And all the combinations of their differences are:

$$\Theta_{\hat{1}} - \Theta_{\hat{2}} = \tfrac{1}{6}S(S+1)(2K_1 - K_1^{\text{out}} - K_1^{\text{in}} + \Gamma_1^{\text{out}} + \Gamma_1^{\text{in}}) \tag{5.42}$$

$$\Theta_{\hat{1}} - \Theta_{\hat{3}} = \tfrac{1}{6}S(S+1)(2K_1 - K_1^{\text{out}} - K_1^{\text{in}} - \Gamma_1^{\text{out}} - \Gamma_1^{\text{in}}) \tag{5.43}$$

$$\Theta_{\hat{2}} - \Theta_{\hat{3}} = -\tfrac{1}{3}S(S+1)(\Gamma_1^{\text{out}} + \Gamma_1^{\text{in}}) \tag{5.44}$$

Similarly to $\beta-Li_2IrO_3$ the Γ_1 on the x and y bonds cancels out due to the bond dependence of the sign.

5.4 Application II: susceptibility and Curie temperature of Sr_2IrO_4 and Ba_2IrO_4

Since it has been suggested [84] that the tetragonal distortion on the two sublattices of Sr_2IrO_4 is different, we use two different non-isotropic gyromagnetic factors for them. Following the notation of section IIB we set the angles θ_A and θ_B, which parametrize the strength of the SOC and the tetragonal distortion on sublattices A and B, respectively. The unit cell gyromagnetic factor then consists of the two blocks corresponding to the sublattices along the diagonal:

$$\hat{g} = \begin{pmatrix} \hat{g}_A & 0 \\ 0 & \hat{g}_B \end{pmatrix} \tag{5.45}$$

where $\hat{g}_A$ and $\hat{g}_B$ are 3x3 matrices identical to 5.20 with the appropriate sublattice index on the θ angles. We consider the model with 4 parameters:

$$\mathcal{H} = \sum_{\langle i,j\rangle_{\gamma=x,y}} J\,\boldsymbol{\mathcal{S}}_i\boldsymbol{\mathcal{S}}_j + K\,\mathcal{S}_i^{\gamma}\mathcal{S}_j^{\gamma} - D_z(\mathcal{S}_i^{x}\mathcal{S}_j^{y} - \mathcal{S}_i^{y}\mathcal{S}_j^{x}) + \delta J_z\,\mathcal{S}_i^{z}\mathcal{S}_j^{z}, \tag{5.46}$$

where J is isotropic Heisenberg interaction, K is the pseudodipolar (or compass) like anisotropy which gives Ising interaction of x components on the horizontal bonds and y components on the vertical bonds, respectively. The D_z is the z component of the DM interaction, and δJ_z is an Ising interaction of z components on all bonds. Using this model we follow the procedure outlined in Sec. 5.2 above to arrive at the CW temperatures and constants. The unit cell susceptibility matrix in this case is diagonal in the cubic basis, so the cubic axes are the principal axes. The Curie constants have a combination of the gyromagnetic factors from both sublattices:

$$\begin{aligned} C_x &= \tfrac{1}{6}\mathcal{S}(\mathcal{S}+1)\lambda_{xy} \\ C_y &= \tfrac{1}{6}\mathcal{S}(\mathcal{S}+1)\lambda_{xy} \\ C_z &= \tfrac{1}{6}\mathcal{S}(\mathcal{S}+1)\lambda_{z} \end{aligned} \tag{5.47}$$

where

$$\lambda_{xy} = 4\left(s_{\theta_A}^2(\sqrt{2}c_{\theta_A} + s_{\theta_A})^2 + s_{\theta_B}^2(\sqrt{2}c_{\theta_B} + s_{\theta_B})^2\right) = ((g_A)_{xy}^2 + (g_B)_{xy}^2) \tag{5.48}$$

$$\lambda_z = \left((1+3c_{2\theta_A})^2 + (1+3c_{2\theta_B})^2\right) = ((g_A)_z^2 + (g_B)_z^2) \tag{5.49}$$

The CW temperatures now also include a dependence on the gyromagnetic factor:

$$\Theta_x = -\frac{4(2J+K)\mathcal{S}(\mathcal{S}+1)(g_A)_{xy}(g_B)_{xy}}{3\lambda_{xy}} \tag{5.50}$$

$$\Theta_y = -\frac{4(2J+K)\mathcal{S}(\mathcal{S}+1)(g_A)_{xy}(g_B)_{xy}}{3\lambda_{xy}} \tag{5.51}$$

$$\Theta_z = -\frac{8(J+\delta J_z)\mathcal{S}(\mathcal{S}+1)(g_A)_z(g_B)_z}{3\lambda_z} \tag{5.52}$$

Note the complete absence of the Dzyaloshinsky-Moriya interaction from these expressions. The interaction canceled out when we added up the contributions from the two sublattices to get the response of the entire unit cell. The first two CW temperatures, Θ_x and Θ_y, are identical. For comparison we also calculate the Curie constants and temperatures for the case when the tetragonal distortion on the two sublattices is the same, namely when $\theta_A = \theta_B = \theta$:

$$C_x = \tfrac{1}{3}S(S+1)g_{xy}^2 \tag{5.53}$$

$$C_y = \tfrac{1}{3}S(S+1)g_{xy}^2 \tag{5.54}$$

$$C_z = \tfrac{1}{3}S(S+1)g_z^2 \tag{5.55}$$

$$\Theta_x = -\tfrac{2}{3}(2J+K)S(S+1) \tag{5.56}$$

$$\Theta_y = -\tfrac{2}{3}(2J+K)S(S+1) \tag{5.57}$$

$$\Theta_z = -\tfrac{4}{3}(J+\delta J_z)S(S+1) \tag{5.58}$$

And the differences between the CW temperatures are:

$$\Theta_x - \Theta_y = 0 \tag{5.59}$$

$$\Theta_x - \Theta_z = -\tfrac{2}{3}(K-2\delta J_z)S(S+1) \tag{5.60}$$

$$\Theta_y - \Theta_z = -\tfrac{2}{3}(K-2\delta J_z)S(S+1) \tag{5.61}$$

5.5 Summary

In this chapter I presented a recipe for computing CW temperatures for generic bilinear anisotropic spin systems. We also calculated the gyromagnetic tensor for magnetic ions with strong spin-orbit coupling in octahedral environment with tetragonal and trigonal distortions. Combining these two results we showed that staggered tetragonal

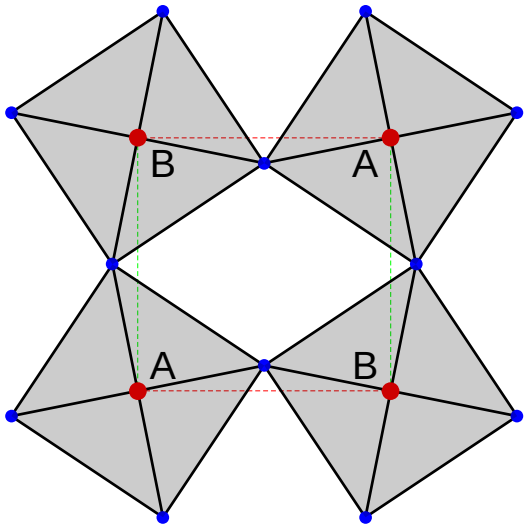

Figure 5.4: Square lattice of canted octahedra in Sr_2IrO_4 and Ba_2IrO_4. The red circles represent the magnetic Ir sites, the blue circles are oxygen atoms that form the octahedra. The dashed red and green lines represent the nearest neighbor bonds with compass interaction of x and y components, respectively. A and B label sublattices with different gyromagnetic tensors.

distortion pattern of Sr_2IrO_4 leads to CW temperatures that depend on the values of the gyromagnetic tensor along its principle axes. We show that the Dzyaloshinsky-Moriya interaction has no effect on the CW temperature expressions.

We also found that the anisotropy of CW temperatures in tri-coordinate systems such as $\alpha-RuCl_3$, Na_2IrO_3, and $(\alpha,\beta,\gamma)-Li_2IrO_3$ stems from two main sources. The first source is the symmetric offdiagonal interaction Γ present to some degree in all of the mentioned materials. Curiously, for the case of the 3D honeycomb $(\beta,\gamma)-Li_2IrO_3$ materials only the Γ interaction on the z-bonds has an effect on the anisotropy, while the contribution from the x- and y- bonds cancels out from the CW expressions due to the bond dependent sign of the Γ interaction. The second source of the CW anisotropy is the bond dependence of the strength of the anisotropic exchange couplings (K_1, K_2, Γ_1). In the case of 2D layered honeycomb materials this is usually due to monoclinic distortions of the crystal, while in 3D honeycomb materials the z-bonds are already separated from x and y in the ideal crystal.

The two sources of the anisotropy can be separated from each other by separate CW measurements along 3 independent axes in each case. When such experimental results are available our work presents a way to estimate the values of Γ and of the differences of the same anisotropic couplings on different bonds in these materials.

Chapter 6

Lifting mean-field degeneracies in anisotropic classical spin systems

6.1 Introduction

In previous chapters I have shown that in transition metal oxides the interplay of the strong spin-orbit coupling (SOC), crystal field (CF) interactions, and electron correlations may lead to compass-like anisotropic interactions between magnetic degrees of freedom [85]. These anisotropic interactions have a generic form $J_{ij}^{\alpha} S_i^{\alpha} S_j^{\alpha}$ in which α depends on the direction of the particular link or bond and S denotes spin or pseudospin degrees of freedom describing magnetic or orbital degrees of freedom.

There are two possible scenarios for the selection of the direction of the order parameter in these systems. In the most generic anisotropic biquadratic models, it might be selected already at the mean field level by off-diagonal pseudospin interactions even if these interactions are subdominant with respect to diagonal couplings [21, 77]. In exchange models with only diagonal interactions, i.e. in the compass-like models [85], the magnetic orders with different directions of the order parameters are degenerate on the mean field level. However, this classical degeneracy is accidental and can, in principle, be lifted by the order by disorder mechanism which selects a discrete set of states, each with a particular direction of the order parameter.

The thermal [17] and quantum order-by-disorder [18] mechanisms selecting a particular spin ordering pattern from a classically degenerate manifold of states have been

proposed to be at play in a number of condensed matter systems [86, 87, 88, 89, 90, 91, 92, 93, 94, 95]. However, while in most of the cases the quantum fluctuations are considered only at zero temperature, only a few works discuss the quantum order by disorder at finite temperatures [94, 95].

The models in which compass-like anisotropies are dominating, or also the pure compass models, have been known for a long time. These models appear naturally in strongly correlated electron systems as minimal models to account for interactions between pseudospins describing orbital degrees of freedom [96, 97, 98, 99, 100, 101]. The compass-like anisotropies also arise as interactions between magnetic degrees of freedom in systems with strong SOC, which might be realized in 4d and 5d transition metal oxides [1]. However, in these systems, due to the extended nature of 4d and 5d orbitals, the compass interactions are always accompanied by the usual SU(2) symmetric Heisenberg-type exchange. These models are especially interesting because while the pure compass-like models are rare, the combined Heisenberg-compass models have been shown to be minimal models describing the magnetic properties of various materials. A review of the different realizations of compass models [96, 97, 98, 99, 100, 101, 1, 102, 103, 3, 46, 104, 105, 106, 107, 108, 9, 10, 109, 110], their physical motivations, symmetries, unconventional orderings and excitations may be found in the recent review by Nussinov and van den Brink [85].

One of the common features induced by compass-like anisotropies is frustration, arising from a competition of interactions along different directions and leading to the macroscopic degeneracy of the classical ground state and in addition to rich quantum behavior. In many cases, the pure compass models do not show conventional magnetic ordering because the degeneracy of the classical ground state is connected to discrete sliding symmetries of the model [98, 102]. Because these symmetries are intrinsic symmetries of the model, they can not be lifted by the order-by disorder mechanisms. Instead, the direct consequence of the existence of these symmetries is that the natural order parameters for pure compass models are nematic, which are invariant under discrete sliding symmetries.

The nematic order present in the compass model is usually fragile and is easily destroyed by the presence of the isotropic Heisenberg interaction which breaks some of the intrinsic symmetries of the model. In Heisenberg-compass models, some of the

degeneracies become accidental. In these models, the true magnetic order might be selected by fluctuations via an order by disorder mechanism [21], removing accidental degeneracies and determining both the nature and the direction of the order parameter. Despite the simplicity of these models, the interplay of the Heisenberg and compass interaction leads to very rich phase diagrams even in the simplest case of the square lattice [106]. For classical systems this mechanism requires finite temperatures, where entropic contributions of fluctuations to the free energy become effective.

In this chapter, we will be interested in studying the directional ordering transitions in the Heisenberg-compass model on the cubic lattice [107]. From a historical perspective, the three-dimensional 90°-compass model was the first model of this kind proposed by Kugel and Khomskii [96] in the context of the ordering of the t_{2g} orbitals in transition metal oxides with perovskite structure and then studied in more details by Khaliullin [107] in application to $LaTiO_3$. The formal procedure which we will be using here is based on the derivation of the fluctuational part of the free energy by integrating out the Gaussian fluctuations, and determining which orientations of the vector order parameter correspond to the free energy minimum. To do so, we first express the partition function as a functional integral over classical fields. In this chapter, we consider classical spins at finite temperature. Our starting point in evaluating this exact representation of the partition function is the mean-field solution, which usually does not reflect the anisotropic character of the interaction referring to the crystal lattice axes. As a next step, we evaluate the contribution of Gaussian fluctuations to the free energy of the mean field ordered state. The latter carries the information embodied in the anisotropic spin interaction and therefore allows to define preferred directions of the spin order with respect to the lattice. We will not go beyond the simple evaluation of the contribution of fluctuations, e.g., by incorporating the fluctuation contribution self-consistently.

For simplicity, we choose the parameters of the model such that the ground state is ferromagnetic, i.e. we consider the Heisenberg interaction to be ferromagnetic and allow the compass interaction to be both ferromagnetic and antiferromagnetic. For any ferromagnetic and weak antiferromagnetic compass interactions, the minima of the fluctuational part of the free energy are attained if the spontaneous magnetization vector points along one of the cubic axes.

This chapter is organized as follows. In section 6.2 we introduce the functional integral representation of the partition function for the spin systems with interactions described by the most general bilinear form of the super-exchange Hamiltonian. In Sec. 6.3, we apply this framework to compute the angular dependence of the fluctuational part of the free energy for the ferromagnetic Heisenberg-compass model on the cubic lattice. Our results are presented and discussed in Section 6.4. At the end of the chapter some technical details are presented.

6.2 Representation of the partition function

We consider a system of identical classical spins $\mathbf{S}$ on a lattice, interacting in an anisotropic fashion as indicated in the introduction, defined by the Hamiltonian

$$H = \frac{1}{2} \sum_{j,j'} \sum_{\alpha\alpha'} J_{j,j'}^{\alpha,\alpha'} \, S_j^{\alpha} \, S_{j'}^{\alpha'}, \tag{6.1}$$

where j, j' label the lattice sites, $\alpha, \alpha' = x, y, z$ label the three components of the spin and $\mathbf{S}^2 = 1$. For the models with compass-like anisotropic and Heisenberg isotropic interactions of spins, the interaction is diagonal in spin space, $\alpha = \alpha'$. The $J_{j,j'}^{\alpha,\alpha}$-matrix elements are different for the (j, j')-bonds along direction γ with $\gamma = \alpha$ and $\gamma \neq \alpha$. However, since our consideration is also valid for the case when $\alpha \neq \alpha'$, in the following, we will keep both indices.

We will be interested in the long-range ordered phases of the system. The mean field approximation of the order parameter usually leads to a highly degenerate manifold of states, e.g., a ferromagnetic state with spontaneous magnetization pointing in any direction. This degeneracy is lifted by the anisotropic components of the spin interaction, but only at the level of the fluctuation contribution to the free energy (action) S_{fl}. In the following, we outline a method allowing to calculate S_{fl}, which is based on the Hubbard-Stratonovich transformation of the partition function for spin systems described by the generic Hamiltonian (6.1). I present the details and discuss justifications for this method in the Technical section at the end of this chapter.

The partition function of the system is given by the integral over the Boltzmann

weights of configurations

$$Z = \int [dS_j] \exp[-\beta \sum_{j\alpha, j'\alpha'} J_{jj'}^{\alpha\alpha'} S_j^{\alpha} S_{j'}^{\alpha'}] \delta(\mathbf{S}_j^2 - 1), \tag{6.2}$$

where $\beta = 1/k_B T$ is the inverse temperature, S_j^{α} are the components of the spin operator at site j.

It is useful to represent the Hamiltonian in the basis of the eigenfunctions $\chi_{n;j,\alpha}$ of the spin exchange matrix, defined by

$$\sum_{j',\alpha'} J_{jj'}^{\alpha\alpha'} \chi_{n;j',\alpha'} = \kappa_n \chi_{n;j,\alpha} \, .$$

For spins on a periodic lattice these eigenstates are labeled by a wavevector $\mathbf{q}$ (inside the first Brillouin zone) and index ν, characterizing three principle axes of the matrix $\hat{J}$. Thus $|n\rangle = |\mathbf{q}, \nu\rangle$ and the normalized eigenfunctions take the form

$$\chi_{\mathbf{q},\nu;j,\alpha} = \frac{1}{\sqrt{N}} e^{i\mathbf{q}\cdot\mathbf{R}_j} u_{\nu,\alpha} \, ,$$

where N is the number of lattice sites, the $u_{\nu,\alpha}$ are orthonormal real-valued eigenvectors, i.e., $\sum_{\alpha} u_{\nu,\alpha} u_{\nu',\alpha} = \delta_{\nu\nu'}$ and $\kappa_{\mathbf{q},\nu}$ are the eigenvalues of the spin exchange interaction matrix.

We now define the normal amplitudes of the spins as

$$S_{\mathbf{q},\nu} = \sum_{j,\alpha} \chi_{\mathbf{q},\nu;j,\alpha} S_j^{\alpha}$$

and express the Hamiltonian as

$$H = \sum_{\mathbf{q},\nu} \kappa_{\mathbf{q},\nu} S_{\mathbf{q},\nu}^* S_{\mathbf{q},\nu} \, , \tag{6.3}$$

where $S_{\mathbf{q},\nu}^* = S_{-\mathbf{q},\nu}$. Commutation of classical spins allows us to employ a Hubbard-Stratonovich transformation in terms of classical fields $\varphi_{\mathbf{q},\nu}$ in order to represent the interaction operator as a Zeeman energy operator of spins in a spatially varying magnetic field. As a result, one finds the following representation of the partition function:

$$Z = \int [d\varphi] \exp\Big(-\beta \big[\sum_{\mathbf{q},\nu} |\kappa_{\mathbf{q},\nu}|^{-1} \varphi_{\mathbf{q},\nu}^* \varphi_{\mathbf{q},\nu} - \mathcal{S}_{loc}(\{\varphi_{\mathbf{q},\nu}^*, \varphi_{\mathbf{q},\nu}\})\big]\Big), \tag{6.4}$$

where the integration volume element is given by

$$[d\varphi] = \Pi_{\mathbf{q},\nu} \frac{i\beta d\varphi^*_{\mathbf{q},\nu} d\varphi_{\mathbf{q},\nu}}{2\pi|\kappa_{\mathbf{q},\nu}|} \,.$$

The contribution to the action in the case of classical spins is given by

$$S_{loc}(\{\varphi^*_{\mathbf{q},\nu}, \varphi_{\mathbf{q},\nu}\}) = \beta^{-1} \sum_j \ln\big[\sinh(2\beta\varphi_j)/2\beta\varphi_j\big], \tag{6.5}$$

where $\varphi_j^2 = (\varphi_j^x)^2 + (\varphi_j^y)^2 + (\varphi_j^z)^2$, with $\varphi_j^\alpha \equiv \sum_{\mathbf{q},\nu} s(\kappa_{\mathbf{q},\nu}) \varphi_{\mathbf{q},\nu} \chi^*_{\mathbf{q},\nu;j,\alpha}$ and $s(\kappa_{\mathbf{q},\nu}) = 1$ for $\kappa_{\mathbf{q},\nu} < 0$ and $s(\kappa_{\mathbf{q},\nu}) = i$ for $\kappa_{\mathbf{q},\nu} > 0$. The Hubbard-Stratonovich identity used to derive the above functional integral is different for eigenmodes $\varphi_{\mathbf{q},\nu}$ with positive or negative eigenvalue $\kappa_{\mathbf{q},\nu}$, leading to the appearance of a complex-valued φ_j. The details of evaluating $\mathcal{S}_{loc}(\{\varphi^*_{\mathbf{q},\nu}, \varphi_{\mathbf{q},\nu}\})$ can be found in the Technical section at the end of the chapter.

6.3 Application to the cubic lattice

6.3.1 Isotropic Heisenberg interaction

In order to demonstrate how to perform the evaluation of the above representation of the partition function, we consider first the isotropic ferromagnetic Heisenberg model with nearest neighbor interactions on the cubic lattice. In this case, the Hamiltonian (6.1) reads

$$H = J \sum_{\langle j;j' \rangle} \sum_\alpha S_j^\alpha S_{j'}^\alpha, \tag{6.6}$$

where the lattice summation is over nearest neighbors $\langle j, j' \rangle -$bonds and $J < 0$. For the isotropic exchange interaction, the eigenvalues, $\kappa_{\mathbf{q},\nu} = J \sum_\alpha \cos q_\alpha$, are independent of ν, $\kappa_{\mathbf{q},\nu} = \kappa_{\mathbf{q}}$, and hence are degenerate.

A uniform ferromagnetic mean-field solution is found by solving the saddle point equation

$$\frac{\partial}{\partial \varphi_{MF}} \mathcal{S} = -\frac{\partial}{\partial \varphi_{MF}} N \Big[|\kappa_{\mathbf{q}=\mathbf{0}}|^{-1} (\varphi_{MF})^2 - \beta^{-1} \ln[\sinh(2\beta\varphi_{MF})/2\beta\varphi_{MF}] \Big] = 0, \tag{6.7}$$

where we used $\varphi^{MF}_{\mathbf{q},\nu} = \sqrt{N} \varphi_{MF} \delta_{\mathbf{q},0} m_{0,\nu}$, $\varphi_j = \varphi_{MF}$, $m_{0,\nu}$ for the components of the unit vector along the magnetization in the reference frame defined by the principal axes

of the interaction matrix (which are the cubic axes in this case), and N is the number of lattice sites. The solution of Eq.(6.7) gives us a non-linear equation for the mean-field parameter:

$$2|\kappa_{\mathbf{q}=\mathbf{0}}|^{-1}\varphi_{MF} - 2\coth(2\beta\varphi_{MF}) + \frac{1}{\beta\varphi_{MF}} = 0 \tag{6.8}$$

We solve this equation numerically at each temperature and get $\varphi_{MF}(T)$. Linearizing Eq. (6.8) near the transition, we find the transition temperature $T_c = \beta_c^{-1} = 2|\kappa_{\mathbf{q}=\mathbf{0}}|/3$. We note in passing that a different length of the classical spin vector $|\mathbf{S}| = S_0$ may be simply scaled back to the unit length by changing the temperature as $T' = S_0^2 T$. Choosing $S_0^2 = 3/4$ appropriate for quantum spin $S = 1/2$, we find the renormalized transition temperature $T_c' = |\kappa_{\mathbf{q}=\mathbf{0}}|/2$, which agrees with the quantum mean-field transition temperature.

The fluctuation contribution is obtained by expanding the action in the fluctuation field $\delta\varphi_{\mathbf{q},\nu} = \varphi_{\mathbf{q},\nu} - \varphi_{\mathbf{q},\nu}^{MF}$ about the mean field solution to the lowest order:

$$\begin{aligned} \mathcal{S} &= \mathcal{S}_0 + \mathcal{S}_{\text{fl}} \\ \mathcal{S}_0 &= N|\kappa_{\mathbf{q}=\mathbf{0}}|^{-1}\varphi_{MF}^2 - NT\ln[\sinh(2\beta\varphi_{MF})/2\beta\varphi_{MF}]. \end{aligned} \tag{6.9}$$

For Gaussian fluctuations, the fluctuation part of the free energy, or equivalently the action, $\mathcal{S}_{\text{fl}}$, is a bilinear function of $\delta\varphi_{\mathbf{q},\nu}$. It is given by

$$\mathcal{S}_{\text{fl}}\{\delta\varphi_{\mathbf{q},\nu}\} = \sum_{\mathbf{q};\nu,\nu'} A_{\mathbf{q},\nu\nu'}\delta\varphi_{\mathbf{q},\nu}^*\delta\varphi_{\mathbf{q},\nu'}, \tag{6.10}$$

where we defined matrix elements of $A_{\mathbf{q},\nu\nu'}$ describing the weight of the Gaussian fluctuations of wavevector $\mathbf{q}$ and polarization ν as

$$A_{\mathbf{q},\nu\nu'} = |\kappa_{\mathbf{q},\nu}|^{-1}\delta_{\nu,\nu'} - \frac{2}{3}\Big[\beta_c(\delta_{\nu,\nu'} - m_{0,\nu}m_{0,\nu'}) + 3\beta r m_{0,\nu}m_{0,\nu'}]s(\kappa_{\mathbf{q},\nu})s(\kappa_{\mathbf{q},\nu'})\Big] \tag{6.11}$$

Here, for shortness we introduced $r = 1/(2\beta\varphi_{MF})^2 - 1/\sinh^2(2\beta\varphi_{MF})$.

In the limit of small $\mathbf{q}$, it is instructive to separate the fluctuations into longitudinal (along $\mathbf{m}_0$) and transverse (perpendicular to $\mathbf{m}_0$) components, $\delta\varphi_{\boldsymbol{q}}^{\text{l}} = \mathbf{m}_0 \cdot \delta\boldsymbol{\varphi}_{\boldsymbol{q}}$ and $\delta\boldsymbol{\varphi}_{\boldsymbol{q}}^{\text{tr}} = \sum_{\mu=1,2}\mathbf{m}_\mu\varphi_{\boldsymbol{q},\mu}^{\text{tr}}$, respectively. We defined $\delta\varphi_{\boldsymbol{q},\mu}^{\text{tr}} = \mathbf{m}_\mu \cdot \delta\boldsymbol{\varphi}_{\boldsymbol{q}}$, with $\mathbf{m}_1 = (\mathbf{m}_0\times\mathbf{z})/|\sin\theta|$ and $\mathbf{m}_2 = \mathbf{m}_1 \times \mathbf{m}_0$, where $\cos\theta = \mathbf{m}_0\cdot\mathbf{z}$. Despite the complex nature of fluctuational fields, their separation into transverse and longitudinal modes is possible in the limit of small $\mathbf{q}$, because the interaction eigenvalues $\kappa_{\mathbf{q},\nu} < 0$ and thus, $s(\kappa_{\mathbf{q},\nu}) = 1$

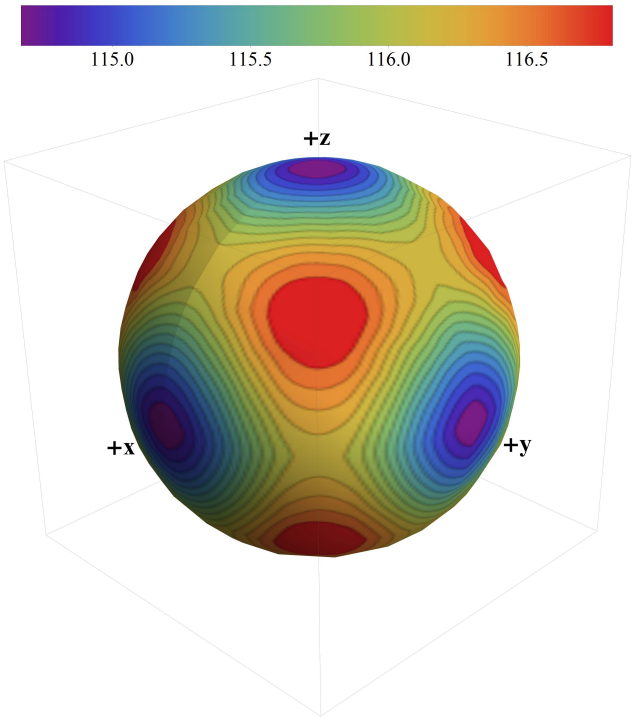

Figure 6.1: The magnitude of the action $\mathcal{S}_{\text{fl}}(\theta, \phi)$ defined by Eq. (6.18) is plotted on the surface of the unit sphere. The preferred directions of the magnetization, corresponding to the minima of the free energy, are shown by deep blue color. The energy scale is shown in units of J. $J = -1$ and $K = 0.75$: the preferred directions of the magnetization are along the cubic axes.

in this region of the BZ for any polarization component ν. Then, the longitudinal fluctuations contribute to the free energy as

$$\mathcal{S}_{\rm fl,l} = \sum_{\boldsymbol{q}} \left[|\kappa_{\boldsymbol{q}}|^{-1} - 2\beta r \right] (\boldsymbol{m}_0 \cdot \delta\boldsymbol{\varphi}^{\rm l}_{\boldsymbol{q}})(\mathbf{m}_0 \cdot \delta\boldsymbol{\varphi}^{\rm l}_{-\boldsymbol{q}}). \tag{6.12}$$

The transverse fluctuations are gapless in agreement with Goldstone's theorem:

$$\mathcal{S}_{\rm fl,tr} = \sum_{\boldsymbol{q}, \kappa_{\mathbf{q}} < 0} \left[|\kappa_{\mathbf{q}}|^{-1} - \frac{2}{3}\beta_c \right] (\delta\boldsymbol{\varphi}^{\rm tr}_{\mathbf{q}} \cdot \delta\boldsymbol{\varphi}^{\rm tr}_{-\mathbf{q}}) \tag{6.13}$$

since $\lim_{\mathbf{q}\to\mathbf{0}} \left[|\kappa_{\mathbf{q}}|^{-1} - \frac{2}{3}\beta_c \right] = 0$.

6.3.2 Fluctuations due to anisotropic compass interactions

Next, in addition to the isotropic Heisenberg term, let us take into consideration an anisotropic compass interaction, K. The constraint that the ferromagnetic mean field solution remains stable is satisfied for all negative (ferromagnetic) values of K and for positive values $K < |J|$.

In the presence of the anisotropic compass interaction, the model (6.1) reads

$$H = \sum_{j;j'} \sum_{\alpha} J^{\alpha}_{jj'} S^{\alpha}_{j} S^{\alpha}_{j'}, \tag{6.14}$$

where the exchange interaction is given by

$$J^{\alpha}_{jj'} = \frac{1}{2} \delta_{j',j+\tau} [J + K\delta_{\alpha,|\tau|}] \tag{6.15}$$

The index $\tau = \pm x, \pm y, \pm z$ labels nearest neighbor sites, where $|\tau| = x, y, z$ specifies a direction in spin space (x for bonds along the x-direction, etc.). The eigenvalues of the operator $J^{\alpha\alpha'}_{jj'}$ defined in the previous section are given by

$$\kappa_{\mathbf{q},\nu} = \sum_{\alpha} (J + K\delta_{\alpha,\nu}) \cos q_{\alpha}. \tag{6.16}$$

The eigenvectors $\mathbf{u}_{\nu}$ are again along the three cubic axes, such that the components are $u_{\nu,\alpha} = \delta_{\nu,\alpha}$. This time the three eigenvalues for given $\mathbf{q}$ are not degenerate (except in the limit $\mathbf{q} \to 0$) and the fluctuation contribution to the free energy will therefore depend on the orientation of the spontaneous magnetization. We may again use the representation

of the partition function Z as a functional integral over the Fourier components $\varphi_{\mathbf{q},\nu}$ of the auxiliary field.

Provided $J < 0$ and $K < |J|$, the mean-field solution φ_{MF} is given as before by solving the transcendental equation (6.8) numerically. The fluctuation contribution to the free energy is obtained by expanding the action in the fluctuation field about the mean field solution to lowest order. We get

$$Z = C \exp(-\beta \mathcal{S}_0) \int [d\delta\varphi] \exp(-\beta \mathcal{S}_{\rm fl}\{\delta\varphi_{\mathbf{q},\nu}\}), \tag{6.17}$$

where the fluctuation part of the action is given by Eqs.(6.10) and (6.11) In the following, we show that by comparison to the isotropic model, Eq. (6.17) manifestly breaks rotational invariance, which results in a selection of preferred directions of the order parameter, which minimize the free energy.

The 3×3-matrix $A_{\mathbf{q},\nu\nu'}$ may be diagonalized and has eigenvalues $\lambda_{\gamma,\boldsymbol{q}}$ and eigenvectors $\boldsymbol{v}_{\gamma,\boldsymbol{q}}$, $\gamma = 0, 1, 2$. This allows us to express $\sum_{\nu\nu'} A_{\mathbf{q},\nu\nu'} \delta\varphi^*_{\mathbf{q},\nu} \delta\varphi_{\mathbf{q},\nu'} = \sum_\gamma \lambda_{\gamma,\boldsymbol{q}} \delta\varphi_{\boldsymbol{q},\gamma} \delta\varphi_{-\boldsymbol{q},\gamma}$, where $\delta\varphi_{\boldsymbol{q},\gamma} = \boldsymbol{v}_{\gamma,\boldsymbol{q}} \cdot \delta\boldsymbol{\varphi}_{\boldsymbol{q}}$. The integration over the fluctuation amplitudes may now be performed and gives

$$S_{\rm fl} = \beta^{-1} \frac{1}{2} \sum_{\mathbf{q}} \ln |\lambda_{0,\boldsymbol{q}} \lambda_{1,\boldsymbol{q}} \lambda_{2,\boldsymbol{q}}|, \tag{6.18}$$

where we chose $s(\kappa_{\mathbf{q},\nu}) = \pm i$ for $\kappa_{\mathbf{q},\nu} > 0$, following the procedure described at the end of the chapter. Alternatively, we may use that $|\lambda_{0,\boldsymbol{q}} \lambda_{1,\boldsymbol{q}} \lambda_{2,\boldsymbol{q}}| = |\det\{A_{\mathbf{q},\nu\nu'}\}|$, saving the trouble of having to determine the eigenstates of $A_{\mathbf{q},\nu\nu'}$.

Let us now derive the explicit expression for the fluctuation contribution for an arbitrary orientation of $\mathbf{m}_0 = (\sin\theta\cos\phi, \sin\theta\sin\phi, \cos\theta)$. Inserting this into the definition of $A_{\mathbf{q},\nu\nu'}$ given by Eq.(6.11), we find its elements to be

$$\begin{aligned}
A_{\boldsymbol{q},00} &= |\kappa_{\boldsymbol{q},x}|^{-1} - \tfrac{2}{3} s(\kappa_{\boldsymbol{q},x}) s(\kappa_{\boldsymbol{q},x}) (\beta_c (1 - s_\theta^2 c_\phi^2) + 3\beta r s_\theta^2 c_\phi^2) \\
A_{\boldsymbol{q},01} &= -\tfrac{2}{3} s(\kappa_{\boldsymbol{q},x}) s(\kappa_{\boldsymbol{q},y}) (3\beta r - \beta_c) c_\phi s_\phi s_\theta^2 \\
A_{\boldsymbol{q},10} &= A_{\boldsymbol{q},01} \\
A_{\boldsymbol{q},02} &= -\tfrac{2}{3} s(\kappa_{\boldsymbol{q},x}) s(\kappa_{\boldsymbol{q},z}) (3\beta r - \beta_c) c_\phi c_\theta s_\theta \\
A_{\boldsymbol{q},20} &= A_{\boldsymbol{q},02} \\
A_{\boldsymbol{q},11} &= |\kappa_{\boldsymbol{q},y}|^{-1} - \tfrac{2}{3} s(\kappa_{\boldsymbol{q},y}) s(\kappa_{\boldsymbol{q},y}) (\beta_c (1 - s_\theta^2 s_\phi^2) + 3\beta r s_\theta^2 s_\phi^2) \\
A_{\boldsymbol{q},12} &= -\tfrac{2}{3} s(\kappa_{\boldsymbol{q},y}) s(\kappa_{\boldsymbol{q},z}) (3\beta r - \beta_c) s_\phi c_\theta s_\theta \\
A_{\boldsymbol{q},21} &= A_{\boldsymbol{q},12} \\
A_{\boldsymbol{q},22} &= |\kappa_{\boldsymbol{q},z}|^{-1} - \tfrac{2}{3} s(\kappa_{\boldsymbol{q},z}) s(\kappa_{\boldsymbol{q},z}) (\beta_c s_\theta^2 + 3\beta r c_\theta^2),
\end{aligned} \tag{6.19}$$

where, to shorten notations, we denote $\sin\theta(\phi) \equiv s_{\theta(\phi)}$ and $\cos\theta(\phi) \equiv c_{\theta(\phi)}$. The interactions are defined as

$$\kappa^{-1}_{\boldsymbol{q},x} = 1/\left[(J+K)\cos q_x + J\cos q_y + J\cos q_z\right] \tag{6.20}$$

$$\kappa^{-1}_{\boldsymbol{q},y} = 1/\left[(J+K)\cos q_y + J\cos q_x + J\cos q_z\right] \tag{6.21}$$

$$\kappa^{-1}_{\boldsymbol{q},z} = 1/\left[(J+K)\cos q_z + J\cos q_x + J\cos q_y\right] \tag{6.22}$$

We see that the matrix $A_{\boldsymbol{q},\nu\nu'}$ has a rather complex structure as a function of $\boldsymbol{q}$ and angles θ and ϕ. This gives rise to a complex behavior of the eigenvalues $\lambda_{0,\boldsymbol{q}}$, $\lambda_{1,\boldsymbol{q}}$ and $\lambda_{2,\boldsymbol{q}}$.

6.4 Results and discussions

We now present the results obtained for $\mathcal{S}_{\text{fl}}(\theta,\phi)$ by performing numerical integration in Eq.(6.18). The angular dependence of $\mathcal{S}_{\text{fl}}(\theta,\phi)$ is presented in Figs. 6.1, where the magnitude of $S_{\text{fl}}(\theta,\phi)$ as a function of orientation of the spontaneous magnetization is shown as a color-coded plot on the unit sphere. The calculations in Figs. 6.1 are performed at temperature $\beta = \beta_c + 1$ and assuming $J = -1$. We see that $\mathcal{S}_{\text{fl}}(\theta,\phi)$ has a non-trivial dependence on the direction of the order parameter defined by angles θ and ϕ. This peculiar angular dependence of $\mathcal{S}_{\text{fl}}(\theta,\phi)$ is inherited from non-trivial angular dependencies of $\lambda_{0,\boldsymbol{q}}$, $\lambda_{1,\boldsymbol{q}}$ and $\lambda_{2,\boldsymbol{q}}$.

In Fig. 6.1, we present the profile of $\mathcal{S}_{\text{fl}}(\theta,\phi)$ computed for $K = 0.75$. We can see that $\mathcal{S}_{\text{fl}}(\theta,\phi)$ is minimized when the magnetization is directed along one of the cubic axes. We note that the cubic directions are also selected for other values of the compass interactions, both antiferromagnetic as well as ferromagnetic, where the ferromagnetic state is the mean field solution ($K < |J|$).

6.5 Summary

The magnetic properties of heavy transition metal oxides such as iridates and others are emerging as a new fascinating field offering opportunities to realize strongly frustrated quantum spin systems in the laboratory. In these systems, the combination of multiband electronic structure and strong Coulomb and Hund's couplings with strong

spin-orbit interaction can give rise to extremely anisotropic spin exchange interactions of the compass type. Mean field solutions of these models are often untouched by the anisotropies of the model and show the full isotropy of pure Heisenberg models, in contrast with experimental observations. In this chapter, we addressed the question how the system selects special preferred directions of the mean field order parameter vector. We restricted ourselves to the case of a ferromagnetic order parameter, but an analogous question exists for antiferromagnetic or more complicated ordered structures. We find that the high degeneracy of the ferromagnetic mean-field solution is lifted by the free energy contribution from thermal fluctuations. We calculated the fluctuation contribution for a Heisenberg-compass model of classical spins on a three dimensional cubic lattice with nearest neighbor interactions - an isotropic Heisenberg coupling $J < 0$ (which we take as the energy unit), and a compass coupling K. The ferromagnetic state is found if $K < |J|$. Rather than exploring the full phase diagram, we focused on one typical temperature $T = T_c/(1 + T_c)$, where T_c is the mean-field transition temperature and all temperatures are measured in units of $|J|$. For values of $K < 1$, the system is found to choose preferred directions of the spontaneous magnetization along one of the cubic axes. In the temperature regime considered here, we expect the classical approximation to be valid.

6.6 Technical details

6.6.1 General formulation

The Hubbard-Stratonovich (H-S) transformation is based on the mathematical identity

$$\exp[-ax^2] = \frac{1}{\sqrt{\pi|a|}} \int dy \exp\left[-\frac{y^2}{|a|} + 2s(a)xy)\right], \tag{6.23}$$

where we defined

$$s(a) = \begin{cases} 1\,, & \text{if } a < 0 \\ \imath\,, & \text{if } a > 0. \end{cases} \tag{6.24}$$

For $a > 0$ we may as well use $s(a) = -i$. We will later make use of this ambiguity when we evaluate the y-integrals approximately, which may lead to imaginary-valued contributions.

In the above H-S-transformation, x may be a number or an operator. In the case it is an operator, we use the eigenfunctions $|n\rangle$ of $\widehat{x}$ defined by

$$\widehat{x}|n\rangle = x_n|n\rangle$$

to prove that

$$\exp\left[-a\widehat{x}^2\right]|n\rangle = \exp\left[-ax_n^2\right]|n\rangle = \frac{1}{\sqrt{\pi|a|}}\int dy \exp\left[-\frac{y^2}{|a|} + 2s(a)x_n y)\right]|n\rangle$$
$$= \frac{1}{\sqrt{\pi|a|}}\int dy \exp\left[-\frac{y^2}{|a|} + 2s(a)\widehat{x}y)\right]|n\rangle.$$

This identity also works for complex (non-Hermitian) x and y:

$$\exp[-a\widehat{x}^\dagger\widehat{x}] = \frac{i}{2\pi|a|}\int dy^* dy \exp\left[-\frac{y^* y}{|a|} + s(a)(\widehat{x}^\dagger y + H.c.)\right]$$

We now turn to the case of the partition function of a spin system with generic interaction Hamiltonian (1). In order to use the mathematical identities we need to represent the Hamiltonian (1) in terms of normal coordinates. To this end we define the normalized eigenstates of the exchange interaction operator

$$\sum_{j',\alpha'} J_{jj'}^{\alpha\alpha'}\chi_{n;j',\alpha'} = \kappa_n\chi_{n;j,\alpha}, \tag{6.25}$$

in terms of which we have

$$J_{jj'}^{\alpha\alpha'} = \sum_n \kappa_n\chi_{n;j,\alpha}^*\chi_{n;j',\alpha'}, \tag{6.26}$$

where $\chi_{n;j',\alpha'}$ form a complete and orthonormal set of eigenfunctions and thus obey

$$\begin{aligned}\textstyle\sum_{j,\alpha}\chi_{n;j,\alpha}^*\chi_{n';j,\alpha} &= \delta_{n,n'}, \\ \textstyle\sum_n \chi_{n;j,\alpha}^*\chi_{n;j',\alpha'} &= \delta_{j,j'}\delta_{\alpha,\alpha'}.\end{aligned} \tag{6.27}$$

For spins on a periodic lattice, the eigenstates $|n\rangle = |\mathbf{q},\nu\rangle$ are labeled by wavevector $\mathbf{q}$ and spin component ν, and the eigenfunctions take the form

$$\chi_{\mathbf{q},\nu;j,\alpha} = \frac{1}{\sqrt{N}}e^{i\mathbf{q}\cdot\mathbf{R}_j}u_{\mathbf{q}\nu}^\alpha \tag{6.28}$$

where $u^{\alpha}_{\mathbf{q}\nu}$ are normalized real valued eigenvectors, i.e. $\sum_{\alpha} u^{\alpha}_{\mathbf{q}\nu} u^{\alpha}_{\mathbf{q},\nu} = 1$, and $\kappa_{\mathbf{q},\nu}$ are the eigenvalues of the spin exchange operator. We now define the normal amplitudes of the spin operators as

$$S_{\mathbf{q},\nu} = \sum_{j,\alpha} \chi_{\mathbf{q},\nu;j,\alpha} S^{\alpha}_{j} \tag{6.29}$$

and express the Hamiltonian (1) as

$$H = \sum_{\mathbf{q},\nu} \kappa_{\mathbf{q},\nu} S^{*}_{\mathbf{q},\nu} S_{\mathbf{q},\nu}, \tag{6.30}$$

where $S^{*}_{\mathbf{q},\nu} = S_{-\mathbf{q},\nu}$.

We seek to apply the above mathematical identities (A1)-(A3) to each normal component separately. This requires the normal components of the spin operators to commute with each other, which is certainly true for the classical spins. Then using the Hubbard-Stratonovich transformation one may express the Boltzmann weight operator of each normal mode in terms of normal field amplitudes $\varphi_{\mathbf{q},\nu}$ as

$$\begin{aligned} \exp[-\beta \kappa_{\mathbf{q},\nu} S^{*}_{\mathbf{q},\nu} S_{\mathbf{q},\nu}] = \tfrac{\imath\beta}{2\pi|\kappa_{\mathbf{q},\nu}|} \int\int d\varphi^{*}_{\mathbf{q},\nu} d\varphi_{\mathbf{q},\nu} \\ \exp\left[-\beta\{|\kappa_{\mathbf{q},\nu}|^{-1} \varphi^{*}_{\mathbf{q},\nu}\varphi_{\mathbf{q},\nu} + s(\kappa_{\mathbf{q},\nu})(S^{*}_{\mathbf{q},\nu}\varphi_{\mathbf{q},\nu} + H.c.)\}\right] \end{aligned} \tag{6.31}$$

The complete Boltzmann weight operator may be expressed, again using the commutability of the normal mode operators, as

$$\begin{aligned} \exp[-\beta \textstyle\sum_{\mathbf{q},\nu} \kappa_{\mathbf{q},\nu} S^{*}_{\mathbf{q},\nu} S_{\mathbf{q},\nu}] = \int [d\varphi] \\ \exp[-\beta \textstyle\sum_{\mathbf{q},\nu} \{|\kappa_{\mathbf{q},\nu}|^{-1} \varphi^{*}_{\mathbf{q},\nu}\varphi_{\mathbf{q},\nu} + s(\kappa_{\mathbf{q},\nu})(S^{*}_{\mathbf{q},\nu}\varphi_{\mathbf{q},\nu} + h.c.)\}], \end{aligned} \tag{6.32}$$

where $\varphi^{*}_{\mathbf{q},\nu} = \varphi_{-\mathbf{q},\nu}$. The integration volume element is given by

$$[d\varphi] = \Pi_{\mathbf{q},\nu} \frac{i\beta d\varphi^{*}_{\mathbf{q},\nu} d\varphi_{\mathbf{q},\nu}}{2\pi|\kappa_{\mathbf{q},\nu}|}$$

Next, we find that the partition function of an interacting classical spin system on an infinite periodic lattice may be expressed as

$$Z = C \int [d\varphi] \exp\left[-\beta \textstyle\sum_{\mathbf{q},\nu} |\kappa_{\mathbf{q},\nu}|^{-1} \varphi^{*}_{\mathbf{q},\nu}\varphi_{\mathbf{q},\nu} - S_{loc}(\{\varphi_{\mathbf{q},\nu}\})\right],$$

where C is a constant. The contribution $\mathcal{S}_{loc}(\{\varphi_{\mathbf{q},\nu}\})$ to the action is given by

$$\mathcal{S}_{loc}(\{\varphi_{\mathbf{q},\nu}\}) = \frac{1}{\beta} \sum_{j} \ln W_j \tag{6.33}$$

and W_j is computed by taking into account the constraint of the unit length of classical spins, $\mathbf{S}_j^2 = 1$, and integrating over all directions of spin at each lattice site:

$$\begin{aligned} W_j &= \int \tfrac{dS_j d\Omega_j}{2\pi} \exp\left[2\beta \textstyle\sum_\alpha \varphi_j^\alpha S_j^\alpha\right] \delta(\mathbf{S}_j^2 - 1) \\ &= \int \tfrac{d\Omega_j}{4\pi} \exp\left[2\beta \textstyle\sum_\alpha \varphi_j^\alpha S_j^\alpha\right] = \tfrac{\sinh 2\beta|\varphi_j|}{2\beta|\varphi_j|}. \end{aligned} \tag{6.34}$$

This gives

$$\mathcal{S}_{loc}(\{\varphi_{\mathbf{q},\nu}\}) = \frac{1}{\beta} \sum_j \ln[\frac{\sinh 2\beta|\varphi_j|}{2\beta|\varphi_j|}]. \tag{6.35}$$

Here we defined the complex-valued three-component field φ_j^α at each lattice site j as

$$\varphi_j^\alpha = \textstyle\sum_{\mathbf{q},\nu} s(\kappa_{\mathbf{q},\nu}) \mathcal{R}e\{\varphi^*_{\mathbf{q},\nu} \chi_{\mathbf{q},\nu;j,\alpha}\} = \sum_{\mathbf{q},\nu} s(\kappa_{\mathbf{q},\nu}) \varphi_{\mathbf{q},\nu} \chi^*_{\mathbf{q},\nu;j,\alpha} = \varphi^\alpha_{R,j} + i\varphi^\alpha_{I,j}.$$

Observing that $\kappa_{\mathbf{q},\nu} = \kappa_{-\mathbf{q},\nu}$, we get

$$\begin{aligned} \varphi^\alpha_{R,j} &= \mathrm{Re}\{\varphi_j^\alpha\} = \textstyle\sum_{\mathbf{q},\nu,\kappa_{\mathbf{q},\nu}<0} \varphi_{\mathbf{q},\nu} \chi^*_{\mathbf{q},\nu;j,\alpha} \\ \varphi^\alpha_{I,j} &= \mathrm{Im}\{\varphi_j^\alpha\} = \textstyle\sum_{\mathbf{q},\nu,\kappa_{\mathbf{q},\nu}>0} \varphi_{\mathbf{q},\nu} \chi^*_{\mathbf{q},\nu;j,\alpha}. \end{aligned} \tag{6.36}$$

The field amplitude is determined by

$$\varphi_j = \sqrt{(\boldsymbol{\varphi}_{R,j} + i\,\boldsymbol{\varphi}_{I,j})^2}, \tag{6.37}$$

where $\boldsymbol{\varphi}_{R,j} = \left(\varphi^x_{R,j},\, \varphi^y_{R,j},\, \varphi^z_{R,j}\right)$ and $\boldsymbol{\varphi}_{I,j} = \left(\varphi^x_{I,j},\, \varphi^y_{I,j},\, \varphi^z_{I,j}\right)$.

We now derive the contribution of Gaussian fluctuations to the free energy for the ferromagnetic mean field state which we denote as $\boldsymbol{\varphi}_{MF}$. To this end, we expand $\mathcal{S}_{loc}(\{\varphi_{\mathbf{q},\nu}\})$ (6.35) in terms of the fluctuation amplitudes and separate the mean-field and fluctuational contributions. First, we expand the field amplitude φ_j to bilinear order in the fluctuation amplitudes:

$$\begin{aligned} \varphi_j &= \varphi_{MF} + \delta\varphi_j, \\ \delta\varphi_j &= \frac{1}{2\varphi_{MF}}[2\boldsymbol{\varphi}_{MF} \cdot (\delta\boldsymbol{\varphi}_{R,j} + i\delta\boldsymbol{\varphi}_{I,j}) + \delta\boldsymbol{\varphi}^2_{R,j} - \delta\boldsymbol{\varphi}^2_{I,j}] \\ &\quad - \frac{1}{2\varphi^3_{MF}}[\boldsymbol{\varphi}_{MF} \cdot (\delta\boldsymbol{\varphi}_{R,j} + i\,\delta\boldsymbol{\varphi}_{I,j})]^2. \end{aligned} \tag{6.38}$$

Using Eq. (6.36), we now obtain the expressions for $\delta\varphi_j$ and $\delta\varphi_j^2$ in terms of $\varphi^*_{\mathbf{q},\nu}$ and $\varphi_{\mathbf{q},\nu}$, keeping quadratic (Gaussian) terms only:

$$\sum_j \delta\varphi_j = \frac{1}{2\varphi_{MF}} \sum_{\mathbf{q},\nu,\nu'} \delta_{\nu,\nu'} s(\kappa_{\mathbf{q},\nu}) s(\kappa_{\mathbf{q},\nu'}) \varphi^*_{\mathbf{q},\nu} \varphi_{\mathbf{q},\nu'} - \frac{1}{2\varphi_{MF}} \sum_j \delta\varphi_j^2 \quad (6.39)$$

$$\sum_j \delta\varphi_j^2 = \sum_{\mathbf{q},\nu,\nu'} s(\kappa_{\mathbf{q},\nu}) s(\kappa_{\mathbf{q},\nu'}) m_{0,\nu} \varphi^*_{\mathbf{q},\nu} \varphi_{\mathbf{q},\nu'} m_{0,\nu'}.$$

Next, we expand Eq. (6.35) step by step as

$$\begin{aligned} \sinh 2\beta|\varphi_j| \quad &= \sinh(2\beta(\varphi_{MF} + \delta\varphi_j)) \\ &= \sinh(2\beta\varphi_{MF})[1 + 2(\beta\delta\varphi_j)^2] + \cosh(2\beta\varphi_{MF}) 2\beta\delta\varphi_j \end{aligned}$$

and further

$$\begin{aligned} &\ln\left[\sinh(2\beta\varphi_j)/2\beta\varphi_j\right] = \ln\left[\sinh(2\beta(\varphi_{MF} + \delta\varphi_j))\right] - \ln\left[2\beta(\varphi_{MF} + \delta\varphi_j)\right] \\ &= \ln\left[\sinh(2\beta\varphi_{MF})/(2\beta\varphi_{MF})\right] + \left[2\beta\varphi_{MF}\coth(2\beta\varphi_{MF}) - 1\right] \frac{\delta\varphi_j}{\varphi_{MF}} \\ &+ \frac{1}{2}\left[-\frac{(2\beta\varphi_{MF})^2}{\sinh^2(2\beta\varphi_{MF})} + 1\right] (\frac{\delta\varphi_j}{\varphi_{MF}})^2. \end{aligned}$$

The fluctuation part of the local part of the free energy is then given by

$$\begin{aligned} -\beta^{-1}\delta \sum_j \ln[\sinh(2\beta\varphi_j)/2\beta\varphi_j] &= -\frac{4}{3}\beta_c\varphi_{MF} \sum_j \delta\varphi_j \quad (6.40) \\ -\frac{1}{2\beta\varphi_{MF}^2}[1 - \frac{(2\beta\varphi_{MF})^2}{\sinh^2(2\beta\varphi_{MF})}] &\sum_j \delta\varphi_j^2, \end{aligned}$$

where we have used that $2\beta\varphi_{MF}\coth(2\beta\varphi_{MF}) - 1 = \frac{4}{3}\beta_c\beta\varphi_{MF}^2$. Substituting the expressions for $\delta\varphi_j, \delta\varphi_j^2$ and defining $r = 1/(2\beta\varphi_{MF})^2 - 1/\sinh^2(2\beta\varphi_{MF})$, we get the fluctuation contribution to the free energy

$$\mathcal{S}_{\text{fl}}\{\delta\varphi_{\mathbf{q},\nu}\} = \sum_{\mathbf{q};\nu,\nu'} A_{\mathbf{q},\nu\nu'} \delta\varphi^*_{\mathbf{q},\nu} \delta\varphi_{\mathbf{q},\nu'}, \quad (6.41)$$

where we defined matrices $A_{\mathbf{q},\nu\nu'}$ describing the weight of Gaussian fluctuations of wavevector $\mathbf{q}$ and polarization ν as

$$\begin{aligned} A_{\mathbf{q},\nu\nu'} \quad &= |\kappa_{\mathbf{q},\nu}|^{-1}\delta_{\nu,\nu'} - \frac{2}{3}[\beta_c(\delta_{\nu,\nu'} - m_{0,\nu}m_{0,\nu'}) + \\ &3\beta r m_{0,\nu}m_{0,\nu'}] s(\kappa_{\mathbf{q},\nu}) s(\kappa_{\mathbf{q},\nu'}) \quad (6.42) \end{aligned}$$

The fluctuation matrix $A_{\mathbf{q},\nu\nu'}$ will in general be non-Hermitian, and its eigenvalues will be complex. We now use that $A_{\mathbf{q},\nu\nu'}$ is an even function of $\mathbf{q}$ and divide $\mathbf{q}$-space into $q_x > 0$ ($M_>$) and $q_x < 0$ ($M_<$). Note that the choice of q_x for dividing the BZ in half is arbitrary, and we could also do it with a help of q_y and q_z. For modes $\varphi_{\mathbf{q},\nu}$ with $\mathbf{q} \in M_>$, we choose $s(\kappa_{\mathbf{q},\nu}) = +i$, whereas for modes with $\mathbf{q} \in M_<$ we choose $s(\kappa_{\mathbf{q},\nu}) = -i$, where $\kappa_{\mathbf{q},\nu} > 0$ in both cases. Then we have $A_{-\mathbf{q},\nu\nu'} = A^*_{\mathbf{q},\nu\nu'}$ and as a result of the functional integration we will get

$$\begin{aligned} Z &= Z_{MF} \int [d\delta\varphi] \exp\left[-\beta \textstyle\sum_{\mathbf{q},\nu,\nu'} A_{\mathbf{q},\nu\nu'} \delta\varphi^*_{\mathbf{q},\nu} \delta\varphi_{\mathbf{q},\nu'}\right] \\ &= Z_{MF} \exp\left[-\tfrac{1}{2} \textstyle\sum_{\mathbf{q}\in M_>} \ln(\det(A_{\mathbf{q},\nu\nu'}) \det(A^*_{\mathbf{q},\nu\nu'}))\right] \\ &= Z_{MF} \exp\left[-\tfrac{1}{2} \textstyle\sum_{\mathbf{q}} \ln|\det(A_{\mathbf{q},\nu\nu'})|\right], \end{aligned} \tag{6.43}$$

where

$$Z_{MF} = \exp\left[-\beta N |\kappa_{\boldsymbol{q}=0}|^{-1} \varphi^2_{MF}\right] \left[\sinh(2\beta\varphi_{MF})/(2\beta\varphi_{MF})\right]^N.$$

Chapter 7

The free energy of quantum spin systems: Functional integral representation

7.1 Introduction

The purpose of this chapter is to present a general approach to compute the free energy of quantum spin systems with anisotropic interactions and study how spin fluctuations explicitly break the degeneracy at the mean-field level and select a particular direction of the order parameter from the manifold of classically degenerate states at finite temperatures. The formal procedure which we will be using here is based on the derivation of the fluctuation-induced part of the free energy on top of the mean field contribution, which then allows to determine the orientations of the vector order parameter corresponding to the symmetry related free energy minima.

In general, the calculation of the free energy of a quantum spin system is complicated by the fact that the spin operators are non-canonical, which limits the usefulness of renormalized perturbation theory, the usual tool in dealing with quantum many-body systems [111, 112]. Here we explore a different approach: decoupling of the bilinear interaction operators by way of HS transformations [113, 114]. Our approach differs from a previous derivation [115, 116, 117] of a path integral representation of interacting

quantum spin systems in terms of Hubbard-Stratonovich fields in that it applies to anisotropic spin systems and is not restricted to ultralow temperatures but allows to calculate the contribution of Gaussian fluctuations to the free energy at all temperatures in the ordered phase. This requires introducing space and time-dependent HS-fields, which are integrated over. The resulting quantum trace over an exponential involving spin operators (a kind of Zeeman interaction of spins with the HS-induced "magnetic field"), may be done explicitly. The result is a representation of the partition function in terms of an infinite power series in the interaction. The series may be summed up explicitly in the case of an Ising-type interaction or in the case of classical spins [19, 21]. In the general case of the bilinear interaction of quantum spins, only the Gaussian fluctuation contribution to the free energy of an ordered state may be derived in a compact form. Higher order corrections are accessible, but involve increasingly complex expressions.

This chapter is organized as follows: In Section 7.2, the representation of the partition function is introduced. Section 7.3 describes the Mean Field approximation. In Section 7.4 we present the evaluation of the free energy in the approximation of Gaussian fluctuations about the mean field order parameter. We apply the derived formalism to the quantum Heisenberg-compass spin model in Section 7.5. Finally, we draw conclusions in Section 7.6.

7.2 Representation of the partition function

The form of the bilinear Hamiltonian as well as the partition function were given in the previous chapter starting with Eq. 6.1. I thus refer the reader there for these first few steps. Here we will start with the HS transformation which we do in a slightly different format that will be more useful for the quantum system.

7.2.1 Hubbard-Stratonovich transformation

We apply the HS transformation to each normal component separately. This transformation is based on the mathematical identity (defining $x = \mathrm{Re}\{S_{\mathbf{q},\nu}\}$, $y = \mathrm{Im}\{S_{\mathbf{q},\nu}\}$,

and $a = \beta\kappa_{\mathbf{q},\nu}$)

$$\exp\left[-a(x^2+y^2)\right] = \frac{1}{\pi|a|}\int dudv \begin{cases} \exp\left[-\frac{u^2+v^2}{|a|} + 2(xu+yv)\right], & a<0, \\ \exp\left[-\frac{u^2+v^2}{|a|} + 2i(-xu+yv)\right], & a>0 \end{cases}$$

In the second equality we made use of the freedom to choose the imaginary prefactor to be $+i$ or $-i$. Here the auxiliary variables u, v are components of the HS field $\varphi_{\mathbf{q},\nu}$, which we choose to be $u = \mathrm{Re}\varphi_{\mathbf{q},\nu}$ and $v = \mathrm{Im}\varphi_{\mathbf{q},\nu}$ in the first equation (valid if $a < 0$) and $v = \mathrm{Re}\varphi_{\mathbf{q},\nu}$ and $u = \mathrm{Im}\varphi_{\mathbf{q},\nu}$ in the second equation (valid if $a > 0$). We may combine both cases by defining a function $s(\kappa_{\mathbf{q},\nu}) = 1$ if $\kappa_{\mathbf{q},\nu} < 0$ and $s(\kappa_{\mathbf{q},\nu}) = -i$ if $\kappa_{\mathbf{q},\nu} > 0$. Then, in the first equation $(xu + yv) = \mathrm{Re}\{s(\kappa_{\mathbf{q},\nu})S_{\mathbf{q},\nu}\varphi^*_{\mathbf{q},\nu}\}$, whereas in the second equation $i(-xu + yv) = \mathrm{Im}\{S_{\mathbf{q},\nu}\varphi^*_{\mathbf{q},\nu}\}$, which may also be expressed as $\mathrm{Re}\{s(\kappa_{\mathbf{q},\nu})S_{\mathbf{q},\nu}\varphi^*_{\mathbf{q},\nu}\}$. In both cases, whether $s(\kappa_{\mathbf{q},\nu})$ is real or imaginary valued, the term in the exponent linear in $S_{\mathbf{q},\nu}$ is real valued. In Eq.(7.1), $x + iy$ may be a number or an operator.

The application of the HS transformation requires the normal components of the spin operators to commute with each other, which is true for classical spins. Then using the HS transformation one may express the Boltzmann weight operator of each normal mode in terms of classical fields $\varphi_{\mathbf{q},\nu}$ and represent the interaction operator as a Zeeman energy operator of spins in a spatially varying magnetic field [19]. Note that in Ref. [19] we used a slightly different convention for the definition of variables u, v above.

In order to make use of the Hubbard-Stratonovich transformation for the computation of the partition function of a quantum spin system, for which the $S_{\mathbf{q},\nu}$ do not commute, we need to represent the Boltzmann operator as an evolution operator in imaginary time and apply the Suzuki-Trotter discretization [118], allowing to write down the partition function in terms of products over time slices [111]. Explicitly, we have

$$Z = \mathrm{Tr}\left[\exp\left(-\beta\mathcal{H}\right)\right] = \mathrm{Tr}\left[T_\tau \exp[-\epsilon\sum_{n=1}^{M}\mathcal{H}(\tau_n)]\right], \tag{7.1}$$

where T_τ is the imaginary time ordering operator, and we sliced the imaginary time interval $[0, \beta]$ into $M = \beta/\epsilon$ infinitesimal intervals each of length ϵ, and $\tau_n = n\epsilon$, $n = 1, 2, ...M$. Since ϵ is small, and will be taken to zero at the end, we may now

expand each exponent in Eq. (7.1) as

$$\exp[-\epsilon\mathcal{H}(\tau_n)] = 1 - \epsilon\mathcal{H}(\tau_n) + O(\epsilon^2), \tag{7.2}$$

and approximate

$$T_\tau \exp[-\epsilon \sum_{n=1}^{M} \mathcal{H}(\tau_n)] = T_\tau \prod_{n=1}^{M} \exp[-\epsilon\mathcal{H}(\tau_n)], \tag{7.3}$$

where

$$\begin{aligned} \exp\left[-\epsilon\mathcal{H}(\tau_n)\right] &= \exp\left[-\epsilon \textstyle\sum_{\mathbf{q},\nu} \kappa_{\mathbf{q},\nu} S^*_{\mathbf{q},\nu}(\tau_n) S_{\mathbf{q},\nu}(\tau_n)\right] \\ &= \textstyle\prod_{\mathbf{q},\nu} \exp[-\epsilon\kappa_{\mathbf{q},\nu} S^*_{\mathbf{q},\nu}(\tau_n) S_{\mathbf{q},\nu}(\tau_n)] + O(\epsilon^2). \end{aligned} \tag{7.4}$$

Now, at each instant τ_n we may perform the HS transformation separately and express the Boltzmann weight operator of each normal mode in terms of normal field amplitudes $\varphi_{\mathbf{q},\nu}(\tau_n)$ as

$$\begin{aligned} &\exp\left[-\epsilon\kappa_{\mathbf{q},\nu} S^*_{\mathbf{q},\nu}(\tau_n) S_{\mathbf{q},\nu}(\tau_n)\right] = \\ &C^{-1}_{\mathbf{q},\nu} \int d\varphi^*_{\mathbf{q},\nu} d\varphi_{\mathbf{q},\nu} \exp\Big[-\epsilon\Big\{|\kappa_{\mathbf{q},\nu}|^{-1} \varphi^*_{\mathbf{q},\nu}(\tau_n)\varphi_{\mathbf{q},\nu}(\tau_n) - 2\mathrm{Re}\{s(\kappa_{\mathbf{q},\nu}) S^*_{\mathbf{q},\nu}(\tau_n)\varphi_{\mathbf{q},\nu}(\tau_n)\}\Big\}\Big]. \end{aligned} \tag{7.5}$$

The partition function (7.1) may therefore be expressed as

$$\begin{aligned} Z = \quad & \frac{1}{C}\mathrm{Tr}\left[T_\tau \int [d\varphi] \prod_{n=1}^{M} \exp\left[-\epsilon\left\{\sum_{\mathbf{q},\nu}\left(|\kappa_{\mathbf{q},\nu}|^{-1}\varphi^*_{\mathbf{q},\nu}(\tau_n)\varphi_{\mathbf{q},\nu}(\tau_n)\right.\right.\right.\right. \\ & \left.\left.\left.\left. -2\mathrm{Re}\{s(\kappa_{\mathbf{q},\nu}) S^*_{\mathbf{q},\nu}(\tau_n)\varphi_{\mathbf{q},\nu}(\tau_n)\}\right)\right\}\right]\right] \\ = \quad & \frac{1}{C}\int [d\varphi] \prod_{n=1}^{M} \exp\left[-\epsilon \sum_{\mathbf{q},\nu} |\kappa_{\mathbf{q},\nu}|^{-1} \varphi^*_{\mathbf{q},\nu}(\tau_n)\varphi_{\mathbf{q},\nu}(\tau_n)\right] \\ & \times \mathrm{Tr}\left[T_\tau \prod_{j,\alpha} \exp\left[-\epsilon B^\alpha_{j,eff}(\tau_n) S^\alpha_j(\tau_n)\right]\right], \end{aligned} \tag{7.6}$$

where the spatially and "temporally" varying local magnetic field $B^\alpha_{j,\mathrm{eff}}(\tau_n)$ is defined by

$$\begin{aligned} B^\alpha_{j,\mathrm{eff}}(\tau_n) \quad &= -2\varphi^\alpha_j(\tau_n), \\ \varphi^\alpha_j(\tau_n) \quad &= \sum_{\mathbf{q},\nu=1}^{3N_s} \mathrm{Re}\{s(\kappa_{\mathbf{q},\nu}) \chi^*_{\mathbf{q},\nu;j,\alpha} \varphi_{\mathbf{q},\nu}(\tau_n)\}. \end{aligned} \tag{7.7}$$

In Eq. (7.6), we also defined the integration volume element as

$$[d\varphi] = \Pi_{\mathbf{q},\nu,n}\, d\varphi^*_{\mathbf{q},\nu}(\tau_n) d\varphi_{\mathbf{q},\nu}(\tau_n)$$

and the normalization factor C as

$$C = \int [d\varphi] \prod_{n=1}^{M} \exp\left[-\epsilon \sum_{\mathbf{q},\nu} |\kappa_{\mathbf{q},\nu}|^{-1} \varphi^*_{\mathbf{q},\nu}(\tau_n)\varphi_{\mathbf{q},\nu}(\tau_n) \right].$$

7.2.2 Trace over quantum spin states

We may now perform the trace over the quantum spin states. As spin operators on different sites commute, the trace may be split up into a product of traces Tr_j over single spin Hilbert space

$$\begin{aligned} Z = \tfrac{1}{C'} \textstyle\int [d\varphi] \\ \exp\left[-\int_0^\beta d\tau \sum_{\mathbf{q},\nu} |\kappa_{\mathbf{q},\nu}|^{-1} \varphi^*_{\mathbf{q},\nu}(\tau)\varphi_{\mathbf{q},\nu}(\tau) \right] \prod_j \Theta_j, \end{aligned} \tag{7.8}$$

where we defined

$$\Theta_j = \frac{1}{2}\mathrm{Tr}_j \Big\{ T_\tau \prod_n \exp\left[2\epsilon \sum_{\alpha=x,y,z} \varphi^\alpha_j(\tau_n) S^\alpha_j \right] \Big\}. \tag{7.9}$$

The factors $\frac{1}{2}$ in front of the trace are compensated by corresponding factors in the normalization, leading to $C' = C/2^{N_t}$, where N_t is the total number of spins.

We note that the factors under the trace, $\exp\left[2\epsilon \boldsymbol{\varphi}_j(\tau_n)\cdot \mathbf{S}_j\right]$, may be cyclically permuted. This suggests that the terms at $n = 1$ and at $n = M$ should be equal, in order to avoid an unphysical discontinuity when passing from $n = 1$ to $n = M$. In other words, we assume periodic boundary conditions, $\varphi_{\mathbf{q},\nu}(\tau_n) = \varphi_{\mathbf{q},\nu}(\tau_n + \beta)$. This implies that the Fourier frequencies ω_n of $\varphi_{\mathbf{q},\nu}(\tau)$ are bosonic Matsubara frequencies.

The spin trace may be performed by inserting suitable representations of the unit operator in single spin space at each time step

$$\hat{\mathbf{1}} = \sum_{s=\pm 1} |s;\mathbf{e}_n\rangle\langle s;\mathbf{e}_n|, \tag{7.10}$$

where $\mathbf{e}_n \equiv \mathbf{e}(\tau_n) = \boldsymbol{\varphi}_j(\tau_n)/|\boldsymbol{\varphi}_j(\tau_n)|$ denotes the spin quantization axis at time τ_n and $|s;\mathbf{e}_n\rangle \equiv |s_n\rangle$, $s = \pm 1$ are corresponding two-component spin eigenvectors, obeying

$(\mathbf{S}\cdot\mathbf{e}_n)|s_n\rangle = \frac{s}{2}|s_n\rangle$. The assumed periodic boundary condition implies that $\mathbf{e}_N = \mathbf{e}_1$ such that $\mathbf{e}(\beta) = \mathbf{e}(0)$ and $\mathbf{e}(\tau)$ is a periodic function of period β.

Now, inserting the unit operator expressed in the basis of eigenstates of each factor $e^{\epsilon\boldsymbol{\varphi}_n\cdot\boldsymbol{\sigma}}$ to the left and right of that factor in the Eq. 7.9, we may express Θ_j as

$$\begin{aligned}\Theta \quad &= \frac{1}{2}\mathrm{Tr}\Big\{e^{\epsilon\boldsymbol{\varphi}_N\cdot\boldsymbol{\sigma}}.....e^{\epsilon\boldsymbol{\varphi}_2\cdot\boldsymbol{\sigma}}e^{\epsilon\boldsymbol{\varphi}_1\cdot\boldsymbol{\sigma}}\Big\}\\ &= \frac{1}{2}\sum_{s_1,s_1',s_2,..}\langle s_1|e^{\epsilon\boldsymbol{\varphi}_N\cdot\boldsymbol{\sigma}}|s_N'\rangle\langle s_N'|...|s_2'\rangle\langle s_2'|e^{\epsilon\boldsymbol{\varphi}_2\cdot\boldsymbol{\sigma}}|s_2\rangle\langle s_2|s_1'\rangle\langle s_1'|e^{\epsilon\boldsymbol{\varphi}_1\cdot\boldsymbol{\sigma}}|s_1\rangle. \quad (7.11)\end{aligned}$$

Here, for notational brevity, we suppressed the site index j and defined $\boldsymbol{\varphi}_n = \boldsymbol{\varphi}_j(\tau_n)$, where $\boldsymbol{\varphi} = (\varphi^x, \varphi^y, \varphi^z)$ is the vector in spin space.

Next, we need to compute the matrix elements $\langle s_n'|e^{\epsilon\boldsymbol{\varphi}_1\cdot\boldsymbol{\sigma}}|s_n\rangle$ and the inner products $\langle s_{n+1}|s_n'\rangle$. The former are diagonal by construction:

$$\langle s_n'|e^{\epsilon\boldsymbol{\varphi}_n\cdot\boldsymbol{\sigma}}|s_n\rangle = \delta_{s_n s_n'}\exp[\epsilon\varphi_n\sigma^z_{s_n s_n}], \quad (7.12)$$

where $\varphi_n = |\varphi(\tau_n)| = \sqrt{(\varphi^x)^2 + (\varphi^y)^2 + (\varphi^z)^2}$. The inner product is given by

$$\begin{aligned}\langle s_{n+1}|s_n'\rangle &= \langle s_{n+1}, \mathbf{e}_{n+1}|s_n', \mathbf{e}_n\rangle\\ &= \langle s_{n+1}|\exp[-i(\mathbf{e}_{n+1}\times\mathbf{e}_n)\cdot\boldsymbol{\sigma}]|s_n'; \mathbf{e}_{n+1}\rangle \quad (7.13)\\ &= \delta_{s_{n+1}s_n'} - i(\mathbf{e}_{n+1}\times\mathbf{e}_n)\cdot\boldsymbol{\sigma}_{s_{n+1}s_n'} + O(\epsilon^2).\end{aligned}$$

Next we define the infinitesimal angle of rotation of the quantization axis $\mathbf{e}_{n+1}$ into $\mathbf{e}_n$ as $\epsilon\,\boldsymbol{\Omega}_{n+1,n} = (\mathbf{e}_n\times\mathbf{e}_{n+1})$ and express Θ as

$$\begin{aligned}\Theta \quad &= \tfrac{1}{2}\mathrm{Tr}\{e^{\epsilon\varphi_N\sigma^z}e^{i\epsilon\boldsymbol{\Omega}_{1,N-1}\cdot\boldsymbol{\sigma}}e^{\epsilon\varphi_{N-1}\sigma^z}...\\ &\quad ...e^{i\epsilon\boldsymbol{\Omega}_{3,2}\cdot\boldsymbol{\sigma}}e^{\epsilon\varphi_2\sigma^z}e^{i\epsilon\boldsymbol{\Omega}_{2,1}\cdot\boldsymbol{\sigma}}e^{\epsilon\varphi_1\sigma^z}\}, \quad (7.14)\end{aligned}$$

where we denote the quantization axis at time $\tau = 0$ as $\mathbf{e}_1 = \mathbf{e}(0) = \widehat{z}$. In a continuum approximation, we have

$$\mathbf{e}_{n+1} = \mathbf{e}(\tau_{n+1}) = \mathbf{e}(\tau_n) + \epsilon\dot{\mathbf{e}}(\tau_n) + O(\epsilon^2), \quad (7.15)$$

where $\dot{\mathbf{e}}(\tau) = \partial\mathbf{e}/\partial\tau$.

The factors in the product on the r.h.s. of the Eq.(7.14) commute under the time ordering operator, so we may now express Θ as

$$\Theta = \frac{1}{2}\mathrm{Tr}\Big\{T_\tau\exp\Big[\int_0^\beta d\tau\{i\boldsymbol{\Omega}(\tau)+\varphi(\tau)\mathbf{e}(0)\}\cdot\boldsymbol{\sigma}\Big]\Big\}, \quad (7.16)$$

where $\mathbf{\Omega}(\tau_n) = \mathbf{\Omega}_{n+1,n} = \mathbf{e}(\tau_n) \times \dot{\mathbf{e}}(\tau_n)$. The term $i\Omega(\tau)$ may be identified with the well-known Berry phase term.

Although a general evaluation of this expression involves only a trace over a single spin, it appears to be difficult. We therefore consider the following approximations. The field $\mathbf{\Omega}$ is by definition a fluctuation field, i.e. it vanishes at the mean field level. It therefore makes sense to expand Θ in powers of $\mathbf{\Omega}$. In zeroth order we have

$$\begin{aligned} \Theta^{(0)} &= \tfrac{1}{2}\mathrm{Tr}\{e^{\epsilon\varphi_N\sigma^z}e^{\epsilon\varphi_{N-1}\sigma^z}.....e^{\epsilon\varphi_2\sigma^z}e^{\epsilon\varphi_1\sigma^z}\} \\ &= \tfrac{1}{2}\mathrm{Tr}\{e^{\int d\tau\varphi(\tau)\sigma^z}\} = \cosh\beta\varphi_0, \end{aligned} \tag{7.17}$$

where the time average φ_0 is defined as

$$\varphi = \beta^{-1}\int_0^\beta d\tau\varphi(\tau). \tag{7.18}$$

We note for later that $\Theta^{(0)}$ contains contributions from both longitudinal and transverse fluctuations about the mean field configuration.

In first order in $\mathbf{\Omega}$ we find

$$\Theta^{(1)} = \tfrac{1}{2}i\epsilon\textstyle\sum_{n_0=1}^{N-1}\mathrm{Tr}\{e^{\epsilon\sigma^z\sum_{n_2=n_0+1}^{N}\varphi_{n_2}}[\mathbf{\Omega}_{n_0+1,n_0}\cdot\boldsymbol{\sigma}]e^{\epsilon\sigma^z\sum_{n_1=1}^{n_0}\varphi_{n_1}}\}. \tag{7.19}$$

Higher order contributions in Ω may be derived but they lead to increasingly complicated expressions. In a continuum approximation, we may express $\Theta^{(1)}$ as

$$\Theta^{(1)} = \frac{i}{2}\int d\tau_0\mathrm{Tr}\{e^{\sigma^z\Phi(\beta,\tau_0)}[\mathbf{\Omega}(\tau_0)\cdot\boldsymbol{\sigma}]e^{\sigma^z\Phi(\tau_0,0)}\}, \tag{7.20}$$

where $\Phi(\beta,\tau_0) = \int_{\tau_0}^{\beta}d\tau\varphi(\tau)$ has been defined. We now recall that $\sigma^z = \mathbf{e}(0)\cdot\boldsymbol{\sigma}$ and use $e^{\sigma^z\Phi} = \cosh\Phi + \sigma^z\sinh\Phi$ to get

$$\begin{aligned} \Theta^{(1)} &= i\int d\tau_0[\cosh\Phi(\beta,\tau_0)\sinh\Phi(\tau_0,0) \\ &\quad + \sinh\Phi(\beta,\tau_0)\cosh\Phi(\tau_0,0)][\mathbf{\Omega}(\tau_0)\cdot\mathbf{e}(0)], \end{aligned} \tag{7.21}$$

where we also used $\mathrm{Tr}\{\boldsymbol{\sigma}\} = 0$, $\mathrm{Tr}\{\sigma^z\sigma^\lambda\} = 2\delta_{\lambda,z} = \mathrm{Tr}\{\sigma^\lambda\sigma^z\}$ and $\mathrm{Tr}\{\sigma^z\sigma^\lambda\sigma^z\} = 0$. Using another identity, $\sinh x\cosh y + \cosh x\sinh y = \sinh(x+y)$, and the periodic boundary condition relations $\Phi(\beta,\tau_0) + \Phi(\tau_0,0) = \Phi(\beta,0) = \beta\varphi_0$ we get

$$\Theta^{(1)} = i[\mathbf{\Omega}_0\cdot\mathbf{e}(0)]\sinh(\beta\varphi_0), \tag{7.22}$$

where $\mathbf{\Omega}_0 \equiv \int d\tau_0 \mathbf{\Omega}(\tau_0)$.

The partition function Eq. (7.8), which includes the first order correction in $\mathbf{\Omega}_0$, is then given by

$$Z = \frac{1}{C'} \int [d\varphi] \exp[-\beta(\mathcal{S}_\kappa + \mathcal{S}_{\rm loc} + \mathcal{S}_0)], \tag{7.23}$$

where the interaction part of the action is given by

$$\mathcal{S}_\kappa = \beta^{-1} \int_0^\beta d\tau \sum_{\mathbf{q},\nu} |\kappa_{\mathbf{q},\nu}|^{-1} \varphi^*_{\mathbf{q},\nu}(\tau) \varphi_{\mathbf{q},\nu}(\tau) \tag{7.24}$$

and the local part of the action $\mathcal{S}_{\rm loc} = \mathcal{S}^{\rm stat}_{\rm loc} + \mathcal{S}^{\rm dyn}_{\rm loc}$ has both static and dynamic contributions:

$$S^{\rm stat}_{\rm loc} = -\beta^{-1} \sum_j \ln\cosh(\beta\varphi_{j,0}) \tag{7.25}$$

$$S^{\rm dyn}_{\rm loc} = -i\beta^{-1} \sum_j \tanh(\beta\varphi_{j,0})[\mathbf{\Omega}_{j,0} \cdot \mathbf{e}_j(0)], \tag{7.26}$$

and $\mathcal{S}_0 = \beta^{-1} \ln C'$.

Our results agree with those of Ref. [115] except for an additional term involving the product of two time derivatives of the transverse field components at equal times. Such a term arises from expansion of Eq.7.16 in second order in Ω, if the time arguments are kept equal. The fluctuations we will be interested in (e.g. spin waves) are long-range correlated in time such that it does not make sense to single out only the equal time products of Ω. We also note that Angelucci and Jug [115] did not pay attention to the fact that the HS transformation changes its character if the eigenvalues $\kappa_{\mathbf{q},\nu}$ of the interaction kernel change sign.

7.3 Mean field solution

In this section, we consider the simplest case and compute the mean field free energy for the range of parameters of the model (6.1), for which the mean-field solution is a collinear magnetic state. In this case we can write $\boldsymbol{\varphi}_{j,\mu}(\tau) = \varphi^{\rm MF}\hat{\mathbf{m}}$, where $\hat{\mathbf{m}}$ is a normalized 3-component vector pointing in the direction of the spontaneous magnetization, which is the same for all sublattice sites μ. The trace in spin space is obtained as

$$\Theta^{\rm MF}_{j,\mu} = \frac{1}{2}{\rm Tr}_j\{e^{-\beta\varphi^{\rm MF}[\boldsymbol{\sigma}\cdot\mathbf{m}]}\} = \cosh(\beta\varphi^{\rm MF}),$$

where the mean field expression for the fields $\varphi_{\mathbf{q},\nu}(\tau)$ is given by $\varphi^{\rm MF}_{\mathbf{q},\nu} = (NN_s)^{1/2}\delta_{\mathbf{q},0}\varphi^{\rm MF}m_{\mathbf{q},\nu}$, where N is the total number of unit cells and N_s is three times the number of the sublattices in the unit cell. The normalized unit vector $m_{\mathbf{q},\nu} = N_s^{-1/2}\sum_{\mu,\alpha} m^{\alpha}u^{\mu\alpha}_{\mathbf{q},\nu}$ is expressed in terms of the eigenvectors $u^{\mu\alpha}_{\mathbf{q},\nu}$. The mean-field partition function (7.8) can be easily evaluated and equals

$$Z^{\rm MF} = \frac{1}{C'}\exp\left[-NN_s\left\{\beta|\kappa_0|^{-1}(\varphi^{\rm MF})^2 - \ln\left(\cosh(\beta\varphi^{\rm MF})\right)\right\}\right], \tag{7.27}$$

provided $\kappa_{\mathbf{q}=0,\nu} = \kappa_0$ is independent of ν. Here $\varphi^{\rm MF}$ is the value minimizing the free energy $F^{\rm MF} = -\beta^{-1}\ln Z^{\rm MF}$ and is given by the solution of the transcendental equation

$$2|\kappa_0|^{-1}\varphi^{\rm MF} = \tanh(\beta\varphi^{\rm MF}). \tag{7.28}$$

The full partition function is given by

$$Z = \frac{Z^{\rm MF}}{C'}\int[d\delta\varphi]\exp\left[-\beta\delta\mathcal{S}\right],$$

where $\delta\mathcal{S} = \delta\mathcal{S}^{\rm stat} + \delta\mathcal{S}^{\rm dyn}$ is the fluctuational part of the action.

Despite the anisotropic form of the interactions in the Hamiltonian (6.1), the mean-field solution is highly degenerate with respect to the orientation of the spontaneous magnetization vector $\hat{\mathbf{m}}$. It is therefore of interest to calculate the corrections to the mean-field solution capturing the anisotropy of the free energy with respect to the order parameter orientation.

7.4 Evaluation of the free energy in the Gaussian approximation

The first systematic free energy correction is that from Gaussian fluctuations about the mean-field solution obtained by expanding the free energy, or equivalently the action, to lowest order in the fluctuation field $\delta\varphi_{\mathbf{q},\nu}(\tau) = \varphi_{\mathbf{q},\nu}(\tau) - \varphi^{\rm MF}_{\mathbf{q},\nu}$. Introducing the time Fourier transform

$$\varphi_{\mathbf{q},\nu}(\tau) = \sum_{\omega_n}\varphi_{\mathbf{q},\nu,\omega_n}\exp\left[i\omega_n\tau\right],$$

where $\omega_n = 2\pi n\beta^{-1}$ are bosonic Matsubara frequencies, we immediately get the following bilinear form of the Gaussian fluctuation part of the action:

$$\delta\mathcal{S}\{\delta\varphi_{\mathbf{q},\nu}\} = \beta^{-1}\sum_{\mathbf{q},\nu,\nu'}\sum_{\omega_n} A_{\mathbf{q},\omega_n;\nu\nu'}\delta\varphi^{(+)*}_{\mathbf{q},\nu,-\omega_n}\delta\varphi^{(+)}_{\mathbf{q},\nu',\omega_n}, \tag{7.29}$$

where we defined

$$\delta\varphi^{(+)}_{\mathbf{q},\nu,\omega_n} = \frac{1}{2}[s(\kappa_{\mathbf{q},\nu})\delta\varphi_{\mathbf{q},\nu,\omega_n} + s^*(\kappa_{\mathbf{q},\nu})\delta\varphi^*_{-\mathbf{q},\nu,\omega_n},]. \tag{7.30}$$

Here the fluctuation matrix elements $A_{\mathbf{q},\omega_n;\nu\nu'}$ describe the weight of the Gaussian fluctuations of wavevector $\mathbf{q}$, frequency ω_n and polarization ν.

Here, a comment is in order. The fields $\delta\varphi$ do not obey the relation $\delta\varphi^*_{\mathbf{q},\nu}(\tau_1) = \delta\varphi_{-\mathbf{q},\nu}(\tau_1)$, i.e. their spatial Fourier transforms are not real-valued, which leads to the combination of fluctuation amplitudes at momenta $\mathbf{q}$ and $-\mathbf{q}$, weighted by the phase factors $s(\kappa_{\mathbf{q},\nu})$. Only symmetric combination of the fields, gives contribution to the free energy because the antisymmetric combination with $\delta\varphi^{(-)}_{\mathbf{q},\nu,\omega_n} = \frac{1}{2}[s(\kappa_{\mathbf{q},\nu})\delta\varphi_{\mathbf{q},\nu,\omega_n} - s^*(\kappa_{\mathbf{q},\nu})\delta\varphi^*_{-\mathbf{q},\nu,\omega_n}]$ drops out.

7.4.1 Static fluctuations

We start by considering the contribution of static Gaussian fluctuations to the free energy. The expansion of $\mathcal{S}^{\rm stat}_{\rm loc}$ in terms of fluctuation amplitudes up to second order is given by

$$\begin{aligned}\delta\mathcal{S}^{\rm stat}_{\rm loc} &= -\beta^{-1}\delta\{\textstyle\sum_j \ln\cosh(\beta[(\varphi^{\rm MF}\hat{\mathbf{m}} + \delta\boldsymbol{\varphi}_{i\mu,0})^2]^{1/2}) \\ &= -\tfrac{1}{2}\textstyle\sum_j\{\beta_c\delta\boldsymbol{\varphi}^2_{i\mu,0} + \beta_m(\hat{\mathbf{m}}\cdot\delta\boldsymbol{\varphi}_{i\mu,0})^2\},\end{aligned} \tag{7.31}$$

where $\beta_m = (1-t^2)\beta - \beta_c$ and $\beta_c = \frac{1}{T_c}$. Here $t = \tanh(\beta\varphi^{\rm MF})$ denotes the dimensionless measure of magnetization, which is zero at T_c and rises monotonically upon cooling to the saturation magnetization ($t = 1$) at $T = 0$. The components of $\delta\boldsymbol{\varphi}_{i\mu,0}$ may be expressed in terms of the momentum space fluctuation amplitudes $\delta\varphi_{\mathbf{q},\nu,0} = \varphi_{\mathbf{q},\nu,0} - \varphi^{\rm MF}_{\mathbf{q},\nu}$ as

$$\delta\varphi^{\alpha}_{i\mu,0} = \sum_{\mathbf{q},\nu}{\rm Re}\{s(\kappa_{\mathbf{q},\nu})\chi^*_{\mathbf{q},\nu;j\alpha}\delta\varphi_{\mathbf{q},\nu,0}\}. \tag{7.32}$$

Now, we can rewrite $\delta\mathcal{S}^{\rm stat}_{\rm loc}$ in the same form as in Eq.(7.29):

$$\delta\mathcal{S}^{\rm stat} = \beta^{-1}\sum_{\mathbf{q};\nu,\nu'} A^{\rm stat}_{\mathbf{q},\nu\nu'}\delta\varphi^{(+)*}_{\mathbf{q},\nu,0}\delta\varphi^{(+)}_{\mathbf{q},\nu',0}, \tag{7.33}$$

with the matrix $A^{\rm stat}_{\mathbf{q},\nu\nu'}$ found to be

$$A^{\rm stat}_{\mathbf{q},\nu\nu'} = \beta[(|\kappa_{\mathbf{q},\nu}|^{-1} - \frac{\beta_c}{2})\delta_{\nu\nu'} - \frac{\beta_m}{2}m_{\mathbf{q}\nu}m_{\mathbf{q}\nu'}]. \tag{7.34}$$

Now the integration over the fluctuation amplitudes may be performed, with the result

$$\begin{aligned} Z^{\rm stat} = &\ \tfrac{Z^{\rm MF}}{C'}\int[d\varphi]\exp\left[-\beta\delta\mathcal{S}^{\rm stat}\right] \\ &= Z^{\rm MF}\exp\left[-\beta\delta\mathcal{F}^{\rm stat}\right], \end{aligned} \tag{7.35}$$

which gives the free energy contribution to be equal to

$$\delta\mathcal{F}^{\rm stat} = \frac{1}{2}\beta^{-1}\sum_{\mathbf{q}}\ln\det\{A^{\rm stat}_{\mathbf{q},\nu\nu'}\}. \tag{7.36}$$

7.4.2 Dynamic fluctuations

We now turn to the dynamic fluctuations, obtained by expanding $\mathcal{S}^{\rm dyn}_{\rm loc}$ to quadratic order in the finite frequency Fourier components $\delta\boldsymbol{\varphi}_{j,\omega_n}$ of the time-dependent fluctuation fields. First we note that $\boldsymbol{\Omega}_0 = \int d\tau_0\boldsymbol{\Omega}(\tau_0)$ may be expressed in terms of the transverse fluctuation amplitudes $\delta\varphi^{{\rm tr},\alpha}_j(\tau) = \sum_{\alpha'}P_{\alpha\alpha'}\delta\varphi^{\alpha'}_j(\tau)$, where $P_{\alpha\alpha'} = \delta_{\alpha\alpha'} - m_\alpha m_{\alpha'}$, as

$$\begin{aligned} \boldsymbol{\Omega}_{j,0} &= \textstyle\int_0^\beta d\tau\delta\mathbf{e}_j(\tau)\times\delta\dot{\mathbf{e}}_j(\tau) \\ &= \tfrac{1}{(\varphi^{\rm MF})^2}\textstyle\int_0^\beta d\tau\delta\boldsymbol{\varphi}^{\rm tr}_j(\tau)\times\tfrac{\partial}{\partial\tau}\delta\boldsymbol{\varphi}^{\rm tr}_j(\tau) \\ &= \tfrac{\beta_c^2\beta}{t^2}\textstyle\sum_{\omega_n} i\omega_n\delta\boldsymbol{\varphi}^{\rm tr}_{j,-\omega_n}\times\delta\boldsymbol{\varphi}^{\rm tr}_{j,\omega_n}. \end{aligned} \tag{7.37}$$

The contribution of this $\boldsymbol{\Omega}_0$-term to the action is then given by (taking $\mathbf{e}_j(0) = \hat{\mathbf{m}}$)

$$\delta\mathcal{S}^{\rm dyn}_{\rm loc} = -\frac{i}{\beta}\sum_j\tanh(\beta\varphi^{\rm MF})[\boldsymbol{\Omega}_{j,0}\cdot\mathbf{e}_j(0)]\}]. \tag{7.38}$$

It is instructive to write components of the fluctuation amplitudes in the following form ($j \equiv (i,\mu)$)

$$\begin{aligned} \delta\varphi^\alpha_{i\mu}(\tau) &= \textstyle\sum_{\mathbf{q},\nu=1}^{3N_s}{\rm Re}\{s(\kappa_{\mathbf{q},\nu})N^{-1/2}e^{-i\mathbf{q}\mathbf{R}_i}u^{\mu\alpha}_{\mathbf{q},\nu}\delta\varphi_{\mathbf{q},\nu}(\tau)\} \\ &= \tfrac{1}{2}N^{-1/2}\textstyle\sum_{\mathbf{q},\nu=1}^{3N_s}u^{\mu\alpha}_{\mathbf{q},\nu}\{s(\kappa_{\mathbf{q},\nu})e^{-i\mathbf{q}\mathbf{R}_i}\delta\varphi_{\mathbf{q},\nu}(\tau) \\ &\qquad + s^*(\kappa_{\mathbf{q},\nu})e^{i\mathbf{q}\mathbf{R}_i}\delta\varphi^*_{\mathbf{q},\nu}(\tau)\}, \end{aligned} \tag{7.39}$$

where we have assumed that eigenfunctions $u^{\mu\alpha}_{\mathbf{q},\nu} = (u^{\mu\alpha}_{\mathbf{q},\nu})^* = u^{\mu\alpha}_{-\mathbf{q},\nu}$ are real-valued and inversion symmetric. Performing the Fourier transform in time, we get

$$\begin{aligned}\delta\varphi^{\alpha}_{i\mu,\omega_n} = \; & \tfrac{1}{2}\tfrac{1}{\sqrt{N}}\textstyle\sum_{\mathbf{q},\nu,\omega_n} u^{\mu\alpha}_{\mathbf{q},\nu}\{s(\kappa_{\mathbf{q},\nu})e^{-i\mathbf{q}\mathbf{R}_i}\delta\varphi_{\mathbf{q},\nu,\omega_n} \\ & + s^*(\kappa_{\mathbf{q},\nu})e^{i\mathbf{q}\mathbf{R}_i}\delta\varphi^*_{\mathbf{q},\nu,-\omega_n}\}. \end{aligned} \tag{7.40}$$

The contribution of the $\mathbf{\Omega}_{j,0}$-term (7.37) to the local action is then given by

$$\begin{aligned}&\delta\mathcal{S}^{\rm dyn}_{\rm loc} = -\frac{i}{\beta}\frac{(i\beta\beta_c^2)}{t}\sum_{\mathbf{q},\omega_n,\nu,\nu'}\omega_n D_{\mathbf{q}\nu\nu'}\Big[s(\kappa_{\mathbf{q},\nu})\delta\varphi_{\mathbf{q},\nu,\omega_n}s(\kappa_{-\mathbf{q},\nu'})\delta\varphi_{-\mathbf{q},\nu',\omega_n} + \\ &s^*(\kappa_{\mathbf{q},\nu})\delta\varphi^*_{\mathbf{q},\nu,-\omega_n}s^*(\kappa_{-\mathbf{q},\nu'})\delta\varphi^*_{-\mathbf{q},\nu',-\omega_n} + s(\kappa_{\mathbf{q},\nu})\delta\varphi_{\mathbf{q},\nu,\omega_n}s^*(\kappa_{\mathbf{q},\nu'})\delta\varphi^*_{\mathbf{q},\nu',-\omega_n} + \\ &s^*(\kappa_{\mathbf{q},\nu})\delta\varphi^*_{\mathbf{q},\nu,-\omega_n}s(\kappa_{\mathbf{q},\nu'})\delta\varphi_{\mathbf{q},\nu',\omega_n}\Big] \\ &= \frac{\beta_c^2}{t}\sum_{\mathbf{q},\omega_n,\nu,\nu'}\omega_n D_{\mathbf{q}\nu\nu'}\delta\varphi^{(+)}_{\mathbf{q},\nu,-\omega_n}\delta\varphi^{(+)*}_{\mathbf{q},\nu',\omega_n}, \\ &D_{\mathbf{q}\nu\nu'} = \sum_{\mu}\sum_{\alpha_1,\alpha_2,\alpha_3}\sum_{\alpha_2',\alpha_3'} m_{\alpha_1}\epsilon_{\alpha_1\alpha_2\alpha_3}P_{\alpha_2\alpha_2'}P_{\alpha_3\alpha_3'}u^{\mu\alpha_2'}_{\mathbf{q}\nu}u^{\mu\alpha_3'}_{\mathbf{q}\nu'}.\end{aligned} \tag{7.41}$$

The dynamic fluctuation expression for the interaction part of the action (7.24) is then given by

$$\begin{aligned}\delta S_\kappa \; &= \tfrac{1}{\beta}\textstyle\int_0^\beta d\tau \sum_{\mathbf{q},\nu}|\kappa_{\mathbf{q},\nu}|^{-1}\delta\varphi_{\mathbf{q},\nu}(\tau)\delta\varphi^*_{\mathbf{q},\nu}(\tau) = \\ &= \textstyle\sum_{\mathbf{q},\omega_n\neq 0,\nu}|\kappa_{\mathbf{q},\nu}|^{-1}\delta\varphi^{(+)}_{\mathbf{q},\nu,\omega_n}\delta\varphi^{(+)*}_{\mathbf{q},\nu,-\omega_n}.\end{aligned} \tag{7.42}$$

Adding the two contributions we find

$$\delta\mathcal{S}^{\rm dyn} = \beta^{-1}\sum_{\mathbf{q},\omega_n\neq 0;\nu,\nu'} A^{\rm dyn}_{\mathbf{q},\omega_n;\nu\nu'}\delta\varphi^{(+)*}_{\mathbf{q},\nu,\omega_n}\delta\varphi^{(+)}_{\mathbf{q},\nu',\omega_n}, \tag{7.43}$$

where $A^{\rm dyn}_{\mathbf{q},\omega_n;\nu\nu'}$ is given by

$$A^{\rm dyn}_{\mathbf{q},\omega_n;\nu\nu'} = \beta[|\kappa_{\mathbf{q},\nu}|^{-1}\delta_{\nu\nu'} + \beta_c^2 t^{-1}\omega_n D_{\mathbf{q}\nu\nu'}]. \tag{7.44}$$

One may now perform the integration over the fluctuation amplitudes resulting in

$$Z^{\rm dyn} = Z^{\rm MF}\exp\left[-\beta\delta\mathcal{F}^{\rm dyn}\right],$$

which gives the free energy contribution to be equal to

$$\delta\mathcal{F}^{\rm dyn} = \frac{1}{2\beta}\sum_{\mathbf{q},\omega_n\neq 0} \ln\det\{A^{\rm dyn}_{\mathbf{q},\omega_n;\nu\nu'}\}. \tag{7.45}$$

In summary, in the approximation in which the corrections to the free energy come predominantly from Gaussian fluctuations, the partition function is found to be

$$Z = \frac{Z^{\rm MF}}{C'}\exp\left[-\beta(\delta\mathcal{F}^{\rm stat}+\delta\mathcal{F}^{\rm dyn})\right].$$

As a sanity check, in the Technical details section at the end of the chapter we compute the contribution of dynamic fluctuations to the free energy at low temperature $T << T_c$ and show that the contribution of transverse fluctuations from the functional integral representation (7.45) recovers the spin wave theory result.

7.5 Lifting mean-field degeneracies in quantum Heisenberg-compass spin model

As a concrete application of the formalism describe above, in this section we compute the contribution of Gaussian fluctuations to the free energy in the quantum Heisenberg-compass model on the cubic lattice. This model is one of the simplest models described by Eq. (6.1), in which the interaction matrix has only diagonal elements:

$$J^{\alpha\alpha}_{j,j'} = \frac{1}{2}\delta_{j',j+\tau_\mu}\left[J + K\delta_{\alpha,\mu}\right],$$

where $\tau_\mu = \pm x, \pm y, \pm z$ labels nearest neighbor bonds. The eigenvalues of the exchange operator are given by

$$\kappa_{\mathbf{q},\nu} = \sum_\alpha (J + K\delta_{\alpha,\nu})\cos q_\alpha.$$

The three eigenvectors $\mathbf{u}_{\mathbf{q}\nu}$ point along the three cubic axes, such that the components are $u^\alpha_{\mathbf{q}\nu} = \delta_{\nu,\alpha}$, $\alpha = x, y, z$. Provided $J < 0$ and $K < |J|$ the ferromagnetic mean field solution $\varphi_{\rm MF}$ is given by the solution of the non-linear equation $2|\kappa_0|^{-1}\varphi_{\rm MF} = \tanh(\beta\varphi_{\rm MF})$.

The fluctuation contribution is described by a 3×3-matrix

$$A_{\mathbf{q},\omega_n,\nu\nu'} = \delta_{\omega_n,0}A^{stat}_{\mathbf{q},\nu\nu'} + (1-\delta_{\omega_n,0})A^{dyn}_{\mathbf{q},\omega_n,\nu\nu'}, \tag{7.46}$$

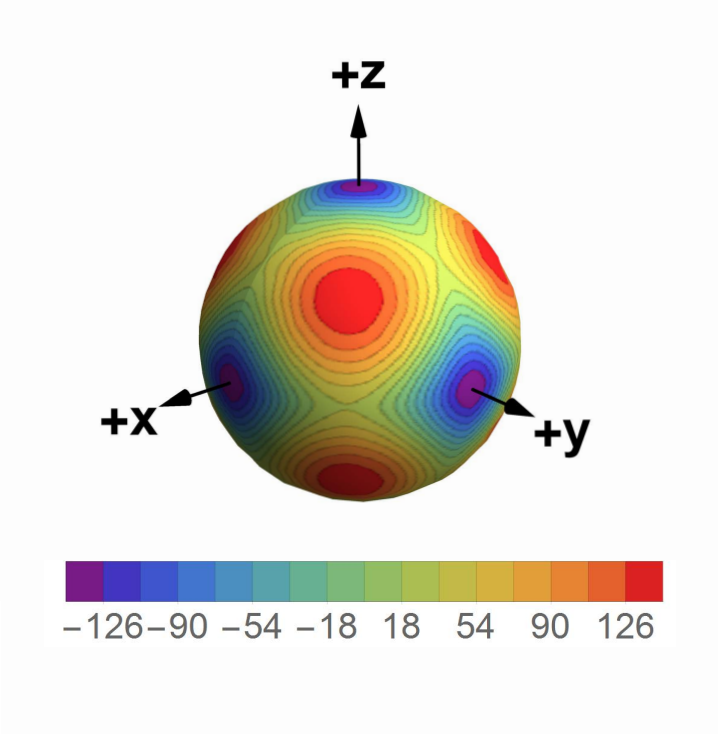

Figure 7.1: (a) The magnitude of the Gaussian contribution to the free energy $\delta\mathcal{F}(\theta,\phi)$ computed for $J=-1$, $K=-1.1$ and $\beta=\beta_c+1$ is plotted on the surface of the unit sphere. The minima of the free energy are shown by deep blue color. The preferred directions of the magnetization are along the cubic axes. The energy scale is shown in units of J.

whose matrix elements can be easily obtained for arbitrary orientation of magnetization, $\hat{\mathbf{m}} = (\sin\theta\cos\phi, \sin\theta\sin\phi, \cos\theta)$. Using Eq.(7.34), we get the following expression for the static contribution:

$$A^{stat}_{\mathbf{q},\nu\nu'} = \begin{pmatrix} d_{\mathbf{q},x} & g_{x,y} & g_{x,z} \\ g_{y,x} & d_{\mathbf{q},y} & g_{y,z} \\ g_{z,x} & g_{z,y} & d_{\mathbf{q},z} \end{pmatrix}, \tag{7.47}$$

where $d_{\mathbf{q},\nu} = |\beta\kappa^{-1}_{\mathbf{q},\nu}| - b_m m_\nu^2 - b_{tr}$, $g_{\nu\nu'} = -b_m m_\nu m_{\nu'}$, $\kappa^{-1}_{\mathbf{q},\nu} = 1/(3J\gamma_{\mathbf{q}} + K\cos q_\nu)$, $\gamma_{\mathbf{q}} = \frac{1}{3}\sum_\beta \cos q_\beta$, $b_m = \frac{1}{2}(1-t^2)$, $b_{tr} = \frac{1}{2}\beta_c\beta$. We recall that $t \equiv \tanh(\beta\varphi_{\rm MF})$ is a dimensionless measure of the magnetization.

The dynamical matrix is defined by Eq. (7.44), which for the cubic lattice simplifies to

$$\begin{aligned} A^{dyn}_{\mathbf{q},\omega_n,\nu\nu'} = & \quad \beta^{-1}[|\kappa_{\mathbf{q},\nu}|^{-1}\delta_{\nu,\nu'} \\ & + \quad \omega_n\beta_c^2 t^{-1}\textstyle\sum_{\alpha_1,\alpha_2,\alpha_3} m_{\alpha_1}\epsilon_{\alpha_1\alpha_2\alpha_3}P_{\alpha_2\nu}P_{\alpha_3\nu'}. \end{aligned} \tag{7.48}$$

The matrix $A_{\mathbf{q},\omega_n,\nu\nu'}$ may be diagonalized for fixed $\mathbf{q}$,ω_n. Its eigenvalues $\lambda_{\nu,\mathbf{q},\omega_n} = \lambda_{\nu,\mathbf{q},\omega_n}(\theta,\phi)$ have a rather complex dependence on angles θ and ϕ, implying an angular dependent profile of the fluctuation free energy $\delta\mathcal{F} = \delta\mathcal{F}(\theta,\phi)$. After integrating over the fluctuations, we obtain

$$\begin{aligned} Z \quad &= \frac{Z^{\rm MF}}{C'}\exp\left[-\beta\delta\mathcal{F}\right], \\ \delta\mathcal{F} \quad &= \frac{1}{2\beta}\sum_{\mathbf{q},\omega_n,\nu}\ln\lambda_{\nu,\mathbf{q},\omega_n} + \text{const}\,. \end{aligned} \tag{7.49}$$

In performing the summation over the Matsubara frequencies, we need to regularize the expression by subtracting a term $\ln[\omega_n\beta_c^2/\beta t]$ from $\ln\lambda_{\nu,\mathbf{q},\omega_n}$, which will guarantee convergence of the ω_n summation. The subtracted term corresponds to the fluctuation free energy at the transition point.

In Fig. 7.1, we show the angular dependence of $\delta\mathcal{F}(\theta,\phi)$ computed for representative parameters $J = -1$ and $K = -1.1$. The magnitude of $\delta\mathcal{F}(\theta,\phi)$ is presented as a color-coded plot on the unit sphere, where the minima and maxima of the free energy are shown by deep blue and red color, correspondingly. We see that the minima of $\delta\mathcal{F}(\theta,\phi)$ are achieved when the magnetization is directed along one of the cubic axes. This finding

clearly shows that while mean field free energy is isotropic, the fluctuation free energy depends upon the direction of the order parameter, indicating that the contribution of fluctuations to the free energy removes the degeneracy of the equilibrium state found on the mean field level.

7.6 Summary

In summary, in this chapter we elaborated on a method for calculating the free energy of quantum spin systems using functional integral techniques. We employ powerful formal technique known as the Hubbard-Stratonovich transformation to map an interacting quantum spin system into a collection of "single spin"-systems coupled to a fictitious fluctuating magnetic field. This method is very general and can be applied to any biquadratic quantum spin model. Indeed, the Hubbard-Stratonovich transformation applied to isotropic Heisenberg systems in the low temperature limit has been considered before [115, 116, 117], but has not been applied, as far as we know, to calculate the free energy of anisotropic quantum spin systems. In this work, we presented a microscopic derivation of the path-integral representation of the quantum-spin-system partition function for a particular class of quantum spin models with anisotropic bond-directional spin interactions. We determined the contribution of Gaussian fluctuations to the free energy at all temperatures in the ordered phase. Our analysis shows explicitly that the fluctuation free energy has a complex angular dependence, thus breaking the rotational degeneracy of the mean-field ground state.

We believe that the proposed method holds good promise to understand directional ordering in systems with anisotropic bilinear interactions, which are common in SOC systems. In these systems, the high degeneracy of the mean-field solution is lifted by the anisotropy of the spin-spin interaction, such that the spontaneous magnetization is pinned along certain preferred directions. The latter may change with temperature.

For illustration, we applied the above analysis to the quantum Heisenberg-compass spin model and show that the direction of the order parameter in spin space is selected by fluctuations and is determined by the competition between Heisenberg and compass terms. For the range of parameters for which the ferromagnetic state is the ground state, the Gaussian fluctuations select the cubic axes as directions of the magnetization.

7.7 Technical details

Here we calculate the contribution of dynamic fluctuations to the free energy at low temperature $T << T_c$. It is known that the leading contribution comes from spin wave excitations. The purpose of this appendix is to show that the contribution of transverse fluctuations from the functional integral representation recovers the spin wave theory result.

As a simple example we calculate the contribution of dynamic fluctuations for the case $\kappa_{\mathbf{q},\nu} = 3J\gamma_q$, where $\gamma_q = \frac{1}{3}\sum_\alpha \cos q_\alpha$ and $J < 0$. The spin wave excitation energy in our representation is given by

$$\omega_{\mathbf{q}} = \frac{t}{\beta_c^2 |\kappa_{\mathbf{q}=0}||\kappa_{\mathbf{q},\nu}|}\Big[|\kappa_{\mathbf{q}=0}| - |\kappa_{\mathbf{q},\nu}|s^2(\kappa_{\mathbf{q}\nu})\Big]. \tag{7.50}$$

In the limit $q \ll 1$, it can also be significantly simplified:

$$\omega_{\mathbf{q}} \approx \frac{3}{4}|J|[1-\gamma_q]. \tag{7.51}$$

In this limit, the dynamic fluctuation matrix then takes the form

$$A^{\rm dyn}_{\mathbf{q},\omega_n;\nu,\nu'} = \frac{\beta_c^2}{\beta t}\begin{pmatrix} \omega_{\mathbf{q}} & \omega_n \\ -\omega_n & \omega_{\mathbf{q}} \end{pmatrix}. \tag{7.52}$$

Its determinant is equal to

$$\det\{A^{\rm dyn}_{\mathbf{q},\omega_n;\nu,\nu'}\} = \left(\frac{\beta_c^2}{\beta t}\right)^2 \left[\omega_n^2 + \omega_{\mathbf{q}}^2\right]. \tag{7.53}$$

Recalling that the transverse fluctuation free energy is given by

$$\delta\mathcal{F}^{\rm tr} = \frac{1}{2\beta}\sum_{\mathbf{q},\omega_n\neq 0} \ln\det\{A^{\rm dyn}_{\mathbf{q},\omega_n;\nu\nu'}\},$$

the contribution to the partition function is found to be

$$\begin{aligned} Z^{\rm tr} &= \exp[-\beta\delta\mathcal{F}^{\rm tr}] = \exp[-\tfrac{1}{2}\textstyle\sum_{\mathbf{q},\omega_n\neq 0}\ln\det\{A^{\rm dyn}_{\mathbf{q},\omega_n;\nu\nu'}\}] \\ &= \exp[-\tfrac{1}{2}\textstyle\sum_{\mathbf{q},\omega_n\neq 0}\{\ln(\beta^{-1}\beta_c^2 t^{-1})^2 + \ln[\omega_n^2+\omega_{\mathbf{q}}^2]\}. \end{aligned} \tag{7.54}$$

The first term in the curly brackets give simple constant renormalization. The summation over Matsubara frequencies in the second term gives

$$X_{\mathbf{q}} = {\rm Re}\tfrac{1}{2}\textstyle\sum_{\omega_n}\ln[\omega_n^2+\omega_{\mathbf{q}}^2] = {\rm Re}\tfrac{1}{2}\sum_{\omega_n}\ln[(i\omega_n)^2-\omega_{\mathbf{q}}^2] \tag{7.55}$$

$$= \tfrac{1}{2}\beta\omega_{\mathbf{q}} + \ln\left[1-\exp(-\beta\omega_{\mathbf{q}})\right], \tag{7.56}$$

which leads to the free energy contribution

$$\delta\mathcal{F}^{\rm tr} = \frac{1}{2}\sum_{\mathbf{q}}\{\omega_{\mathbf{q}} + 2\beta^{-1}\ln[1-\exp(-\beta\omega_{\mathbf{q}})]\} + const. \tag{7.57}$$

To get this result we differentiate $X_{\mathbf{q}}$ with respect to $\omega_{\mathbf{q}}$

$$\frac{\partial}{\partial\omega_{\mathbf{q}}}X_{\mathbf{q}} = \tfrac{1}{2}\textstyle\sum_{\omega_n}[\frac{1}{i\omega_n+\omega_{\mathbf{q}}} - \frac{1}{i\omega_n-\omega_{\mathbf{q}}}] \tag{7.58}$$

$$= \tfrac{1}{2}\beta[-n_B(-\omega_{\mathbf{q}}) + n_B(\omega_{\mathbf{q}})] \tag{7.59}$$

where $n_B(\omega_{\mathbf{q}}) = [\exp(\beta\omega_{\mathbf{q}})-1]^{-1}$ is the Bose distribution function.

The term $\sum_{\mathbf{q}}\omega_{\mathbf{q}}$ is the zero point fluctuation contribution of the two transverse modes to the ground state energy (note that $\omega_{\mathbf{q}}$ is independent of ν for the isotropic model considered). There must be an additional constant contribution $\delta\omega_0$ to the ground state energy, which is not completely captured by the Gaussian fluctuation contribution, such that $\sum_{\mathbf{q}}\omega_{\mathbf{q}} + \delta\omega_0 \propto \sum_{\mathbf{q}}\gamma_{\mathbf{q}}$, which sums to zero. Recall that for the isotropic model the ground state is identical to the mean field ground state, such that the fluctuation contribution to the ground state energy vanishes. The fluctuation contribution to the internal energy is then given

$$\delta U^{\rm dyn} = \delta\mathcal{F}^{\rm dyn} + \beta\frac{\partial\delta\mathcal{F}^{\rm dyn}}{\partial\beta} = \sum_{\mathbf{q}}\omega_{\mathbf{q}}\{\frac{1}{2} + n_B(\omega_{\mathbf{q}})\} \tag{7.60}$$

This is identical with the standard result of spin wave theory, except that $\omega_{\mathbf{q}}$ differs from the spin wave result at higher q. At low temperatures $\delta F^{\rm dyn}$ provides the leading contribution to the thermodynamic quantities, e.g. $\delta U^{\rm dyn} \propto T^{5/2}$, whereas the longitudinal fluctuations contribute an exponentially small term. As $\omega_{\mathbf{q}} = \frac{1}{2}|J|q^2 + O(q^4)$, the leading low temperature behavior of $\delta U^{\rm dyn}$ agrees exactly with the conventional spin wave result.

Chapter 8

Selection of direction of the ordered moments in Na_2IrO_3 and $\alpha-RuCl_3$

8.1 Introduction

In this chapter, we discuss in detail the models and the mechanisms which lead to the stabilization of magnetic ordering in two compounds: Na_2IrO_3 and $\alpha-RuCl_3$. Several experiments have shown that the low-temperature phase of Na_2IrO_3 has collinear zigzag long-range magnetic order [8, 47, 48, 49, 59, 119, 120]. In addition, recent diffuse magnetic x-ray scattering data have determined the spin orientation in this zigzag state and showed that it is along the 44.3° direction with respect to the a axis, which corresponds to approximately half way in between the cubic x and y axes [120]. Both of these findings are in disagreement with the original KH model [46, 14], which predicts the zigzag phase only for the antiferromagnetic nearest neighbor Kitaev interaction with the magnetic moments along the cubic axes, while the Kitaev interaction in Na_2IrO_3 is ferromagnetic [61]. The direction also contradicts our order-by-disorder predictions from the previous two chapters. This shows that one needs to extend the nearest neighbor model by including some additional interactions in order to explain these experimental observations.

$\alpha-RuCl_3$ also shows collinear antiferromagnetic zigzag ground state [15, 121, 122, 123]. Recent X-ray and neutron scattering diffraction data [122, 123] indicate that the best fit to the collinear structure is obtained for the antiferromagnetic nearest neighbor Kitaev interaction and when the spin direction points 35° out of the ab-plane, i.e. along one of the cubic directions. This suggests that the microscopic origin of the zigzag ground state in $\alpha-RuCl_3$ might be quite different from the one in Na_2IrO_3, and that it can be described by the nearest neighbor KH model [14].

In both cases, the available experimental data provides an important check of the validity of any model proposed to describe the magnetic properties of Na_2IrO_3 and $\alpha-RuCl_3$, as it should correctly predict not only the type of the magnetic order but also its orientation in space.

In this work we consider two models, the nearest neighbor KH model [1, 46, 14] and its more complicated counterpart, dubbed J_1-K_1-J_2-K_2-J_3 model [10], and study how the preferred directions of the mean field order parameter are selected in these models. The formal procedure which we will be using here is based on the derivation of the fluctuational part of the free energy by integrating out the leading thermal fluctuations, and by determining which orientations of the order parameter correspond to the free energy minimum. This approach is based on the HS transformation and was outlined in Refs. [19, 20] to which we refer the reader for technical details. In both models, the thermal fluctuations select the cubic axes as the preferred directions for spins, which describes the experimental situation in $\alpha-RuCl_3$ but not in Na_2IrO_3.

We have also checked that in both models the quantum fluctuations (taken into account either using the quantum version of HS approach or within the semiclassical spin-wave approach) lift the accidental degeneracy of the classical solution and also select the cubic axes as the preferred directions for spins. We did not present these calculations here as they bring no new results compared with more simple analysis of thermal fluctuations.

The important point which we stress in this chapter is that the selection of correct "diagonal" direction of the spins observed in Na_2IrO_3 might happen already on the mean-field level by inclusion small off-diagonal positive interaction Γ as soon as it is larger than the energy gain of order $1/S$ due to the quantum fluctuations.

This chapter is organized as follows. In Sec. 8.2 we study the order by disorder

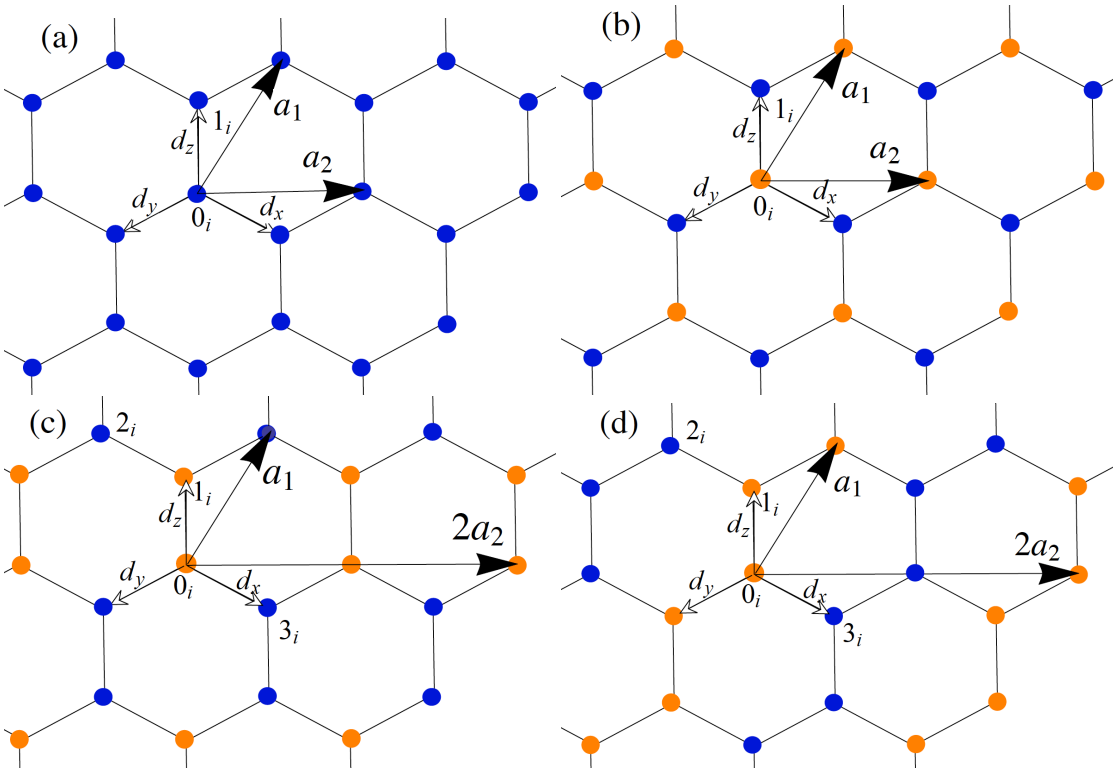

Figure 8.1: Four possible magnetic configurations: (a) FM ordering; (b) AF Néel order; (c) AF stripy order; (d) AF zigzag order. Red and blue circles correspond to up and down spins. Here $\boldsymbol{a}_1 = (\frac{\sqrt{3}}{2}\hat{x} + \frac{3}{2}\hat{y})$ and $\boldsymbol{a}_2 = \sqrt{3}\hat{x}$ are two primitive translations. The bond vectors are $\boldsymbol{d}_x = (\frac{\sqrt{3}}{2}\hat{x} - \frac{1}{2}\hat{y})$, $\boldsymbol{d}_y = (-\frac{\sqrt{3}}{2}\hat{x} - \frac{1}{2}\hat{y})$ and $\boldsymbol{d}_z = \hat{y}$.

mechanism of the selection of the direction of the order parameter in the nearest neighbor KH model on the honeycomb lattice. In Sec. 8.3 we extend our consideration to the J_1-K_1-J_2-K_2-J_3 model. In Sec. 8.4, we discuss the role of the off-diagonal Γ-term and study the selection of the direction of the magnetic order in Na_2IrO_3 and in $\alpha-RuCl_3$. We summarize our conclusions in Sec. 8.5. At the end of the chapter some technical details and calculations are shown.

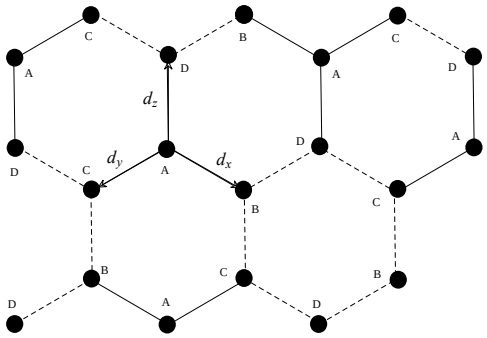

Figure 8.2: A, B, C and D designate the four sublattices of the Klein transformation. Solid and dashed bonds shows the change of the sign of the Γ interaction in the four-sublattice transformation: Γ picks up a negative sign on the solid bonds but keeps the sign from unrotated reference frame on the dashed bonds.

8.2 Order by disorder in the extended nearest neighbor KH model

The KH model on the honeycomb lattice reads [14]

$$H = \sum_{\langle ij\rangle_\alpha} \sum_{\gamma} J^{\alpha\gamma} S^{\gamma}_{0,i} S^{\gamma}_{1,j}, \tag{8.1}$$

where $J^{\alpha\gamma} = J + K\delta_{\alpha,\gamma}$ is the interaction between γ-component of the pseudospin $S^{\gamma}_{\nu,j} = 1/2$, on sublattices $\nu = 0, 1$. Hereafter, we call these pseudospins simply spins. J and K correspond to the Heisenberg and Kitaev interactions, which in the extended model can be both AF and FM. $\gamma = x, y, z$ denote the spin components in the global reference frame.

The classical phase diagram of the model 8.1 contains four magnetic phases [14, 51]: the ferromagnetic phase (Fig. 8.1 (a)), the Néel antiferromagnet (Fig. 8.1 (b)), the stripy antiferromagnet (Fig. 8.1 (c)) and the zigzag antiferromagnet (Fig. 8.1 (d)). The latter two magnetic states have a four sublattice structure.

All these phases have macroscopic classical degeneracy. While the classical degeneracy of the simple FM state and of the AF Néel state comes straightforwardly from the infinite number of degenerate collinear states, the macroscopic degeneracy of the AF stripy and zigzag phases is more complex, and the degenerate ground state manifold consists of six collinear states and a set of non-collinear multi-Q states. In Appendix A

we discuss this question in detail and show that using the four-sublattice Klein transformation for the stripy and the zigzag AF states [46, 124, 76], the nature of the classical degeneracy of all four magnetically ordered states can be understood in a similar way. Importantly, in all cases, the classical degeneracy is accidental and is removed by the order by disorder mechanism which selects a set of collinear states, each with a particular direction of the order parameter.

Following Chaloupka *et al* [46], we introduce four auxiliary sublattices A, B, C and D (see Fig. 8.2), fix the direction of the spins on the sublattice A and rotate the spins on the subllatices B, C, and D such that the component of spin corresponding to the bond direction (x for B, y for C and z for D) stays the same but two other spin components change sign. This results in the transformed Hamiltonian with the same form as (8.1) but with transformed couplings.

Here we consider the KH model in the full parameter space. For the parameters of the model for which either stripy or zigzag are the ground states, we perform four-sublattice transformation and treat the model (8.1) in the rotated basis, in which the stripy order maps to the FM and the zigzag order maps to the simple two-sublattice AFM Néel state.

Next, using a HS transformation of the partition function [19, 20], we discuss how the preferred directions of the order parameter in all these phases are selected by thermal or quantum fluctuations below the ordering temperature. We have checked that for this model thermal and quantum fluctuations choose the same state and thus, for simplicity of discussion, here we only consider the case of classical spins.

The partition function of the system of classical spins is given by the integral over the Boltzmann weights of the configurations as we have seen in Chapter 6

$$Z = \int\int [d\mathbf{S}_{0,i}][d\mathbf{S}_{1,j}]\, \delta(\mathbf{S}_{0,i}^2 - 1)\delta(\mathbf{S}_{1,j}^2 - 1)$$
$$\exp\left[-\beta \sum_{\langle ij\rangle_\alpha} \sum_{\gamma} J^{\alpha\gamma} S_{0,i}^{\gamma} S_{1,j}^{\gamma}\right], \tag{8.2}$$

where $\mathbf{S}_{0,j}$ and $\mathbf{S}_{1,j}$ are classical spins on sublattices 0 and 1, and $\beta = 1/(k_B T)$ is the inverse temperature. Similarly in the case of a quantum system the partition function is a trace of the Boltzman weights over the spin operators, $Z = Tr\left[\exp\left(-\beta \sum_{\langle ij\rangle_\alpha} \sum_{\gamma} J^{\alpha\gamma} S_{0,i}^{\gamma} S_{1,j}^{\gamma}\right)\right]$.

It is more convenient to perform the HS transformation by representing the Hamiltonian matrix in the basis of the eigenfunctions of the exchange matrix, which can be easily obtained in the momentum space. To this end, we first introduce a six-component vector $\boldsymbol{S_q} = (S^x_{0,\boldsymbol{q}}, S^y_{0,\boldsymbol{q}}, S^z_{0,\boldsymbol{q}}, S^x_{1,\boldsymbol{q}}, S^y_{1,\boldsymbol{q}}, S^z_{1,\boldsymbol{q}})$, with the components given by the Fourier transforms of the x, y, z components of the spins on $0-$ and $1-$sublattices, correspondingly. This allows us to write the Hamiltonian matrix in the momentum space as

$$H = \sum_{\boldsymbol{q}} \boldsymbol{S}^\dagger_{\boldsymbol{q}} \cdot \hat{J}_{\boldsymbol{q}} \cdot \boldsymbol{S}_{\boldsymbol{q}}, \tag{8.3}$$

where the 6×6 exchange matrix $\hat{J}_{\boldsymbol{q}}$ is defined as

$$\hat{J}_{\boldsymbol{q}} = \begin{pmatrix} 0 & 0 & 0 & J^x_{\boldsymbol{q}} & 0 & 0 \\ 0 & 0 & 0 & 0 & J^y_{\boldsymbol{q}} & 0 \\ 0 & 0 & 0 & 0 & 0 & J^z_{\boldsymbol{q}} \\ \left(J^x_{\boldsymbol{q}}\right)^* & 0 & 0 & 0 & 0 & 0 \\ 0 & \left(J^y_{\boldsymbol{q}}\right)^* & 0 & 0 & 0 & 0 \\ 0 & 0 & \left(J^z_{\boldsymbol{q}}\right)^* & 0 & 0 & 0 \end{pmatrix}, \tag{8.4}$$

with matrix elements given by

$$J^\gamma_{\boldsymbol{q}} = \sum_{\alpha=x,y,z} \left[J + K\delta_{\alpha,\gamma}\right] e^{\imath \boldsymbol{q}\cdot(\boldsymbol{d}_\alpha - \boldsymbol{d}_z)} = J_{\boldsymbol{q}} + K^\gamma_{\boldsymbol{q}}. \tag{8.5}$$

Here we drop the overall phase factor $e^{\imath \boldsymbol{q}\cdot\boldsymbol{d}_z} = e^{\imath \boldsymbol{q}\cdot(0,1)} = e^{\imath q_y}$ and denote $J_{\boldsymbol{q}} = J(1 + e^{-\imath \boldsymbol{q}\cdot\boldsymbol{a}_1} + e^{-\imath \boldsymbol{q}\cdot\boldsymbol{a}_2})$, $K^\gamma_{\boldsymbol{q}} = Ke^{\imath \boldsymbol{q}\cdot(\boldsymbol{d}_\gamma - \boldsymbol{d}_z)}$, where $\boldsymbol{a}_1 = (\frac{\sqrt{3}}{2}\hat{x} + \frac{3}{2}\hat{y})$ and $\boldsymbol{a}_2 = \sqrt{3}\vec{x}$ are the lattice vectors. The matrix $\hat{J}_{\boldsymbol{q}}$ is then diagonalized by a unitary transformation, $\hat{\kappa}_{\boldsymbol{q}} = U^{-1}_{\boldsymbol{q}} \hat{J}_{\boldsymbol{q}} U_{\boldsymbol{q}}$, leading to the following form of the Hamiltonian

$$H = \sum_{\boldsymbol{q},\nu} \kappa_{\boldsymbol{q},\nu} \tilde{S}^*_{\boldsymbol{q},\nu} \tilde{S}_{\boldsymbol{q},\nu}, \tag{8.6}$$

where the normal amplitudes of spin-like variables are defined as

$$\tilde{S}^\nu_{\boldsymbol{q}} = U_{\boldsymbol{q},\nu\eta} S^\eta_{\boldsymbol{q}}. \tag{8.7}$$

Note that, depending on the form of the interaction matrix, this transformation in general will mix the spin operators on different sites of the unit cell as well as different

components of the spin. However, in the case of the KH model, while the two sublattices of the honeycomb lattice are mixed, the x, y, and z components stay separate. The partition function (8.2) then looks like:

$$Z = \int\int [d\mathbf{S}_{0,j}][d\mathbf{S}_{1,j+\boldsymbol{d}_z}]\, \delta(\mathbf{S}_{0,j}^2 - 1)\delta(\mathbf{S}_{1,j+\boldsymbol{d}_z}^2 - 1)$$
$$\exp\left[-\beta \sum_{\boldsymbol{q},\nu} \kappa_{\boldsymbol{q},\nu} \tilde{S}^*_{\boldsymbol{q},\nu} \tilde{S}_{\boldsymbol{q},\nu}\right]. \tag{8.8}$$

Following the steps outlined in Refs. [19, 20], we can separate the mean-field and the fluctuational contributions to the partition function, $Z = Z_{\rm MF} Z_{\rm fluct}$. In the Gaussian approximation, the fluctuation part of the partition function,

$$Z_{\rm fluct} = \int [d\varphi] \exp\left[-\beta \mathcal{S}_{\rm fluct}\right], \tag{8.9}$$

where $\mathcal{S}_{\rm fluct} = \sum_{\mathbf{q};\nu,\nu'} A_{\mathbf{q},\nu\nu'} \delta\varphi^*_{\mathbf{q},\nu} \delta\varphi_{\mathbf{q},\nu'}$ can be obtained by integration over the fluctuation amplitudes $\delta\varphi_{\mathbf{q},\nu}$. The explicit expression for the matrix elements of the fluctuation matrix $\hat{A}_{\mathbf{q}}$ computed for an orientation of the mean-field order parameter along arbitrary direction $(\sin\theta\cos\phi, \sin\theta\sin\phi, \cos\theta)$ are given in Appendix B.

Now, the fluctuation contribution to the free energy can be written as

$$\mathcal{F}_{\rm fluct} = -\frac{1}{\beta} \ln Z_{\rm fluct} = \frac{1}{2\beta} \sum_{\mathbf{q}} \ln\left|\det\{A_{\mathbf{q},\nu\nu'}\}\right|. \tag{8.10}$$

While the mean-field part of the free energy has the full rotational symmetry, its fluctuational part, $\mathcal{F}_{\rm fluct}$, is sensitive to the direction of the mean-field order parameter. Thus, by finding the minima of the fluctuational part of the free energy, we can pin the spontaneous magnetization along some preferred direction of the lattice.

Fig. 8.3 (a) shows the angular dependence of fluctuational free energy $\mathcal{F}_{\rm fluct}(\theta,\phi)$ computed for representative parameters $J = -2.9$ meV and $K = 8.1$ meV, at which the ground state order is the AF zigzag. The magnitude of $\mathcal{F}_{\rm fluct}(\theta,\phi)$ is presented as a color-coded plot on the unit sphere, where the minima and maxima of the free energy are shown by the deep blue and red colors, correspondingly. We see that the minima of $\mathcal{F}_{\rm fluct}(\theta,\phi)$ are achieved when the magnetization is directed along one of the cubic axes.

This finding shows that the contribution of the fluctuations to the free energy removes the degeneracy of the ground state found on the mean field level. The states

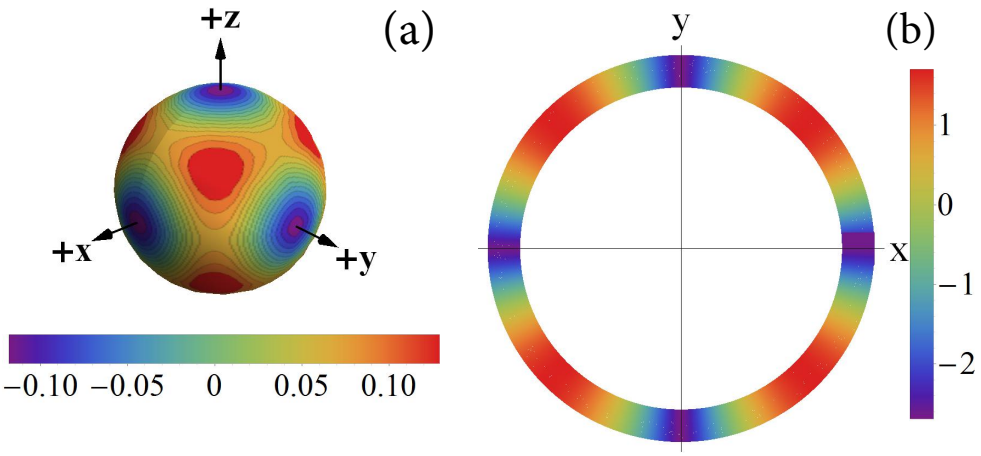

Figure 8.3: Fluctuational corrections to the free energy in (a) nearest neighbor KH model computed with $J = -2.9$ meV and $K = 8.1$ meV and (b) $J_1 - K_1 - J_2 - K_2 - J_3$ model computed with $J_1 = 5$ meV, $K_1 = -17$ meV, $J_2 = -4$ meV, $K_2 = 8$ meV, and $J_3 = 1$ meV.

which are selected by the thermal fluctuations are the collinear states with the order parameter pointing along one of the cubic axes, thus confirming previous results of the Monte Carlo simulations [50, 51, 74] and spin wave analysis by Chaloupka et al [46].

We discuss the relevance of our findings for the nearest neighbor KH model for $\alpha-RuCl_3$ in Sec. 8.4.2. However in the next section, we will first consider the selection of the direction of the order parameter in the extensions of the KH model relevant for Na_2IrO_3.

8.3 Order by disorder in J_1-K_1-J_2-K_2-J_3 model

Despite extensive efforts, no consensus concerning the minimal model for Na_2IrO_3 has been reached yet. The most natural extension of the KH model with ferromagnetic Kitaev interaction which captures the zigzag magnetic order can be obtained by inclusion of farther neighbor couplings. In Na_2IrO_3, these couplings might not be negligible due to the extended nature of the 5*d*-orbitals of the Ir ions. In the early works suggesting this possible extension [12, 59], second and third neighbor couplings were taken into

account phenomenologically and only the isotropic part of these interactions was included. The importance of additional nearest neighbor C_3-symmetric anisotropic terms (Γ-terms) [71, 76] or of the spatial anisotropy of the nearest neighbor Kitaev interactions [62], were also discussed in the literature as a possible source for the stabilization of the zigzag phase.

Here we consider the J_1-K_1-J_2-K_2-J_3 model [10], which still has the same symmetry as the original KH model but contains Kitaev interactions between both nearest and second nearest neighbors. The model reads

$$\mathcal{H} = J_1 \sum_{\langle i,j\rangle_\gamma} \mathbf{S}_i \mathbf{S}_j + K_1 \sum_{\langle i,j\rangle_\gamma} S_j^\gamma S_j^\gamma + \tag{8.11}$$
$$J_2 \sum_{\langle\langle i,j\rangle\rangle_{\tilde{\gamma}}} \mathbf{S}_i \mathbf{S}_j + K_2 \sum_{\langle\langle i,j\rangle\rangle_{\tilde{\gamma}}} S_i^{\tilde{\gamma}} S_j^{\tilde{\gamma}} + J_3 \sum_{\langle\langle\langle i,j\rangle\rangle\rangle} \mathbf{S}_i \mathbf{S}_j,$$

where $J_1 > 0$, $K_1 < 0$, $J_2 < 0$, $K_2 > 0$, and $J_3 > 0$; $\langle\,\rangle$, $\langle\langle\,\rangle\rangle$ and $\langle\langle\langle\,\rangle\rangle\rangle$ denote nearest neighbor, second nearest neighbor and third nearest neighbor, respectively. $\gamma = x, y, z$ and $\tilde{\gamma} = \tilde{x}, \tilde{y}, \tilde{z}$ denote the three types of nearest neighbor and second nearest neighbor bonds of the honeycomb lattice, respectively. It is important to note that the second neighbor Kitaev interactions do not change the space group symmetries of the original KH model.

For realistic sets of the parameters describing Na_2IrO_3, the second neighbor Kitaev interaction, K_2, computed from the microscopic approach based on the ab-initio calculation by Foevtsova *et al* [63], appeared to be the largest interaction after the nearest neighbor Kitaev interaction, K_1, and turn out to be antiferromagnetic. The mechanism behind the large magnitude of K_2 in Na_2IrO_3 is physically very clear: It originates from the large diffusive Na ions that reside in the middle of the exchange pathways, and the constructive interference of a large number of pathways. Moreover, the K_1-K_2 model, that only includes Kitaev interactions [86], already stabilizes the zigzag phase for the proper signs of K_1 and K_2. However, as we have discussed in Ref. [86], the K_1-K_2 model is still not sufficient to comply with all available experimental data.

The classical degeneracy of the zigzag state obtained within the J_1-K_1-J_2-K_2-J_3 model with FM K_1 is different from the one of the zigzag state realized in the extended KH model with AFM K_1 interaction. To see what difference the sign of K_1 makes, let us consider the zigzag pattern in Fig.8.1 (d). With AFM K_1, the pattern, that

minimizes the classical energy in the zigzag state with ferromagnegnetic y and z bonds, has the spins pointing along the $x-$axis to take advantage of the Kitaev interaction on the AFM x-bonds. On the other hand the same pattern with FM K_1 takes advantage of the Kitaev interaction on the FM $y-$ and $z-$ bonds by putting spins in the $yz-$plane. Thus the degenerate ground state manifold for a given zigzag pattern with FM K_1 is one of $xy-$, $yz-$, or $zx-$ planes. Furthermore, when the Klein duality 4-sublattice transformation [46] is applied to the J_1-K_1-J_2-K_2-J_3 zigzags, these states do not turn into Néel AFM state, and instead turn into non-collinear states, that are more difficult to work with than the original zigzag states. Working with the zigzag states directly increases the magnetic unit cell to 4 sites, labeled in Fig 8.1(d).

The Hamiltonian matrix in the momentum space can be again written in the form of Eq. (8.3), however this time due to the larger unit cell the exchange matrix $\hat{J}_{\boldsymbol{q}}$ is 12×12, instead of 6×6. Its matrix elements are given in Appendix C. The fluctuations matrix $A_{\mathbf{q},\nu\nu'}$ is calculated as before according to equation (8.15), with the constraint matrix $C_{\boldsymbol{q},\mu,\mu'}$ of equation (8.17) now containing 4 identical blocks instead of 2. The fluctuation matrix again contains the information on the direction of the spins and transmits this information to the free energy corrections that we plot in Fig. 8.3(b). Since the spins are confined to a plane for a given zigzag state we have only the angle of the direction of spins in that plane. The color of the band at a given angle then gives the size of the fluctuational correction to the free energy, with violet being lowest and red highest energy states. We see that again the Kitaev anisotropies prefer to align the magnetization along the cubic axes. Note, however, that unlike the extended KH model, where there were 6 equivalent states, here there are 4 directions for each of the three zigzag patterns, giving a total of 12 states.

8.4 The role of off-diagonal symmetric Γ-term.

8.4.1 Directions of the ordered moments in Na_2IrO_3.

The discussion above has clearly shown, that neither the original Kitaev model nor the extended J_1-K_1-J_2-K_2-J_3 model can correctly explain the experimental data in Na_2IrO_3. Since the easy axes directions are determined solely by the anisotropy terms, only the inclusion of other types of the anisotropies can improve the situation. Here we consider

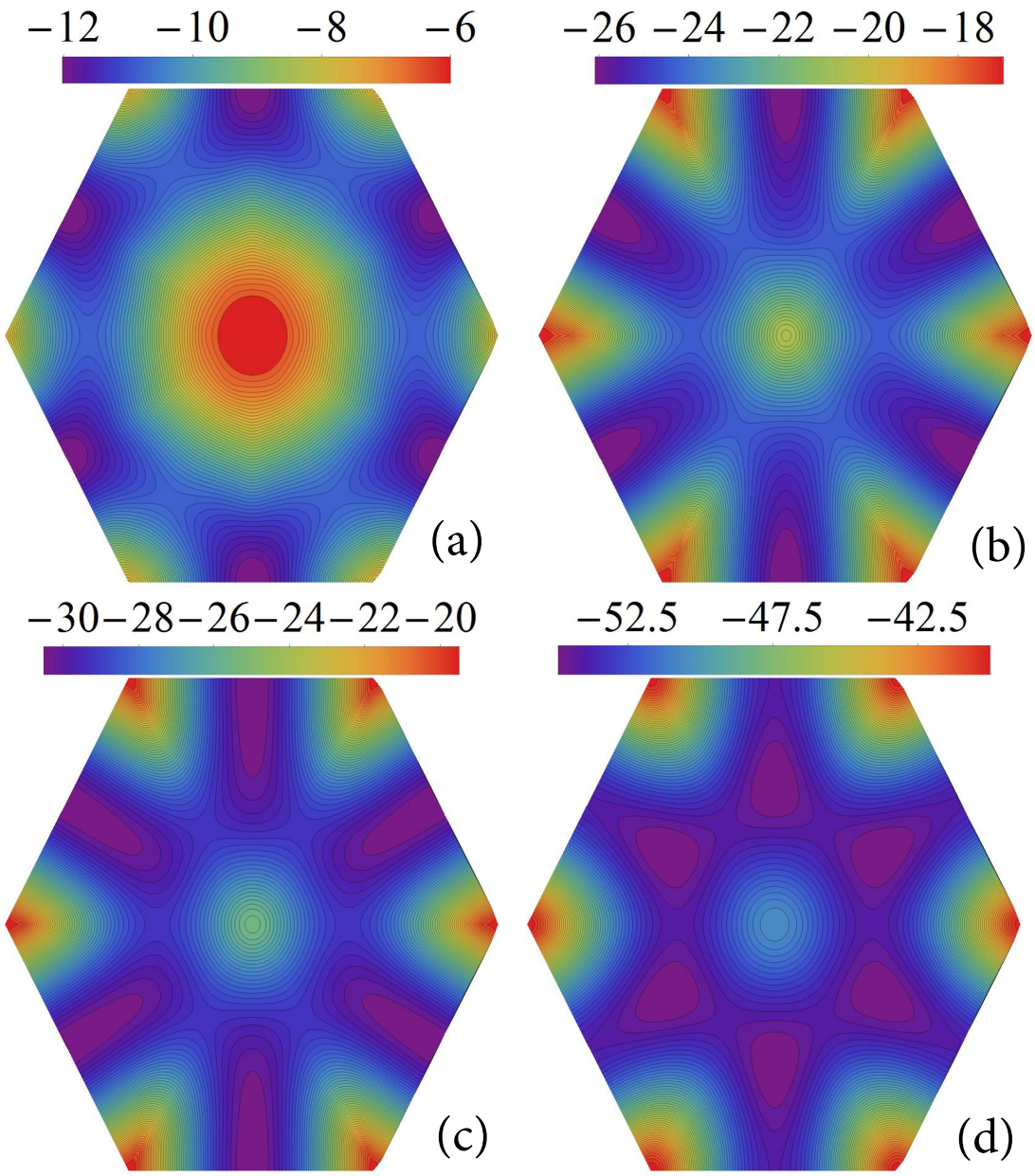

Figure 8.4: The lowest eigenvalue of the $J_1 - K_1 - J_2 - K_2 - J_3 - \Gamma_1$ model obtained with the Luttinger-Tisza method is shown on the first Brillouin zone. We use $J_1 = 3$ meV, $K_1 = -17$ meV, $J_2 = -3$ meV, $K_2 = 6$ meV, $J_3 = 1$ meV, and (a) $\Gamma_1 = 1$ meV, (b) $\Gamma_1 = 20$ meV, (c) $\Gamma_1 = 25$ meV, and (d) $\Gamma_1 = 50$ meV.

the off-diagonal symmetric Γ-terms. The role of these terms in the nearest-neighbor Kitaev model has been studied in Refs. [71, 76]. These studies have shown that the small Γ-terms do not immediately destabilize the zigzag phase, but lead to a deviation of the magnetic moments from the cubic axes.

The origin of Γ-terms can be easily seen from the most general form of the bilinear exchange coupling matrix, which on the bond (i, j) has the form given by

$$\Xi_{i,j} = \begin{pmatrix} J^{xx} & J^{xy} & J^{xz} \\ J^{yx} & J^{yy} & J^{yz} \\ J^{zx} & J^{zy} & J^{zz} \end{pmatrix}. \tag{8.12}$$

While the Kitaev term comes from the anisotropy of the diagonal matrix elements of $\Xi_{i,j}$, e.g. $K_1 = J_1^{zz} - J_1^{xx}$, the symmetric and antisymmetric combinations of off-diagonal elements represent other types of possible bond-anisotropies. In the absence of the trigonal distortion, the inversion symmetry prohibits the existence of antisymmetric interactions but some of the symmetric combinations are allowed, i.e. on a given γ-bond, the interaction between the other two spin components, $\Gamma^\gamma(S_i^\alpha S_j^\beta + S_i^\beta S_j^\alpha)$, where $\Gamma^\gamma = \frac{1}{2}(J_1^{\alpha\beta} + J_1^{\beta\alpha})$, is non-zero. Our previous results [10] suggest that in Na_2IrO_3 the magnitude of the strength of Γ on the nearest neighbor bonds is about 2-3 meV and vanishes for the second neighbors.

Here we consider the J_1-K_1-J_2-K_2-J_3-Γ model with the previous choice of Heisenberg and Kitaev interactions and treat Γ as a free parameter. A straightforward classical minimization in momentum space using Luttinger-Tisza approach [125, 126, 127] shows that up to very large values of $\Gamma \sim 20$ meV the minima of the classical energy are located at the M points corresponding to the zigzag states. This is clearly seen in Fig. 8.4 (a) where we plot the lowest eigenvalues obtained for $\Gamma = 1$ meV. At larger values of Γ, the minima shift along the lines connecting M points and the center of the Brillouin zone (see Fig. 8.4 (b) for $\Gamma = 20$ meV), indicating the transition to incommensurate order. The incommensurability of the Luttinger-Tisza solution increases further with larger values of Γ, which is shown in Figs. 8.4 (c) and (d). The exact value of Γ at which the transition occurs is difficult to determine due to the transition being so smooth, Note, however, that the transition occurs at values of Γ far beyond those predicted from our microscopic calculations at ambient pressure [10].

After we have demonstrated that adding small Γ interactions to the $J_1 - K_1 - J_2 - K_2 - J_3$ model does not destabilize the zigzag order, let us now show that in the presence of Γ the mean-field degeneracy is already lifted and the preferred directions of the order parameter are selected. This is clearly seen in Fig. 8.5 (a) and (b), where the mean field energy of the zigzag order is computed for $\Gamma = 1$ meV and $\Gamma = -1$ meV, respectively. By inspection, we can see that non-zero Γ selects the face diagonals as easy axes for magnetic ordering, and the sign of Γ determines which of the two face diagonals are preferred. For concreteness, let us consider the zigzag with AFM $z-$bonds. As we discussed above the case for $\Gamma = 0$, the easy xy-plane is selected at the mean-field level of the $J_1 - K_1 - J_2 - K_2 - J_3$ model. Then, the inclusion of positive Γ interaction on x and y bonds gives zero contribution to the energy since on these bonds it involves the spin component perpendicular to the easy plane, but it gives maximal lowering of the energy on the z-bonds if the spins point along [110] and $[\bar{1}\bar{1}0]$, $[\bar{1}10]$ and $[\bar{1}10]$ directions correspondingly for positive and negative values of Γ. The estimate for the smallest Γ, at which the selection of face diagonals takes place, can be done by comparing the mean-field energy gain due to Γ with the energy gain due to fluctuations at $\Gamma = 0$, which at $T = 0$ is equal to the zero point energy and is a function of K_1 and K_2. At finite temperature, the contribution to the energy from the Gaussian fluctuations at each T can be computed by our method, and this energy will give the lower bound for the magnitude of Γ needed to change the orientation of magnetic order from the cubic to the face diagonal.

8.4.2 Directions of the ordered moments in $\alpha-\mathbf{RuCl_3}$.

The microscopic calculations for $\alpha-\mathrm{RuCl_3}$ emphasized the importance of the off-diagonal nearest neighbor Γ interactions [128]. The effect of adding Γ interaction to the nearest neighbor KH model is easiest to understand in the rotated reference frame of the four-sublattice Klein transformation [76, 124]. The Kitaev and Heisenberg interactions do not change their form and only change the value of the coupling constants under this transformation. On the other hand, Γ-interaction picks up a bond dependent sign as shown in Fig. 8.2. In fact, Γ changes the sign on half of the bonds, i.e. there are just as many negative bonds as there are positive bonds for each Kitaev type of bonds. Since the Klein transformed version of the zigzag state is the AFM Néel state, all the bonds

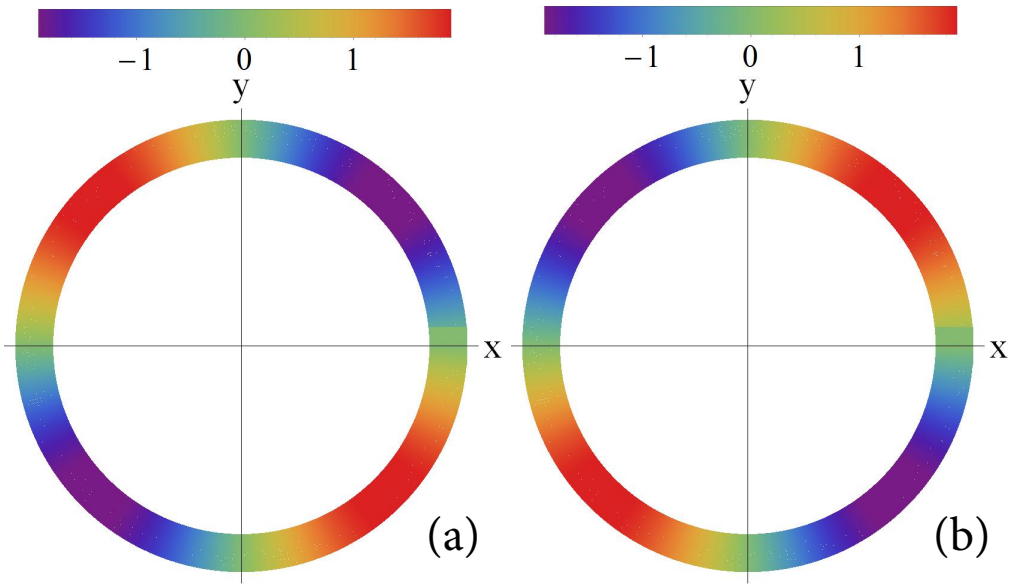

Figure 8.5: Mean field energy of the zigzag orders in $J_1 - K_1 - J_2 - K_2 - J_3$ model with the contribution of (a) $\Gamma = 1$ meV and (b) $\Gamma = -1$ meV.

are AFM and involve the same pair of spins. Thus the contribution of the Γ interaction to the mean-field energy cancels out, and the set of states remains degenerate. This means that as long as we remain in the small window where Γ does not destabilize the zigzag order found by Rau et al. [71], we can perform our order-by-disorder approach to see what state is chosen.

Figs. 8.6 (a)-(c) show the fluctuation free energy computed for the $J-K-\Gamma$ model for $J_1 = -2.9$ meV and $K_1 = 8.1$ meV, suggested by Banerjee *et al.* [122], and $\Gamma = 0.7$ meV, 0.8 meV and 0.9 meV, respectively. In Fig. 8.6 (a), $\Gamma = 0.7$ meV, the minima of the fluctuational free energy are still along cubic directions. For larger Γ-interaction, the system prefers the states with at least two nonzero spin components and, therefore, the transition towards [111] preferred directions of the order parameter takes place. This is shown in Fig. 8.6 (b) and (c), in which the fluctuational energy is plotted for $\Gamma = 0.8$ meV and 0.9 meV. While in Fig. 8.6 (b) only very shallow minima are seen along [111] directions, in Fig. 8.6 (c) both the pronounced minima along the cubic body diagonals and maxima along the cubic axes are very clearly seen. Remember that the computation is done in the rotated reference frame. Therefore, only the states with the orientation of

the order parameter along the cubic axes will give the collinear states in the unrotated reference frame. The states with order parameter pointing along [111] directions in the rotated reference frame correspond to non-collinear states in the unrotated reference frame. Since recent experiments by Cao et al. [123] have established that spins point along a cubic axis, by calculating the fluctuational corrections as a function of Γ, we can find an upper bound on its value, such that the Kitaev fluctuations dominate and keep the cubic axes as the preferred directions. From our calculations it follows that for $J_1 = -2.9$ meV and $K_1 = 8.1$ meV the upper bound for Γ is about 0.8 meV. Finally, for this set of parameters the transition to the 120°- AFM order occurs around $\Gamma = 1.6$ meV. Note that this estimate is far smaller than the Γ values resulting from *ab initio* calculations [128].

8.5 Concluding remarks

In this chapter we explored how the direction of the magnetic moments in the zigzag ground state order is chosen in Na_2IrO_3 and $\alpha-RuCl_3$. In both compounds, the Kitaev interaction plays an important role. For the case of FM nearest neighbor Kitaev interaction, like in Na_2IrO_3, farther neighbor interactions are essential for stabilizing the zigzag ground state. For the AFM nearest neighbor Kitaev interaction, which was widely suggested to be the dominant interaction in $\alpha-RuCl_3$ [15, 121, 122, 123, 128], the zigzag order can be stabilized already within the nearest neighbor model.

We proposed that the $J_1-K_1-J_2-K_2-J_3-\Gamma$ model can explain all the experimental finding in Na_2IrO_3. In this model the selection of the experimentally observed face diagonal direction of the order parameter happens already on the mean-field level due to the small bond-dependent anisotropic term Γ.

In $\alpha-RuCl_3$, if the the n.n. Kitaev interaction is AFM, the original KH model [14] is sufficient to explain both the collinear zigzag ground state and the cubic directions of the order parameter. We studied the effect of the Γ-term and showed that while on the mean-field level it doesn't effect the ground state degeneracy, it favors non-collinear three-$\mathbf{Q}$ states, instead of the experimentally observed zigzag state with spins along cubic axes, once the Gaussian fluctuations are included. Thus, it appears to be an upper bound for Γ-term, which can be estimated for a given set of n.n. parameters.

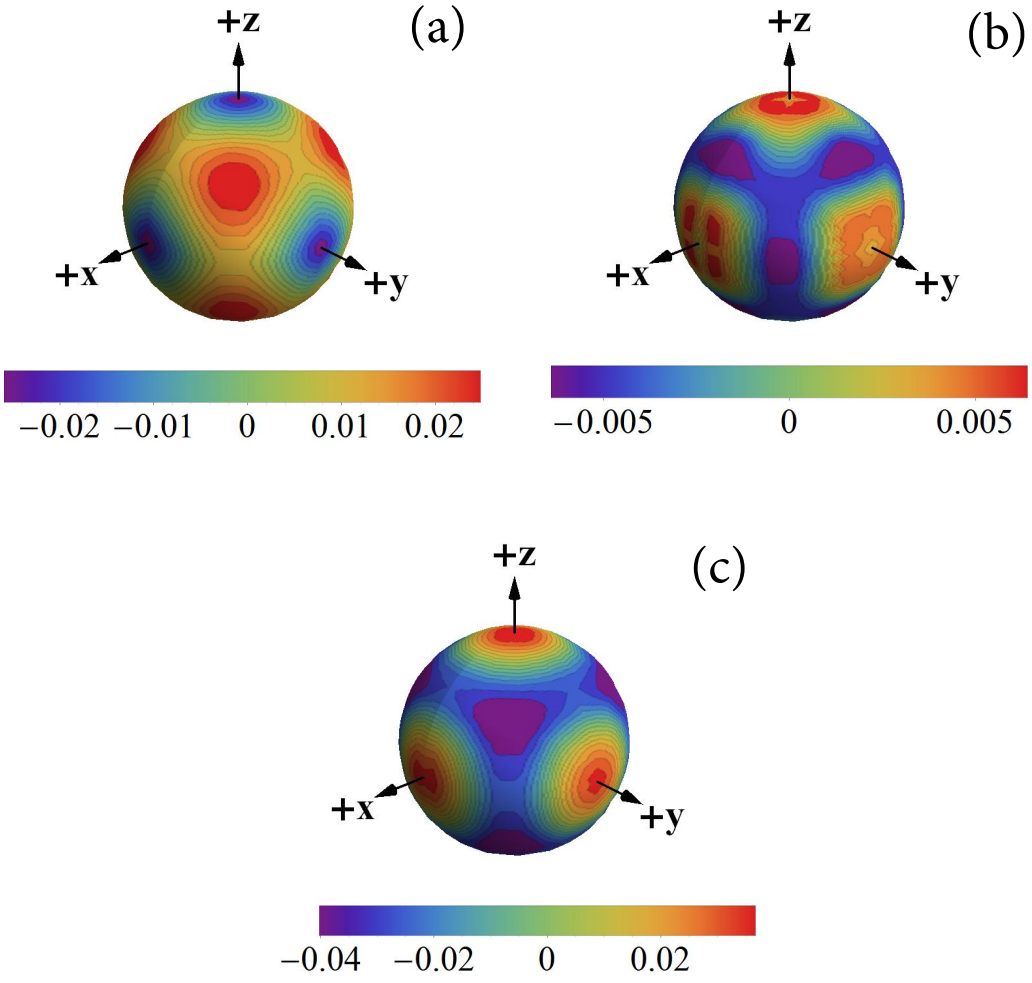

Figure 8.6: Fluctuational corrections to the free energy in the nearest neighbor KH model with Γ interaction. We used the following parameters: $J = -2.9$ meV, $K = 8.1$ meV and (a) $\Gamma = 0.7$ meV, (b) $\Gamma = 0.8$ meV, and (c) $\Gamma = 0.9$ meV. The minima of the free energy are shown by deep blue color and the maxima by intense red color.

8.6 Technical details

8.6.1 The classical degeneracy of the extended KH model

In this technical section we provide detailed discussion of the classical degeneracy of the extended KH model at parameters for which either the stripy or the zigzag AF phases are realized as the ground state and the manifold of classically degenerate states is rather complex.

To be specific, let us first consider the stripy phase. It contains six inequivalent collinear stripy states with FM bonds along either Kitaev $x-$, $y-$ or $z-$bonds. It also contains infinite number of non-collinear (coplanar and non-coplanar) states. The spin order in the $x-$, $y-$ or $z-$ stripy states can be described either with a help of four magnetic sublattices or by a simple spiral characterized by a single-Q wave vector: $\mathbf{Q}_x = (\pi/\sqrt{3}, \pi)$, $\mathbf{Q}_y = (\pi/\sqrt{3}, -\pi)$ and $\mathbf{Q}_z = (-2\pi/\sqrt{3}, 0)$. One of the stripy states with FM z-bonds is shown in Fig. 8.1 (c). In each of these stripy states the spins are aligned along one of the cubic directions which is locked to the spatial orientation of a stripy pattern by the Kitaev interaction, i.e. the direction of the order parameter is defined by the wave vector $\mathbf{Q} = \mathbf{Q}_x, \mathbf{Q}_y$ or $\mathbf{Q}_z$ determining the breaking of the translation symmetry.

The structure of the manifold of the non-collinear states, which looks rather complex in the original model, can be easily understood with the help of the four-sublattice transformation (see Fig. 8.2) based on the Klein duality [46, 76, 124]. In the new rotated basis, the stripy phase is mapped to the FM order with a unique ordering vector $\mathbf{Q} = 0$. Classically, all states with arbitrary direction of the FM order have the same energy. FM states with order parameter along the cubic axes give the six stripy phases in the unrotated spin basis discussed above. Arbitrary directions of the FM order parameter lead to a set of non-coplanar states in which each component of spin, S_x, S_y, and S_z, transforms with its own $\mathbf{Q}_x$, $\mathbf{Q}_y$ and $\mathbf{Q}_z$ wavevector, which coincide with the $\mathbf{Q}$ vectors describing the spatial orientation of the stripes in the respective collinear states.

Using these three ordering vectors, we can write the non-coplanar phase of the unrotated spins as

$$\mathbf{S}_{i,0} = (s_\theta c_\phi \, e^{\imath \mathbf{Q}_x \cdot \boldsymbol{R}_i}, s_\theta s_\phi \, e^{\imath \mathbf{Q}_y \cdot \boldsymbol{R}_i}, c_\theta \, e^{\imath \mathbf{Q}_z \cdot \boldsymbol{R}_i}), \tag{8.13}$$

where θ and ϕ are the polar and azimuthal angles of the FM order parameter. $\mathbf{S}_{i,0}$ denote the spins on the sublattice 0 and the spins on the sublattice 1 are obtained from $\mathbf{S}_{i,0}$ by a constant phase shift coming from the spin rotation on that bond as prescribed by the four sublattice transformation. As in Fig. 8.1 (c), the sublattices 0 and 1 are connected by the z bond, the order of the spins on the subllatice 1 is given by

$$\mathbf{S}_{i,1} = (S^x_{i,0}\, e^{\imath\pi},\, S^y_{i,0}\, e^{\imath\pi}, S^z_{i,0}) \tag{8.14}$$

In the zigzag phase, the structure of the classical states manifold is very similar to the stripy phase. The four-sublattice transformation maps the zigzag phase onto the Néel AF phase. The generic state is again described by the three-$\mathbf{Q}$ spiral state. The only difference is that the spins on sublattice 1 have an overall phase factor of π, $\mathbf{S}_{i,1} = (S^x_{i,0},\, S^y_{i,0},\, S^z_{i,0}e^{\imath\pi})$.

8.6.2 The matrix elements $A_{\mathbf{q},\nu\nu'}$ computed for the KH model.

The matrix elements $A_{\mathbf{q},\nu\nu'}$ can be written as

$$A_{\mathbf{q},\nu\nu'} = \frac{\delta_{\nu,\nu'}}{\kappa_{\boldsymbol{q},\nu}} + s(\kappa_{\boldsymbol{q},\nu})s(\kappa_{\boldsymbol{q},\nu'})U^{-1}_{\boldsymbol{q},\nu,\mu}C_{\boldsymbol{q},\mu,\mu'}U_{\boldsymbol{q},\nu,\mu}, \tag{8.15}$$

where a repeated index implies a summation over. The first term in (8.15) is the contribution from the interaction term and the second term is from the constraint term [19, 20]. For convenience, the constraint matrix $\hat{C}_{\boldsymbol{q}}$ can be first written in the original basis, in which the interaction term is not diagonal, and then transformed to the eigenbasis of the Hamiltonian with a help of the unitary transformation $U_{\boldsymbol{q}}$. In the original basis the constraint matrix $\hat{C}_{\boldsymbol{q}}$ consists of two blocks, one for each sublattice. The A-sublattice block has elements $C_{\boldsymbol{q},\mu,\mu'}$ with $\mu,\mu' = 1,2,3$ and the B-sublattice block has the elements with $\mu,\mu' = 4,5,6$. The two blocks are identical, so $\hat{C}_{\boldsymbol{q}}$ takes the following form:

$$\hat{C}_{\boldsymbol{q}} = \begin{pmatrix} C_{\boldsymbol{q},11} & C_{\boldsymbol{q},12} & C_{\boldsymbol{q},13} & 0 & 0 & 0 \\ C_{\boldsymbol{q},21} & C_{\boldsymbol{q},22} & C_{\boldsymbol{q},23} & 0 & 0 & 0 \\ C_{\boldsymbol{q},31} & C_{\boldsymbol{q},32} & C_{\boldsymbol{q},33} & 0 & 0 & 0 \\ 0 & 0 & 0 & C_{\boldsymbol{q},11} & C_{\boldsymbol{q},12} & C_{\boldsymbol{q},13} \\ 0 & 0 & 0 & C_{\boldsymbol{q},21} & C_{\boldsymbol{q},22} & C_{\boldsymbol{q},23} \\ 0 & 0 & 0 & C_{\boldsymbol{q},31} & C_{\boldsymbol{q},32} & C_{\boldsymbol{q},33} \end{pmatrix} \tag{8.16}$$

with matrix elements given by

$$\begin{aligned}
C_{\boldsymbol{q},11} &= -\tfrac{2}{3}\big[\beta_c(1-s_\theta^2 c_\phi^2)+3\beta r s_\theta^2 c_\phi^2\big],\\
C_{\boldsymbol{q},22} &= -\tfrac{2}{3}\big[\beta_c(1-s_\theta^2 s_\phi^2)+3\beta r s_\theta^2 s_\phi^2\big],\\
C_{\boldsymbol{q},33} &= -\tfrac{2}{3}\big[\beta_c s_\theta^2+3\beta r c_\theta^2\big],\\
C_{\boldsymbol{q},12} &= C_{\boldsymbol{q},21} = -\tfrac{2}{3}(3\beta r-\beta_c)s_\theta^2 c_\phi s_\phi,\\
C_{\boldsymbol{q},13} &= C_{\boldsymbol{q},31} = -\tfrac{2}{3}(3\beta r-\beta_c)s_\theta s_\theta c_\phi,\\
C_{\boldsymbol{q},23} &= C_{\boldsymbol{q},32} = -\tfrac{2}{3}(3\beta r-\beta_c)s_\theta s_\phi c_\phi,
\end{aligned} \tag{8.17}$$

where, to shorten notations, we denote $\sin\theta(\phi) \equiv s_{\theta(\phi)}$ and $\cos\theta(\phi) \equiv c_{\theta(\phi)}$.

8.6.3 Coupling $J_{\mu,\nu}(\mathbf{q})$ of the $J_1 - K_1 - J_2 - K_2 - J_3$ model.

For shortness we define $q_1 = \mathbf{q}\cdot\mathbf{a}_1$, $q_2 = \mathbf{q}\cdot\mathbf{a}_2$, and $q_z = \mathbf{q}\cdot\mathbf{d}_z$. The diagonal matrix elements for $\mu = 1, 4, 7$ and 10 are equal to $J_{\mu,\mu}(\boldsymbol{q}) = (J_2 + K_2)\cos q_1$, all other diagonal elements are equal to $J_{\mu,\mu}(\boldsymbol{q}) = J_2 \cos q_1$. The non-zero off-diagonal elements $J_{\mu,\nu}(\boldsymbol{q})$

for $\nu > \mu$ are

$$
\begin{aligned}
J_{1,4}(\boldsymbol{q}) &= \frac{1}{2} J_1 (e^{\imath q_z} + e^{\imath(-q_1+q_z)}) \\
J_{2,5}(\boldsymbol{q}) &= \frac{1}{2} \Big(J_1 (e^{\imath q_z} + (J_1 + K_1) e^{\imath(-q_1+q_z)}) \Big) \\
J_{3,6}(\boldsymbol{q}) &= \frac{1}{2} \Big((J_1 + K_1)(e^{\imath q_z} + J_1 e^{\imath(-q_1+q_z)}) \Big) \\
J_{1,7}(\boldsymbol{q}) &= J_2 (\cos(q_1 - q_2) + \cos q_2) \\
J_{2,8}(\boldsymbol{q}) &= (J_2 + K_2) \cos(q_1 - q_2) + J_2 \cos q_2 \\
J_{3,9}(\boldsymbol{q}) &= J_2 \cos(q_1 - q_2) + (J_2 + K_2) \cos q_2 \\
J_{1,10}(\boldsymbol{q}) &= \frac{1}{2} \Big((J_1 + K_1) e^{\imath(q_2 - q_1 + q_z)} + \\
&\qquad J_3 (e^{\imath(q_2+q_z)} + e^{\imath(q_2 - 2q_1 + q_z)} + e^{\imath(-q_2+q_z)}) \Big) \\
J_{2,11}(\boldsymbol{q}) &= \frac{1}{2} \Big(J_1 e^{\imath(q_2 - q_1 + q_z)} + \\
&\qquad J_3 (e^{\imath(q_2+q_z)} + e^{\imath(q_2 - 2q_1 + q_z)} + e^{\imath(-q_2+q_z)}) \Big) \\
J_{3,12}(\boldsymbol{q}) &= \frac{1}{2} \Big(J_1 e^{\imath(q_2 - q_1 + q_z)} + \\
&\qquad J_3 (e^{\imath(q_2+q_z)} + e^{\imath(q_2 - 2q_1 + q_z)} + e^{\imath(-q_2+q_z)}) \Big) \\
J_{4,7}(\boldsymbol{q}) &= \frac{1}{2} \Big((J_1 + K_1) e^{\imath(q_1 - q_2 - q_z)} + \\
&\qquad J_3 (e^{\imath(2q_1 - q_2 - q_z)} + e^{\imath(-q_2 - q_z)} + e^{\imath(q_2 - q_z)}) \Big) \\
J_{5,8}(\boldsymbol{q}) &= \frac{1}{2} \Big(J_1 e^{\imath(q_1 - q_2 - q_z)} + \\
&\qquad J_3 (e^{\imath(2q_1 - q_2 - q_z)} + e^{\imath(-q_2 - q_z)} + e^{\imath(q_2 - q_z)}) \Big) \\
J_{6,9}(\boldsymbol{q}) &= \frac{1}{2} \Big(J_1 e^{\imath(q_1 - q_2 - q_z)} + \\
&\qquad J_3 (e^{\imath(2q_1 - q_2 - q_z)} + e^{\imath(-q_2 - q_z)} + e^{\imath(q_2 - q_z)}) \Big) \\
J_{4,10}(\boldsymbol{q}) &= J_2 \Big(\cos q_2 + \cos(q_2 - q_1) \Big) \\
J_{5,11}(\boldsymbol{q}) &= J_2 \cos q_2 + (J_2 + K_2) \cos(q_2 - q_1) \\
J_{6,12}(\boldsymbol{q}) &= (J_2 + K_2) \cos q_2 + J_2 \cos(q_2 - q_1) \\
J_{7,10}(\boldsymbol{q}) &= \frac{1}{2} J_1 (e^{\imath q_z} + e^{\imath(-q_1+q_z)}) \\
J_{8,11}(\boldsymbol{q}) &= \frac{1}{2} \Big(J_1 e^{\imath q_z} + (J_1 + K_1) e^{\imath(-q_1+q_z)} \Big) \\
J_{9,12}(\boldsymbol{q}) &= \frac{1}{2} \Big((J_1 + K_1) e^{\imath q_z} + J_1 e^{\imath(-q_1+q_z)} \Big)
\end{aligned}
$$

Chapter 9

Conclusion and Discussion

The long-standing quest for a solid state realization of the Kitaev honeycomb model [3] along with the search for a new family of superconductors [4, 5] has triggered much of the experimental and theoretical interest in 4d and 5d compounds in which the interplay of the strong spin-orbit coupling (SOC) and electronic correlations leads to the dominance of the strongly anisotropic interactions [1]. Some limited success has been recently achieved on both fronts: observation of a d-wave pseudogap in doped Sr_2IrO_4 [6] and observation of a spin liquid phase in α-$RuCl_3$ subjected to an external magnetic field [129, 130]. However, both the superconductivity and the Kitaev model remain elusive for now and the search continues.

What is more interesting is that the 4d and 5d transition metal compounds have developed into a field of their own right, worthy of study outside the scope of the two goals stated above. For instance the seemingly simple zigzag magnetic state found in Na_2IrO_3 turned out to be a complex system of competing and cooperating anisotropies as I have shown in Chapters 3 and 8. The zigzag pattern of the order is a result of the cooperation of Kitaev interactions K_1 and K_2 with the isotropic J_3 interaction. At the same time the direction of the magnetic moments in the zigzag pattern stems from the competition of the the Kitaev interaction fluctuations with the symmetric off-diagonal interaction Γ_1 mean field contribution. Such complexity of magnetically ordered states is rarely seen outside the systems with strong SOC.

To summarize, in my dissertation I presented the effect that strong spin-orbit coupling has on the magnetic properties of 4d and 5d transition metal compounds. In the

first half of the dissertation I have shown that spin-orbit coupling combined with lattice geometry is a source of many anisotropic magnetic interactions. I have also shown how these interactions can be measured experimentally. In the second half of the dissertation I have focused on what effect the anisotropies have on the magnetic ground state of various compounds. I presented a general method for calculating free energy corrections due to fluctuations in anisotropic Hamiltonians. I have shown how the fluctuations lead to pinning of the direction of the order parameter via order-by-disorder mechanism.

The possibility of enhancing or suppressing particular anisotropic magnetic interactions using chemical doping, pressure and other experimental methods, sparked a flurry of research on both the individual anisotropic interactions and on how they compete and cooperate with each other. For example, it has recently been shown that isolating the symmetric off-diagonal Γ_1 interaction on the honeycomb lattice as well as its 3D variations leads to a classical spin liquid state [78]. From the experimental side, the counter-rotating non-coplanar incommesurate spiral ground states found [131, 132] in (β, γ)-Li_2IrO_3 remain a mystery. The search for a combination of competing and/or cooperating anisotropic interactions that would produce such an unusual order has been entertaining the minds of many in the community for a couple of years now with little success. The 4d and 5d compounds became a playground of anisotropic spin physics, and one that is unlikely to leave the field of view of physicists any time soon.

References

[1] G. Jackeli and G. Khaliullin. Mott insulators in the strong spin-orbit coupling limit: From heisenberg to a quantum compass and kitaev models. *Phys. Rev. Lett.*, 102:017205, Jan 2009.

[2] B. J. Kim, Hosub Jin, S. J. Moon, J.-Y. Kim, B.-G. Park, C. S. Leem, Jaejun Yu, T. W. Noh, C. Kim, S.-J. Oh, J.-H. Park, V. Durairaj, G. Cao, and E. Rotenberg. Novel $J_{\text{eff}} = 1/2$ mott state induced by relativistic spin-orbit coupling in Sr_2IrO_4. *Phys. Rev. Lett.*, 101:076402, Aug 2008.

[3] A. Kitaev. Anyons in an exactly solved model and beyond. *Annals of Physics*, 321:2–111, January 2006, cond-mat/0506438.

[4] M. K. Crawford, M. A. Subramanian, R. L. Harlow, J. A. Fernandez-Baca, Z. R. Wang, and D. C. Johnston. Structural and magnetic studies of Sr_2IrO_4. *Phys. Rev. B*, 49:9198–9201, Apr 1994.

[5] G. Cao, J. Bolivar, S. McCall, J. E. Crow, and R. P. Guertin. Weak ferromagnetism, metal-to-nonmetal transition, and negative differential resistivity in single-crystal Sr_2IrO_4. *Phys. Rev. B*, 57:R11039–R11042, May 1998.

[6] Y. K. Kim, O. Krupin, J. D. Denlinger, A. Bostwick, E. Rotenberg, Q. Zhao, J. F. Mitchell, J. W. Allen, and B. J. Kim. Fermi arcs in a doped pseudospin-1/2 heisenberg antiferromagnet. *Science*, 345(6193):187–190, 2014, http://science.sciencemag.org/content/345/6193/187.full.pdf.

[7] N F Mott and R Peierls. Discussion of the paper by de boer and verwey. *Proceedings of the Physical Society*, 49(4S):72, 1937.

[8] Yogesh Singh and P. Gegenwart. Antiferromagnetic mott insulating state in single crystals of the honeycomb lattice material Na_2IrO_3. *Phys. Rev. B*, 82:064412, Aug 2010.

[9] Natalia B. Perkins, Yuriy Sizyuk, and Peter Wölfle. Interplay of many-body and single-particle interactions in iridates and rhodates. *Phys. Rev. B*, 89:035143, Jan 2014.

[10] Yuriy Sizyuk, Craig Price, Peter Wölfle, and Natalia B. Perkins. Importance of anisotropic exchange interactions in honeycomb iridates: Minimal model for zigzag antiferromagnetic order in Na_2IrO_3. *Phys. Rev. B*, 90:155126, Oct 2014.

[11] Stephen M. Winter, Ying Li, Harald O. Jeschke, and Roser Valentí. Challenges in design of kitaev materials: Magnetic interactions from competing energy scales. *Phys. Rev. B*, 93:214431, Jun 2016.

[12] Itamar Kimchi and Yi-Zhuang You. Kitaev-heisenberg-J_2-J_3 model for the iridates A_2iro_3. *Phys. Rev. B*, 84:180407, Nov 2011.

[13] I. Pollini. Electronic properties of the narrow-band material α-$RuCl_3$. *Phys. Rev. B*, 53:12769–12776, May 1996.

[14] Ji ří Chaloupka, George Jackeli, and Giniyat Khaliullin. Zigzag magnetic order in the iridium oxide Na_2IrO_3. *Phys. Rev. Lett.*, 110:097204, Feb 2013.

[15] J. A. Sears, M. Songvilay, K. W. Plumb, J. P. Clancy, Y. Qiu, Y. Zhao, D. Parshall, and Young-June Kim. Magnetic order in α-$RuCl_3$: A honeycomb-lattice quantum magnet with strong spin-orbit coupling. *Phys. Rev. B*, 91:144420, Apr 2015.

[16] Gia-Wei Chern, Yuriy Sizyuk, Craig Price, and Natalia B. Perkins. Kitaev-heisenberg model in a magnetic field: Order-by-disorder and commensurate-incommensurate transitions. *Phys. Rev. B*, 95:144427, Apr 2017.

[17] Villain, J., Bidaux, R., Carton, J.-P., and Conte, R. Order as an effect of disorder. *J. Phys. France*, 41(11):1263–1272, 1980.

[18] E.F. Shender. Antiferromagnetic garnets with fluctuationally interacting sublattices. *Sov. Phys. JETP*, 56(1):178, 1982.

[19] Yuriy Sizyuk, Natalia B. Perkins, and Peter Wölfle. Lifting mean-field degeneracies in anisotropic classical spin systems. *Phys. Rev. B*, 92:155131, Oct 2015.

[20] Peter Wölfle, Natalia B. Perkins, and Yuriy Sizyuk. Free energy of quantum spin systems: Functional integral representation. *Phys. Rev. B*, 95:184408, May 2017.

[21] Yuriy Sizyuk, Peter Wölfle, and Natalia B. Perkins. Selection of direction of the ordered moments in Na_2IrO_3 and α-$RuCl_3$. *Phys. Rev. B*, 94:085109, Aug 2016.

[22] Lukas Janssen, Eric C. Andrade, and Matthias Vojta. Honeycomb-lattice heisenberg-kitaev model in a magnetic field: Spin canting, metamagnetism, and vortex crystals. *Phys. Rev. Lett.*, 117:277202, Dec 2016.

[23] S. J. Moon, Hosub Jin, W. S. Choi, J. S. Lee, S. S. A. Seo, J. Yu, G. Cao, T. W. Noh, and Y. S. Lee. Temperature dependence of the electronic structure of the $J_{\text{eff}} = \frac{1}{2}$ mott insulator Sr_2IrO_4 studied by optical spectroscopy. *Phys. Rev. B*, 80:195110, Nov 2009.

[24] B. J. Kim, H. Ohsumi, T. Komesu, S. Sakai, T. Morita, H. Takagi, and T. Arima. Phase-sensitive observation of a spin-orbital mott state in Sr_2IrO_4. *Science*, 323(5919):1329–1332, 2009, http://science.sciencemag.org/content/323/5919/1329.full.pdf.

[25] Jungho Kim, D. Casa, M. H. Upton, T. Gog, Young-June Kim, J. F. Mitchell, M. van Veenendaal, M. Daghofer, J. van den Brink, G. Khaliullin, and B. J. Kim. Magnetic excitation spectra of Sr_2IrO_4 probed by resonant inelastic x-ray scattering: Establishing links to cuprate superconductors. *Phys. Rev. Lett.*, 108:177003, Apr 2012.

[26] J. W. Kim, Y. Choi, Jungho Kim, J. F. Mitchell, G. Jackeli, M. Daghofer, J. van den Brink, G. Khaliullin, and B. J. Kim. Dimensionality driven spin-flop transition in layered iridates. *Phys. Rev. Lett.*, 109:037204, Jul 2012.

[27] S. Fujiyama, H. Ohsumi, T. Komesu, J. Matsuno, B. J. Kim, M. Takata, T. Arima, and H. Takagi. Two-dimensional heisenberg behavior of J_{eff}=1/2 isospins in the paramagnetic state of the spin-orbital mott insulator Sr_2IrO_4. *Phys. Rev. Lett.*, 108:247212, Jun 2012.

[28] D. Haskel, G. Fabbris, Mikhail Zhernenkov, P. P. Kong, C. Q. Jin, G. Cao, and M. van Veenendaal. Pressure tuning of the spin-orbit coupled ground state in Sr_2IrO_4. *Phys. Rev. Lett.*, 109:027204, Jul 2012.

[29] S. Boseggia, R. Springell, H. C. Walker, H. M. Rønnow, Ch. Rüegg, H. Okabe, M. Isobe, R. S. Perry, S. P. Collins, and D. F. McMorrow. Robustness of basal-plane antiferromagnetic order and the J_{eff}=1/2 state in single-layer iridate spin-orbit mott insulators. *Phys. Rev. Lett.*, 110:117207, Mar 2013.

[30] Mehmet Fatih Cetin, Peter Lemmens, Vladimir Gnezdilov, Dirk Wulferding, Dirk Menzel, Tomohiro Takayama, Kei Ohashi, and Hidenori Takagi. Crossover from coherent to incoherent scattering in spin-orbit dominated Sr_2IrO_4. *Phys. Rev. B*, 85:195148, May 2012.

[31] Fa Wang and T. Senthil. Twisted hubbard model for Sr_2IrO_4: Magnetism and possible high temperature superconductivity. *Phys. Rev. Lett.*, 106:136402, Mar 2011.

[32] Cyril Martins, Markus Aichhorn, Loïg Vaugier, and Silke Biermann. Reduced effective spin-orbital degeneracy and spin-orbital ordering in paramagnetic transition-metal oxides: Sr_2IrO_4 versus Sr_2RhO_4. *Phys. Rev. Lett.*, 107:266404, Dec 2011.

[33] Beom Hyun Kim, G. Khaliullin, and B. I. Min. Magnetic couplings, optical spectra, and spin-orbit exciton in $5d$ electron mott insulator Sr_2IrO_4. *Phys. Rev. Lett.*, 109:167205, Oct 2012.

[34] R. Arita, J. Kuneš, A. V. Kozhevnikov, A. G. Eguiluz, and M. Imada. Ab initio. *Phys. Rev. Lett.*, 108:086403, Feb 2012.

[35] Yoshihiko Okamoto, Minoru Nohara, Hiroko Aruga-Katori, and Hidenori Takagi. Spin-liquid state in the $s = 1/2$ hyperkagome antiferromagnet $Na_4Ir_3O_8$. *Phys. Rev. Lett.*, 99:137207, Sep 2007.

[36] Michael J. Lawler, Hae-Young Kee, Yong Baek Kim, and Ashvin Vishwanath. Topological spin liquid on the hyperkagome lattice of $Na_4Ir_3O_8$. *Phys. Rev. Lett.*, 100:227201, Jun 2008.

[37] S. Nakatsuji, Y. Machida, Y. Maeno, T. Tayama, T. Sakakibara, J. van Duijn, L. Balicas, J. N. Millican, R. T. Macaluso, and Julia Y. Chan. Metallic spin-liquid behavior of the geometrically frustrated kondo lattice $Pr_2Ir_2O_7$. *Phys. Rev. Lett.*, 96:087204, Mar 2006.

[38] Y. Machida, S. Nakatsuji, Y. Maeno, T. Tayama, T. Sakakibara, and S. Onoda. Unconventional anomalous hall effect enhanced by a noncoplanar spin texture in the frustrated kondo lattice $Pr_2Ir_2O_7$. *Phys. Rev. Lett.*, 98:057203, Jan 2007.

[39] Yo Machida, Satoru Nakatsuji, Shigeki Onoda, Takashi Tayama, and Toshiro Sakakibara. Time-reversal symmetry breaking and spontaneous hall effect without magnetic dipole order. *Nature*, 463(7278):210–213, Jan 2010.

[40] Dmytro Pesin and Leon Balents. Mott physics and band topology in materials with strong spin-orbit interaction. *Nat Phys*, 6(5):376–381, May 2010.

[41] Bohm-Jung Yang and Yong Baek Kim. Topological insulators and metal-insulator transition in the pyrochlore iridates. *Phys. Rev. B*, 82:085111, Aug 2010.

[42] Eric Kin-Ho Lee, Subhro Bhattacharjee, and Yong Baek Kim. Magnetic excitation spectra in pyrochlore iridates. *Phys. Rev. B*, 87:214416, Jun 2013.

[43] Songrui Zhao, J. M. Mackie, D. E. MacLaughlin, O. O. Bernal, J. J. Ishikawa, Y. Ohta, and S. Nakatsuji. Magnetic transition, long-range order, and moment fluctuations in the pyrochlore iridate $eu_2ir_2o_7$. *Phys. Rev. B*, 83:180402, May 2011.

[44] Jun J. Ishikawa, Eoin C. T. O'Farrell, and Satoru Nakatsuji. Continuous transition between antiferromagnetic insulator and paramagnetic metal in the pyrochlore iridate $eu_2ir_2o_7$. *Phys. Rev. B*, 85:245109, Jun 2012.

[45] Atsuo Shitade, Hosho Katsura, Jan Kuneš, Xiao-Liang Qi, Shou-Cheng Zhang, and Naoto Nagaosa. Quantum spin hall effect in a transition metal oxide Na_2IrO_3. *Phys. Rev. Lett.*, 102:256403, Jun 2009.

[46] Ji ří Chaloupka, George Jackeli, and Giniyat Khaliullin. Kitaev-heisenberg model on a honeycomb lattice: Possible exotic phases in iridium oxides A_2IrO_3. *Phys. Rev. Lett.*, 105:027204, Jul 2010.

[47] Yogesh Singh, S. Manni, J. Reuther, T. Berlijn, R. Thomale, W. Ku, S. Trebst, and P. Gegenwart. Relevance of the heisenberg-kitaev model for the honeycomb lattice iridates A_2IrO_3. *Phys. Rev. Lett.*, 108:127203, Mar 2012.

[48] X. Liu, T. Berlijn, W.-G. Yin, W. Ku, A. Tsvelik, Young-June Kim, H. Gretarsson, Yogesh Singh, P. Gegenwart, and J. P. Hill. Long-range magnetic ordering in na_2iro_3. *Phys. Rev. B*, 83:220403, Jun 2011.

[49] Feng Ye, Songxue Chi, Huibo Cao, Bryan C. Chakoumakos, Jaime A. Fernandez-Baca, Radu Custelcean, T. F. Qi, O. B. Korneta, and G. Cao. Direct evidence of a zigzag spin-chain structure in the honeycomb lattice: A neutron and x-ray diffraction investigation of single-crystal na_2iro_3. *Phys. Rev. B*, 85:180403, May 2012.

[50] Craig C. Price and Natalia B. Perkins. Critical properties of the kitaev-heisenberg model. *Phys. Rev. Lett.*, 109:187201, Nov 2012.

[51] Craig Price and Natalia B. Perkins. Finite-temperature phase diagram of the classical kitaev-heisenberg model. *Phys. Rev. B*, 88:024410, Jul 2013.

[52] T. F. Qi, O. B. Korneta, L. Li, K. Butrouna, V. S. Cao, Xiangang Wan, P. Schlottmann, R. K. Kaul, and G. Cao. Spin-orbit tuned metal-insulator transitions in single-crystal $Sr_2Ir_{1-x}Rh_xO_4$ ($0 \leq x \leq 1$). *Phys. Rev. B*, 86:125105, Sep 2012.

[53] Yongkang Luo, Chao Cao, Bingqi Si, Yuke Li, Jinke Bao, Hanjie Guo, Xiaojun Yang, Chenyi Shen, Chunmu Feng, Jianhui Dai, Guanghan Cao, and Zhu-an Xu. Li_2rho_3: A spin-glassy relativistic mott insulator. *Phys. Rev. B*, 87:161121, Apr 2013.

[54] Vamshi M. Katukuri, Hermann Stoll, Jeroen van den Brink, and Liviu Hozoi. Ab initio. *Phys. Rev. B*, 85:220402, Jun 2012.

[55] I. Dzyaloshinsky. A thermodynamic theory of weak ferromagnetism of antiferromagnetics. *Journal of Physics and Chemistry of Solids*, 4(4):241 – 255, 1958.

[56] Tôru Moriya. New mechanism of anisotropic superexchange interaction. *Phys. Rev. Lett.*, 4:228–230, Mar 1960.

[57] R. Comin, G. Levy, B. Ludbrook, Z.-H. Zhu, C. N. Veenstra, J. A. Rosen, Yogesh Singh, P. Gegenwart, D. Stricker, J. N. Hancock, D. van der Marel, I. S. Elfimov, and A. Damascelli. Na_2IrO_3 as a novel relativistic mott insulator with a 340-mev gap. *Phys. Rev. Lett.*, 109:266406, Dec 2012.

[58] S. Fujiyama, H. Ohsumi, K. Ohashi, D. Hirai, B. J. Kim, T. Arima, M. Takata, and H. Takagi. Spin and orbital contributions to magnetically ordered moments in 5*d* layered perovskite Sr_2IrO_4. *Phys. Rev. Lett.*, 112:016405, Jan 2014.

[59] S. K. Choi, R. Coldea, A. N. Kolmogorov, T. Lancaster, I. I. Mazin, S. J. Blundell, P. G. Radaelli, Yogesh Singh, P. Gegenwart, K. R. Choi, S.-W. Cheong, P. J. Baker, C. Stock, and J. Taylor. Spin waves and revised crystal structure of honeycomb iridate Na_2IrO_3. *Phys. Rev. Lett.*, 108:127204, Mar 2012.

[60] Subhro Bhattacharjee, Sung-Sik Lee, and Yong Baek Kim. Spinorbital locking, emergent pseudo-spin and magnetic order in honeycomb lattice iridates. *New Journal of Physics*, 14(7):073015, 2012.

[61] Vamshi M Katukuri, S Nishimoto, V Yushankhai, A Stoyanova, H Kandpal, Sungkyun Choi, R Coldea, I Rousochatzakis, L Hozoi, and Jeroen van den Brink. Kitaev interactions between j = 1/2 moments in honeycomb na 2 iro 3 are large and ferromagnetic: insights from ab initio quantum chemistry calculations. *New Journal of Physics*, 16(1):013056, 2014.

[62] Youhei Yamaji, Yusuke Nomura, Moyuru Kurita, Ryotaro Arita, and Masatoshi Imada. First-principles study of the honeycomb-lattice iridates Na_2IrO_3 in the presence of strong spin-orbit interaction and electron correlations. *Phys. Rev. Lett.*, 113:107201, Sep 2014.

[63] Kateryna Foyevtsova, Harald O. Jeschke, I. I. Mazin, D. I. Khomskii, and Roser Valentí. Ab initio. *Phys. Rev. B*, 88:035107, Jul 2013.

[64] H. Gretarsson, J. P. Clancy, X. Liu, J. P. Hill, Emil Bozin, Yogesh Singh, S. Manni, P. Gegenwart, Jungho Kim, A. H. Said, D. Casa, T. Gog, M. H. Upton, Heung-Sik

Kim, J. Yu, Vamshi M. Katukuri, L. Hozoi, Jeroen van den Brink, and Young-June Kim. Crystal-field splitting and correlation effect on the electronic structure of A_2IrO_3. *Phys. Rev. Lett.*, 110:076402, Feb 2013.

[65] Giniyat Khaliullin. Orbital order and fluctuations in mott insulators. *Progress of Theoretical Physics Supplement*, 160:155, 2005.

[66] Stephan Rachel and Karyn Le Hur. Topological insulators and mott physics from the hubbard interaction. *Phys. Rev. B*, 82:075106, Aug 2010.

[67] Johannes Reuther, Ronny Thomale, and Stephan Rachel. Magnetic ordering phenomena of interacting quantum spin hall models. *Phys. Rev. B*, 86:155127, Oct 2012.

[68] C. L. Kane and E. J. Mele. Z_2 topological order and the quantum spin hall effect. *Phys. Rev. Lett.*, 95:146802, Sep 2005.

[69] C. L. Kane and E. J. Mele. Quantum spin hall effect in graphene. *Phys. Rev. Lett.*, 95:226801, Nov 2005.

[70] Johannes Reuther, Ronny Thomale, and Stephan Rachel. Spiral order in the honeycomb iridate Li_2IrO_3. *Phys. Rev. B*, 90:100405, Sep 2014.

[71] Jeffrey G. Rau, Eric Kin-Ho Lee, and Hae-Young Kee. Generic spin model for the honeycomb iridates beyond the kitaev limit. *Phys. Rev. Lett.*, 112:077204, Feb 2014.

[72] Ioannis Rousochatzakis, Ulrich K. Rössler, Jeroen van den Brink, and Maria Daghofer. Kitaev anisotropy induces mesoscopic F_2 vortex crystals in frustrated hexagonal antiferromagnets. *Phys. Rev. B*, 93:104417, Mar 2016.

[73] Michael Becker, Maria Hermanns, Bela Bauer, Markus Garst, and Simon Trebst. Spin-orbit physics of $j = \frac{1}{2}$ mott insulators on the triangular lattice. *Phys. Rev. B*, 91:155135, Apr 2015.

[74] Eran Sela, Hong-Chen Jiang, Max H. Gerlach, and Simon Trebst. Order-by-disorder and spin-orbital liquids in a distorted heisenberg-kitaev model. *Phys. Rev. B*, 90:035113, Jul 2014.

[75] P. M. Chaikin and T. C. Lubensky. *Principles of condensed matter physics*. Cambridge University Press,, 1995.

[76] Ji ří Chaloupka and Giniyat Khaliullin. Hidden symmetries of the extended kitaev-heisenberg model: Implications for the honeycomb-lattice iridates A_2IrO_3. *Phys. Rev. B*, 92:024413, Jul 2015.

[77] Ji ří Chaloupka and Giniyat Khaliullin. Magnetic anisotropy in the kitaev model systems Na_2IrO_3 and $RuCl_3$. *Phys. Rev. B*, 94:064435, Aug 2016.

[78] Ioannis Rousochatzakis and Natalia B. Perkins. Classical spin liquid instability driven by off-diagonal exchange in strong spin-orbit magnets. *Phys. Rev. Lett.*, 118:147204, Apr 2017.

[79] A. Catuneanu, Y. Yamaji, G. Wachtel, H.-Y. Kee, and Y. B. Kim. Realizing quantum spin liquid phases in spin-orbit driven correlated materials. *arXiv:1701.07837*.

[80] K. A. Modic, Tess E. Smidt, Itamar Kimchi, Nicholas P. Breznay, Alun Biffin, Sungkyun Choi, Roger D. Johnson, Radu Coldea, Pilanda Watkins-Curry, Gregory T. McCandless, Julia Y. Chan, Felipe Gandara, Z. Islam, Ashvin Vishwanath, Arkady Shekhter, Ross D. McDonald, and James G. Analytis. Realization of a three-dimensional spinanisotropic harmonic honeycomb iridate. 5:4203 EP –, Jun 2014. Article.

[81] Heung-Sik Kim and Hae-Young Kee. Crystal structure and magnetism in α-$RuCl_3$: An ab initio study. *Phys. Rev. B*, 93:155143, Apr 2016.

[82] Ravi Yadav, Nikolay A. Bogdanov, Vamshi M. Katukuri, Satoshi Nishimoto, Jeroen van den Brink, and Liviu Hozoi. Kitaev exchange and field-induced quantum spin-liquid states in honeycomb α-$rucl_3$. 6:37925 EP –, Nov 2016. Article.

[83] Eric Kin-Ho Lee and Yong Baek Kim. Theory of magnetic phase diagrams in hyperhoneycomb and harmonic-honeycomb iridates. *Phys. Rev. B*, 91:064407, Feb 2015.

[84] D. H. Torchinsky, H. Chu, L. Zhao, N. B. Perkins, Y. Sizyuk, T. Qi, G. Cao, and D. Hsieh. Structural distortion-induced magnetoelastic locking in sr_2iro_4 revealed

through nonlinear optical harmonic generation. *Phys. Rev. Lett.*, 114:096404, Mar 2015.

[85] Zohar Nussinov and Jeroen van den Brink. Compass models: Theory and physical motivations. *Rev. Mod. Phys.*, 87:1–59, Jan 2015.

[86] Ioannis Rousochatzakis, Johannes Reuther, Ronny Thomale, Stephan Rachel, and N. B. Perkins. Phase diagram and quantum order by disorder in the kitaev K_1-K_2 honeycomb magnet. *Phys. Rev. X*, 5:041035, Dec 2015.

[87] Andrey Chubukov. Order from disorder in a kagomé antiferromagnet. *Phys. Rev. Lett.*, 69:832–835, Aug 1992.

[88] M. E. Zhitomirsky, M. V. Gvozdikova, P. C. W. Holdsworth, and R. Moessner. Quantum order by disorder and accidental soft mode in $Er_2Ti_2O_7$. *Phys. Rev. Lett.*, 109:077204, Aug 2012.

[89] Gia-Wei Chern and R. Moessner. Dipolar order by disorder in the classical heisenberg antiferromagnet on the kagome lattice. *Phys. Rev. Lett.*, 110:077201, Feb 2013.

[90] Paul A. McClarty, Pawel Stasiak, and Michel J. P. Gingras. Order-by-disorder in the xy pyrochlore antiferromagnet. *Phys. Rev. B*, 89:024425, Jan 2014.

[91] A. L. Chernyshev and M. E. Zhitomirsky. Quantum selection of order in an xxz antiferromagnet on a kagome lattice. *Phys. Rev. Lett.*, 113:237202, Dec 2014.

[92] A. L. Chernyshev and M. E. Zhitomirsky. Order and excitations in large - S kagome-lattice antiferromagnets. *Phys. Rev. B*, 92:144415, Oct 2015.

[93] Behnam Javanparast, Zhihao Hao, Matthew Enjalran, and Michel J. P. Gingras. Fluctuation-driven selection at criticality in a frustrated magnetic system: The case of multiple-**k** partial order on the pyrochlore lattice. *Phys. Rev. Lett.*, 114:130601, Apr 2015.

[94] Behnam Javanparast, Alexandre G. R. Day, Zhihao Hao, and Michel J. P. Gingras. Order-by-disorder near criticality in xy pyrochlore magnets. *Phys. Rev. B*, 91:174424, May 2015.

[95] L. D. C. Jaubert, Owen Benton, Jeffrey G. Rau, J. Oitmaa, R. R. P. Singh, Nic Shannon, and Michel J. P. Gingras. Are multiphase competition and order by disorder the keys to understanding $Yb_2Ti_2O_7$? *Phys. Rev. Lett.*, 115:267208, Dec 2015.

[96] K. I. Kugel and D. I. Khomskii. The jahn-teller effect and magnetism: transition metal compounds. *Phys. Usp.*, 25(4):231–256, 1982.

[97] Z. Nussinov, M. Biskup, L. Chayes, and J. van den Brink. Orbital order in classical models of transition-metal compounds. *EPL (Europhysics Letters)*, 67(6):990, 2004.

[98] Zohar Nussinov and Eduardo Fradkin. Discrete sliding symmetries, dualities, and self-dualities of quantum orbital compass models and $p + ip$ superconducting arrays. *Phys. Rev. B*, 71:195120, May 2005.

[99] Lukasz Cincio, Jacek Dziarmaga, and Andrzej M. Oleś. Spontaneous symmetry breaking in a generalized orbital compass model. *Phys. Rev. B*, 82:104416, Sep 2010.

[100] Joji Nasu, Synge Todo, and Sumio Ishihara. Ordering and excitation in orbital compass model on a checkerboard lattice. *Phys. Rev. B*, 85:205141, May 2012.

[101] Wojciech Brzezicki and Andrzej M. Oleś. Symmetry properties and spectra of the two-dimensional quantum compass model. *Phys. Rev. B*, 87:214421, Jun 2013.

[102] C. D. Batista and Zohar Nussinov. Generalized elitzur's theorem and dimensional reductions. *Phys. Rev. B*, 72:045137, Jul 2005.

[103] M. Biskup, L. Chayes, and Z. Nussinov. Orbital ordering in transition-metal compounds: I. the 120-degree model. *Communications in Mathematical Physics*, 255(2):253–292, 2005.

[104] Gia-Wei Chern, Natalia Perkins, and Zhihao Hao. Quantum 120° model on pyrochlore lattice: Orbital ordering in MnV_2O_4. *Phys. Rev. B*, 81:125127, Mar 2010.

[105] J. Oitmaa and C. J. Hamer. Quantum compass model on the square and simple-cubic lattices. *Phys. Rev. B*, 83:094437, Mar 2011.

[106] F. Trousselet, A. M. Ole, and P. Horsch. Compass-heisenberg model on the square lattice spin order and elementary excitations. *EPL (Europhysics Letters)*, 91(4):40005, 2010.

[107] G. Khaliullin. Order from disorder: Quantum spin gap in magnon spectra of $LaTiO_3$. *Phys. Rev. B*, 64:212405, Nov 2001.

[108] Sandro Wenzel, Wolfhard Janke, and Andreas M. Läuchli. Re-examining the directional-ordering transition in the compass model with screw-periodic boundary conditions. *Phys. Rev. E*, 81:066702, Jun 2010.

[109] A. A. Vladimirov, D. Ihle, and N. M. Plakida. Magnetic order and spin excitations in layered heisenberg antiferromagnets with compass-model anisotropies. *JETP Letters*, 100(12):780–785, 2015.

[110] Max H. Gerlach and Wolfhard Janke. First-order directional ordering transition in the three-dimensional compass model. *Phys. Rev. B*, 91:045119, Jan 2015.

[111] J. W. Negele and H. Orland. *Quantum Many Particle Systems*. Westview Press, Boulder, 1998.

[112] E. Fradkin. *Field Theories of Condensed Matter Physics*. Cambridge University Press, Cambridge, UK, 2013.

[113] J. Hubbard. Calculation of partition functions. *Phys. Rev. Lett.*, 3:77–78, Jul 1959.

[114] R. L. Stratonovich. On a Method of Calculating Quantum Distribution Functions. *Soviet Physics Doklady*, 2:416, July 1957.

[115] ANTIMO ANGELUCCI and GIANCARLO JUG. Novel path integral approach to effective field theories for d-dimensional quantum spin systems. *International Journal of Modern Physics B*, 03(07):1069–1083, 1989, http://www.worldscientific.com/doi/pdf/10.1142/S0217979289000737.

[116] Antimo Angelucci. Path-integral analysis of frustrated quantum heisenberg models. *Phys. Rev. B*, 44:6849–6857, Oct 1991.

[117] Antimo Angelucci. Incommensurate correlations in quantum spin models. *Phys. Rev. B*, 45:5387–5394, Mar 1992.

[118] H. F. Trotter. On the product of semi-groups of operators. *Proc. Amer. Math. Soc.*, 10(4):545–551, 1959.

[119] H. Gretarsson, J. P. Clancy, Yogesh Singh, P. Gegenwart, J. P. Hill, Jungho Kim, M. H. Upton, A. H. Said, D. Casa, T. Gog, and Young-June Kim. Magnetic excitation spectrum of na_2iro_3 probed with resonant inelastic x-ray scattering. *Phys. Rev. B*, 87:220407, Jun 2013.

[120] Sae Hwan Chun, Jong-Woo Kim, Jungho Kim, H. Zheng, Constantinos C. Stoumpos, C. D. Malliakas, J. F. Mitchell, Kavita Mehlawat, Yogesh Singh, Y. Choi, T. Gog, A. Al-Zein, M. Moretti Sala, M. Krisch, J. Chaloupka, G. Jackeli, G. Khaliullin, and B. J. Kim. Direct evidence for dominant bond-directional interactions in a honeycomb lattice iridate na2iro3. *Nat Phys*, 11(6):462–466, Jun 2015. Letter.

[121] R. D. Johnson, S. C. Williams, A. A. Haghighirad, J. Singleton, V. Zapf, P. Manuel, I. I. Mazin, Y. Li, H. O. Jeschke, R. Valentí, and R. Coldea. Monoclinic crystal structure of α-$RuCl_3$ and the zigzag antiferromagnetic ground state. *Phys. Rev. B*, 92:235119, Dec 2015.

[122] A. Banerjee, C. A. Bridges, J.-Q. Yan, A. A. Aczel, L. Li, M. B. Stone, G. E. Granroth, M. D. Lumsden, Y. Yiu, J. Knolle, S. Bhattacharjee, D. L. Kovrizhin, R. Moessner, D. A. Tennant, D. G. Mandrus, and S. E. Nagler. Proximate kitaev quantum spin liquid behaviour in a honeycomb magnet. *Nat Mater*, 15(7):733–740, Jul 2016. Article.

[123] H. B. Cao, A. Banerjee, J.-Q. Yan, C. A. Bridges, M. D. Lumsden, D. G. Mandrus, D. A. Tennant, B. C. Chakoumakos, and S. E. Nagler. Low-temperature crystal and magnetic structure of α-$RuCl_3$. *Phys. Rev. B*, 93:134423, Apr 2016.

[124] Itamar Kimchi and Ashvin Vishwanath. Kitaev-heisenberg models for iridates on the triangular, hyperkagome, kagome, fcc, and pyrochlore lattices. *Phys. Rev. B*, 89:014414, Jan 2014.

[125] J. M. Luttinger and L. Tisza. Theory of dipole interaction in crystals. *Phys. Rev.*, 70:954–964, Dec 1946.

[126] D. B. Litvin. The luttinger-tisza method. *Physica*, 77:205–219, oct 1974.

[127] T. A. Kaplan and N. Menyuk. Spin ordering in three-dimensional crystals with strong competing exchange interactions. *Philosophical Magazine*, 87(25):3711–3785, 2007, http://dx.doi.org/10.1080/14786430601080229.

[128] Heung-Sik Kim, Vijay Shankar V., Andrei Catuneanu, and Hae-Young Kee. Kitaev magnetism in honeycomb $RuCl_3$ with intermediate spin-orbit coupling. *Phys. Rev. B*, 91:241110, Jun 2015.

[129] J. Zheng, K. Ran, T. Li, J. Wang, P. Wang, B. Liu, Z. Liu, B. Normand, J. Wen, and W. Yu. Gapless spin excitations in the field-induced quantum spin liquid phase of α-$RuCl_3$. *arXiv:1703.08474*.

[130] S.-H. Baek, S.-H. Do, K.-Y. Choi, Y. S. Kwon, A.U.B. Wolter, S. Nishimoto, Jeroen van den Brink, and B. Buchner. Observation of a field-induced quantum spin liquid in α-$RuCl_3$. *arXiv:1702.01671*.

[131] A. Biffin, R. D. Johnson, Sungkyun Choi, F. Freund, S. Manni, A. Bombardi, P. Manuel, P. Gegenwart, and R. Coldea. Unconventional magnetic order on the hyperhoneycomb kitaev lattice in β-Li_2IrO_3: Full solution via magnetic resonant x-ray diffraction. *Phys. Rev. B*, 90:205116, Nov 2014.

[132] A. Biffin, R. D. Johnson, I. Kimchi, R. Morris, A. Bombardi, J. G. Analytis, A. Vishwanath, and R. Coldea. Noncoplanar and counterrotating incommensurate magnetic order stabilized by kitaev interactions in γ-Li_2IrO_3. *Phys. Rev. Lett.*, 113:197201, Nov 2014.

Appendix A

Glossary and Acronyms

Care has been taken in this thesis to minimize the use of jargon and acronyms, but this cannot always be achieved. This appendix defines jargon terms in a glossary, and contains a table of acronyms and their meaning.

A.1 Glossary

- **Pseudospin** – A localized magnetic moment that has an orbital component in addition to spin.
- **Jackeli-Khaliullin Kitaev materials** (**JKK**) – Materials in which the Kitaev anisotropic interaction is realized by interference of 2 hopping paths of the edge sharing octahedra and with large spin orbit coupling, a scheme originally proposed by Jackeli and Khaliullin. These include Na_2IrO_3, (α, β, γ)-Li_2IrO_3 and α-$RuCl_3$.

A.2 Acronyms

Table A.1: Acronyms

Acronym	Meaning
SO/SOC	Spin-Orbit coupling
	Continued on next page

Table A.1 – continued from previous page

Acronym	Meaning
CF	Crystal field
DM	Dzyaloshinsky-Moriya interaction
TM	Transition metal
KH	Kitaev-Heisenberg (model)
n. n.	Nearest neighbor
n. n. n.	Next nearest neighbor
QSL	Quantum spin liquid
JKK	Jackeli-Khaliullin Kitaev (materials)
BZ	Brillouin zone
CW	Curie-Weiss (temperature)
FM	Ferromagnetic
AFM	Antiferromagnetic